Silicon-Integrated Two-Dimensional Phononic Band Gap Quasi-Crystal Architecture

by

Ryan Christopher Norris

A thesis
presented to the University of Waterloo
in fulfilment of the
thesis requirement for the degree of
Doctor of Philosophy
in
Electrical and Computer Engineering

Waterloo, Ontario, Canada, 2011

I hereby declare that I am the sole author of this thesis. This is a true copy of the thesis, including any required final revisions, as accepted by my examiners.

I understand that my thesis may be made electronically available to the public.

Abstract

Silicon integrated phononics, dealing with the integration of phononic band gap (P^nBG) crystals, also referred to as the acoustic or elastic band gap crystals, into silicon is an area of research originating within the last two decades and has important implications for the study of basic physics as well as for the realization of a device platform that may be utilized to build important and practical signal processing and sensor devices and other structures in engineering applications. P^nBG research appears to display the potential for application in electronics to heat and noise control (e.g. insulators), photonics for enhanced photon-phonon interaction and control, mechatronics and reliability in micro-electro-mechanical system (MEMS) for anchor loss reduction and vibration stabilization, energy harvesting, acoustics for impedance matching layers and metamaterials, material science and nanotechnology, nano-acoustics (for example, graphene based structures), nano-photonics (for example, to control the P^nBG of materials utilized in tera-hertz lasers), communications for low power signal processing elements and so forth. This thesis is focused on researching the realization of the relatively new phenomenon of two-dimensional classical elastic wave P^nBG phenomenon to create novel MEMS technologies utilizing silicon processing techniques. Within the thesis a new device architecture is proposed and referred to as the phononic band gap quasi-crystal (P^nBG QC) architecture. Numerical simulations report that behavior that resembles P^nBG behavior will only occur for limited combinations of P^nBG QC feature dimensions and silicon plate thicknesses. Utilizing novel geometries we have fabricated practical silicon-plate P^nBG QC MEMS devices that appear to be the first of their kind in a silicon MEMS technology.

Current approaches to the micro-integration of P^nBG crystals rely on exotic piezo-

electric transduction, P^{n}BG crystals etched into semi-infinite or finite-thickness slabs through which surface or slab elastic waves travel and P^{n}BG crystal truncation typically by homogeneous mediums or piezoelectric transducers. The P^{n}BG QC architecture presented in this thesis is a solution that utilizes electrostatic transduction to provide an alternative to the use of piezoelectric transduction thereby eliminating the need for piezoelectric materials. Electrostatic actuation mitigates the use of piezoelectric transducers and provides action at a distance type forces so that P^{n}BG QC edges may be free standing for potentially reduced anchor loss. The P^{n}BG QC architecture requires only one material layer and utilizes free standing serrated edges along the truncation boundary of the P^{n}BG QC. While the literature presents the use of a rectangular P^{n}BG crystal truncation boundary, this thesis investigates the utilization of both circular and square truncation boundary geometries. The literature does not appear to report methods to optimize the P^{n}BG crystal truncation boundary, while this thesis develops a tuning methodology for serrated edges and tethers to enable complete band gap formation in the presence of the non-idealities of finite periodicity of the P^{n}BG QC and attachment of anchored tethers to the P^{n}BG QC. The freestanding P^{n}BG QC may improve energy confinement for potentially reduced substrate mode loss, and potentially improved in-plane energy confinement, compared with contemporary surface, and slab, respectively, wave P^{n}BG crystals. Air inclusions are utilized in the P^{n}BG QC to provide a high acoustic impedance contrast with a solid host material and potentially reduced motional resistance (higher compliance than a solid inclusion).

The P^{n}BG QC architecture represents a significantly new geometry and so an extensive model is developed to characterize the performance starting with analytical models of the lumped element electrical circuit and electrostatic transducers, and advancing to

multi-physics finite element method models of mode shape, dynamic harmonic response, and electromechanical coupling, then progressing to lumped element mechanical models of harmonic response, and semi-analytical structural and vibration models. Lastly, the finite element method is utilized to perform a sensitivity analysis versus geometrical parameters and characterize the mechanical scaling properties of the P^{n}BG QC architecture. The models verify the design methodology for yielding complete band gap formation. Moreover, the models indicate that while the proposed P^{n}BG QC architecture resembles a distributed mechanical system, the P^{n}BG QC architecture may yield insight into unique design approaches for two-dimensional mechanically coupled lumped element resonators by providing a relatively easy to utilize method to interconnect large arrays of mass-spring resonator elements where the order of the P^{n}BG QC based resonator array may be controlled relatively easily by adjusting the P^{n}BG QC truncation boundary location.

A set of P^{n}BG QC devices that is representative of the proposed P^{n}BG QC architecture is fabricated in a multi-user silicon-on-insulator process. Reasonable experimental verification of the electrostatically actuated P^{n}BG QC architecture is obtained through dynamic harmonic analysis and mode shape topography measurements obtained utilizing optical non-destructive laser-Doppler velocimetry. The measurements provide fundamental information regarding the novel electrostatic transduction mechanisms, effects of damping and process non-idealities, and unique behavioral characteristics of the P^{n}BG QC architecture in the spatial and frequency vibration domain. This represents to the best of our knowledge, for the first time, both the theory, design methodology and experiment of an electrostatically actuated architecture for the integration of devices based on two-dimensional P^{n}BG crystal geometries into silicon and displays the potential to

serve as a platform for the development of a new generation of silicon-integrated sensors and signal processing elements and improved mechanical systems.

Furthermore, an investigation is presented into the applicability of the P^{n}BG QC architecture to the development of physical temperature sensors and advanced signal processing elements. Experimental measurements at elevated temperatures created utilizing an infrared radiation source indicate that one of the fabricated P^{n}BG QC devices displays a negative temperature coefficient and comparable temperature dependence to a bulk resonator. The thermomechanical performance is also characterized utilizing a finite element method model. Lastly, to investigate applicability to signal processing elements and achieve a more complex mechanical frequency response, a modification to the P^{n}BG QC architecture is proposed by introducing defect states into a P^{n}BG QC to create intentionally induced vibration modes (also referred to as defect states) within the band gap. These defect state vibrations modes are numerically illustrated to be localized within the core of the P^{n}BG QC and may illustrate potential mechanisms for vibration stabilization and anchor loss reduction in mechanical systems, the engineering of complex frequency characteristics for signal processing elements and general mechanical system design.

Acknowledgments

First and foremost, I would like to express my sincere gratitude to my advisors Professor Patricia Nieva, Professor C.R. Selvakumar and Professor John Hamel for their engaging technical discussions and intellectual leadership throughout my graduate studies.

I thank my colleagues, family and friends and my committee members Professor Amir Khajepour, Professor Dayan Ban and Professor Siva Sivoththaman for their suggestions and support.

This thesis is in part a treatment of a small contribution to knowledge and in part to show that through unrelenting dedication dreams can become goals, visions can become reality, and some philosophical conjectures can become answerable scientific questions.

This thesis is dedicated to my mother and father, their love and guidance is without measure.

Contents

List of Figures

List of Tables

List of Abbreviations

3D: Three-Dimensional

AC: Alternating Current

AlN: Aluminium Nitride

BAW: Bulk Acoustic Wave

BCC: Body Centered Cubic

CMC: Canadian Microelectronics Corporation

CMOS: Complementary Metal Oxide Semiconductor

CMUT: Capacitive MEMS Ultrasonic Transducer

DC: Direct Current

DFEM: Dynamic Finite Element Method

DOF: Degrees of Freedom

DOS: Density of States

DUT: Device Under Test

FBAR: Film Bulk Acoustic Resonator

FCC: Face Centered Cubic

FD-FEM: Frequency Domain-Finite Element Method

FDTD: Finite Difference Time Domain

FEM: Finite Element Method

GPIB: General Purpose Interface Bus

HCP: Hexagonal Close Packed

HF: High Frequency

IDT: Inter-Digital Transducer

IPMS: Infinitely Periodic Mass-Spring

LA: Longitudinal Acoustical

LAW: Lamb Acoustic Wave

LBAW: Lateral Bulk Acoustic Wave

LF: Low Frequency

$LiNbO_3$: Lithium Niobate

LM: Lumped Mass

LO: Longitudinal Optical

LRSM: Locally Resonant Sonic Materials

MEMS: Micro-Electro-Mechanical-Systems

MST: Multiple Scattering Technique

N/A: Not Applicable

PCF: Photonic Crystal Fiber

P^nBG: Phononic Band Gap

P^nBG QC: Phononic Band Gap Quasi-Crystal

PSG: Phosphosilicate Glass

P^tBG: Photonic Band Gap

PWE: Plane Wave Expansion

PZT5A: Lead Zirconate Titanate 5A

RF: Radio Frequency

SAW: Surface Acoustic Wave

SC: Simple Cubic

SC-PWE: Super Cell-Plane Wave Expansion

SEM: Scanning Electron Microscope

SFIT: Slanted Finger Interdigital Transducer

Si: Silicon

SiC: Silicon Carbide

SiO_2: Silicon Dioxide

SMR: Solidly Mounted Resonator

SOI: Silicon-On-Insulator

SOIMUMPs: Silicon-On-Insulator Multi-User-MEMS-Process

TD-FEM: Time Domain-Finite Element Method

TFR: Thin Film Resonator

VM: Variational Method

W: Tungsten

WM: Wavelet Method

ZnO: Zinc Oxide

Chapter 1

Introduction

Phononic band gap (P^nBG) phenomenon for classical elastic wave localization is a relatively new area of study originating within the last two decades [1, 2, 3, 4]. P^nBG crystals, for classical elastic wave localization, are composite structures created through the N-dimensional (N = 1, 2, 3, or 4, for up to three physical dimensions and one time dimension) periodic or aperiodic arrangement of inclusion media within a host medium of contrasting characteristic acoustic impedance [5]. The energy carrying entities typically of interest within a P^nBG crystal have been elastic, acoustic, or phononic waves, and more recently optical electromagnetic waves with respect to studies involving acousto-optic interaction [6]. The solution of the elastic wave equation within unbounded P^nBG crystals results in an elastic band structure with characteristic bands of frequencies where traveling waves are permitted, ranges of frequencies referred to as the phononic band gap where all polarizations of elastic waves are attenuated, and frequencies corresponding to phononic band gap edges where standing waves may be permitted. This behavior has important implications for the study of basic physics as well as for the realization of important and practical signal processing element and sensor devices and

other structures in engineering applications.

P^{n}BG crystals may be formed through the repeated placement of one-, two- or three-dimensional unit cells. As illustrated in Figure 1.1 for a two-dimensional space centered cubic crystal lattice, a unit cell is comprised of a host medium into which an inclusion medium is embedded. Each unit cell is centered at a lattice point of the space centered cubic lattice and the distance between lattice points is the lattice constant, a. Each unit cell is characterized by a fill factor, ff, which for one-, two- or three-dimensional P^{n}BG crystals is the ratio of inclusion length, area, or volume, to total unit cell length, area, or volume:

$$\begin{aligned} ff_{1D} &= \frac{inclusion\ length}{unit\ cell\ length} \quad (one-dimensional\ P^{n}BG\ crystal), \\ ff_{2D} &= \frac{inclusion\ area}{unit\ cell\ area} \quad (two-dimensional\ P^{n}BG\ crystal), \quad or \\ ff_{3D} &= \frac{inclusion\ volume}{unit\ cell\ volume} \quad (three-dimensional\ P^{n}BG\ crystal), \end{aligned} \tag{1.1}$$

respectively. The host medium and inclusion medium differ in their acoustic impedance, which is given by:

$$\begin{aligned} Z &= \rho c \\ &= \sqrt{\rho E} \end{aligned} \tag{1.2}$$

where ρ is the material density, c is the acoustic or elastic wave velocity and E is Young's modulus. P^{n}BG crystals may also be referred to as acoustic band gap, elastic band gap or sonic band gap crystals.

The elastic band structure of a P^{n}BG crystal is analogous to the electronic band structure of semiconductors and the electromagnetic band structure of Photonic Band Gap (P^{t}BG) or electromagnetic band gap crystals. The electronic band structure of a

semiconductor crystal is a consequence of the wave nature of the electrons present in the periodically varying electric potential field that is produced by the periodic array of atomic nuclei. The electromagnetic band structure of a P$^{\mathrm{t}}$BG crystal results from the presence of electromagnetic waves in a periodic array of inclusions, whose dielectric constant contrasts that of the host medium. The presence of elastic waves in the periodic P$^{\mathrm{n}}$BG crystal results in the elastic band structure and phononic band gap formation via Bragg and Mie resonance produced scattering of elastic waves off of the centers of dissimilar characteristic acoustic impedance [7]. Figure 1.1 illustrates the Bragg conditions between two of the crystal planes of a two-dimensional P$^{\mathrm{n}}$BG crystal in directions denoted by ΓX and ΓM. Assuming isotropic host and inclusion materials, the Bragg conditions may be analytically approximated for two Bragg planes of the square lattice in Figure 1.1 as [7]:

$$\begin{aligned} f_{\Gamma X} &= \frac{c_{avg}}{2a} \\ f_{\Gamma M} &= \frac{c_{avg}}{2\sqrt{2}a} \end{aligned} \tag{1.3}$$

where for circular inclusions:

$$\begin{aligned} c_{avg,circle\ inclusion} &= ff \times c_i + (1 - ff)\, c_h \\ ff &= \frac{\pi r^2}{a^2}, \end{aligned} \tag{1.4}$$

where r is the circular inclusion radius, c_i is the elastic wave velocity of the isotropic inclusion material and c_h is the elastic wave velocity of the isotropic host material, and a is the lattice constant. The ratio $ff = \frac{\pi r^2}{a^2}$ is the fill factor of a square unit cell that contains a circular inclusion of radius r. For the case of a square unit cell that contains a square inclusion, as shown in Figure 1.1, the average elastic wave velocity and fill factor

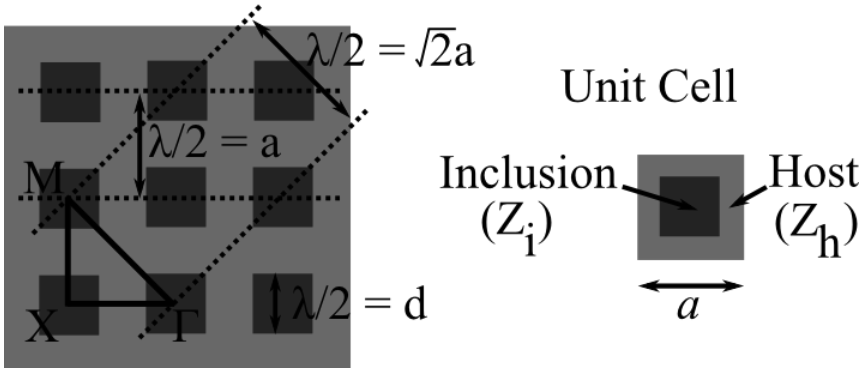

Figure 1.1: A two-dimensional simple cubic phononic band gap crystal and its corresponding unit cell. Variables: a (lattice constant), $Z_h = \rho_h c_h$ (host characteristic impedance), $Z_i = \rho_i c_i$ (inclusion characteristic impedance), ρ_h (host density), ρ_i (inclusion density), $c_{t,h}$ (host transverse velocity), $c_{l,h}$ (host longitudinal velocity), $c_{t,i}$ (inclusion transverse velocity), $c_{l,i}$ (inclusion longitudinal).

would be:

$$\begin{aligned} c_{avg,square\ inclusion} &= ff \times c_i + (1 - ff)\, c_h \\ ff &= \frac{w^2}{a^2} \end{aligned} \tag{1.5}$$

where w is width of the square inclusion.

The design parameters available to engineer the phononic band gap of P$^{\text{n}}$BG crystals include: (1) lattice type: SC (Simple Cubic), FCC (Face Centered Cubic), BCC (Body Centered Cubic), HCP (Hexagonal Close Packed), super-lattices, a-periodic lattices (e.g. random), quasi-crystal lattices (lattices of finite periodicity), and so on; (2) acoustic impedance mismatch to control the reflection coefficient involved in Bragg and Mie scattering; (3) tertiary composites to create local resonance [8]; (4) fill factor; (5) composite topology (cermet versus network topology); (6) macro and micro features: incorporation of sub-wavelength feature sizes; (7) inclusion geometry including the bulk geometry (which may overall be a circle, square, fractal [9, 10], and so on) and inclu-

sion boundary geometry (which may include finer features); (8) inclusion orientation; (9) advanced architectures: cascading P^{n}BG crystals, time varying inclusions [5], and so on; (10) dimensionality: one- (Bragg grating), two-, and three-dimensional; (11) P^{n}BG crystal alloys: hetero-mass and hetero-geometry inclusions (combine more than one material and inclusion type); (12) physical state of the host and inclusion: solid-solid, solid-fluid, solid-vacuum, fluid-solid, fluid-fluid, and so on (material systems realizable in silicon processes include semiconductor-air, semiconductor-metal, semiconductor-vacuum, semiconductor-polymer, metal-metal, metal-polymer, metal-air, polymer-air, and so on); (13) silicon-compatible materials: poly-silicon, single-crystal-silicon, silicon dioxide, silicon-germanium, silicon carbide, silicon nitride, aluminum, tungsten, copper, gold, polimide, organic materials, air, vacuum, and so forth. In addition, topology optimization [11] and genetic algorithms [12] provide methods to systematically engineer P^{n}BG crystals and often lead to non-obvious P^{n}BG crystal geometries.

The required conditions for phononic band gap formation can be case specific and may be assessed for each geometry and material system. However, guidelines to create the conditions for phononic band gap formation are available, including the utilization of hexagonal lattices [13]. In addition, it has been found that for some fluid-host fluid-inclusion systems, phononic band gaps may favor (that is, are widest for) a host medium with a high density and high velocity and an inclusion medium with a low density and low velocity [14, 15]. For solid-host solid-inclusion systems, phononic band gaps may favor a host medium with a low density and high velocity and an inclusion medium with a high density and low velocity, with the ratio of longitudinal to transverse wave velocity of host and inclusion near the $\sqrt{2}$ limit [15]. These guidelines both suggest the utilization of a high contrast in material density between the host and inclusion but further specify requirements on the material properties of both elastic wave velocity and

material density. For the cermet topology (where host density is lower than inclusion density), phononic band gaps may favor lower fill factors and occur for the widest range of fill factors [14, 13]. For the network topology (where host density is higher than inclusion density), phononic band gaps may occur at lower density contrasts but a narrower range of fill factors [13]. In some cases, phononic band gaps may favor fill factors on the order of 10% to 50% [14] and the cermet topology. The aforementioned guidelines may not all hold in general and the optimal conditions for band gap formation may be case specific and so should be assessed on a case by case basis utilizing parametric studies for each geometry and material system.

1.1 Motivation

Differences between the nature of electromagnetic waves and elastic waves may lead to different behavior between P^tBG and P^nBG crystals. Unlike electromagnetic waves, which display transverse components in lossless mediums [16], elastic waves possess both transverse and longitudinal field components and acoustic fields posses only longitudinal field components [17]. In addition, for P^tBG crystals each material is characterized by one material property: electromagnetic wave velocity or equivalently the refractive index. In contrast, each material in a P^nBG crystal is described by two material properties: material density and wave velocity, thus providing more parameters in the band gap engineering of P^nBG crystals [15]. The material density term in the elastic wave equation has no analog in electromagnetic wave equations [14]. Moreover, the longitudinal and transverse components of an elastic wave have different wave velocities, thereby further increasing the number of P^nBG crystal design parameters. This increase in complexity increases the difficulty in obtaining localization of elastic waves due to the increased number of vibrational modes [18]. On the other hand the possibility of mixing solids

with fluids in the same P^{n}BG crystal where fluids support only the longitudinal component of vibration and the transverse modes are rejected appears to lead to new behavior [18, 10]. The existence of a longitudinal component of vibration and the mixing of fluids and solids in the same crystal increases the diversity of P^{n}BG crystal structures and may potentially increase the diversity of phenomena that can be studied compared to P^{t}BG crystals. Moreover, acoustic and elastic waves behave differently from electromagnetic waves at boundaries where there is a change in characteristic impedance [19, 20]. For example, for the case of reflection from a free boundary, the longitudinal component of an elastic wave undergoes a 180^{o} phase inversion, while the transverse component undergoes no phase inversion [17, 19]. This behavior at free boundaries contrasts that of electromagnetic fields, and has the consequence that no closed form analytic expressions may be developed to describe rectangular elastic waveguides that are bounded by free boundaries [19, 20]. Acoustic and elastic waves are also more sensitive than electromagnetic waves to changes in characteristic impedance [20]. In addition, acoustic and elastic wave reflections at boundaries also display a higher level of n-refringence (where n- may be bi-, tri-, and so on) for a given level of material anisotropy as compared to electromagnetic waves [17, 19]. Thus, for a given level of anisotropy, upon reflection from a boundary, more reflected elastic waves may be produced than reflected electromagnetic waves. In addition, the high acoustic impedance contrast between an air ambient and a solid yields excellent energy confinement even within two-dimensional P^{n}BG crystals that are crafted out of a layer that is surrounded by an air ambient (since air displays a relatively low density and so high characteristic acoustic impedance contrast with a solid host), as may be the case for a P^{n}BG crystal created in a planar fabrication processes. In contrast, the index of refraction contrast between common host materials for P^{t}BG crystals and an air ambient (which displays a refractive index of approximately one) may be relatively low [21] and so P^{t}BG crystals may tend to be three-dimensional

structures that are designed to localize energy in all three directions to compensate for the low index of refraction contrast that may occur at the boundary between homogeneous optical materials and air. Hence, two-dimensional P^nBG crystals may be crafted in a simple planar fabrication process yet may still display lower loss due to leakage of energy into the ambient as compared to a comparable two-dimensional P^tBG crystal. Thus, two-dimensional P^nBG crystals are compatible with development in planar fabrication processes. Additional differences between elastic and electromagnetic waves may be found in [19, 20]. These differing governing physics suggests that only loose analogies may exist between P^nBG crystals and electromagnetic and P^tBG crystals. These unique elastic wave properties may lead to unique structures and functionalities for phonon control. The study of P^nBG crystals thus appears to be unique. This may justify the study of P^nBG crystals to pursue the potential discovery of important physical phenomenon and practical structures.

Numerous MEMS devices in which the vibrational mode wavelength is comparable to the MEMS device size have recently been developed and employ electrostatic actuation (as an alternative to piezoelectric actuation), including Lamé mode resonators [22], disc resonators [23], lateral bulk acoustic wave resonators [24, 25], CMUT (Capacitive MEMS Ultrasonic Transducer) transducers [26, 27, 28], elastic wave transmission lines [29] and delay lines [30]. There has also been a recent effort toward coupling increasingly large numbers of MEMS resonators in arrays [31]. P^nBG crystals may leverage electrostatic transduction techniques and provide significantly unique, elegant and insightful methods of designing high frequency traveling and standing wave MEMS devices and coupled resonators.

P^nBG crystal theory provides a basis for designing coupled resonators following a cell based approach, where relatively simple P^nBG crystal cells may be combined to create

more complex structures. This process somewhat mimics the cellular construction of organisms in nature, where different cells provide different functionality and interact to form a system that displays complex behavior. Similarly, different P^{n}BG crystal cells may perform specialized tasks, and these cells may be combined to perform more complex functionality all within the mechanical energy domain.

Utilizing traditional methods to create mechanically coupled resonators may require the cumbersome interconnection of numerous discrete mass-spring elements via more discrete elements each of which in themselves may display complex geometries (for example, crab leg, folded beam, ...). In contrast, P^{n}BG crystal cells may provide a relatively simple geometrical basis that could be utilized to produce a distributed mechanical system to form large arrays of resonator elements. The P^{n}BG crystal displays complex behavior where physical regions that effectively behave as a spring element at one frequency may double as a mass element at another frequency, and vice versa, potentially leading to a compact footprint, high element integration density and possibility of using relatively large arrays of distributed mass-spring elements to achieve a high filter order (quality factor).

The diversity of P^{n}BG crystal behavior may enable multiple functionalities to be integrated into a single chip ("System On Chip") utilizing just a P^{n}BG crystal as the basis for all components. Multiple functionalities may be provided by simply introducing defect states into P^{n}BG crystals. Due to the scalability of the elastic wave equation, P^{n}BG effects scale linearly with device size, and display a potential for miniaturization, saving silicon die real estate.

The study of practical P^{n}BG crystal structures may also yield important insight into the behavior of traditional MEMS at high frequency. For example, when the wavelength of traveling or standing wave vibrational modes becomes comparable to the spacing of

the periodic arrays of etch holes or dimples that are frequently incorporated into MEMS, the periodic array of etch holes or dimples become a dominant design feature to account for and could potentially be modeled as a P^{n}BG crystal in which etch holes form the inclusions. The phononic band gap effects that may be observed are illustrated by the sample frequency response of a P^{n}BG crystal in Figure 1.2 where regions of the spectrum display strong attenuation or an absence of vibrational modes. These phononic band gap effects may be leveraged or mitigated in MEMS device design.

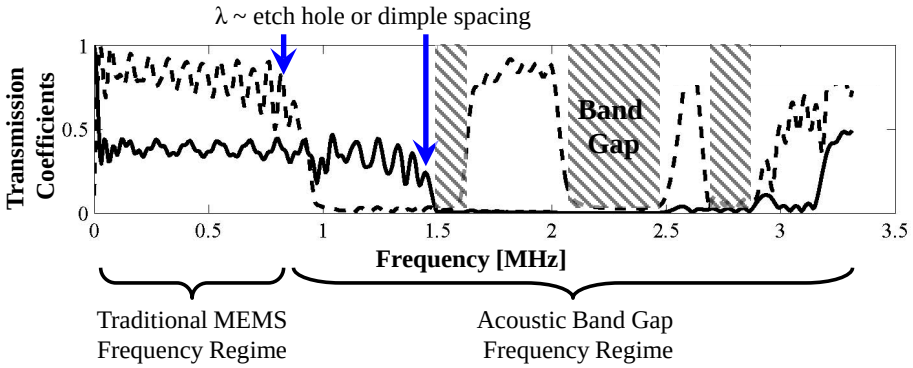

Figure 1.2: Sample phononic band gap crystal transmission coefficients over a frequency range extending from the operating frequencies of traditional MEMS devices, extending up to frequencies at which phononic band gap effects may become prevalent. The transmission coefficients for the longitudinal (transverse) elastic wave components are depicted by the solid (dotted) line. The frequency at which the operating wavelength, λ, becomes comparable to the spacing of the periodically placed etched holes, in the phononic band gap crystal, denotes the beginning of the phononic band gap frequency regime.

Phononic band gap effects may have application to filters [32], resonators, elastic wave cross talk reduction [33], vibration stabilization, support and anchor loss reduction [34], waveguides, multiplexers, demultiplexers [35], sensors [36], distributed mechanical system design, high-order resonators and so on. Hence, P^{n}BG crystals may provide an elegant paradigm for the design of new MEMS technologies.

Piezoelectric Surface Acoustic Wave (SAW) devices perform signal filtering by uti-

lizing a piezoelectric material for the conversion of an electrical field into a mechanical displacement field in a way that a filtering operation is performed [37]. In contrast, a P^{n}BG crystal may be utilized to perform signal processing purely in the mechanical energy domain, after electrical to mechanical energy transduction has occurred, and so a piezoelectric material is not necessitated. Thus, utilizing P^{n}BG crystals there is freedom to employ electrostatic transduction. Electrostatic transduction performs energy conversion while the frequency selective filtering operation is performed by the P^{n}BG crystal solely in the mechanical energy domain, though the frequency response of the electrostatic transducer is also accounted for. Thus, an electrostatically actuated P^{n}BG crystal-based signal processing element may have reduced material requirements (no need for exotic piezoelectric materials) and so may achieve higher compatibility with fabrication processes such as CMOS and those based in silicon. Improved process compatibility may assist with miniaturization through on-chip integration of P^{n}BG crystal-based signal processing and sensing facilities with electronics.

Lastly, while P^{n}BG crystal theory appears to provide a unique approach to the design of mechanical systems, the literature on traditional MEMS devices presents an abundance of data on high frequency electrostatic transduction [26, 27, 28, 38, 39, 40, 41], high frequency MEMS [22, 23, 24, 25, 26, 27, 28, 29, 30, 31], elastic wave device support methods including low-loss quarter wave transformer and nodal tether supports [22, 23, 24, 25], a variety of material systems (for example, silicon [42, 32], tungsten [43], aluminium [44], nickel [4]), and so forth) that are known to be useful for creating P^{n}BG crystals and which are available in silicon processes to make the development of an electrostatically actuated P^{n}BG crystal architecture feasible and timely.

1.2 Linguistic Stipulations

This thesis develops a new electrostatically actuated device architecture, which is as a whole is referred to as the Phononic Band Gap Quasi-Crystal (P^{n}BG QC) architecture. The portion of the P^{n}BG QC architecture that bares the geometry of a P^{n}BG crystal, that is periodicity in material properties with respect to position in space, will be referred to as the Phononic Band Gap Quasi-Crystal (P^{n}BG QC). The term quasi-crystal (or QC) has be utilized since the P^{n}BG QC may not display the infinite periodicity or identical behavior of an ideal infinitely periodic P^{n}BG crystal. The range of frequencies over which the P^{n}BG QC displays and absence of normal modes will be referred to as the band gap. Models and experiments will be utilized to support that P^{n}BG QCs displays some of the behavior and frequency selectivity that is characteristic of P^{n}BG crystals.

1.3 Objectives

This thesis develops the P^{n}BG QC architecture by leveraging the theory of P^{n}BG crystals and electrostatic transduction to develop a potential platform for next generation silicon-integrated sensors and signal processing elements [45] and improved MEMS and mechanical systems. Traditional approaches are reviewed. Then the unique geometry of the P^{n}BG QC architecture is introduced. The proposed P^{n}BG QC architecture must be realizable in a single layer (for maximal compatibility with planar fabrication processes) where the layer thickness is restricted by the fabrication process. The material and geometrical properties are given. The proposed design methodologies are then detailed for band gap engineering, P^{n}BG crystal truncation, P^{n}BG QC anchoring, P^{n}BG QC boundary and tether tuning for complete band gap formation and the implementation of unique geometries of electrostatic transducers. The electrostatic transducers perform

transduction of energy from the electrical energy domain to the mechanical energy domain to actuate the P^{n}BG QC over a range of frequencies sufficient for experimental investigation of the P^{n}BG QC behavior. However, optimal transducer design is not the subject of this thesis.

The proposed design methodologies are first supported via numerical, analytical and semi-analytical models of the electrical, mechanical and electromechanical behavior of the P^{n}BG QC architecture. Then a set of P^{n}BG QCs are fabricated in the Silicon-On-Insulator Multi-User-MEMS-Process (SOIMUMPs) Silicon-On-Insulator (SOI) bulk micromachining fabrication process to first demonstrate the feasibility of realizing the P^{n}BG QC architecture. Metrology is utilized to assess fabrication errors in the geometrical properties of the fabricated P^{n}BG QC devices. Extensive multi-mode experimental characterization of the fabricated P^{n}BG QC devices is performed in the frequency and spatial domains utilizing a laser-Doppler interferometer for a set of devices with varying geometrical properties. Extensive experimental measurements build reasonable evidence that could be used to deduce that the fabricated P^{n}BG QC devices display reasonable agreement with the model.

To asses whether the observed behavior of the P^{n}BG QC architecture is a function of the specific geometrical properties of the P^{n}BG QC architecture, several P^{n}BG QCs with varying geometrical properties are compared to search for predictable trends. In addition, the behavior of the P^{n}BG QCs are numerically and experimentally compared with that of similar homogeneous bulk mode resonators which provide a reference behavior. In this fashion, evidence is built that may be used to deduce whether the observed characteristic behavior may be a specific property of the P^{n}BG QC devices.

The final objective is to provide a reasonable level of insight into the application of the proposed P^{n}BG QC architecture to the improvement of MEMS and mechanical

systems and construction of temperature sensors and signal processing elements. Thermomechanical numerical models and experiments at elevated temperature reveal the temperature dependence of the P^{n}BG QCs. Lastly, numerical models are developed to determine how defect states may modify the P^{n}BG QC behavior to create complex frequency response characteristics that may have application to signal processing elements, localization, vibration stabilization and reduced anchor loss in resonators.

1.4 Organization of the Thesis

The thesis is comprised of three main parts. First, Chapters 2 and 3 present a literature review, background information and the proposition of the new electrostatically actuated architecture for the integration of P^{n}BG crystal-like structures into finite thickness plates; this architecture is given the name P^{n}BG QC architecture. Second, the P^{n}BG QC architecture model, fabrication and experimental characterization is presented in Chapters 4, 5 and 6. Lastly, in Chapter 7, the potential applicability of the proposed P^{n}BG QCs is developed numerically and experimentally for physical temperature sensors and numerically for signal processing elements, vibration stabilization, anchor loss reduction and improved MEMS and mechanical systems. Contributions and future work are given in Chapter 8.

Chapter 2 introduces the history of classical elastic wave P^{n}BG crystal research from the seminal discovery to the present micro-integration of P^{n}BG crystals. Background information on the science of periodic structures, numerical modeling of P^{n}BG crystals and relation between the proposed P^{n}BG QC architecture and present day MEMS is provided.

Chapter 3 describes the development of the proposed P^{n}BG QC architecture, in-

cluding the design methodologies, electrostatic transducer geometry, crystal truncation methodologies, and tether and P^{n}BG QC edge tuning methodologies. The intent of the architecture and design methodologies is to produce an electrostatically actuated P^{n}BG QC that displays two separate groups of modes, each of which display characteristic mode shapes. The two groups of modes are separated by a wide range of frequencies over which the P^{n}BG QC displays no normal modes.

The focus of Chapter 4 is the development of an extensive analytical, numerical and semi-analytical model of the P^{n}BG QC architecture. The model includes the analytical characterization of the electrical circuit and electrostatic forces in the transducer gap and narrow band dynamic harmonic behavior, as well as numerical models of mechanical normal mode shape and wideband dynamic harmonic response. Virtually no complete analytical models are available in the literature to describe the specific P^{n}BG QC architecture structure proposed here and the complete behavior of the P^{n}BG QC architecture is difficult to accurately describe with a single simple equation. Analytical and semi-analytical structural and vibration models are developed as much as possible. Chapter 4 concludes with a numerical electromechanical multi-physics model of the proposed P^{n}BG QC architecture.

Chapter 5 discusses the fabrication of a set of the proposed P^{n}BG QC devices in the SOIMUMPs bulk micromachining process of the MEMSCAP Foundry [46]. The fabricated set of P^{n}BG QCs [47] have varying geometrical properties to allow for the experimental investigation of trends in P^{n}BG QC behavior versus geometry. Fabrication errors in the P^{n}BG QC devices are characterized utilizing a scanning electron microscope and optical profilometer. Lastly, the fabricated chip is bond wired into a surface mount package and a test fixture is designed to provide an electrical interface to the P^{n}BG QCs. The test fixture utilizes an in-house fabricated printed circuit board and surface

mount technology.

Chapter 6 presents the experimental characterization of the P^{n}BG QC devices. The P^{n}BG QC devices are actuated via their electrostatic transducers and the response of the P^{n}BG QC devices is measured utilizing a laser Doppler interferometer. The measurement setup is presented. For several P^{n}BG QC devices with varying geometries extensive measurement results are given for the dynamic harmonic analysis over a frequency range from 50 kHz to 20 MHz. The mode shape topography is measured over the top surface of the P^{n}BG QC devices. From the mode shape topography measurements, the measured frequency versus finite element method mode number characteristic is constructed. A homogeneous bulk mode resonator is characterized in a similar fashion and provides a reference behavior against which the experimental behavior of the P^{n}BG QC devices is qualified. The experimental results are compared to the model of Chapter 4 and display reasonable agreement.

Chapter 7 investigates the applicability of the P^{n}BG QC architecture to physical thermal sensors and signal processing element. A brief numerical thermomechanical multi-physics model is given. One of the fabricated P^{n}BG QC devices is then heated utilizing an infrared radiation source, and the dynamic harmonic response is measured about several normal modes within the 50 kHz to 20 MHz frequency range. The dependence of the normal mode frequency and amplitude is observed versus temperature. The dependence with respect to temperature of the P^{n}BG QC is experimentally compared with that of a homogeneous bulk mode resonator which provides a reference behavior. Lastly, the potential applicability of the proposed P^{n}BG QCs to the study of signal processing elements, MEMS and mechanical systems is developed numerically. Defect states are introduced into a P^{n}BG QC to create a localized resonator within the core of the P^{n}BG QC. The localized resonator appears to be isolated in space and frequency

from adjacent vibrations and may have application to vibration stabilization, anchor loss reduction and MEMS and mechanical system design.

Chapter 8 lists the contributions of this thesis and elaborate suggestions for further study. Contributions are listed in the areas of P^nBG QC architecture design methodologies, modeling and theory of operation, fabrication and realization, experimental demonstration of the proposed P^nBG QC architecture and development of the applicability of the proposed P^nBG QC architecture to temperature sensors, signal processing elements and the potential improvement of MEMS and mechanical systems.

Chapter 2

Background on Multi-Dimensional Phononic Band Gap Crystals for Classical Elastic Wave Localization

This chapter first presents a literature review on the field of multi-dimensional P^{n}BG crystals, from the seminal work in the early 1990s to the present micro-integration of P^{n}BG crystals. Amidst the literature review, the P^{n}BG QC architecture that is presented in this thesis is placed into context relative to the body of related work. The P^{n}BG QC architecture will ultimately be realized utilizing MEMS technology. Hence, the relationship is presented between the P^{n}BG QC architecture and the field of Radio Frequency Micro-Electro-Mechanical-System (RF MEMS). The numerical techniques utilized to model P^{n}BG crystals are then introduced. The P^{n}BG QC architecture will employ the geometry of a honeycomb crystal and relevant background information on the crystallography of honeycomb P^{n}BG crystals is presented as the last topic in this chapter.

2.1 Literature Review of Classical Elastic Wave Localization in Multi-Dimensional Phononic Band Gap Crystals

In 1958, Anderson proposed the notion of wave localization for electronic systems [48]. Electron localization proved challenging due to electron-electron interactions, hence, in the 1980s the research world refocused efforts toward photon localization [49, 50, 4]. For over a decade, interest remained on P^tBG crystals. In 1992, two-dimensional P^nBG crystals for classical elastic wave localization began receiving attention in the literature [2]. Both P^tBG and P^nBG crystals offered different properties from their electronic analogues, and possess the advantage of localizing photons (quantized electromagnetic waves) and phonons (quantized acoustic or elastic vibrations) utilizing relatively simple structures. Just as P^tBG crystals offered new properties and possibilities over and above electronic systems, P^nBG crystals display radically different properties from P^tBG crystals (in part due to the differing governing physics, as discussed in Section 1.1).

2.1.1 1992 to 1994: Seminal Theoretical Verification of Classical Elastic Wave Localization in Two- and Three-Dimensional Phononic Band Gap Crystals

The seminal papers on two-dimensional P^nBG crystal band structure for classical elastic waves appear to have been presented by Sigalas (1992) [2] and Kushwaha (1993) [3]. To determine the optimal conditions for acoustic band gap formation, early theoretical and experimental studies performed parametric studies of acoustic material systems (solid/solid, solid/fluid, fluid/solid, and fluid/fluid systems, ...), lattice types (SC, HCP,

and FCC, ...), fill factor, inclusion geometry (circular, cylindrical, spherical, square, ...), characteristic impedance contrasts and material composition (aluminium, mercury, water, steel, air, ...) [2, 3, 4, 51, 13, 52, 53, 54, 55, 56, 57, 58, 59]. P^{n}BG crystals were designed to demonstrate low pass, band pass and band stop filter responses.

2.1.2 1993 to 2010: Advancements in the Theory Classical Elastic Wave Phononic Band Gap Crystals

Localization and defect states were studied in 1993 [60]. Defect states were introduced into P^{n}BG crystals to create pass bands in the phononic band gaps (1998) [52], tunable band gaps (2001) [61, 62], waveguides (2001) [63] (2004) [35], and multiplexers and demultilexers (2004) [35].

Early on, many studies were of P^{n}BG crystals that were infinite in dimension in at least one physical direction. The first study of finite thickness structures appears to be for bending wave plate P^{n}BG crystals investigated in 1994 [13]. Rayleigh wave attenuation by P^{n}BG crystals in infinite half-space host materials was presented in 1999 [64]. The band structure of one-dimensional layered systems was presented in 1995 [65].

To validate theoretical calculations, macroscopic experiments were performed on bulk wave (1998) [66, 67] (1999) [68] and surface wave (1999) [64, 51] structures using macroscopic two-dimensional P^{n}BG crystal structures. Experimental results displayed reasonable agreement with the corresponding theory and provided support for some phononic band gap phenomenon.

Initial studies dealt with binary composites (P^{n}BG crystals composed of two materials), for which phononic band gap formation and localization were largely based on the mechanism of Bragg scattering. Liu proposed the use of tertiary composites (P^{n}BG

crystals composed of three materials), for which the inclusion is composed of two materials, and illustrated the phenomenon of local resonance as a new mechanism for phononic band gap formation in P^{n}BG crystals (2000) [8]. Local resonance allows for the formation of band gaps at wavelengths that are much larger than the wavelengths at which Bragg scattering operates. Local resonance was proposed to occur for fractal inclusion based binary composites in (2005) [9].

Elastic wave tunneling through P^{n}BG crystals (governed by Bragg scattering) at in-gap frequencies and phonon focusing in tungsten-based P^{n}BG crystals was examined in 2002 [43]. Topology optimization was first applied to systematically maximize acoustic band gaps in 2003 [69]. In 2005, experimental data began to appear in the literature on P^{n}BG crystals integrated in microelectronic processes [36, 32].

After approximately 15 years of examination predominantly into bulk wave band gaps in P^{n}BG crystals, the number of publications on the topic of P^{n}BG crystals crafted out of finite thickness plates began to increase in 2006 (though the first study on plate P^{n}BG crystals appeared to be conducted far ahead of their time by Sigalas et. al. in 1994 [13]). The modeling of plate P^{n}BG crystals represented a move toward the study of more practically realizable structures in comparison to preceding studies of P^{n}BG crystals that displayed infinite size in at least one physical dimension. Free standing plate P^{n}BG crystals with semi-infinite periodicity were examined for exotic materials in 2006-2007 [70, 71, 72, 73] and silicon in 2007 [42]. Non-freestanding PZT5A-Air and AlN-Air plate P^{n}BG crystals were examined in 2007 [74].

Most studies regarding inclusion geometry focused principally on regular shaped geometries such as polygons. Fractal inclusion geometries were investigated in 2008 [10]. P^{n}BG crystals with time varying material properties were studied in 2010 [5], adding a fourth dimension (time) in which the material properties of P^{n}BG crystals may vary

periodically.

P^nBG crystal research progressively developed sub-areas, including: (i) acoustic band gaps (for bulk [2, 3], Rayleigh [32], and Lamb [42, 13, 11, 70, 71, 72, 73, 75] waves); (ii) localization and defect states [13, 35], (iii) LRSMs (Locally Resonant Sonic Materials) [8, 9], (iv) systematic phononic band gap design [12], (v) phonon focusing [43], and (vi) micro-integration of P^nBG devices (signal processing elements [32] and sensors [36]). Innovative theoretical and experimental research opportunities abound in all six of these research areas, and so there has been motivation to perform research on these topics.

2.1.3 2003 to 2008: Simultaneous Phononic-Photonic Band Gap Crystals for Classical Electromagnetic and Elastic Waves

In 2003, Russel [76] identified that Photonic Crystal Fiber (PCF) structures, which display periodicity in mechanical material properties in two-dimensions, were single structures that exhibited both a photonic and phononic band gap. The phonons in the PCF were generated by light interactions. In 2005, Laude and Dainese also utilized two-dimensional phononic crystals in PCFs for phonon control to suppress stimulated Brillouin scattering and enhance acousto-optic interaction [77, 78]. In 2007, Delmar and Barker patented an optical switch [79] by placing a P^tBG crystal in the defect state of a P^nBG crystal which was used to localized phonons into the region of the P^tBG crystal, and through the photoelastic effect, the phonons would modify the refractive index of the P^tBG crystal, thereby perturbing the photonic band gap location so as to transmit or reflect the optical signal. In 2008, Mohammadi theoretically illustrated simultaneous photonic and phononic band gaps for silicon-plate P^tBG and P^nBG crystals of various

lattice types [6, 80].

2.1.4 2005 to 2011: Micro-Integration of Classical Wave Phononic Band Gap Crystals with Piezoelectric Transducers

From the seminal study in the early 1990s of classical elastic wave localization in two-dimensional P^{n}BG crystals, approximately a decade of theoretical work and macroscopic experiments occurred. Microfabrication processes then became utilized to introduce P^{n}BG crystals into integrated devices that utilized piezoelectric transducers and the architectures of traditional Surface Acoustic Wave (SAW) filters.

The first appearance in the literature of a SAW based P^{n}BG crystal device was reported in 2005 [32] utilizing the architecture illustrated in Figure 2.1(a). Acoustic waves are actuated and sensed utilizing piezoelectric slanted finger interdigital transducers to enable wide band actuation and sensing of SAWs, though the slanted fingers generate elastic waves in multiple directions at different frequencies. The P^{n}BG crystal is placed into the SAW propagation path and experimentally demonstrated phononic band gap effects, displayed 20 dB of loss and was prone to the loss of SAW energy into bulk modes (the substrate, away from the surface). The P^{n}BG crystal had a square lattice that is constrained to a square area, was composed of a silicon host and air inclusions and etched into the bulk of a substrate thereby approximating a P^{n}BG crystal in a semi-infinite half-space. The P^{n}BG crystal is truncated on one pair of sides by piezoelectric transducers and may appear to be truncated on the other pair of sides by a region of homogeneous silicon. Also around 2005, nano-scale P^{n}BG crystals were fabricated in crystalline silicon; however, were experimentally characterized utilizing Brillouin light

scattering [81] and so did not integrate elastic or acoustic wave transducers.

In 2006, SAW P^{n}BG crystal structures were created utilizing multiple devices with narrow band interdigital transducers tuned to different frequency regions to assemble the frequency characteristics of a $LiNbO_3$-Air P^{n}BG crystal [82, 83].

Proposals and models of electrostatically actuated P^{n}BG crystal architectures appear in 2006 [84] and 2008 [85]; however, the proposed electrostatically actuated P^{n}BG crystal do not appear to have been fabricated and so corresponding experimental data is absent. In 2008, as a subset of this thesis work, a lumped element approximation of an electrostatically actuated P^{n}BG crystal was modeled and fabricated [86]; however, experimental characterization was not published.

The next significant change in the architecture of micro-integrated P^{n}BG crystals occurred in 2007 and 2008 as P^{n}BG crystals were fabricated in finite thickness slabs [87, 88] and El-Kady and others introduced line defect states into P^{n}BG crystals by removing rows of inclusions to form a path through the P^{n}BG crystal between the actuator and sensor transducer [89] utilizing an architecture illustrated in Figure 2.1(b). Mohammadi presented slab P^{n}BG crystal structures in 2008 [90] as illustrated in Figure 2.1(c). El-Kady utilized Aluminium-Nitride (AlN) piezoelectric transducers which truncated the P^{n}BG crystal in one direction, and the P^{n}BG crystal is a square lattice, silicon-dioxide host and tungsten inclusion (SiO_2-W) material system and may be the thinnest reported P^{n}BG crystal. In contrast, Mohammadi utilized Zinc-Oxide (ZnO) interdigital piezoelectric transducers which truncate the P^{n}BG crystal in one direction, along with a honeycomb P^{n}BG crystal with a silicon-air (Si-Air) material system, and the remaining two sides of the P^{n}BG crystal appear to be truncated by a homogeneous region [90]. The aforementioned P^{n}BG crystals that have been fabricated within finite thickness slabs display improved energy confinement in comparison to P^{n}BG crystals

that are etched into semi-infinite half-spaces. In 2007 and 2009, the cermet P^{n}BG topology appears to have been first employed [91], while the majority of devices still employ the network topology.

Next, in 2009 and 2011 line defect states were utilized to create resonant cavities in the center of piezoelectrically actuated and sensed slab P^{n}BG crystals [92, 7] as illustrated in Figure 2.1(d). This resonant cavity configuration of line defect states is differentiated from the line defect state structures of El-Kady and others [89], which utilized the line defect state to form a waveguide between the actuator and sensor transducer.

In 2011, the work of Kuo appears to have presented the first departure from the use of circular inclusions and employed an X-shaped inclusion [93]. In 2011, the works of Ziaei [7] and Kuo [93] increased the operating frequency of micro-integrated P^{n}BG crystals by an order of magnitude illustrating the scalability of the phenomenon to 1 to 2 GHz. In 2010 the potential of P^{n}BG crystals for support loss reduction in resonator structures was examined [34]. At least three application areas for P^{n}BG crystal have then precipitated: (i) sensors, (ii) signal processing elements and (iii) auxiliary structures (e.g. low loss anchors) for the improvement of MEMS and mechanical systems. The applicability of the P^{n}BG QC architecture that is proposed in this thesis will be assessed with respect to all three of the aforementioned application areas.

The evolution of the P^{n}BG crystal architectures discussed here is summarized in Figure 2.1. Table 2.1.4 summarizes significant works in the micro-integration of P^{n}BG crystals. The works are described in terms of (i) transducer type, (ii) material composition (which may provide insight into CMOS- or silicon-compatibility), (iii) type of energy carrying wave or vibration, (iv) extent of the periodicity of the P^{n}BG crystal, (v) the ratio of lattice constant, a, to P^{n}BG crystal thickness, t, (vi) the approximate

frequency of the experimental phononic band gap, (vii) the P^{n}BG crystal boundary geometry, (viii) the P^{n}BG crystal topology (network or cermet), (ix) the inclusion geometry, (x) the host structure geometry, (xi) the P^{n}BG crystal boundary type, (xii) the P^{n}BG crystal support structure type and (xiii) P^{n}BG crystal lattice type. As may be seen in Table 2.1.4, the ratio d/a, of crystal thickness, d, to lattice constant, a, is utilized to compare the ability of the P^{n}BG crystal to be realized in thin layers.

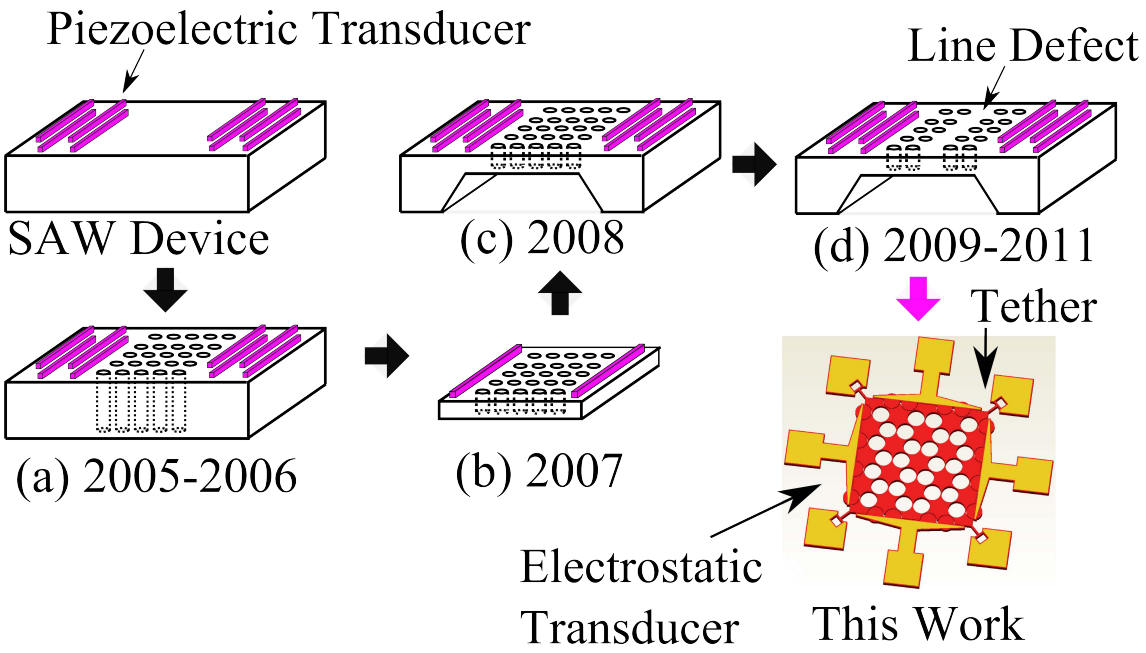

Figure 2.1: Illustration of the evolution of micro-integrated phononic band gap crystals from 2005 and leading up to the work presented in this thesis. In 2005-2006, phononic band gap crystals were initially etched into the Surface Acoustic Wave (SAW) propagation path between the piezoelectric transducers of a SAW device. In 2007, piezoelectric transducers were utilized to actuate and sense waves in a phononic band gap crystals that were crafted out of relatively thin plates. In 2008, devices resembling those created in 2005 were modified to reduce the thickness of the phononic band gap crystals. In 2009-2011, line defect states were introduced into the phononic band gap crystals. For the phononic band gap crystal architecture presented in this work, piezoelectric transducers are abandoned in favor of electrostatic transducers and the phononic band gap crystal-like structures are suspended from the substrate by utilizing tethers.

Lastly, in 2011, the primary work of this thesis presented what appears to be the first theoretical and experimental demonstration of an electrostatically actuated architecture

Table 2.1: Summary of works for micro-integrated phononic band gap devices.

Author	Year	Transducer	Host-Inclusion Material	Energy Carrier	Crystal Size §	Ratio of d/a	Approximate Experimental Band Gap Center	Crystal Bounding Geometry	Crystal Topology	Inclusion Geometry	Host	Crystal Boundaries	Crystal Anchor Structure	Lattice
Wu [32]	2005	Piezo SFIT (ZnO)	Si-Air	SAW	$6a$ $a \approx 10$ µm	80/10 = 8	200 MHz	Rectangle	Network	Circle	Semi-infinite half-space	Fixed	Substrate	Square
Benchabane, Khelif [82]	2006	Piezo IDT ($LiNbO_3$)	$LiNbO_3$-Air	SAW	Various $a \approx 10$ µm	10/10 = 1	215 MHz	Rectangle	Network	Circle	Semi-infinite half-space	Unspecified	Substrate	Square
Olsson, El-Kady [87]	2007	Piezo Coupler (AlN)	SiO_2-W	BAW	$a \approx 45$ µm	0.6/45 = 0.013	33 MHz and 67 MHz	Rectangle	Cermet	Circle	Slab	Unspecified	Unspecified	Square
Olsson, El-Kady [89]	2007	Piezo Coupler (AlN)	SiO_2-W	BAW	$a \approx 45$ µm	0.6/45 = 0.013	70 MHz	Rectangle	Cermet	Circle	Slab	Unspecified	Unspecified	Square, Line defects
Mohammadi [90]	2008	Piezo IDT (ZnO)	Si-Air	'Slab wave'	~$8a$ $a \approx 15$ µm	15/15 = 1	193 MHz	Rectangle	Network	Circle	Slab	Fixed	Substrate	Honeycomb
Mohammadi [92]	2009	Piezo IDT (ZnO)	Si-Air	'Slab wave'	~$7a$ $a \approx 15$ µm	15/15 = 1	134 MHz	Rectangle	Network	Circle	Slab	Fixed	Substrate	Honeycomb with line defect
Kuo [91]	2009	Piezo IDT, SFIT (AlN)	AlN-Air	BAW	$10a$ $a = 8.6$ µm	2/8.6 = 0.23	218 MHz	Square	'Cermet'	Tethered Circle	Slab	Two Stress-Free, Two Fixed	Substrate	Square
Mohammadi [34]	2010	Piezo (ZnO)	Si-Air	'Slab wave'	N/A $a \approx 15$ µm	15/12 = 1	134 MHz	Rectangle	Network	Circle	Slab	Fixed	Substrate via P^nBG crystal	Honeycomb with line defect
Kuo [93]	2011	Piezo	AlN-Air	Symmetric Lamb	$11a$ $a \approx 5$ µm	1/5 = 0.2	1030 MHz	Rectangle	Network	X-shaped	Slab	Two Fixed Two Unspecified	Substrate	Square
Ziaei-Moayyed, El-Kady [7]	2011	Piezo IDT (AlN)	SiC-Air	Unspecified	N/A $a \approx 1.83$ µm	Unspecified	2300 MHz	Rectangle	Network	Circle	Slab	Two Fixed Two Unspecified	Substrate	Square with various line defects
This Work [94]	2011	Electrostatic	Si-Air	N/A	~$3a$ to $4a$ $a \approx 161$ µm	25/161 = 0.155	13 MHz	Square and Circle	Network	Circle	Plate	Stress-Free, Serrated (all sides)	Tuned Tethers	Honeycomb

SFIT = Slanted Finger Interdigital Transducer, IDT = Inter-Digital Transducer, ZnO = Zinc Oxide, AlN = Aluminium Nitrude, $LiNbO_3$ = Lithium Niobate, a is the lattice constant parameter of the P^nBG crystal, SAW = Surface Acoustic Wave, BAW = Bulk Acoustic Wave, § The number of lattice constants in the propagation direction. N/A = Not Applicable.

that is designed leveraging two-dimensional P^{n}BG crystal theory, utilizing a silicon host material, air inclusion and honeycomb P^{n}BG crystal geometry [94]. This architecture is referred to as the P^{n}BG QC architecture and will be realized in this thesis as a Radio Frequency Micro-Electro-Mechanical-System.

2.2 Phononic Band Gap Crystals as Radio Frequency Micro-Electro-Mechanical-Systems

In 2011, to the best of the author's knowledge, the primary work of this thesis presented in the literature the theory and experiments, for a MEMS implementation, of the first electrostatically actuated and distributed mechanical architecture that employs the geometry of a honeycomb P^{n}BG crystal which has a silicon host and circular air inclusions and appears to display the frequency selective characteristics associated with P^{n}BG crystals [94]. This architecture is referred to as the P^{n}BG QC architecture.

The P^{n}BG QC architecture is designed for implementation in a single layer planar fabrication process and will be released so that the top and bottom surfaces of the P^{n}BG crystal are free standing. The P^{n}BG QC does not display the infinitely periodic geometry of an ideal P^{n}BG crystal, which would not be physically realizable in a MEMS fabrication process. Moreover, the geometry of the P^{n}BG QC differs significantly from the micro-integrated piezoelectrically actuated P^{n}BG crystals that appear in the literature. This is in-part due to the air gap that is employed in the electrostatic transducer. The presence of the air gap results in the edges of the P^{n}BG QC being free-standing. Hence, with the exception of the tethers that attach the P^{n}BG QC to the substrate, all surfaces (top, bottom and edges) of the P^{n}BG QC may be approximated by free boundaries. In contrast, in the literature, the micro-integrated P^{n}BG crystals appear to be bounded

to square or rectangular areas and along two sides of this square or rectangular area the piezoelectric transducers appear to be fabricated directly upon the solid medium that acts as the host medium of the P^{n}BG crystal; the two sides, along which the piezoelectric transducers are located, truncate the P^{n}BG crystal with a solid medium (not a free-standing edge); the other two boundaries appear to be placed away from the acoustic wave signal flow path or are truncated by a free-standing flat edge [32, 82, 87, 88, 89, 90, 90, 92, 7, 93, 34].

Hence, the P^{n}BG QC architecture appears to be unique in the utilization of electrostatic transducers to actuate the P^{n}BG QC and in the implementation of free boundaries on all edges (except at the tether attachment points) of the P^{n}BG crystal. Moreover, in the plane of periodicity of the P^{n}BG QC, both square and circular bounding geometries are utilized to truncate the P^{n}BG crystal (where as in the literature the bounding area appears always to be square or rectangular [32, 82, 87, 88, 89, 90, 90, 92, 7, 93, 34]). In addition, the geometry of the edges of the square or circular truncation boundary of the P^{n}BG QC are not flat (where as in the literature any potentially free standing edges appear to utilize a flat edge [87]). In this thesis, the edges of the P^{n}BG QC over the square or circular truncation boundary are serrated (not flat), to mimic a periodic boundary, as will be illustrated in Chapter 3, and to provide unconstrained motion of the boundary and a methodology is developed to tune the edges and tethers to shift local edge and tether resonant modes away from band gap frequencies and enable complete band gap formation (the absence of normal modes over a wide range of frequencies). To the best of the author's knowledge, a detailed study does not appear in the literature for different truncation boundary geometries for micro-integrated P^{n}BG crystals, and so the circular and square truncation boundary and boundary and tether tuning methodologies studied in this thesis appear to be the first of their kind.

The development of the P^{n}BG QC architecture also appears to have a relation to the design of two-dimensional coupled resonators. The P^{n}BG QC architecture was initially derived from the architecture of single-mode square extensional [95], Lamé mode [31] and wine glass [96] resonators. These single-mode architectures provided an electrostatically actuated electromechanical platform that would serve as the starting point for the development of the P^{n}BG QC architecture. The detailed development of the P^{n}BG QC architecture is contained in Chapter 3, and will be summarized here to show the significant differences between the P^{n}BG QC architecture and the architectures of single-mode square extensional [95], Lamé mode [31] and wine glass [96] resonators. First, to realize the P^{n}BG QC, a periodic array of etch holes (which serve as the P^{n}BG QC inclusions) is embedded into the homogeneous plate for both square and circular plate geometries. This transforms the homogeneous plate into a periodic structure, meaning that the material properties of the structure are a periodic function of position (not homogeneous) within the structure. This periodic structure, referred to as the P^{n}BG QC, may be approximated as a two-dimensional array of distributed mass and spring elements, where the distribution of mass and spring elements may be different at different normal mode frequencies, and so represents a significant departure from the initial single-mode resonator architecture. Moreover, the P^{n}BG QC mode shapes, which will be presented in Chapter 4, appear to display the properties of flexural mode resonators, while single-mode square extensional [95], Lamé mode [31] and wine glass [96] resonators are considered bulk mode resonators.

The multiple normal modes of the periodic P^{n}BG QC need to be systematically orchestrated in order to realize band gap behavior. Thus, the design methods for the P^{n}BG QC must consider multi-mode, as oppose to single-mode, behavior. For a careful selection of inclusion (etch hole) radius and spacing, modal analysis (which will be

presented in Chapter 4) of the P^{n}BG QC will indicate that over some frequency ranges the P^{n}BG QC displays a complete absence of normal modes - these frequency ranges are referred to as band gaps. The intentional overlap of the etch holes and the edges of the host plate, result in the edges of the P^{n}BG QC being serrated (not flat) unlike the flat edges of single-mode square extensional [95], Lamé mode [31] and wine glass [96] resonators, yet also unlike comb-drive transducer geometry [97]. For a given etch hole (P^{n}BG QC inclusion) radius and lattice constant, the P^{n}BG QC truncating boundary location has to be carefully chosen relative to the P^{n}BG QC inclusion locations and so cannot be relatively arbitrary as in the single-mode square extensional [95], Lamé mode [31] and wine glass [96] resonators. Tuning methodologies are developed to carefully select the P^{n}BG QC truncation boundary location relative to the P^{n}BG QC inclusions so the P^{n}BG QC structure displays a complete band gap. Lastly, the geometry of the tethers is also tuned to ensure that the local resonant modes of the tethers do not occur at band gap frequencies. This design methodology for the P^{n}BG QC architecture is contained in full in Chapter 3 and also represents a significant departure from single-mode resonator design.

The development of the P^{n}BG QC architecture will also be shown to yield frequency selective properties that are significantly different from single-mode homogeneous square extensional [95], Lamé mode [31] and wine glass [96] resonators, which will act as reference devices to which the behavior of the P^{n}BG QC architecture is compared.

The P^{n}BG QC architecture presented within this thesis may be geometrically classified as a two-dimensional array of coupled mass-spring resonators with distributed mass and spring elements. Moreover, in Chapter 4, the set of modes below the band gap of the P^{n}BG QC, appear to display the behavior of a two-dimensional array of mechanically coupled masses with 19, and 23, mass elements for P^{n}BG QCs with circular, and square,

truncation geometry, respectively; this may be of the largest two-dimensional arrays of couple resonators realized in MEMS. Two-dimensional mechanically coupled arrays of five mass elements to produce a band-pass frequency response are presented in [31]. One-dimensional mechanically coupled arrays of approximately 80 elements to produce a band-pass frequency response are shown in [30]. Unlike the previously mentioned one- [30, 98] and two-dimensional [31] mechanically coupled arrays which provide band-pass characteristics, the low frequency end of the spectrum of the P^{n}BG QC displays a low-pass characteristic, which may be due to the internal mass elements of the P^{n}BG QC not being anchored to mechanical ground (see Appendix I and [86]). Overall the frequency selective characteristics of the P^{n}BG QCs are intended to resemble those of a band-stop filter, where the low frequency pass band extends down to DC and is separated from the high frequency pass band by a stop band (band gap), as in P^{n}BG crystals. The order of (number of mass-elements in) the proposed P^{n}BG QC may be controlled relatively easily by adjusting the P^{n}BG crystal truncation boundary location. Thus, the P^{n}BG QC architecture may have application to the design of coupled mass-spring resonators.

Contemporary piezoelectric LAW, SAW, BAW and P^{n}BG crystal architectures are described by elastic wave mechanics and may be collectively referred to as microwave acoustic devices [99]. The proposed P^{n}BG QCs may potentially manipulate both elastic traveling and standing waves in plates. Figure 2.2 organizes contemporary LAW, SAW and BAW devices along side the proposed P^{n}BG QC architecture. In SAW devices, elastic traveling waves are present on the surface of the device. In BAW devices, elastic standing waves are present within the bulk of the device. In LAW devices, the energy carrier is a Lamb acoustic wave with elastic wave energy distributed throughout the thickness of a plate. In this thesis, the P^{n}BG QCs are studied under steady state time harmonic conditions, in which vibrations appear to form standing waves. Next, methods

for the numerical modeling of P^{n}BG crystals are assessed comparatively.

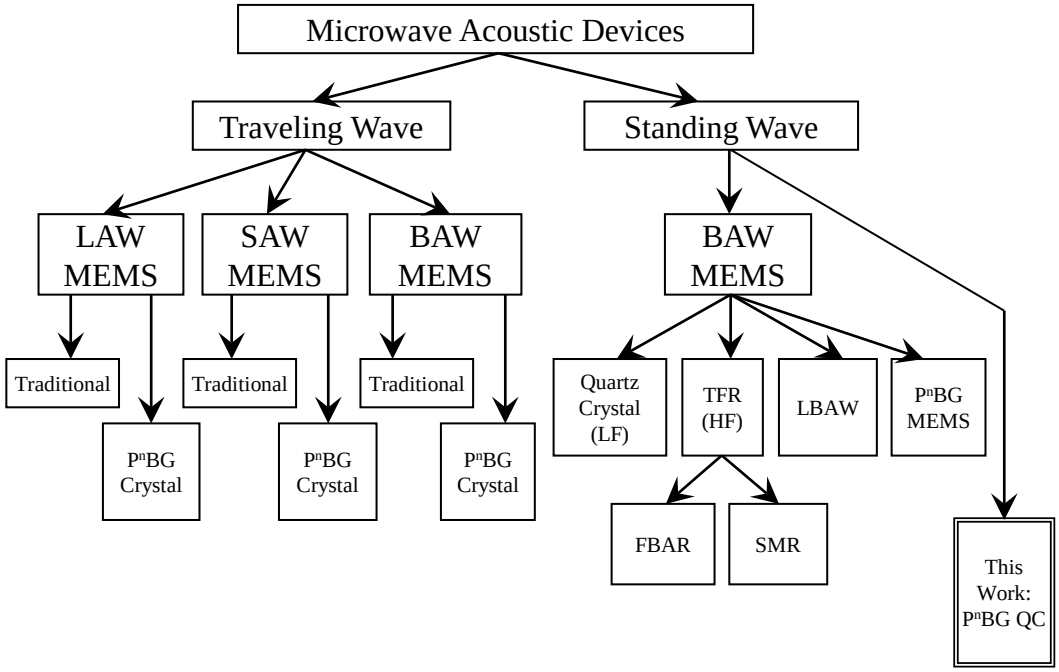

Figure 2.2: Types of microwave acoustic devices. List of acronyms: SAW (Surface Acoustic Wave), BAW (Bulk Acoustic Wave), LAW (Lamb Acoustic Wave), LF (Low Frequency), TFR (Thin Film Resonator), LBAW (Lateral Bulk Acoustic Wave), HF (High Frequency), P^{n}BG (Phononic Band Gap), QC (Quasi-Crystal), FBAR (Film Bulk Acoustic Resonator), SMR (Solidly Mounted Resonator).

2.3 Numerical Modeling of Phononic Band Gap Crystals

To deduce the frequency response of a P^{n}BG crystal, a number of numerical methods may be utilized, including Finite-Difference Time-Domain (FDTD) [100, 101, 102], Plane Wave Expansion (PWE) [15, 60, 32], Super Cell-Plane Wave Expansion (SC-PWE), Finite Element Method (FEM) [92], Frequency Domain-Finite Element Method (FD-FEM) [103], Time Domain-Finite Element Method (TD-FEM) [104], Dynamic Finite Element

Method (DFEM) [105], Multiple Scattering Technique (MST) [14], Variational Method (VM) [67, 106], method of Hou [107], Wavelet Method (WM) [108] and the Lumped Mass (LM) method [109, 110]. Table 2.2 summarizes the strengths and weaknesses of these numerical methods.

PWE and SC-PWE are utilized to compute P^{n}BG crystal band structure (as oppose to transmission coefficients) and may not be applied to mixed material (fluid-solid and solid-fluid) P^{n}BG crystals due to the material density term in the denominator which may approach zero for fluids or vacuum which display a low material density [15, 60]. MST [14], VM [67, 106], the method of Hou [107], and WM [108] were developed to handle mixed material systems, for which PWE fails [14] [67]. MST may only be applied to systems with cylindrical and spherical inclusion geometries [14]. The LM method displays a low sensitivity to host to inclusion density contrast and high computational efficiency relative to PWE and FDTD; however, may not be applied to mixed material systems [109, 110]. The methods discussed thus far require a matrix inversion to obtain the solution, and may not be applied to finite-sized practically realizable systems [74, 107]. Moreover, the described methods do not provide time varying elastic or acoustic field propagation information, which may be utilized to generate the magnitude-phase information of the P^{n}BG crystal response. In addition, the described methods cannot handle arbitrary time-domain source pulse shapes and source and detector configurations.

Unlike the frequency domain methods, time domain formulations, such as TD-FEM [104], DFEM and FDTD [14], provide the capacity to perform transient analysis on physically-realizable finite-sized structures, of arbitrary material composition (including mixed fluid-solid and solid-fluid material systems which display high density mismatches), geometry, time domain source pulse shape, source and detector geometry

and time-varying inclusions. FDTD, like FEM, is utilized for solving partial differential equations. In contrast to the PWE method, FEM and FDTD methods provides the flexibility to simulate finite-sized physically realizable experimental structures [74].

FEM and finite-difference methods differ in their discretization of space. The discretization of space in FEM methods may be performed using relatively arbitrarily shaped mesh elements (such as triangles, and so on) and so may accurately describe structures that possess complex geometries. FDTD formulations typically utilize a square mesh, which results in a staircase approximation of curved surfaces. FDTD can include an arbitrary number of materials.

The FDTD method is a time-domain approach and involves discretizing the elastic wave differential equation in both space and time [100]. Many boundary condition formulations have been developed for the FDTD method and can be utilized to model a multitude of physical devices. FDTD provides time varying elastic field propagation information, at all points in the device, and is easily converted to the frequency domain to compute both the transmission coefficients and the band structure [101, 102]. Due to the interlacing of fields in space, FDTD is an explicit formulation (the field components at any given time step are explicitly a function of field values at previous time steps and neighboring points in space) and so no matrix inversion is needed to obtain the solution; this is advantageous for large systems or in cases where a sparse matrix may not be formulated. FDTD simulation codes are easily parallelized for computation on parallel computing systems.

The FEM did not appear to become widely utilized in P^{n}BG research until 2006 [71], when interest in finite-sized plate P^{n}BG crystals increased. In contrast, FDTD has been in widespread use in P^{n}BG crystal research since at least 2000 [100], and FDTD boundary condition formulations for the simulation of finite-sized plates have

been available since at least 1997 [111].

2.3.1 Chosen Numerical Method

Many of the surfaces of the P^{n}BG QC architecture, which is developed in this thesis, are curved and the P^{n}BG QCs are physically realizable and so finite in all dimensions, bounded by both fixed and free boundaries and potentially surrounded by vacuum or air. Thus, the ability, such as that provided by methods like PWE, to model an infinitely periodic system is not required. As mentioned above, FEM accurately represents curved surfaces and can model finite sized structures.

The experimental studies performed on the P^{n}BG QC architecture will be dynamic harmonic experiments and so a harmonic model is sufficient. Thus, the ability to model arbitrary time domain pulse shapes (as provided by methods such as FDTD) is not required. To obtain detailed understanding of the experimental behavior of the P^{n}BG QC architecture, the elastic wave field across the entire top surface of the P^{n}BG QC will be measured to determine the mode shape topography. Thus, for comparison with experiment, the desired numerical method also requires modal analysis capability. Lastly, transducer and applicability studies will require multi-physics (electromechanical and thermomechanical) capability.

There are an abundance of third party FEM implementations, such as ANSYS® COMSOL® and CoventorWare®, which provide the needed capability to model curved surfaces, fixed and free boundaries, mode shape and thermomechanical and electromechanical multi-physics. For these reasons, FEM was the chosen numerical method for modeling the P^{n}BG QC architecture.

The primary crystal geometry that will be studied in association with the P^{n}BG QC

architecture is the honeycomb crystal geometry, which can be readily represented by FEM meshes, and is described analytically in the next section.

2.4 Honeycomb Phononic Band Gap Crystallography

Honeycomb P^{n}BG crystals are formed from a hexagonal lattice (also referred to as an equilateral triangular lattice) such as that displayed in Figure 2.3(a). The hexagonal lattice is one of the five two-dimensional Bravais lattices [112]. The first Brillouin zone and irreducible Brillouin zone of the hexagonal lattice are displayed in Figure 2.3(b). To create a honeycomb crystal from a hexagonal lattice a diamond shaped unit cell with two inclusions, as shown in Figure 2.3(c), is placed at each lattice point. The resultant honeycomb crystal of Figure 2.3(d) is obtained.

The primitive vectors that are illustrated in Figure 2.3(a) of the two-dimensional hexagonal lattice are given by [113]:

$$\begin{aligned} \vec{a_1} &= \frac{a}{2}\hat{x} + \frac{\sqrt{3}a}{2}\hat{y} \\ \vec{a_2} &= -\frac{a}{2}\hat{x} + \frac{\sqrt{3}a}{2}\hat{y}, \end{aligned} \tag{2.1}$$

where a is the lattice constant. The reciprocal lattice vectors of a three-dimensional lattice are given by [112]:

$$\begin{aligned} \vec{b_1} &= 2\pi\frac{\vec{a_2}\times\vec{a_3}}{\vec{a_1}\cdot\vec{a_2}\times\vec{a_3}} \\ \vec{b_2} &= 2\pi\frac{\vec{a_3}\times\vec{a_1}}{\vec{a_1}\cdot\vec{a_2}\times\vec{a_3}} \\ \vec{b_3} &= 2\pi\frac{\vec{a_1}\times\vec{a_2}}{\vec{a_1}\cdot\vec{a_2}\times\vec{a_3}}. \end{aligned} \tag{2.2}$$

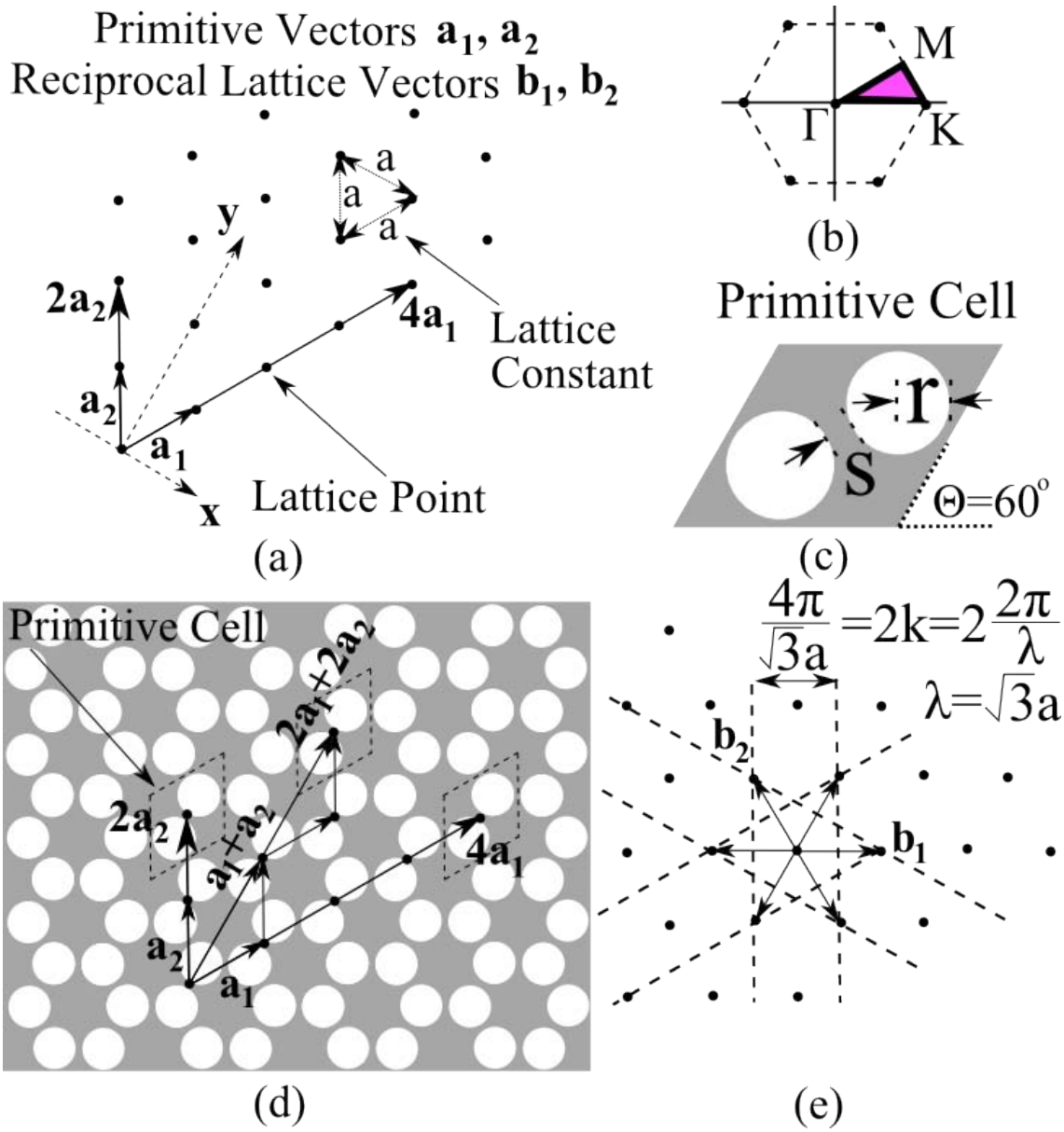

Figure 2.3: Construction of the two-dimensional honeycomb crystal, with the (a) hexagonal (equilateral triangle) lattice, (b) the first Brillouin zone (hexagon with center Γ) and irreducible Brillouin zone (right angle triangle with critical points Γ, K and M) of the hexagonal lattice. The diamond shaped primitive cell in (c) is utilized in the formation of the honeycomb crystal in (d). The primitive cell contains two circular inclusions that have a radius r and spacing s. The Bragg planes of the hexagonal lattice are displayed in (e).

Inserting Equation 2.1 into Equation 2.2 with $\vec{a_3} = 0\hat{x}+0\hat{y}+\infty\hat{z}$, the two-dimensional hexagonal reciprocal lattice vectors may be computed as:

$$\begin{aligned} \vec{b_1} &= 2\pi\left(\frac{1}{a}\hat{x} + \frac{1}{\sqrt{3}a}\hat{y}\right) \\ \vec{b_2} &= 2\pi\left(-\frac{1}{a}\hat{x} + \frac{1}{\sqrt{3}a}\hat{y}\right). \end{aligned} \tag{2.3}$$

The lattice constant, a, of the honeycomb crystal is related to the inclusion spacing, s, and radius, r, by:

$$a = 2(2r + s)cos(30^o). \tag{2.4}$$

As displayed in Figure 2.3(e), the wavelength satisfying the Bragg condition between the first Bragg planes of the hexagonal lattice is $\lambda = \sqrt{3}a$ where a is the lattice constant given by Equation 2.4. The first Bragg frequency of the honeycomb P$^{\text{n}}$BG crystal may then be:

$$f_{\Gamma M} = \frac{c_{avg,hex,circle}}{\lambda} = \frac{c_{avg,hex,circle}}{\sqrt{3}a}. \tag{2.5}$$

where $c_{avg,hex,circle}$ is the average elastic wave velocity. Assuming isotropic host and inclusion materials the average elastic wave velocity, $c_{avg,hex,circle}$, of the honeycomb lattice may be modeled as:

$$\begin{aligned} c_{avg,hex,circle} &= ff \times c_i + (1 - ff)\, c_h, \\ ff &= \frac{2\pi r^2}{A}, \\ A &= |\vec{a_1} \times \vec{a_2}| = a^2 sin(60^o), \end{aligned} \tag{2.6}$$

where ff is the fill factor of the primitive cell, r is the inclusion radius, A is the area of the hexagonal lattice primitive cell that is displayed in Figure 2.3, and c_i, and c_h, are the inclusion, and host, elastic wave velocities, respectively.

Table 2.2: Strengths and weaknesses of the numerical methods utilized, in the literature, to study classical elastic wave phononic band gap crystals.

Numerical Method	Domain	Defects	Finite Periodicity	Infinite Periodicity	Plates	Arbitrary Pulse Shapes	Arbitrary Source & Detector Shape	Transient Response	Band Structure	Transmission Coefficients	Phase Response	Mixed Material Systems	Arbitrary Inclusion Geometry
PWE	Frequency			Yes	Yes				Yes				Yes
SC-PWE	Frequency	Yes		Yes	Yes				Yes				Yes
VM	Frequency			Yes					Yes			Yes	Yes
LM	Frequency			Yes					Yes				Yes
FD-FEM	Frequency			Yes					Yes			Yes	Yes
TD-FEM	Time		Yes	Yes		Yes	Yes	Yes	Yes	Yes	Yes	Yes	Yes
DFEM	Time		Yes	Yes		Yes	Yes	Yes	Yes	Yes	Yes	Yes	Yes
MST	Frequency			Yes					Yes			Yes	
Hou	Frequency			Yes					Yes	Yes		Yes	Yes
WM	Frequency	Yes		Yes					Yes			Yes	
FDTD	Time	Yes	Yes	Yes	Yes	Yes	Yes	Yes	Yes	Yes	Yes	Yes	Yes

Chapter 3

Proposed Phononic Band Gap Quasi-Crystal Architecture and Design Methodology

As presented in Section 2.1.4, micro-integration of P^{n}BG crystals as reported in the literature utilizes exotic piezoelectric transduction, P^{n}BG crystals that are etched into semi-infinite or finite-thickness slabs that support surface or slab traveling waves, crystal lattices between approximately six and 12 lattice constants in dimension, crystal truncation by homogeneous mediums or piezoelectric transducers and don't appear to optimize the boundary region of the P^{n}BG crystal.

This thesis reports, to the best of the author's knowledge, for the first time, the theory and experiment of a new architecture, referred to as the P^{n}BG QC architecture [94]. In light of the work presented in the literature review of Chapter 2, the development of the P^{n}BG QC architecture in this thesis appears to present several studies that are the first of their kind, including the development and utilization of (i) unique air gap electro-

static transducer geometries for the wide band electrostatic actuation of standing waves, including in-plane and out-of-plane modes, in the silicon P^{n}BG QC resonator structure that is based on the geometry of honeycomb P^{n}BG crystals, (ii) free standing boundaries (except at tether attachment points) about the P^{n}BG QC for potentially improved energy confinement and reduced motional resistance, (iii) a serrated truncation boundary on the P^{n}BG QC to provide unconstrained motion of the truncation boundary and assist with complete band gap formation, (iv) circular and square truncation boundary geometries on P^{n}BG QCs, (v) tethered support of P^{n}BG crystal-like structures, (vi) a tuning methodology for tethers and serrated edges to enable complete band gap (which is an uninterrupted frequency range where no normal modes are permitted) formation in the presence of the non-idealities of finite periodicity of the P^{n}BG QC lattice and attachment of anchored tethers to the P^{n}BG QC, and (vii) the resultant provisioning for the potential incorporation of electrostatic sensing of P^{n}BG QC motion at the P^{n}BG QC boundaries. The development of the P^{n}BG QC architecture may also yield insight into anchor loss reduction, vibration stabilization and the unique design of two-dimensional mechanically coupled resonators, providing a relatively elegant method to interconnect large arrays of mass and spring elements. The geometry of the P^{n}BG QC is amenable to fabrication in a finite thickness layer of a planar fabrication process.

In block diagram form, the proposed P^{n}BG QC architecture is comprised of three main components, as depicted in Figure 3.1: the P^{n}BG QC, tethers and anchors (support) and the electrostatic transducers.

Electrostatic transducers mitigate the use of exotic piezoelectric materials, improving silicon compatibility and provide action at a distance type forces so that edges of the P^{n}BG crystal are free standing for reduced anchor loss. The free standing P^{n}BG crystal may improve energy confinement for potentially reduced substrate mode loss,

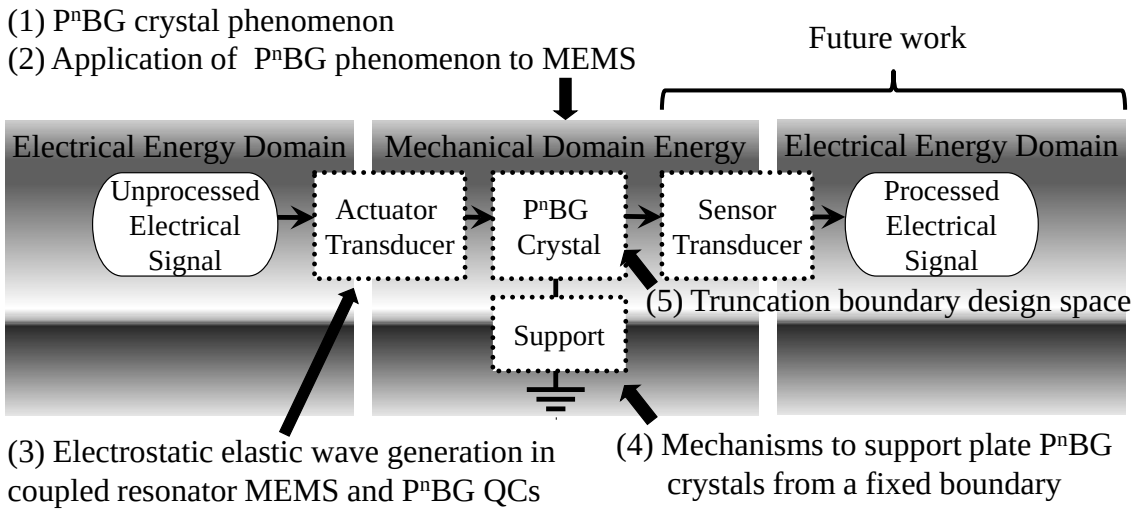

Figure 3.1: Block diagram of the subcomponents of phononic band gap quasi-crystal (P^{n}BG QC) architecture. Five areas for research contributions are denoted: (i) research into phononic band gap crystal phenomenon, (ii) research into the integration of phononic band gap crystals into MEMS, (iii) electrostatic transducer design for actuation of phononic band gap crystals, (iv) mechanisms to support phononic band gap crystals from mechanically fixed boundaries, and (v) the study of a (square and circular) truncation boundary design space. The sensing of vibrations and transduction back to the electrical energy domain is left for future work.

and potentially improved in-plane energy confinement, compared with surface [32], and slab [90], wave P^{n}BG crystals, respectively. Air inclusions may be utilized to provide a high acoustic impedance contrast with a solid host material and, in comparison with solid inclusions, may reduce motional resistance (increase compliance).

The functional potion of this P^{n}BG QC architecture requires only a single layer to realize, one additional layer of metallization may be applied for bond wire and signal conduction to electrodes. The requirement of a single layer provides flexibility over some piezoelectric P^{n}BG crystal architectures which in the cases where the P^{n}BG crystal is to have a material composition different from the piezoelectric material employ one piezoelectric layer over and above the host layer in which the functional portion of the P^{n}BG crystal is fabricated.

The geometrical parameters and design methodologies of the P^{n}BG QC architecture were developed subject to equipment and fabrication process constraints. First, the non-destructive Laser doppler optical diagnostic test equipment that is utilized for experimental characterization of the fabricated devices has a frequency response that is flat to within $\pm 1dB$ over the range from 50 kHz to 20 MHz. Hence, the first constraint on the geometry of the P^{n}BG QCs is that the upper edge of the band gap, and behavior of interest, lie below 20 MHz so that the behavior of interest lies within the measurable range. Second, several P^{n}BG QC devices were to be fabricated so that the effect of varying geometry can be observed; however, only one chip could be fabricated due time constraints, and so die area is constrained. P^{n}BG QC devices need to be sized to fit as many devices as possible within the maximum usable area of 4.3 mm by 4.3 mm of the SOIMUMPs chip [114]. Lastly, the thickness of the single-crystal-silicon functional layer in the SOIMUMPs fabrication process is optionally either $10\mu m$ or $25\mu m$ [115]; the thickness of $25\mu m$ was chosen since the complete band gap formation was found to be more difficult as the layer thickness becomes small relative to lattice constant (this will be illustrated in the sensitivity analysis of Chapter 4). A few less restrictive SOIMUMPs fabrication process constraints place size limits on the electrostatic transducer gap size, inclusion spacing and anchor width and will be addressed within this chapter.

This chapter presents the geometry and design methodologies for the (i) P^{n}BG QC (Section 3.1), (ii) T-shaped tethers (Section 3.2) and (iii) electrostatic transducers (Section 3.4). Geometrical design parameters are summarized in Section 3.3 for the P^{n}BG QC and Section 3.4 for the electrostatic transducers.

3.1 Phononic Band Gap Quasi-Crystal Architecture and Key Geometrical Parameters

The P^{n}BG QC architecture employs the geometry of a two-dimensional honeycomb P^{n}BG crystal. The primitive cell contains two circular inclusions, of radius r, and spacing s, and for compatibility with planar fabrication processes has a finite thickness of t. A primitive cell is located at each hexagonal crystal lattice point as shown in Figure 3.2.

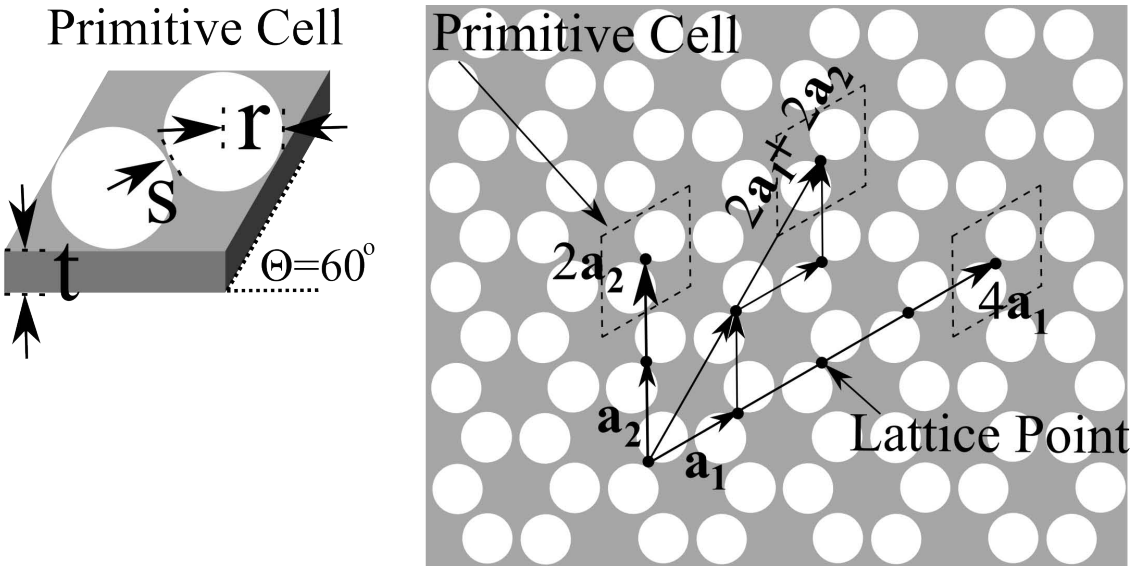

Figure 3.2: Geometrical parameters of a two-dimensional honeycomb phononic band gap crystal with circular inclusions centered on the lattice points. The primitive cell contains two circular inclusions, of radius, r, and spacing s, and for compatibility with planar fabrication processes has a finite thickness of t. The primitive cell is located at each lattice point to form the honeycomb crystal.

The two-dimensional honeycomb P^{n}BG crystal is truncated by utilizing circular and square truncating boundary geometries as shown in Figure 3.3. To achieve symmetry, planes of mirror symmetry in the circle or square truncating boundary geometries should align with planes of mirror symmetry in the honeycomb P^{n}BG crystal. Two possible

alignments that achieve symmetry and provide four equally spaced points to which anchors may be attached to the host material region are displayed in Figure 3.3 for circle and square truncating boundary geometries.

As illustrated in Figure 3.4 a T-shaped tether was implemented to suspend the P^{n}BG QC from the substrate. In comparison with straight tethers, T-shaped tethers have more degrees of freedom in mechanical design, and for a given beam compliance may provide a larger beam thickness. Since fabrication processes may have a minimum anchor size rule, larger beam widths may be advantageous.

The tether and anchor geometry is chosen to yield a P^{n}BG QC that has no defect states in the band gap thereby enabling complete band gap formation. The choice of tether size may be coupled to the sizing of circular, or square, truncation boundary diameter, or width, respectively, and so these design choices are discussed together next in Section 3.2.

3.2 Phononic Band Gap Crystal Lattice Truncation and Tether Tuning Design Methodologies

Figure 3.4 contains geometrical objects that now have to be designed to yield the desired band gap behavior. In order to choose the circular, or square, truncating geometry boundary diameter, or width, respectively, and tether size, modal analysis is performed on the P^{n}BG QC utilizing fixed boundaries to model substrate anchor locations, which are shown in Figure 3.4. The frequency range of the modal analysis is 0 to 20 MHz, within which the band gap must be present for compatibility with Laser-doppler test equipment. One result of the modal analysis is the mode frequency versus mode number curve. The potential band gap location may be indicated in the mode frequency versus

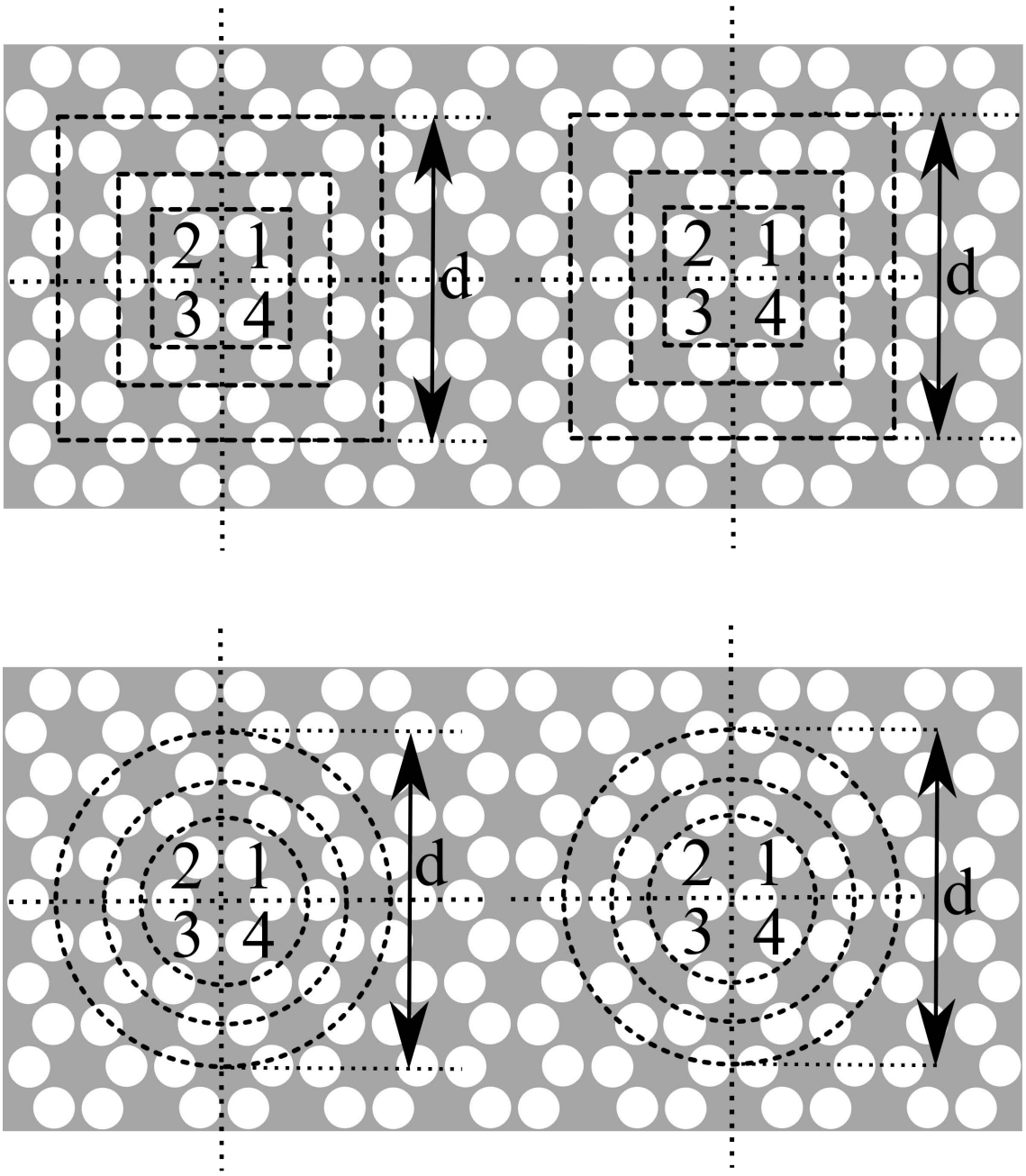

Figure 3.3: Phononic band gap crystal truncation for square and circular truncation geometries at different truncation diameters. The truncation boundaries are chosen to ensure that quadrants 1, 2, 3 and 4 display the same geometry.

mode number curve by either: (i) a complete absence of modes as shown in Figure 3.5(c), (ii) a few defect states within the band gap as shown in Figure 3.5(b) or (iii)

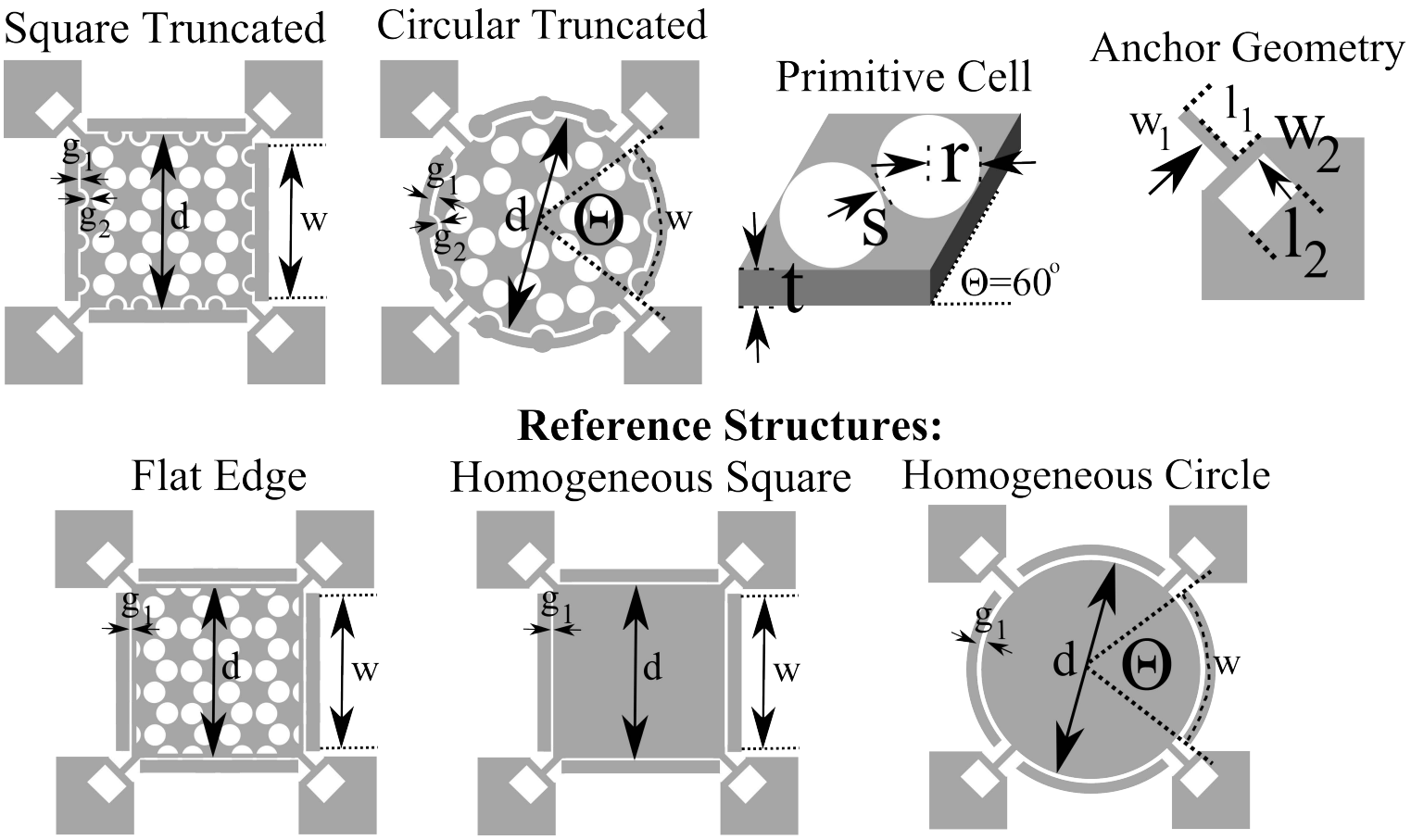

Figure 3.4: Schematic of the phononic band gap quasi-crystal architecture implemented with a hexagonal lattice, circular inclusions and square and circular truncating boundary geometry. The geometrical parameters of interest are truncation width, d, inclusion spacing and radius, s and r, and plate thickness, t. Three reference structures were developed: (i) a square truncated phononic band gap quasi-crystal with flat edges, and homogeneous (ii) square and (iii) circular reference plates.

a frequency range where the slope of the mode frequency versus mode number curve displays inflection points as shown in Figure 3.5(a) - these characteristics all indicate a decrease in the density of normal modes which could potentially be evidence of band gap behavior. In the latter two cases, additional tuning of either the tethers, P^{n}BG QC boundary, or P^{n}BG QC parameters, including crystal type and unit cell, may often need to be performed to eliminate the normal modes, which are referred to as defect states, from the in-gap frequencies.

Once the band gap location has been identified, the mode shapes of the defect state modes are observed to determine which part of the P^{n}BG QC has to be modified to eliminate the defect state modes. Usually defect state modes display localized resonant activity, the normal mode shapes of the structure may be examined to determine where the localized resonant activity is occurring and these portions of the structure may be tuned or removed to eliminate their local resonance thereby eliminating the defect state modes. The appearance of defect state modes will be presented in Chapter 4.

Defect state modes whose primary vibrational activity is localized to edges of the P^{n}BG QC can potentially be eliminated by either (i) performing a sweep of the truncation boundary (edge) location to eliminate defect state modes or (ii) cutting off local features that are resonating on the edges of the P^{n}BG QC or choosing a different P^{n}BG geometry. Defect states whose primary vibrational activity is localized to the tethers of the P^{n}BG QC may often be eliminated by tuning the tether geometry. For the P^{n}BG QCs presented in this thesis, the tethers were tuned so that defect states produced by resonant modes that are localized to the tethers were shifted to frequencies above the band gap (alternatively, tethers tuned to frequencies below the band gap may be more compliant for lower motional resistance). The justification for tuning the tether resonances to frequencies above band gap, as oppose to below the band gap, was chosen to

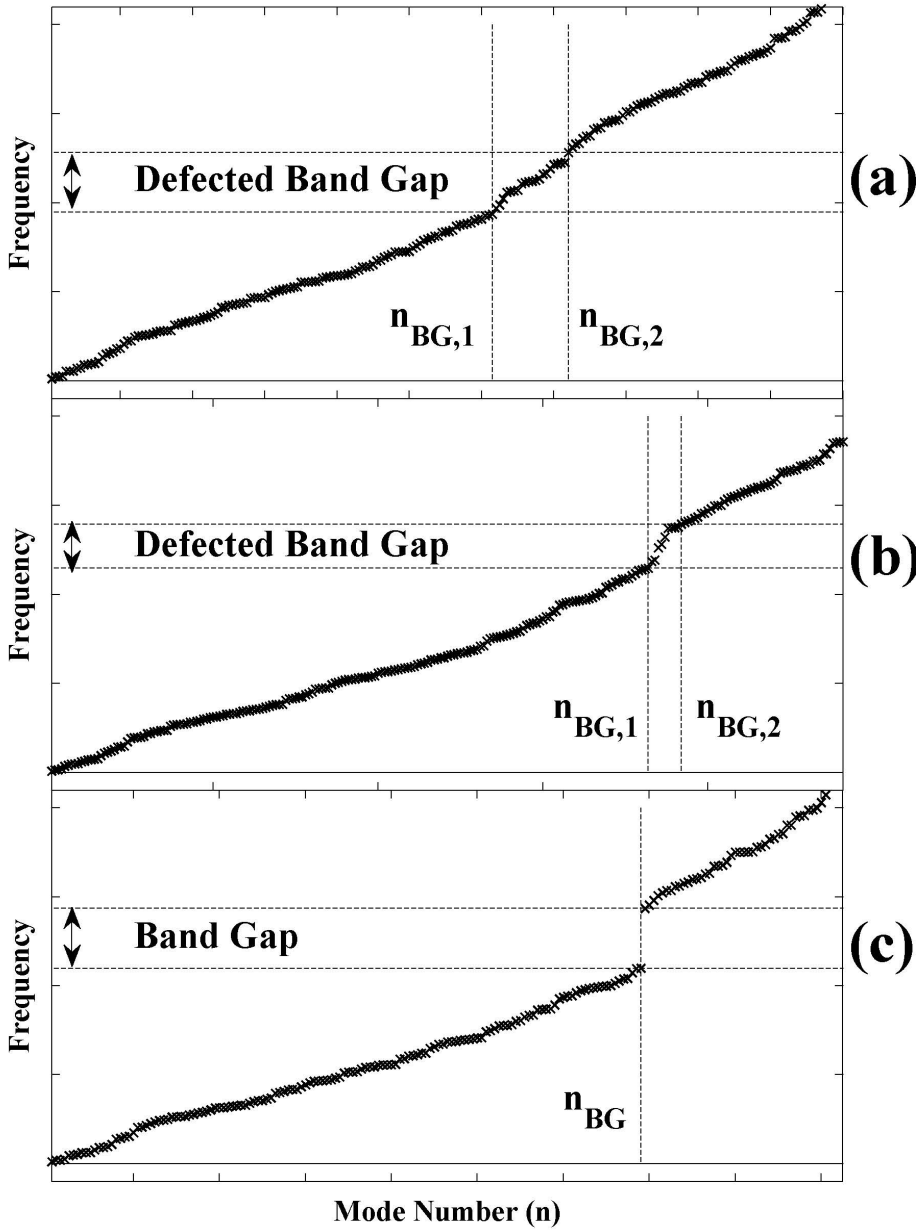

Figure 3.5: Sample frequency versus mode number characteristics for three phononic band gap quasi-crystals with differing truncation boundary locations: (a) a band gap does not appear but inflection points may indicate a potential band gap that contains defect states, (b) a few defect states appear within the band gap and (c) a band gap appears and is an indication of a phononic band gap quasi-crystal that behaves as desired.

produce more structurally rigid tethers at the expense of higher tether compliance. More structurally rigid (larger w_1 and w_2 in Figure 3.4) tethers may also be more conducive to meeting minimum anchor size requirements of a fabrication process.

The end result of the previously described truncation boundary location tuning, the removal of features that may be producing localized edge resonances and tether tuning is a P^{n}BG QC that displays a complete band gap in the frequency versus mode number characteristic, such as that shown in Figure 3.5(c).

It may be noted that a lattice is a discrete set of points in space, and while the P^{n}BG crystal truncation methods applied here do truncate the hexagonal lattice that underlies a P^{n}BG crystal, the truncation most importantly applies to the continuous medium that forms the host of a P^{n}BG crystal. The truncation of a lattice would have a discrete set of truncation locations, while the truncation of the continuous host medium has a theoretically infinite set of truncation locations. Thus, truncation of the P^{n}BG crystal host medium is a more complex problem than lattice truncation. The multitude of possibilities for the truncation of the continuous host medium of a P^{n}BG crystal have to be diligently modeled and evaluated following the methodology described above to find the truncation boundary that yields a complete band gap.

The design methodology presented here was discussed for the specific case of a P^{n}BG QC that is comprised of a two-dimensional honeycomb crystal with circular inclusions; however, the methodology may be applicable to other crystals. An attempt was made to apply the methodology presented here to P^{n}BG crystals that have square lattices and circular inclusions; however, in the given search time, a complete band gap could not be found so further investigation is required. In some cases the P^{n}BG crystal lattice and geometry may have to be changed.

In addition to choosing a truncation boundary location to yield complete band gap

formation, the choice of truncation boundary location must also result in a P^{n}BG QC to which four equally spaced tethers may be attached - this further restricts the choice of truncation boundary location. As may be observed in Figure 3.3, some truncation boundaries may result in the tether attachment points being located within the inclusion medium, which if the inclusion is composed of air cannot serve as a physical attachment point for the tether. Hence, at the desired tether attachment points on the truncation boundary, the truncation boundary has to intersect the host medium, which for the P^{n}BG QC architecture presented here is comprised of a solid material to which the tethers can be attached. In some cases, if an air inclusion is present at or near the desired tether attachment point, this inclusion may be removed so long as the modal analysis indicates that removing the inclusion does not interfere with complete band gap formation.

Through the scalability of the elastic wave equation which governs the behavior of the P^{n}BG QCs, the P^{n}BG crystal truncation and design methodology that has been presented here should be scalable to different frequency regimes, by simply scaling the size of the structure.

While the studies presented in this thesis could not find a flat edge geometry that displayed no defect states, it may be possible that for P^{n}BG QCs that are a relatively large number of lattice constants in dimension (so that the P^{n}BG QC dominates the behavior of the device), or through very careful design, the defect states produced by resonant modes that are localized to the edges of the P^{n}BG QC may be mitigated or made negligible without the use of a serrated edge. Other edge geometries may be investigated, for example a hybrid of a flat and serrated edge. It may be noted that one problem associated with the use of flat edges is that the flat edge couples adjacent regions of the P^{n}BG QC together so that they are not free to move out-of-phase or

independently and thus significantly perturb the behavior of the P^{n}BG QC. In contrast, the serrated edge allows different regions on the edge of the P^{n}BG QC to move relatively independently, and mechanical coupling occurs primarily through the P^{n}BG QC. Further study of flat and other edge geometries may be performed for the P^{n}BG QCs. The behavior of flat edged P^{n}BG QCs will be numerically illustrated in Section 4.2.3.

3.3 Geometrical Properties of the Proposed Phononic Band Gap Quasi-Crystal Architecture

Following the design methodology presented here, six P^{n}BG QCs were produced that have serrated edges and display a complete band gap: three for circular and three for square truncation boundary geometries. A P^{n}BG QC was also created utilizing a square truncation boundary geometry and flat (not serrated) edges to act as reference that illustrates the difficulty that arises in forming a complete band gap when utilizing flat edges (as will be numerically illustrated in Section 4.2). Homogeneous circle and square reference devices were also designed. The geometrical parameters of all these structures are quantified in Tables 3.1 and 3.2.

As may be viewed in Tables 3.1 and 3.2, each structure has been assigned a name. The three P^{n}BG QCs that have serrated edges and square (circular) truncation boundary geometries are named S1, S2 and S3 (C1, C2 and C3). The reference P^{n}BG QC that has flat edges and a square truncation boundary is named S4. The homogeneous reference structures that have a square and circular boundaries are named Square and Circular reference.

Table 3.1: Geometrical parameters of the proposed phononic band gap quasi-crystals and reference devices. Units are in microns (μm) unless otherwise specified.

Device	Plate Diameter, d	Plate Thickness, t	Plate Tether Length, l_1	Plate Tether Width, w_1	Anchor Tether Length, l_2	Anchor Tether Width, w_2	Low Curvature Gap, g_1	High Curvature Gap, g_2	Transducer Width‡, w
Square	650	25	60.104	9.899	50.001	10.00	2	-	575
S1	650	25	60.104	9.899	50.001	10.00	2	3	575
S2	650	25	60.104	9.899	50.001	10.00	2	3	575
S3	650	25	60.104	9.899	50.001	10.00	2	3	575
S4	650	25	60.104	9.899	50.001	10.00	2	-	575
Circle	575	25	60.104	9.899	50.001	10.00	2	-	324.613 μm (64.692^o)
C1	575	25	60.104	9.899	50.001	10.00	2	3	~385.34 μm (74.218^o)
C2	575	25	60.104	9.899	50.001	10.00	2	3	
C3	575	25	60.104	9.899	50.001	10.00	2	3	

‡ For the circular plate devices this is the transducer arc length (arc angle).

Table 3.2: Geometrical parameters of the proposed phononic band gap quasi-crystals and reference devices (continued). Units are in microns (μm) unless otherwise specified.

Device	Circular Inclusion Radius, *r*	Circular Inclusion Spacing, *s*
Square	-	-
S1	45	2
S2	45	3
S3	45	4
S4	45	2
Circle	-	-
C1	40	2
C2	40	3
C3	40	4

3.4 Embedded Electrostatic Transducer Design Concept and Geometrical Parameters

In addition to choosing a truncation boundary location to yield complete band gap formation and four equally spaced points to which the tethers may be attached, ideally, the choice of truncation boundary location should also yield a P^{n}BG QC that allows for four identical transducers to interface with the P^{n}BG QC so that forces that are equal, or relatively comparable, in magnitude are imparted by all transducers (unless the P^{n}BG QC was designed to compensate for transducers that imparted forces with relatively different magnitudes). If the transducers didn't impart comparable forces, the unbalanced forces may distort the excited normal mode shape which could potentially make comparison difficult with models of the normal mode shape. Thus, the truncation boundary location was chosen to result in a P^{n}BG QC that displays some degree of symmetry.

As may be observed in Figure 3.4, the circular truncated P^{n}BG QC has four rela-

tively similar transducers, whereas the square plate device displays similar transducers on only diametrically opposite sides. Figure 3.4 illustrates that one pair of transducers on the square truncated P^{n}BG QC has closely spaced inclusions, while the other pair of transducers has widely spaced inclusions. The circular truncated device thus helps eliminate asymmetry in the transducer geometry and overlap areas. While differing electrostatic transducer geometries and overlap areas may still result in equal magnitudes of electrostatic force in a given (set of) direction(s), it may be more challenging for differing geometries to produce the same magnitude of electrostatic force in all directions. For the P^{n}BG QC geometries presented in Figure 3.4, the greater degree of symmetry in the geometry of the electrodes along the circular truncation boundary, relative to the square truncation boundary, may assist in applying forces with more balanced magnitudes and directions to the four edges of the P^{n}BG QC.

To interface electrostatic transducers with the serrated edge of the P^{n}BG QCs, the transducer electrode is embedded into the P^{n}BG QC as illustrated in Figure 3.4. The overlap areas of the resultant electrostatic transducers are now analyzed. Figure 3.6 displays the overlap areas of the electrodes for the square truncated P^{n}BG QCs. As may be observed in Figure 3.6, for the square truncated P^{n}BG QCs, the transducers with widely spaced inclusions have smaller overlap areas than the transducers with closely spaced inclusions.

Figure 3.7 provides a side by side comparison of the electrode areas of the circular truncated P^{n}BG QCs with the electrode areas of the electrodes with widely and closely space inclusions of the square truncated P^{n}BG QCs. Each P^{n}BG QC is designed to lie within approximately the same die area. Thus, per unit die area, it may be noted from Figure 3.7 that the square truncated P^{n}BG QCs display larger transducer overlap areas as compared to the circular truncated P^{n}BG QCs. It may also be observed that the

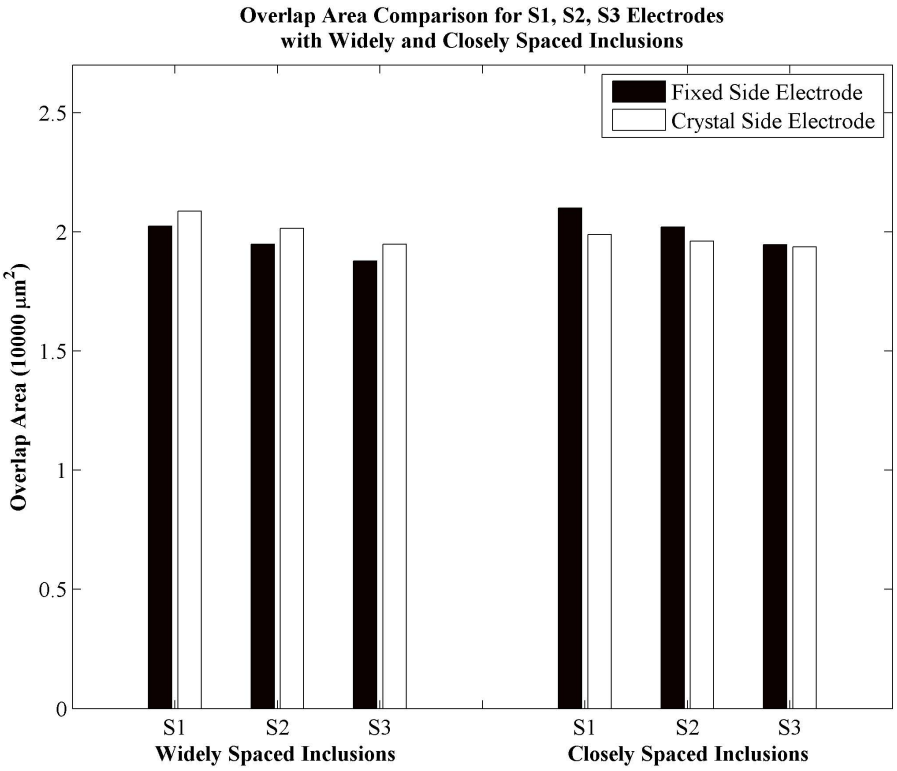

Figure 3.6: Comparison of transducer electrode areas for the transducer electrodes with widely and closely spaced inclusions for devices S1, S2 and S3.

P^nBG QCs display larger transducer electrode areas as compared to the homogeneous Square and Circular reference devices, due to the increased surface area produced by the serrated edge of the P^nBG QC.

Table 3.3 quantitatively summarizes the overlap areas that have been displayed in Figure 3.6 and 3.7. These overlap areas will be utilized in Section 4.1 to analytically model the magnitude of the electrostatic forces that are generated by the transducers.

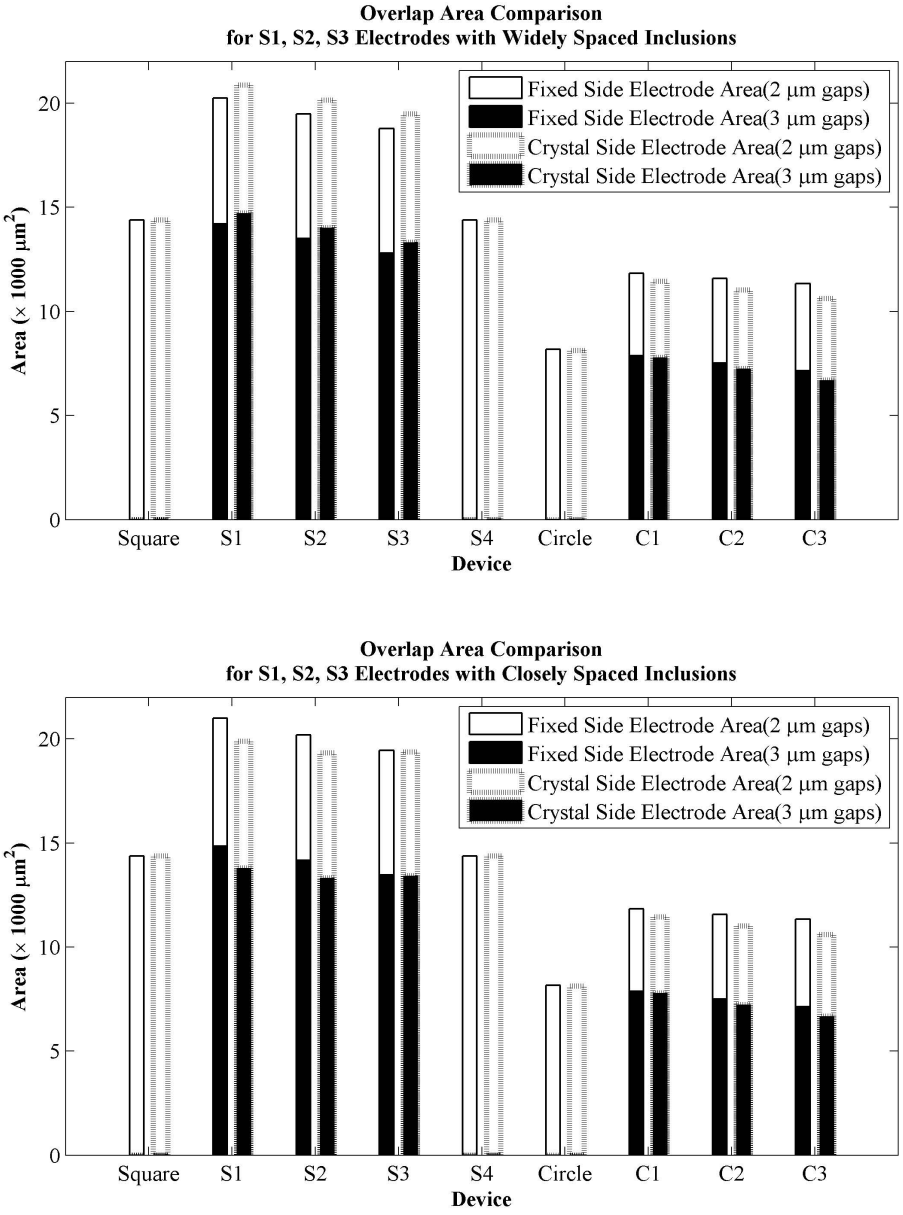

Figure 3.7: Comparison of electrode areas of all device transducers. The total electrode area is comprised of the electrode areas over electrode segments where the electrode gap is $2\mu m$ and $3\mu m$. The fraction of the total electrode area comprised by the electrode segments electrode gap is 2 is shown in white and 3 is shown in black. As may be seen, for S1, S2, S3, C1, C2 and C3 the majority of the electrode area occurs over the electrode segments where the electrode gap is 3.

Table 3.3: Transducer overlap areas for the S1, S2, S3, S4, C1, C2, C3 P^{n}BG QCs and square and circular homogeneous reference structures. Tables 3.1 and 3.2 list the geometry of structure and the geometrical parameters are described in Figure 3.4.

Device	Fixed-Side Transducer Overlap-Area		Mid-Gap Surface Area	Crystal-Side Transducer Overlap-Area	
	CW§	Calculated‡	Calculated‡	ANSYS†	Calculated‡
Square	14375	14375	14375	14375	14375
S1	20233/20994	19170	19341	20863/19880	19512
S2	19469/20196	19170	19341	20144/19609	19512
S3	18781/19450	19170	19341	19481/19359	19512
S4	14375	14375	14375	14375	14375
Circle	8172	8172	8144	8115	8115
C1	11829	10497	10876	11442.5	11257
C2	11574	10497	10876	11014	11257
C3	11340	10497	10876	10604	11257

All units are (μm^2). § Computed by CoventorWare solid model environment. ‡ Analytical calculation, based on simplified geometry. † Computed by ANSYS solid model environment. The value before, and after, the "/" is for the transducer that has widely, and closely, spaced inclusions, respectively.

Chapter 4

Electro-Mechanical Model of Phononic Band Gap Quasi-Crystal Architecture

The characteristics of the proposed P^{n}BG QC architecture, including truncation of the unique P^{n}BG QC geometry by free boundaries and the attachment of the P^{n}BG QC to mechanically grounded tethers, introduce a unique set of boundary conditions on the elastic wave equation. Crystal lattice truncation yields a quasi-crystal (as oppose to an infinitely periodic crystal), which will be defined as a structure that displays periodicity with respect to space in its material properties but that is a finite number of lattice constants in physical dimension. In the finite quasi-crystal, the elastic band structure is quantized. The finite dimension may cause some frequency characteristics to display a low cut-off frequency, similar to the behavior of rectangular electromagnetic waveguides [116]. The geometry of the supporting tethers in the P^{n}BG QC is not a continuation of the periodic mechanical structure of the P^{n}BG QC. The tethers thus disrupt the

periodicity in the mechanical properties of the P^{n}BG QC, and so may be considered a physical crystal defect state and thus are designed according to the methodology of Chapter 3 to appropriately shift the vibrational response of the tethers to outside the band gap frequency range. Due to the aforementioned features of the P^{n}BG QC architecture, generic models of infinitely periodic P^{n}BG crystals do not provide a complete model of the proposed P^{n}BG QC architecture. Thus, unique models of the P^{n}BG QC architecture are required.

The model in this chapter illustrates that the proposed P^{n}BG QC architecture appears to display some of the characteristic behavior of a P^{n}BG crystal. The model will suggest that the shape of the modes above and below the band gap of the proposed P^{n}BG QC display different characteristic shapes, similar to how the acoustical and optical branch modes of a P^{n}BG crystal each display characteristic shapes. The unique behavior of the P^{n}BG QC architecture will be demonstrated, in part, by comparing the model of the P^{n}BG QC architecture with the model of homogeneous reference resonators that have identical truncation diameter and tether geometry to first illustrate that the P^{n}BG QC architecture displays behavior that is different from homogeneous reference resonators. Relative to the homogeneous reference resonators, the P^{n}BG QC architecture will be shown to provide a methodology to increase the density of normal modes in certain frequency regions, and simultaneously be utilized to decrease the density of modes (in theory to zero) in other frequency regions to provide a broadband absence of normal modes modes, which is analogous to the characteristic behavior of a P^{n}BG crystal. In the frequency region of the band gap, the P^{n}BG QC architecture may be considered to be the antithesis of a resonator: the band gap frequency region of operation displays an absence of resonant modes. While a homogeneous plate may have frequency regimes were there is an absence of normal modes, the P^{n}BG QC architecture

provides one means to systematically design the location and width of the region where normal modes are absent and for comparable geometries may yield a wider frequency range where modes are absent.

The models will also help to differentiate between the behavior of a P^{n}BG QC and a plate with an arbitrary array of periodically placed etch holes. In theory, the band gap of a P^{n}BG crystal is caused by a carefully designed geometry which sets up the conditions for phenomenon such as Bragg and Mie reflections to yield broadband constructive interference of elastic waves and thus a phononic band gap. Hence, a plate with arbitrarily placed etch holes does not necessarily display a band gap. Furthermore, the P^{n}BG QC architecture design methodologies that were presented in Chapter 3, wherein a honeycomb crystal geometry is created by placing etch holes into a finite thickness plate, of unspecified material composition, which is truncated by free boundaries to a low number of lattice constants then suspended by tethers to fixed boundaries, does not necessarily yield a structure that displays the characteristics (namely a band gap) of an ideal infinitely periodic P^{n}BG crystal. The models of this chapter will support that the design methodologies that were presented in Chapter 3 can produce P^{n}BG QCs with the non-obvious and desired band gap behavior for specific geometries.

The models will also illustrate what may be non-obvious behavior with respect to the frequency versus mode number characteristic of the P^{n}BG QCs, namely that (i) at low frequencies the P^{n}BG QCs displays similar characteristics to a homogeneous plate, while (ii) at intermediate frequencies the P^{n}BG QC behavior dramatically deviates away from homogeneous plate behavior then (iii) at high frequencies the behavior of the P^{n}BG QC and homogeneous plate appear to converge. The model will contrast the effects of circular and square truncation boundary geometry on the properties of the band gap. Even if it may be argued that the approximate effect, on the band

gap properties, of the unique structural characteristics of the P^{n}BG QC architecture may be qualitatively anticipated utilizing sufficient experience (that is, obvious to some observers), the models presented here will provide evidence to numerically substantiate and quantify the behavior of the P^{n}BG QC architecture.

Section 4.1 presents the analytical model of the electrical integrated circuit formed by the P^{n}BG QCs. In Section 4.2 a numerical model is presented for the P^{n}BG QC normal mode frequency versus mode number, normal mode shape and multi-mode dynamic harmonic response within the 0 to 20 MHz frequency range. An analytical lumped element mass-spring model is utilized to model the dynamic harmonic response over a narrow band of frequencies situated near select resonant modes. The characteristics of these mechanical models of the P^{n}BG QC architecture are compared with analytical models of the Bragg frequencies of P^{n}BG crystals to identify similarities in behavior, between P^{n}BG QCs and ideal infinitely periodic P^{n}BG crystals, versus geometrical parameters and unit cell fill factor. The P^{n}BG QC architecture is then analyzed as a two-dimensional network of mass-spring elements where each mass element is granted six degrees of freedom (DOF). Next, a structural analysis of sub-sections, of the P^{n}BG QCs, that lie between the virtual mechanical grounds within the numerical mode shape models is performed to obtain semi-analytical flexural plate and beam models of the compliance and mass of each sub-section. These compliance and mass values are utilized in a lumped element vibration model. More complete periodic two-dimensional mass-spring network models are proposed for further study. A numerical sensitivity analysis versus geometry and material composition is also presented. Lastly, in Section 4.3, the mechanical and electric models are combined to model the coupled electromechanical behavior of the P^{n}BG QC architecture.

The mechanical models assume that the host, and inclusion, materials are comprised

of isotropic single-crystal-silicon, and air, respectively. The P^{n}BG QC is crafted out of what may be considered to be a thin plate and the material properties of the thin single-crystal-silicon films of the SOIMUMPs process may differ from the bulk material properties of single-crystal-silicon. Hence, a review of devices from the SOIMUMPs process was performed to determine the documented mechanical material properties of the single-crystal-silicon layer utilized in SOIMUMPs and is summarized in Table 4.1. Table 4.1 indicates that the material density, ρ, poisson ratio, ν, and Young's modulus, E, of the thin single-crystal-silicon layer in SOIMUMPs may be bounded between approximately 2330 kg/m^3 and 2500 kg/m^3, 0.064 to 0.29, and 170 GPa to 180 GPa, respectively. Table 4.1 lists the design values for the material density, Young's modulus, and poisson ratio, utilized (unless otherwise specific) in this thesis as 2300 kg/m^3, 180 GPa, and 0.29, respectively.

Table 4.1: Literature review of the mechanical material properties, and design values, for the single-crystal-silicon layer in the SOIMUMPs fabrication process [117] [118] [96].

	Young's Modulus, E (GPa)	Poisson Ratio, υ	Material Density, (kg/m^3)
Khine	180	0.29	2330
Lee	168	0.064	2500
This Work	180	0.29	2300

4.1 Electrical Radio Frequency Integrated Circuit Model

In this section the P^{n}BG QCs are modeled as purely electrical devices and the electrical circuit elements are extracted from the P^{n}BG QC structures to generate an electrical circuit model. The electrical circuit model will be utilized to quantify the electrical

signal that is transferred from the signal generator to the electrostatic transducers. The magnitude of the electrical signal on the electrostatic transducers will then be utilized to model the electrostatic force generated between the electrodes of the electrostatic transducer. For a given electrical signal, this magnitude of the electrostatic force may later be utilized to model the mechanical displacement of the P^{n}BG QCs, and be compared with numerical multi-physics model results.

4.1.1 Electrical Circuit Extraction from the Phononic Band Gap Quasi-Crystal Structure

A schematic of the electrical circuit components overlayed upon a P^{n}BG QC is displayed in Figure 4.1 for the case of a square truncation boundary, while approximately the same electrical circuit model may apply to P^{n}BG QCs with circular truncation, though higher order effects such as fringing of electrostatic fields, and so forth, may differ between the square and circular truncation types.

The resistance, capacitance and inductance of the RG-58 coaxial cables and printed circuit board interconnects, for RF and DC signals, are not accounted for in the electrical circuit models of Figure 4.1. In practice, relatively large signals are utilized, DC voltages on the order of 100 VDC and RF sinusoidal signals with an amplitude of 10 V, and series resistive and inductive voltage drops along cables are observed to be negligible. Electrical frequencies are relatively small and assist in limiting parasitic inductive impedances. Device and cable dimensions are small compared with the electrical signal wavelength (for the maximum experimental frequency of 20 MHz the $\lambda_{electrical,min} = \frac{c_o}{f_{max}} = 299,792,458m/s/20MHz \approx 15m$) so distributed effects may be negligible in the electrical system. The maximum electrical frequency of 20 MHz is orders of magnitude below the maximum usable operating frequency of 50Ω BNC con-

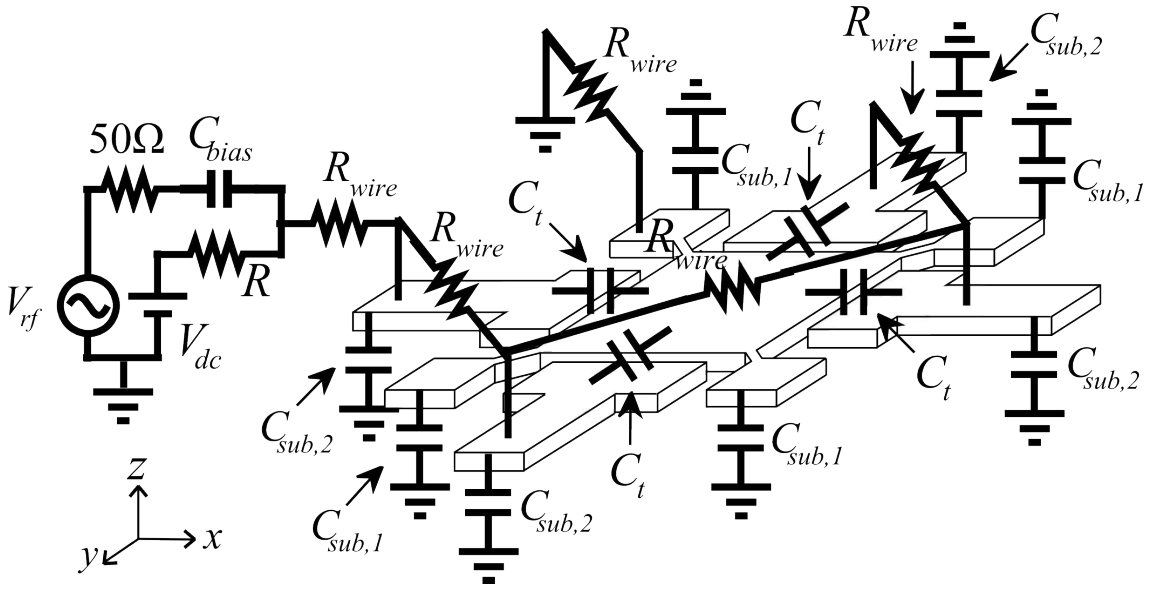

Figure 4.1: Extraction of the electrical circuit model from the approximate structure of a square truncated phononic band gap quasi-crystal. The source circuit impedance, bias tee circuit, and bond wire resistances are also illustrated. The resistance of package leads, and printed circuit board copper traces is not denoted here.

nectors, so connector parasitics may be negligible. RG-58 coaxial cable lengths were limited to one meter and may typically display an attenuation under 3 dB/m below 20 MHz. Where possible, unshielded wires that carry DC and ground voltages were twisted around one another to mitigate ground loops and noise coupling by Faraday induction.

Utilizing the electrostatic transducer mid-gap overlap areas from Table 3.3 the transducer capacitance values, C_t, were modeled utilizing the equation for the capacitance of a parallel plate capacitor:

$$C = \frac{\epsilon_o A}{g} \tag{4.1}$$

where $\epsilon_o = 8.854 \times 10^{-12} \quad F/m$, A is the transducer capacitor overlap area, and g is the capacitor gap. Equation 4.1 ignores fringe fields which may contribute additional capacitance. For each structure the computed transducer capacitance values are listed

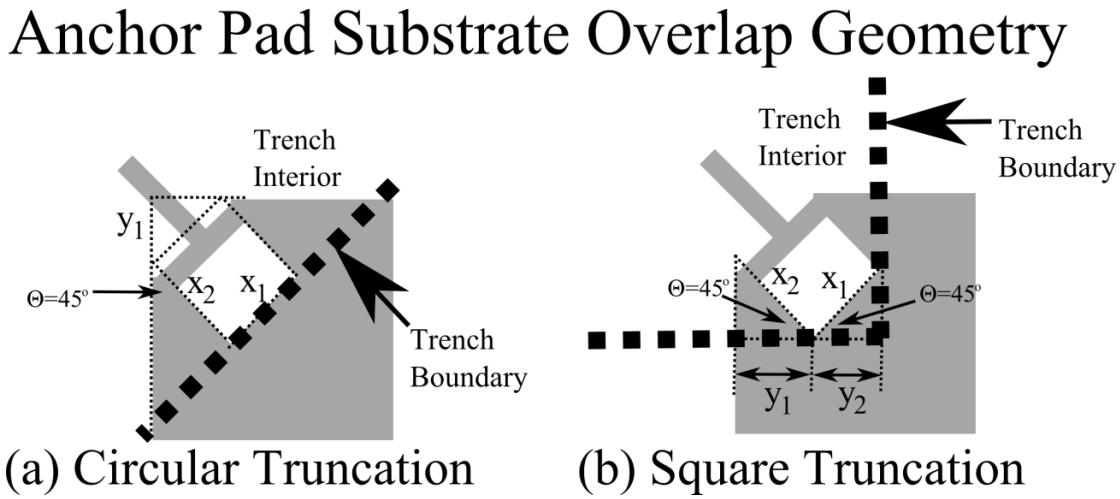

Figure 4.2: Anchor pad substrate overlap capacitance geometry for (a) circular and (b) square truncation geometry, where $x_1 = 50.001\mu m$, $x_2 = 75.48\mu m$. The anchor pad is created from a $200\mu m \times 200\mu m$ square pad. The region of this pad that has not been removed to incorporate the tether and that lies over the substrate contributes substrate capacitance. Fringe fields will be neglected. For the case of circular truncation, $y_1 = x_1 cos(45^o) = 35.356\mu m$, $A_{sub,1} = 200 \times 200\mu m^2 - (y_1 y_1/2 + x_2 x_2/2 + x_2 x_2/2 + x_1 x_2) = 29904\mu m^2$. For the case of square truncation, $y_1 = x_1 cos(45^o) = 35.356\mu m$, $y_2 = x_2 cos(45^o) = 53.372\mu m$, $A_{sub,1} = 200 \times 200\mu m^2 - (y_1 + y_2)^2 = 32127\mu m^2$.

in Table 4.2.

The geometry of the P^{n}BG QC anchor pads is displayed in Figure 4.2 where the anchor pad substrate overlap area is approximately $29904\mu m^2$ for circular truncation and $32127\mu m^2$ for square truncation due to the differing shape of the trench. To compute the approximate anchor pad capacitance these substrate overlap areas are utilized in Equation 4.2 along with a dielectric comprised of the $1\mu m$ oxide (which is the insulator layer of the SOI wafer) in series with a $25\mu m$ single-crystal-silicon layer and the computed anchor pad capacitance values are listed in Table 4.3.

Using the computed capacitance values from Tables 4.2 and 4.3, the electrical circuit displayed in Figure 4.1 was input into ADS®2009 as shown in Figure 4.3. The results of the AC analysis are depicted in Figure 4.4 and illustrate that for a source signal with

a source impedance of 50Ω and internal 10 V amplitude the voltage at the electrostatic transducer has an amplitude of approximately 9.985 V from approximately DC to 20 MHz. The voltage at the electrostatic transducer is small near DC due to the high series impedance of the bias-Tee capacitor depicted in Figures 4.1 and 4.3. However, the electrical circuit model of Figure 4.4 predicts what should be a sufficiently uniform transfer of voltage to the electrostatic transducers over the frequency range above DC and up to and including 20 MHz.

The aforementioned uniform transfer of voltage to the electrostatic transducers may have been anticipated analytically since the signal source has an output impedance of 50Ω and is connected to the input of the P^{n}BG QC which presents a load capacitor that has a relatively small capacitance value on the order of approximately 50 fF to 100 fF (as seen in Table 4.2) and so relatively large impedance. Figure 4.5 displays the AC equivalent circuit of the circuit model in Figure 4.3. Utilizing the AC equivalent circuit of Figure 4.5 and the component values from Figure 4.3, which include $C_{BIAS} = 1000pF$, $C_{TRANSDUCER} = 78fF$, $C_{TRANSDUCER\_PAD} = 200fF$, the impedances associated with the circuit capacitors may be expressed as:

$$\begin{aligned} Z_{BIAS} &= 1/(j\omega C_{BIAS}) \\ Z_{TRANSDUCER} &= 1/(j\omega 4C_{TRANSDUCER}) \\ Z_{TRANSDUCER\_PAD} &= 1/(j\omega 4C_{TRANSDUCER\_PAD}) \end{aligned} \tag{4.2}$$

where the four transducer capacitors, $4C_{TRANSDUCER}$, and transducer pad capacitors, $4C_{TRANSDUCER\_PAD}$, have been combined in parallel. Given the bias-tee AC blocking impedance value, $R_{BIAS} = 100k\Omega$, from Figure 4.3, the input impedance denoted in

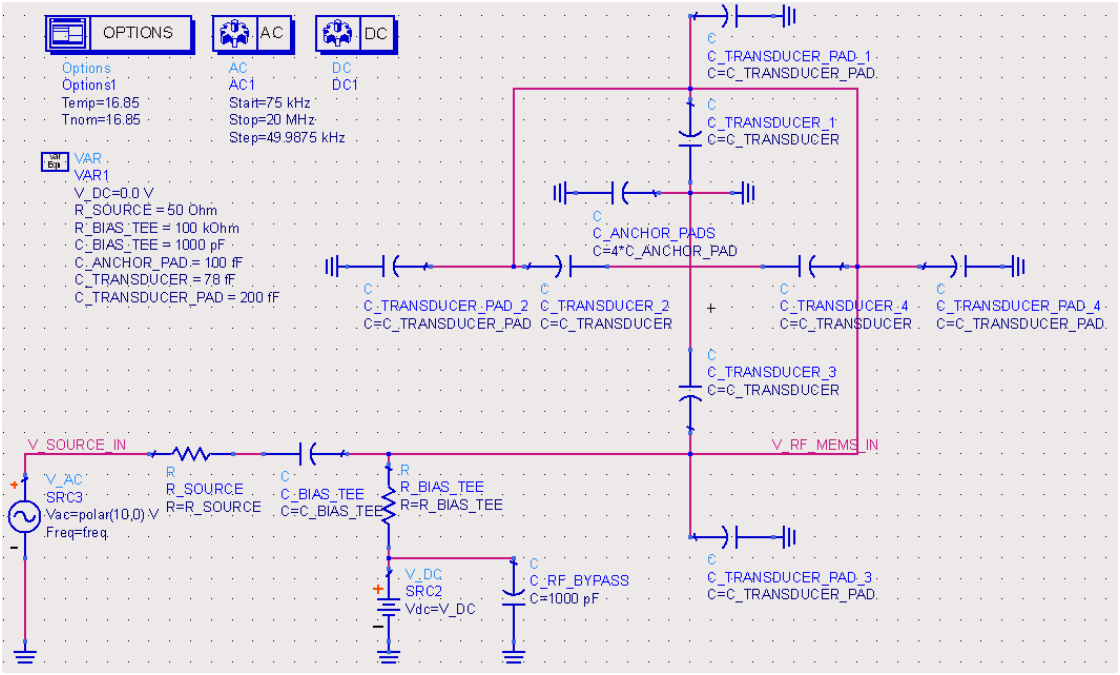

Figure 4.3: Electrical circuit schematic from ADS®2009. The average of the transducer capacitance values from Table 4.2 is $C_{t,avg} = 78fF$ and was utilized for the transducer capacitance shown in the schematic, this represents an open circuit impedance at $f = 0Hz$ (DC) to and $Z_t = \frac{1}{j\omega C_{t,avg}} = \frac{1}{j2\pi \times 20MHz \times 78fF} = -j102k\Omega$ at $f = 20MHz$, where $\omega = 2\pi f$ is the angular frequency. The anchor pad, and transducer pad, capacitance values from Table 4.3 are approximated as 100 fF ($\equiv Z = -j80k\Omega$@20 MHz), and 200 fF ($\equiv Z = -j40k\Omega$@20 MHz), respectively. Gold bond wire with a diameter of 0.001" was utilized, for a resistivity, ρ, of $2.2 \times 10^{-8}\Omega m$ [120] the resistance of a 0.5 mm length of bond wire of circular diameter is $R_{wire} = Z_{wire} = \frac{\rho L}{A} = 5.4m\Omega$, where R_{wire} is as shown in Figure 4.1. The impedance of the gold bond wire is relatively small relative to the source and capacitor impedances; bond wire impedance is approximated as zero in the electrical circuit simulation.

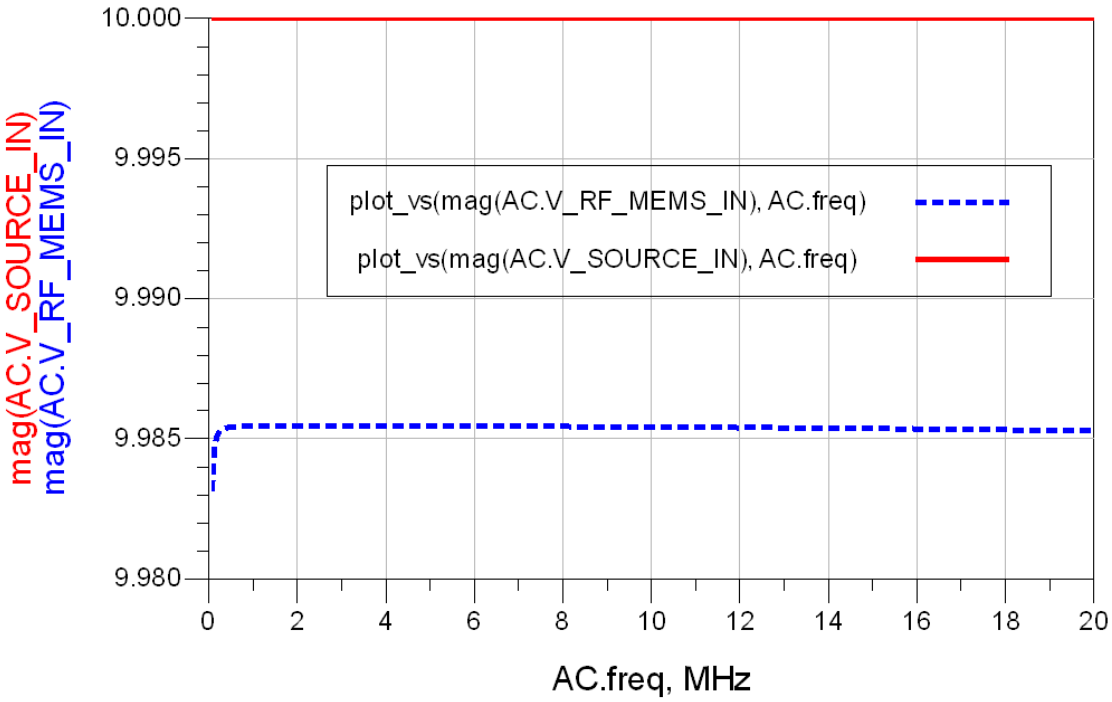

Figure 4.4: AC analysis of the electrical circuit extracted from the phononic band gap quasi-crystal architecture structure from ADS®2009 for the circuit schematic of Figure 4.3. Due to the high AC impedance of the electrostatic transducers, for a 10 VAC signal, the magnitude of the voltage at the electrostatic transducer is approximately 9.985 VAC in the frequency range of interested.

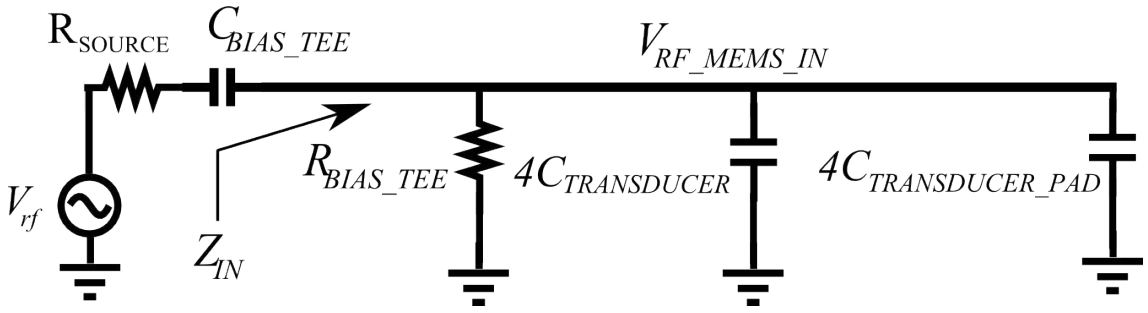

Figure 4.5: The AC equivalent circuit of the electrical circuit depicted in Figure 4.3. The voltage $V_{RF\_MEMS\_IN}$ is the voltage that is applied across the electrostatic transducers.

Figure 4.5 may then be computed as:

$$Z_{IN} = \frac{R_{BIAS}(Z_{TRANSDUCER} + Z_{TRANSDUCER\_PAD})}{R_{BIAS} + (Z_{TRANSDUCER} + Z_{TRANSDUCER\_PAD})} \tag{4.3}$$

by combining in parallel the bias-tee resistor, R_{BIAS}, transducer capacitor impedance, $Z_{TRANSDUCER}$, and transducer pad impedance, $Z_{TRANSDUCER\_PAD}$. For the source voltage amplitude, $V_{RF} = 10V$, and source resistance, $R_{SOURCE} = 50\Omega$, in Figure 4.3, utilizing the input impedance Z_{IN} from Equation 4.3, and the voltage divider principle, the transducer voltage, which is denoted as $V_{RF\_MEMS\_IN}$ in Figures 4.5 and 4.3, may be expressed analytically as:

$$\begin{aligned} Z_{DIVIDER} &= \frac{Z_{IN}}{Z_{IN} + R_{SOURCE} + Z_{BIAS}} \\ V_{RF\_MEMS\_IN} &= V_{RF} Z_{DIVIDER}. \end{aligned} \tag{4.4}$$

Utilizing Equations 4.2, 4.3 and 4.4, for a sample frequency of 10 MHz, or $\omega = 2\pi 10 \times 10^6 rad/s$, $Z_{BIAS} = -j15.9155\Omega$, $Z_{IN} = 33456 - j47184\Omega$, $Z_{DIVIDER} = 0.9993 - j0.0005\Omega$, which illustrates that the dominant impedance is the input impedance, Z_{IN}, formed by the transducer capacitors and transducer pad capacitors, which displays an impedance three to four orders of magnitude larger than the other impedances that form the voltage divider in the AC equivalent circuit of Figure 4.5. The corresponding magnitude of the transducer voltage, $V_{RF\_MEMS\_IN}$, at 10 MHz is 9.993 V, which is in reasonable agreement with the result of 9.985 V obtained from ADS®2009 and displayed in Figure 4.4. Due to the large impedance mismatch between the 50Ω source impedance and Z_{IN}, the voltage that appears on the transducer electrodes is effectively approximately equal to the internal source voltage of the signal source. The result of Equation 4.4 for the entire frequency range from approximately DC to 20 MHz is dis-

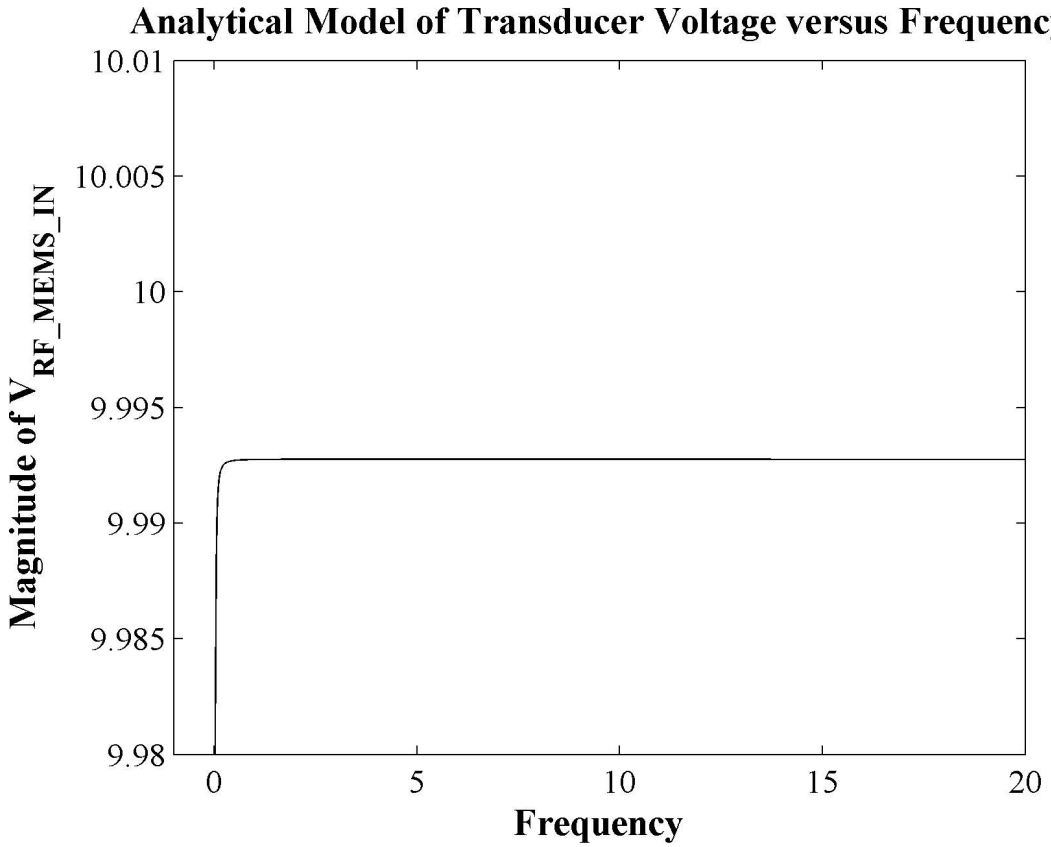

Figure 4.6: Transducer electrode voltage computed from the AC equivalent circuit in Figure 4.5 and Equation 4.4. Due to the high AC impedance of the electrostatic transducers, for a signal source with an amplitude of 10 V, the magnitude of the voltage across the electrostatic transducer capacitor is approximately constant at 9.993 VAC in the frequency range from approximately DC to 20 MHz.

played in Figure 4.6 and displays a trend that is in reasonable agreement with the result from ADS®2009 that is displayed in Figure 4.4.

Table 4.2: Transducer capacitance values for the phononic band gap quasi-crystal design space.

Device	Crystal Side Overlap Area at Low Curvature Gap‡, A_1 (μm^2)	Low Curvature Gap, g_1 (μm)	Transducer Capacitance in Low Curvature Gap $C_{t,1}$ (fF)	Crystal Side Overlap Area at High Curvature Gap‡, A_2 (μm^2)	High Curvature Gap, g_2 (μm)	Transducer Capacitance in High Curvature Gap, $C_{t,2}$ (fF)	Total Transducer Capacitance, C_t (fF)
Square	14375	2	63.638	-	-	-	63.638
S1	6157/6081	2	27.257/26.921	14706/13545+255	3	65.103/61.093	92.360/88.014
S2	6138/5996	2	27.173/26.544	14006/13058+271	3	62.005/59.007	89.178/85.551
S3	6173/5937	2	27.328/26.283	13309/13129+293	3	58.919/59.419	86.247/85.702
S4	14375	2	63.638	-	-	-	63.638
Circle	8144	2	36.053	-	-	-	36.053
C1	3660	2	16.203	7783	3	34.455	50.658
C2	3773	2	16.703	7241	3	32.056	48.759
C3	3922	2	17.362	6682	3	29.581	46.943

‡ The value before, and after, the "/" is for the transducer that has widely, and closely, spaced inclusions, respectively. For the transducer that has closely spaced inclusions, a region of the transducer has a gap that is neither 2 μm or 3 μm, the area of this region may be approximately 250 μm^2 and 300 μm^2; since the size of the gap in this is difficult to define in this region it is summed with the overlap area of the 3 μm gap regions.

Table 4.3: Substrate capacitance values for the anchor and transducer pads, see Figure 4.2 for capacitor locations. The substrate capacitors are modeled as a parallel plate capacitors. The capacitor dielectric is a $1\mu m$ thick oxide dielectric layer in series with a $25\mu m$ thick single-crystal-silicon dielectric layer. The top plate of the substrate capacitor is comprised of a gold layer which lies upon the single-crystal silicon layer and is assumed to have the same area as the substrate overlap area, while the bottom plate of the substrate capacitor is comprised of wafer handle that lies under the oxide layer. The gold, oxide and single-crystal-silicon dielectric layers are assumed to have the same overlap areas, despite the $1.8 - 2.0\mu m$ lateral undercut of the oxide that occurs during HF vapor release [115] and inset of the gold layer. The substrate capacitance may then be modeled as the series combination of the oxide and single-crystal-silicon capacitors as $C_{sub} = \frac{C_{sub,ox}C_{sub,Si}}{C_{sub,ox}+C_{sub,Si}}$ where $C_{sub,ox} = \frac{\epsilon_{r,ox}A_{sub}}{t_{ox}}$ and $C_{sub,Si} = \frac{\epsilon_{r,Si}A_{sub}}{t_{Si}}$. The static relative permittivities at room temperature are approximated as $\epsilon_{r,ox} \approx 3.9F/m$ [119] and $\epsilon_{r,Si} \approx 11.9F/m$ [120].

Device	Insulator Oxide Thickness, t_{ox} (µm)	Silicon Oxide Thickness, t_{Si} (µm)	Anchor Pad Substrate Overlap Area, $A_{sub,1}$ (µm^2)	Anchor Pad Substrate Capacitance, $C_{sub,1}$ (fF)	Transducer Pad Substrate Overlap Area†, $A_{sub,2}$ (µm^2)	Transducer Pad Substrate Capacitance, $C_{sub,2}$ (fF)
Square						
S1						
S2			32127.259	120.672	200×200 + 90×108‡ = 49720	186.752
S3						
S4	1 ± 0.05	25 ± 1				
Circle						
C1						
C2			29903.669	111.348	200×200 + 90×119‡ = 50710	190.470
C3						

Dimensions are drawn width unless otherwise noted. ‡ This dimension is the length of the electrode that connects a square contact pad to the transducer electrode and was measured using the Veeco NT1100 since this dimension is heavily dependent on the process. † The transducer pad is comprised of a 200 µm square contact pad as well as a 90 µm wide interconnect that connects the square contact pad to the transducer electrode.

4.1.2 Analytical Model of Electrostatic Forces within the Capacitive Transducer Gap

Neglecting fringing and utilizing a parallel plate capacitor model (neglecting the effect of the curvature of the transducer electrode plates), the attractive force between the electrodes of the electrostatic transducer in vacuum for an applied voltage V is [97]:

$$F = \frac{\epsilon_o A V^2}{2g^2} \tag{4.5}$$

where $\epsilon_o = 8.854 \times 10^{-12} F/m$ is the permittivity of free space, A is the transducer overlap area, and g is the transducer gap. For a voltage, V, which is the sum of an AC voltage, V_{RF}, applied in series with a DC voltage, V_{DC}, the resultant instantaneous electrostatic force may be expressed as:

$$F = \frac{\epsilon_o A (V_{DC} + V_{RF})^2}{2g^2}. \tag{4.6}$$

Utilizing Equation 4.6 and the crystal-side overlap areas listed in Table 3.3, the approximate electrostatic forces within the transducers were computed and listed in Table 4.4. As may be seen in Table 4.4, the electrostatic attractive force between the plates of each transducer electrode is around $100\mu N$. In addition, despite the asymmetry between the transducers for a square truncation boundary, the electrostatic forces for the different transducers are within $5\mu N$ of one another. Hence, the model suggests that approximately balanced forces are applied to the four edges of each P$^{\text{n}}$BG QC. Moreover, as the inclusion spacing varies by a few microns between structures, the total transducer force varies by less than $10\mu N$, so the transducers of each device may generate approximately the same electrostatic force.

Lastly, though the serrated edges of the P^{n}BG QCs increase the surface area of the transducer electrodes, the generated electrostatic forces are less than those for the flat electrode of the Square and Circular reference devices. The reduced electrostatic force within the transducers along the serrated edges, occurs because in the regions of high curvature (which comprise the majority of the serrated edge) the gap between the serrated edges is $3\mu m$ while the flat electrodes have a gap of $2\mu m$ along their entire length. Hence, the constraint of the SOIMUMPs fabrication rules, which suggest to create a larger gap size between features of high radius of curvature (to avoid bridging), mitigates the potential increase in electrostatic force that could have been produced by the increase in electrode surface area of the serrated transducers. It may be recommended to attempt to violate the suggested SOIMUMPs fabrication rules and decrease the gap size between the features of high radius of curvature to the minimum feature size of $2\mu m$, in an attempt to yield a larger electrostatic force within the electrodes of the serrated edge P^{n}BG QCs.

Table 4.4: Electrostatic forces within the electrostatic transducers of the phononic band gap quasi-crystals and reference devices.

Device	Crystal Side Overlap Area at Low Curvature Gap‡, A_1 (μm^2)	Low Curvature Gap, g_1 (μm)	Transducer Force in Low Curvature Gap[1] $F_{t,1}$ (μN)	Crystal Side Overlap Area at High Curvature Gap‡, A_2 (μm^2)	High Curvature Gap, g_2 (μm)	Transducer Force in High Curvature Gap[1], $F_{t,2}$ (μN)	Total Transducer Force[1], F_t (μN)
Square	14375	2	128.809 **(192.418)**	-	-	-	128.809 **(192.418)**
S1	6157/6081	2	55.171/54.490 **(82.415/81.398)**	14706/13545+255	3	58.567/54.959 **(87.488/82.098)**	113.737/109.448 **(169.904/163.497)**
S2	6138/5996	2	55.000/53.728 **(82.161/80.260)**	14006/13058+271	3	55.779/53.083 **(83.324/79.296)**	110.779/106.811 **(165.485/159.557)**
S3	6173/5937	2	55.314/53.199 **(82.630/79.470)**	13309/13129+293	3	53.003/53.453 **(79.178/79.850)**	108.317/106.652 **(161.807/159.320)**
S4	14375	2	128.809 **(192.418)**	-	-	-	128.809 **(192.418)**
Circle	8144	2	72.975 **(109.013)**	-	-	-	72.975 **(109.013)**
C1	3660	2	32.796 **(48.991)**	7783	3	30.9960 **(46.302)**	63.792 **(95.294)**
C2	3773	2	33.808 **(50.504)**	7241	3	28.837 **(43.078)**	62.646 **(93.582)**
C3	3922	2	35.144 **(52.498)**	6682	3	26.611 **(39.752)**	61.755 **(92.251)**

‡ The value before, and after, the "/" is for the transducer that has widely, and closely, spaced inclusions, respectively. For the transducer that has closely spaced inclusions, a region of the transducer has a gap that is neither 2 μm or 3 μm, the area of this region may be approximately 250 μm^2 and 300 μm^2; since the size of the gap in this is difficult to define in this region it is summed with the overlap area of the 3 μm gap regions. [1] The maximum transducer forces are denoted in bold text within brackets, while the minimum transducer forces are denoted in regular text. The minimum (**maximum**) transducer force is generated when the instantaneous AC voltage is at its minimum (**maximum**) value of -10 V (**10 V**), which combined with the 100 VDC, produces a net instantaneous minimum (**maximum**) voltage of 90 V (**110 V**).

4.2 Phononic Band Gap Quasi-Crystal Mechanical Model

In this section, the Finite Element Method (FEM) in ANSYS® [121] is utilized (as discussed in Section 2.3) to perform modal, dynamic harmonic and sensitivity analysis on the P^{n}BG QCs and reference devices that are listed in Tables 3.1 and 3.2. A FEM mesh convergence study is contained in Appendix B. An analytical dynamic harmonic analysis is also presented. Semi-analytical structural and lumped element vibration models of P^{n}BG QCs are then developed. Lastly, a more complete approach to lumped element vibration modeling of the P^{n}BG QCs is proposed.

4.2.1 Frequency Versus Mode Number Characteristic

Figures 4.7, and 4.8, illustrate the results of the FEM model for the mode frequency versus mode number characteristic of the S1, S2 and S3, and C1, C2 and C3, P^{n}BG QCs that have square, and circular, truncation boundary geometries, respectively. The geometrical parameters of these P^{n}BG QCs are listed in Tables 3.1 and 3.2. The mode frequency versus mode number characteristics display seven notable regions:

(I) near DC the mode frequency versus mode number characteristic of the P^{n}BG QCs approximately overlap with one another as well as with those of the homogeneous Square and Circular reference structures,

(II) next occurs a range of frequencies where the mode number versus mode frequency characteristic of the P^{n}BG QCs deviate from those for the homogeneous Square and Circular reference structures but where the mode number versus mode frequency characteristics of the P^{n}BG QCs still overlap,

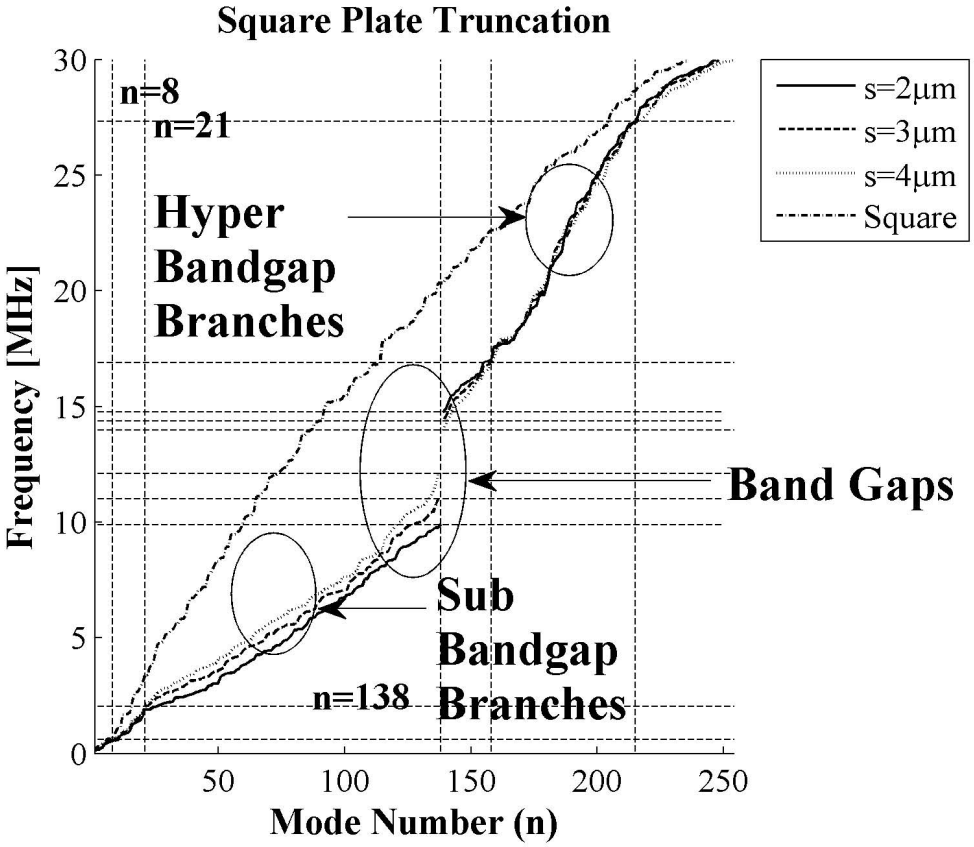

Figure 4.7: Finite element method model of mode frequency versus mode number for phononic band gap quasi-crystals S1, S2 and S3, as well as the homogeneous square plate. The upper mode numbers and frequencies of the behavioral zone boundaries are, I: ($n = 0$, $f = 0MHz$), II: ($n = 8$, $f = 0.616MHz$), III: ($n = 21$, $f = 2.036MHz$), IV: ($n = 138$), V: ($n = 158$, $f = 16.88MHz$), and VI: ($n = 215$, $27.32MHz$). Band gap frequencies are summarized in Table 4.5.

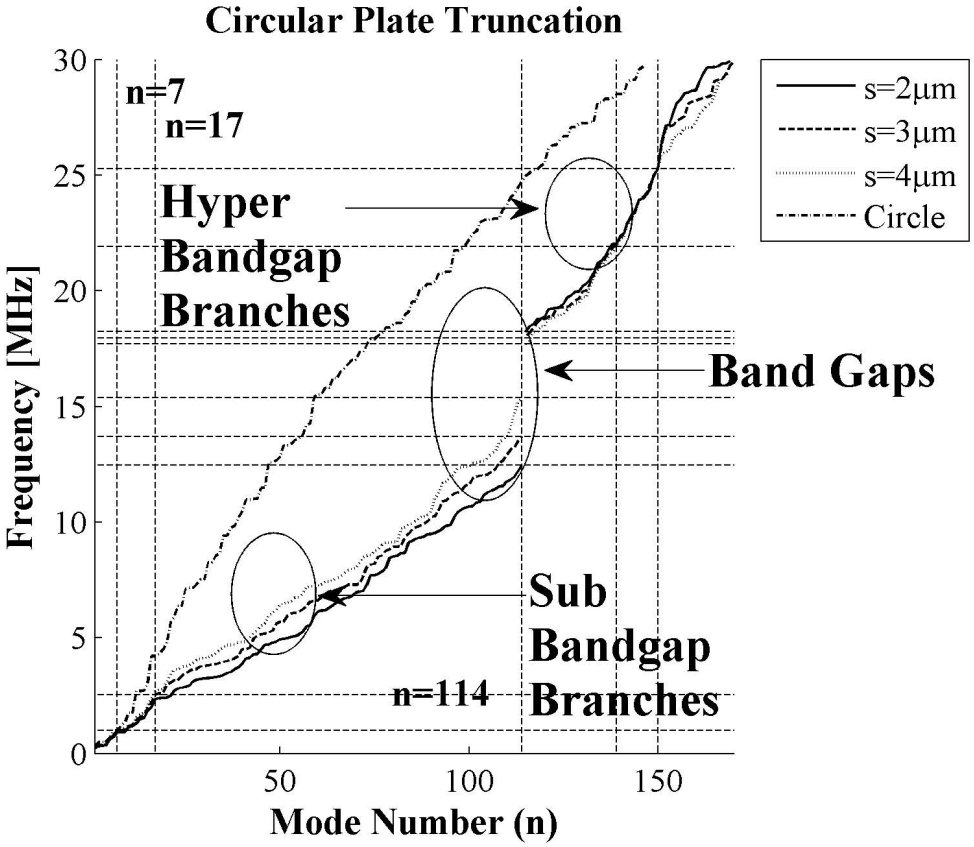

Figure 4.8: Finite element method model of mode frequency versus mode number for phononic band gap quasi-crystals C1, C2 and C3, as well as the homogeneous circular plate. The upper mode numbers of the behavioral zone boundaries and their frequencies are, I: ($n = 0$, $f = 0MHz$), II: ($n = 7$, $f = 0.9835MHz$), III: ($n = 17$, $f = 2.5350MHz$), IV: ($n = 114$), V: ($n = 139$, $f = 21.92MHz$) and VI: ($n = 150$, $f = 25.28MHz$). Band gap frequencies are summarized in Table 4.5.

(III) a range of frequencies where the mode number versus mode frequency characteristic of each P^{n}BG QC is approximately linear and unique (different from that of the other P^{n}BG QCs),

(IV) a range of frequencies where no modes occur, this range begins at mode 138 for the P^{n}BG QCs with square truncation and mode 114 for the P^{n}BG QCs with circular truncation, and is referred to as the band gap,

(V) a range of frequencies starting at the top of the band gap, beginning at mode 139 for square truncation and mode 115 for circular truncation, where the frequency versus mode number characteristic is approximately linear (with a positive slope) and unique for each P^{n}BG QC,

(VI) a frequency range, above the aforementioned frequency range, where the frequency versus mode number characteristics increase in slope and approximately converge towards one another, and lastly

(VII) a range where the frequency versus mode number characteristics of the P^{n}BG QCs decrease in slope and begin to converge with that of the homogeneous Square and Circular reference structures.

Lastly, it may be observed that in the frequency versus mode number characteristics of Figures 4.7 and 4.8, where the sub- and hyper-band gap branches extend into the band gap, the tangent to these characteristics appears to have a positive slope. The notable properties of the seven behavioral zones (I, II, III, IV, V, VI and VII), that have been listed above, are illustrated in Figure 4.9. As seen in Figure 4.9, the mode frequency versus mode number characteristics may be approximated as piecewise linear utilizing linear segments each of which may have different slopes.

The set of modes that lie below (and above) the band gap will be referred to as sub-band gap (and hyper-band gap) modes. The terms of sub-band gap, and hyper-band

gap, branches have been coined here to refer to frequency regimes of the P^{n}BG QCs that may be analogous to the acoustical, and optical, branches, respectively, of infinitely periodic P^{n}BG crystals.

From Figures 4.7 and 4.8, the total width of behavioral zones I, and II, is approximately 21, and 17, and so differ by four modes for square, and circular, truncation boundary geometries, respectively. Figure 4.7, and Figure 4.8, also indicate that the total number of sub-band gap modes, N_{SBGM}, is 138, and 114, for square, and circular, truncation boundary geometries, respectively. An analysis of the density of states of the P^{n}BG QCs may be found in Appendix C.

Figure 4.10 combines the P^{n}BG QC mode frequency versus mode number characteristics of Figure 4.7 for square truncation and Figure 4.8 for circular truncation geometry. As may be seen in Figure 4.10, in comparison with circular truncation, the mode frequency versus mode number characteristic for square truncation displays lower normal mode and band gap frequencies, which may in part be due to the shorter lattice constant of the circular truncated structures.

The effective material parameters, for example effective acoustic velocity, c_{eff}, effective mass, m_{eff}, effective stiffness, k_{eff}, may vary between P^{n}BG QCs due to the differing geometrical parameters of lattice constant, inclusion spacing, inclusion radius or truncation boundary geometry. Often resonant frequency displays a proportional relationship with mass and inverse proportional relationship with stiffness, and so the lower mode frequencies of the square, in comparison to circular, truncated P^{n}BG QCs may indicate that the square truncated P^{n}BG QCs may have a lower associated global effective stiffness or higher global effective mass. A lower stiffness and larger mass may be expected for square truncation, as compared to circular truncation, due to the larger inclusion radius which produces more slender regions (of potentially lower stiffness) in

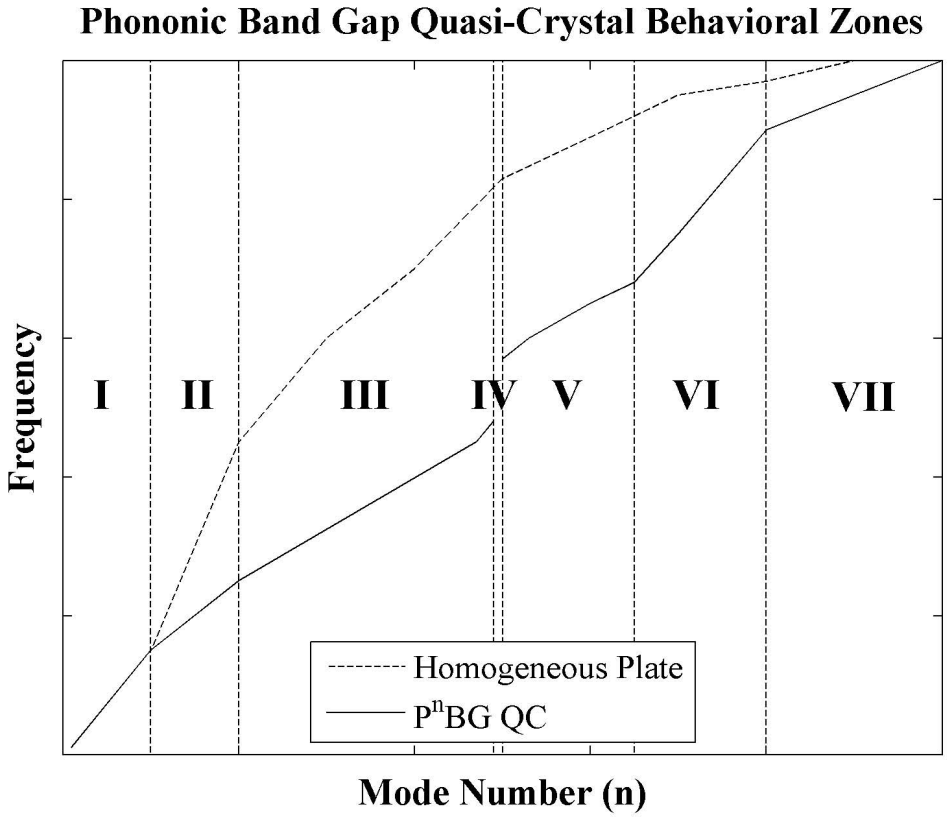

Figure 4.9: Illustration of the behavioral zones (not to scale) of the proposed phononic band gap quasi-crystal architecture compared with a homogeneous plate: (I) low frequency band gap homogeneous plate zone, (II) non-unique sub-band gap zone, (III) unique sub-band gap zone, (IV) band gap zone, (V) unique hyper-band gap zone, (VI) non-unique hyper-band gap zone and (VII) high frequency homogeneous plate zone.

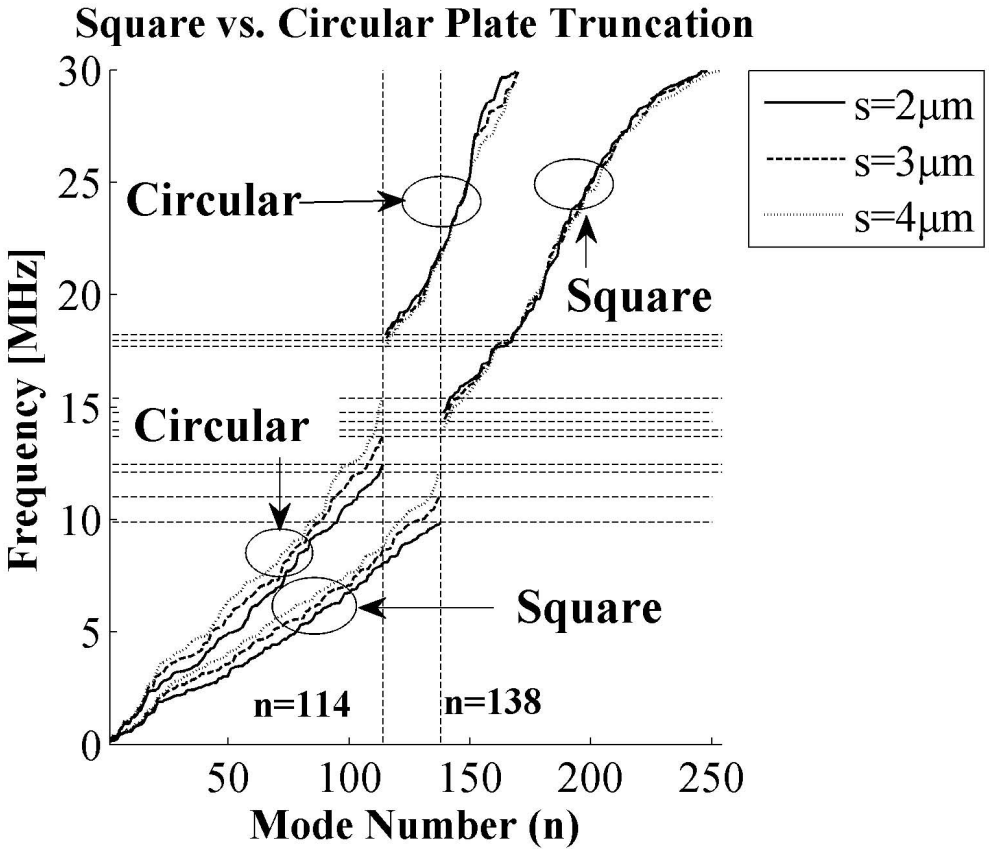

Figure 4.10: Finite Element Method model of the mode frequency versus mode number characteristic for all (S1, S2, S3, C1, C2, C3) phononic band gap quasi-crystals.

the areas of minimum inclusion spacing and more massive regions in the areas of maximum inclusion spacing (refer to Tables 3.1 and 3.2 for the geometrical parameters of the square and circular truncated P^{n}BG QCs).

In addition to the potentially differing effective material parameters between square and circular P^{n}BG QCs, the more distant truncation boundary geometry and anchor locations of square, versus circular, P^{n}BG QCs may also account for the lower mode frequencies observed in Figure 4.10 for square, in comparison to circular, P^{n}BG QCs. In analogy with quantum wells [122] or fixed-fixed strings [122], if a relation that resembles $c_{eff} = f\lambda$ (where c_{eff} is effective velocity) governs the system, for a given set of effective material parameters (c_{eff}) in the medium between the P^{n}BG QC edges or anchors and for a given mode shape, then an increased distance between P^{n}BG QC edges or anchors may correspond to an increased mode wavelength, λ, and thus lower frequency, f. If this were the case, since the distance between the truncation boundaries and anchors is larger for the square, in comparison with circular, truncated P^{n}BG QCs presented in Tables 3.1 and 3.2, then, according to the analogy with quantum wells and fixed-fixed strings, for comparable effective material parameters, square truncation may be expected to yield a lower set of mode frequencies. The sensitivity analysis of Section 4.2.6 will illustrate such a decrease in mode frequency versus truncation diameter.

If the P^{n}BG QC truncation boundaries and anchors were allowed to approach infinity it may be expected that normal mode frequencies and band gap location should depend primarily on the P^{n}BG QC inclusion spacing and radius (as oppose to boundary or anchor location). In contrast, for finite truncation boundaries and anchor locations, P^{n}BG QC normal mode frequency may be expected to depend on both the anchor location, truncation boundary geometry as well as P^{n}BG QC lattice constant and inclusion spacing and radius.

The FEM models of the band gap locations observed in Figure 4.10 are summarized in Table 4.5. The homogeneous reference structures and S4 reference structure, which has flat edges, did not display a band gap for any of the investigated geometries. Hence, the FEM models appear to indicate that for the structures listed in Tables 3.1 and 3.2, the implementation of the design methodologies of Chapter 3 and the use of serrated edges in association with the P^{n}BG QC geometry may be mandatory to produce a structure that displays the band gap behavior of a P^{n}BG crystal. This supports the significance of the P^{n}BG QC architecture.

As seen in Table 4.5, complete band gaps are observed to be centered at approximately 12 MHz to 13 MHz for square truncation and approximately 15 MHz to 16 MHz for circular truncation. In addition, as the lattice constant is increased, the lower band gap edge and band gap center frequency increase, while the upper band gap edge frequency decreases and band gap width decreases. Thus, as the lattice constant is increased, the lower band gap edge increases at a rate higher than the rate the upper band gap edge decreases. Hence, the sub-band gap modes, in comparison to the hyper-band gap modes, appear to be more sensitive to the variation of the lattice constant, a.

4.2.2 Comparison with the Analytical Bragg Frequencies

For an infinitely periodic honeycomb P^{n}BG crystal, utilizing the primitive cell of Figure 3.2 with inclusion spacings $s = [2, 3, 4]\mu m$, a circular inclusion radius of $r = 45\mu m$, corresponding lattice constants $a = [159.349, 161.081, 162.813]\mu m$ and fill factors $ff = \frac{\pi r^2}{a^2} = [0.579, 0.566, 0.554]$, in a silicon host and air inclusion system (see Appendix A for the elastic wave velocities of silicon and air), the Bragg frequency may be approximated analytically utilizing Equations 2.5 and 2.6 for the transverse elastic wave component

as:

$$f_{\Gamma M} = \frac{c_{avg,hex,circle,transverse}}{\sqrt{3}a} = [9.250, 9.435, 9.606]MHz \tag{4.7}$$

where:

$$\begin{aligned} c_{avg,hex,circle,transverse} &= ff \times c_{i,transverse} + (1 - ff)\, c_{h,transverse} \\ &= ff \times 0m/s + (1 - ff)\, 5360m/s \\ &= [2275.498, 2349.376, 2420.630]m/s \end{aligned} \tag{4.8}$$

and for the longitudinal elastic wave component as:

$$f_{\Gamma M} = \frac{c_{avg,hex,circle,longitudinal}}{\sqrt{3}a} = [16.147, 16.432, 16.690]MHz \tag{4.9}$$

where:

$$\begin{aligned} c_{avg,hex,circle,longidudinal} &= ff \times c_{i,longitudinal} + (1 - ff)\, c_{h,longitudinal} \\ &= ff \times 300m/s + (1 - ff)\, 8950m/s \\ &= [3972.212, 4091.437, 4206.428]m/s. \end{aligned} \tag{4.10}$$

Hence, this analytical model suggests that the honeycomb silicon-air P^{n}BG crystal, for the primitive cell of Figure 3.2, would have a band gap within the range of approximately 9 MHz to 16 MHz. These band gap frequencies are in reasonable agreement with the ranges of band gap locations predicted by the FEM models in Figure 4.10 and Table 4.5 of the P^{n}BG QCs. The similarities between the band gap frequencies of this analytical model of infinitely periodic honeycomb P^{n}BG crystals and the FEM model of the P^{n}BG QCs may support the notion that the proposed P^{n}BG QC architecture may adhere to,

or approximate, some infinitely periodic P^{n}BG crystal behavior.

As seen in Equations 4.7 and 4.9, the Bragg frequencies for both transverse, and longitudinal, waves suggest that the phononic band gap location increases by 0.25 MHz and 0.384 MHz, respectively, as the inclusion spacing, s, is scaled up from $2\mu m$ to $4\mu m$ for the infinitely periodic P^{n}BG crystal, while Bragg frequencies may be expected to decrease as the lattice constant is increased; however, because the fill factor is not held constant, and is in fact decreasing as the lattice constant is being increased, the average velocity, c_{avg}, increases towards that of the silicon host material. Thus, for this case, the model suggests that the Bragg frequencies may increase as the lattice constant is increased. The FEM models of Figure 4.10 and Table 4.5 for the P^{n}BG QCs also suggest that the band gap location increases as the lattice constant increases. However, the FEM models of P^{n}BG QCs predict an increase in the frequency of the band gap of 2.196 MHz for the square truncated device and 2.930 MHz for the circular truncated device. Hence, the FEM models of the P^{n}BG QC predict more dramatic increases in the band gap location as the inclusion spacing, s, is increased from $2\mu m$ to $4\mu m$. If the P^{n}BG QC is adhering to P^{n}BG crystal theory, the difference between the location and sensitivity of the analytical Bragg frequencies of P^{n}BG crystal theory and the band gap frequencies of the FEM models of the P^{n}BG QCs may in part be accounted for by the geometrical differences between an infinitely periodic honeycomb P^{n}BG crystal and the proposed P^{n}BG QC architecture, including the use of tethers to support the P^{n}BG QC which is created in a plate of finite thickness and truncated to finite periodicity by fixed and stress-free boundaries, and utilization of the primitive cell of Figure 3.2 to produce a honeycomb crystal from the hexagonal lattice (the analytical model of Equations 2.5 and 2.6 only generally account for the primitive cell geometry via the effective velocity).

To assess the potential sources of the differences between the aforementioned ana-

lytical Bragg frequencies of infinitely periodic hexagonal lattice P^{n}BG crystals and the FEM model of the band gap location of the proposed P^{n}BG QC architecture, a test was performed by removing the fixed boundary conditions from the FEM model of the S2 P^{n}BG QC, then performing a modal analysis. The maximum frequency of the sub-band gap branch was observed to decrease by approximately 1% while the minimum frequency of the hyper-band gap branch was observed to decrease by approximately 0.007%, indicating that the band gap location is not strongly controlled by the fixed boundary condition that is applied via the tether elements.

Alternatively, if the P^{n}BG QC should reflect the behavior of the infinitely periodic honeycomb P^{n}BG crystal from which the P^{n}BG QC is derived, the discrepancy between the band gap location of the P^{n}BG QC architecture and the analytical Bragg frequencies of infinitely periodic honeycomb P^{n}BG crystals may be assessed versus the stress-free boundaries that truncate (to finite thickness and periodicity) the P^{n}BG QC. To develop an understanding of the sensitivity to the in-plane stress-free boundaries, studies may be performed to gradually move the stress-free boundaries out to infinity (this is performed for the in-plane stress-free truncation boundary in the sensitivity analysis of Section 4.2.6 and is not observed to strongly control the band gap location), or to apply periodic boundary conditions in place of the in-plane stress-free truncation boundaries, or to apply artificial boundary conditions in place of the in-plane stress-free truncation boundaries to observe how, for example, small but non-zero stress, and so forth, may control P^{n}BG QC band gap location.

To develop an understanding of the sensitivity of P^{n}BG QC band gap to the out-of-plane stress-free boundaries, plate thickness may be varied as in Section 4.2.6 where it may be observed that for one truncation diameter both hyper- and sub-band gap frequencies vary with plate thickness with hyper-band gap frequencies displaying the

greater sensitivity. The finite plate thickness may then be a source of the discrepancy between P^{n}BG QC band gap location and the Bragg frequencies of the infinitely periodic honeycomb P^{n}BG crystal. Band gap sensitivity to plate thickness may be further investigated for additional truncation boundary diameters.

Lastly, if the P^{n}BG QC should reflect the behavior of the infinitely periodic honeycomb P^{n}BG crystal from which the P^{n}BG QC is derived, the discrepancy between the band gap location of the P^{n}BG QC architecture and the analytical Bragg frequencies of infinitely periodic honeycomb P^{n}BG crystals may be assessed versus primitive cell geometry. While the FEM model of the P^{n}BG QC takes into account the specific geometry of the primitive cell of Figure 3.2, the analytical Bragg equations do not, and so the band gap sensitivity may be modeled versus primitive cell geometry utilizing the FEM model. A complete study of the discrepancies between the behavior of the P^{n}BG QCs and corresponding infinitely periodic honeycomb P^{n}BG crystal is left for future study.

4.2.3 Physical Shape of the Normal Modes

Two representative mode shapes are displayed for the S2 P^{n}BG QC in Figure 4.11 and Figure 4.12 and the C2 P^{n}BG QC in Figure 4.13 and Figure 4.14. Independent of the inclusion spacing, inclusion radius and truncation geometry, the mode shapes of the modeled P^{n}BG QC architecture display similar characteristic shapes at sub-band gap (Figure 4.11 and Figure 4.13) and hyper-band gap (Figure 4.12 and Figure 4.14) frequencies. In addition, independent of geometry, for the P^{n}BG QCs studied here, within the frequency range examined here, sub-band gap modes are always comprised of a mixture of in-plane and out-of-plane modes, while hyper-band gap modes are purely out-of-plane (with the exception of a few local tether resonant modes). These characteristic mode shapes will be discussed in detail next in Section 4.2.4.

The normal mode shape of a localized tether resonant mode of the S2 P^{n}BG QC is displayed in Figure 4.15(a). In the tether resonant mode of Figure 4.15(a), nodes appear at each end of the tether. Approximating these two nodes with fixed boundaries, the tether resonant mode of Figure 4.15(a) may be modeled as shown in Figure 4.15(b) with a percentage error of -14.5347%.

Lastly, the effect of the flat edges of the S4 P^{n}BG QC may be observed in Figure 4.16. The edge resonances observed in Figure 4.16 occur at in-gap frequencies and so produce defect states within the band gap. Several variations on the geometry of the flat edges were attempted unsuccessfully in order to eliminate the edge resonance defect states while utilizing flat edges; the development of a flat edge that yields no defect state is left for future study. The apparent difficulty of realizing a complete band gap while utilizing flat edges highlights the significance of the implementation of the serrated edges that are employed in the P^{n}BG QC architecture.

Table 4.5: Band gap locations of the phononic band gap quasi-crystals and reference structures.

Device		Lower band gap edge f_{low} [MHz]	Band gap center frequency f_{center} [MHz]	Upper band gap edge f_{high} [MHz]	Band gap width f_{width} [MHz]	Normalized band gap width f_{center}/f_{width}
Square		none	none	none	none	none
S1	Increasing	9.894	12.327	14.76	4.866	2.533
S2	lattice	10.982	12.664	14.346	3.364	3.765
S3	constant	12.09	13.035	13.98	1.890	6.897
S4		none	none	none	none	none
Circle		none	none	none	none	none
C1	Increasing	12.45	15.34	18.23	5.780	2.654
C2	lattice	13.69	15.830	17.97	4.280	3.699
C3	constant	15.38	16.54	17.70	2.320	7.129

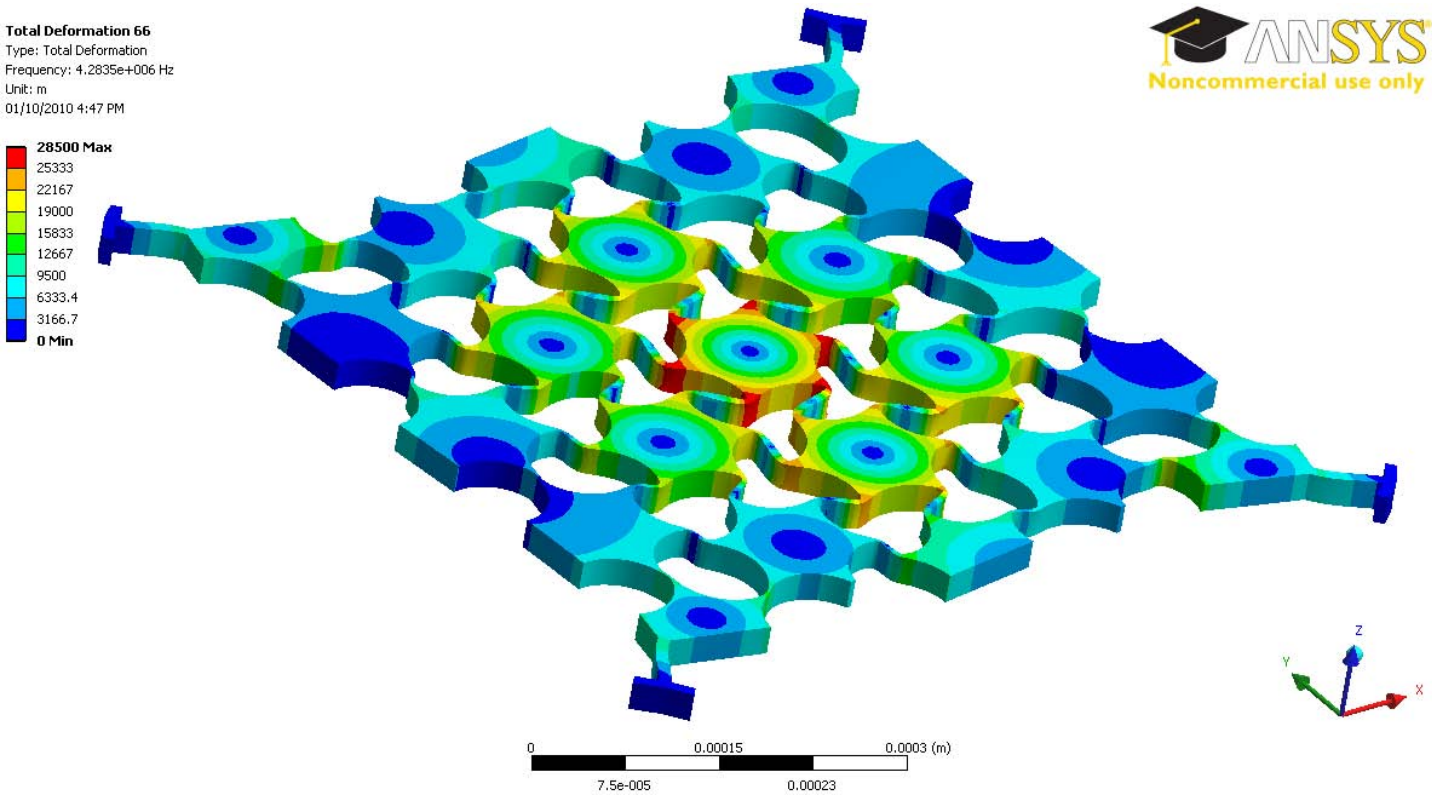

Figure 4.11: Finite element method model (15,372 elements) of mode shape for sub-band gap mode $N = 66$ for a square truncated phononic band gap quasi-crystal with spacing and radius, s and r, of $2\mu m$ and $45\mu m$, respectively. The vibrational motion of this mode is primarily in the in-plane direction.

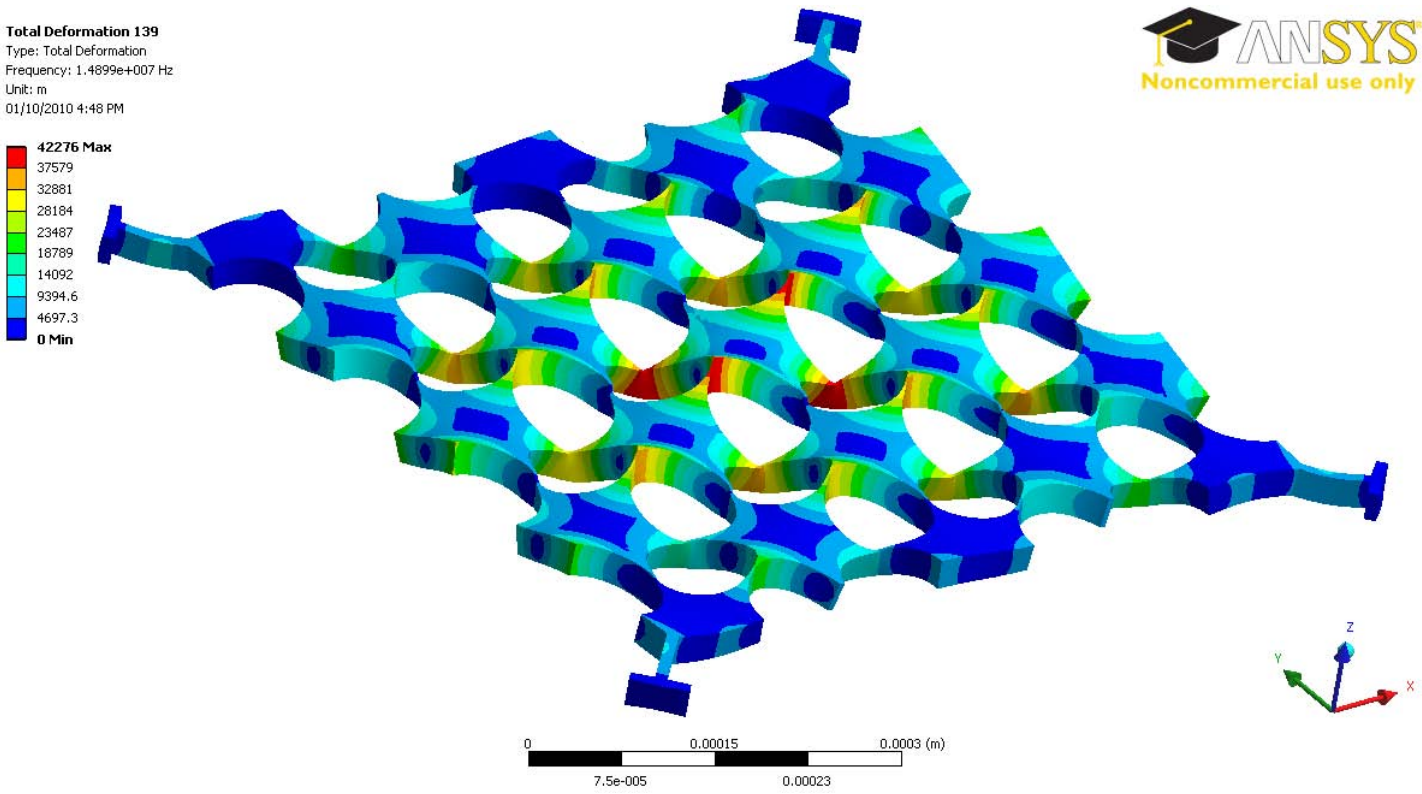

Figure 4.12: Finite element method model (15,372 elements) of mode shape for hyper-band gap mode $N = 139$ for a square truncated phononic band gap crystal with inclusion spacing and radius, s and r, of $2\mu m$ and $45\mu m$, respectively. The vibrational motion of this mode is primarily in the out-of-plane direction.

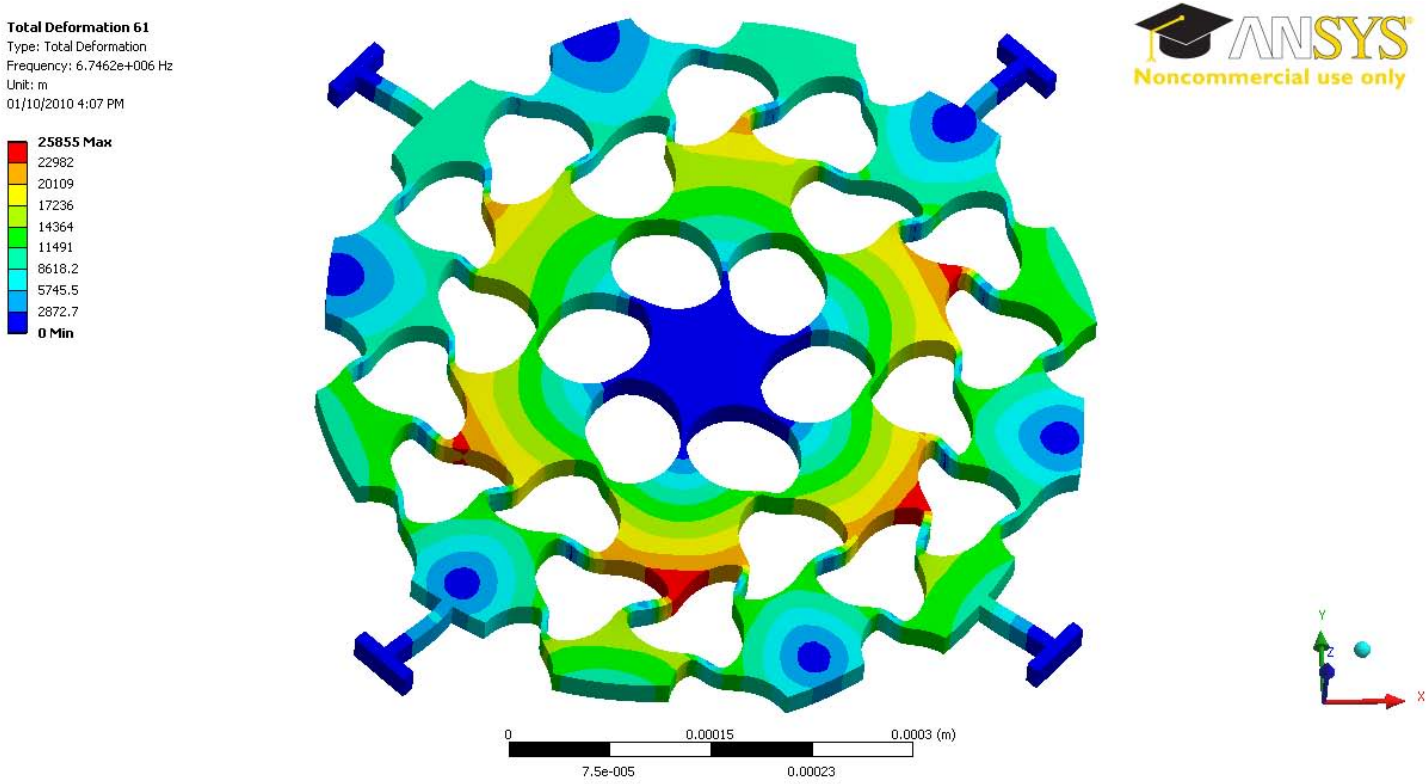

Figure 4.13: Finite element method model (15,372 elements) of mode shape for sub-band gap mode $N = 61$ for a square truncated phononic band gap quasi-crystal with spacing and radius, s and r, of $3\mu m$ and $40\mu m$, respectively. The vibrational motion of this mode is primarily in the in-plane direction.

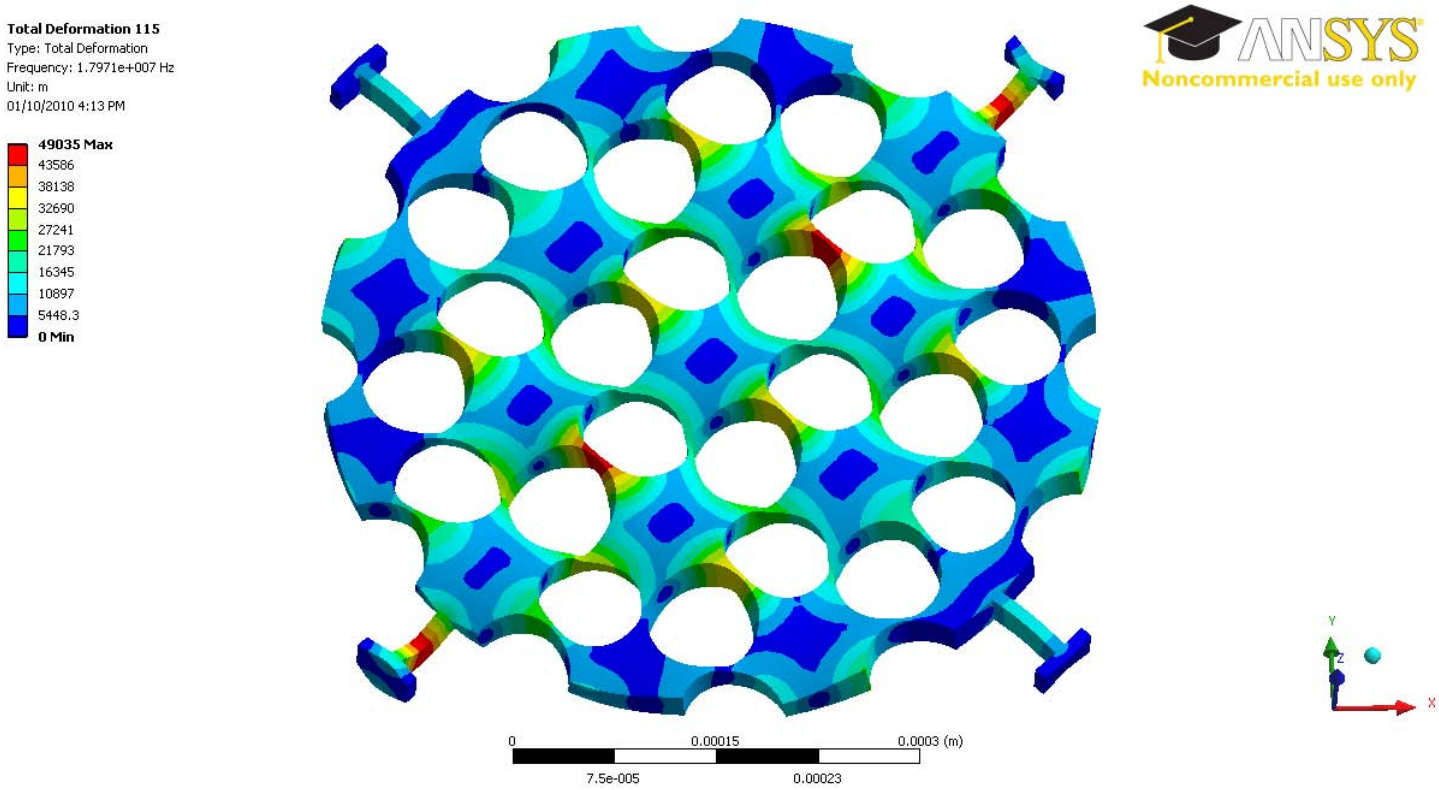

Figure 4.14: Finite element method model (15,372 elements) of mode shape for hyper-band gap mode $N = 115$ for a square truncated phononic band gap quasi-crystal with inclusion spacing and radius, s and r, of $3\mu m$ and $40\mu m$, respectively. The vibrational motion of this mode is primarily in the out-of-plane direction.

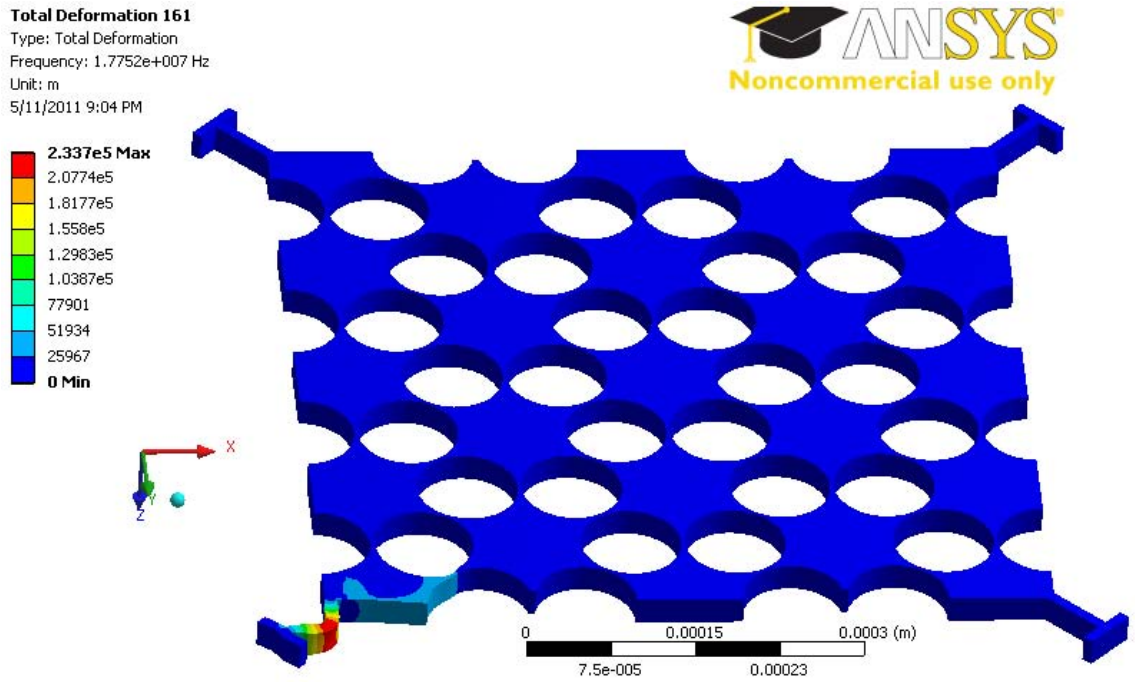

(a)

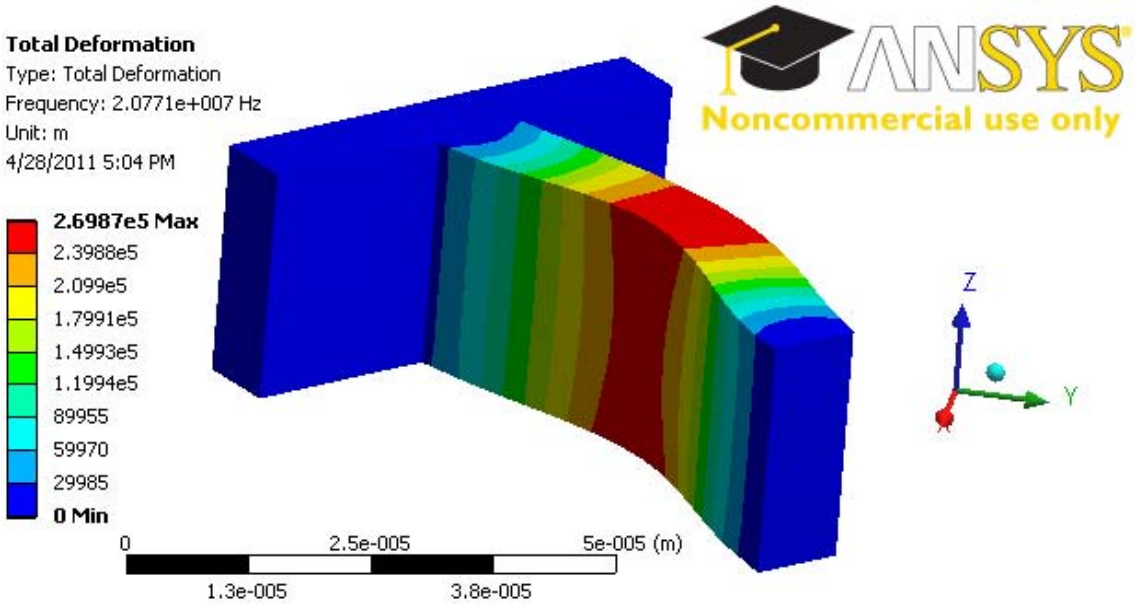

(b)

Figure 4.15: (a) The hyper-band gap mode 161 at $17.752MHz$ with the resonance of the tether element. (b) Approximate finite element method model of the resonance of the tethers utilizing fixed boundary conditions at the ends of the tethers indicates tether resonance at $20.771MHz$, which lies in the hyper-band gap frequency range as intended.

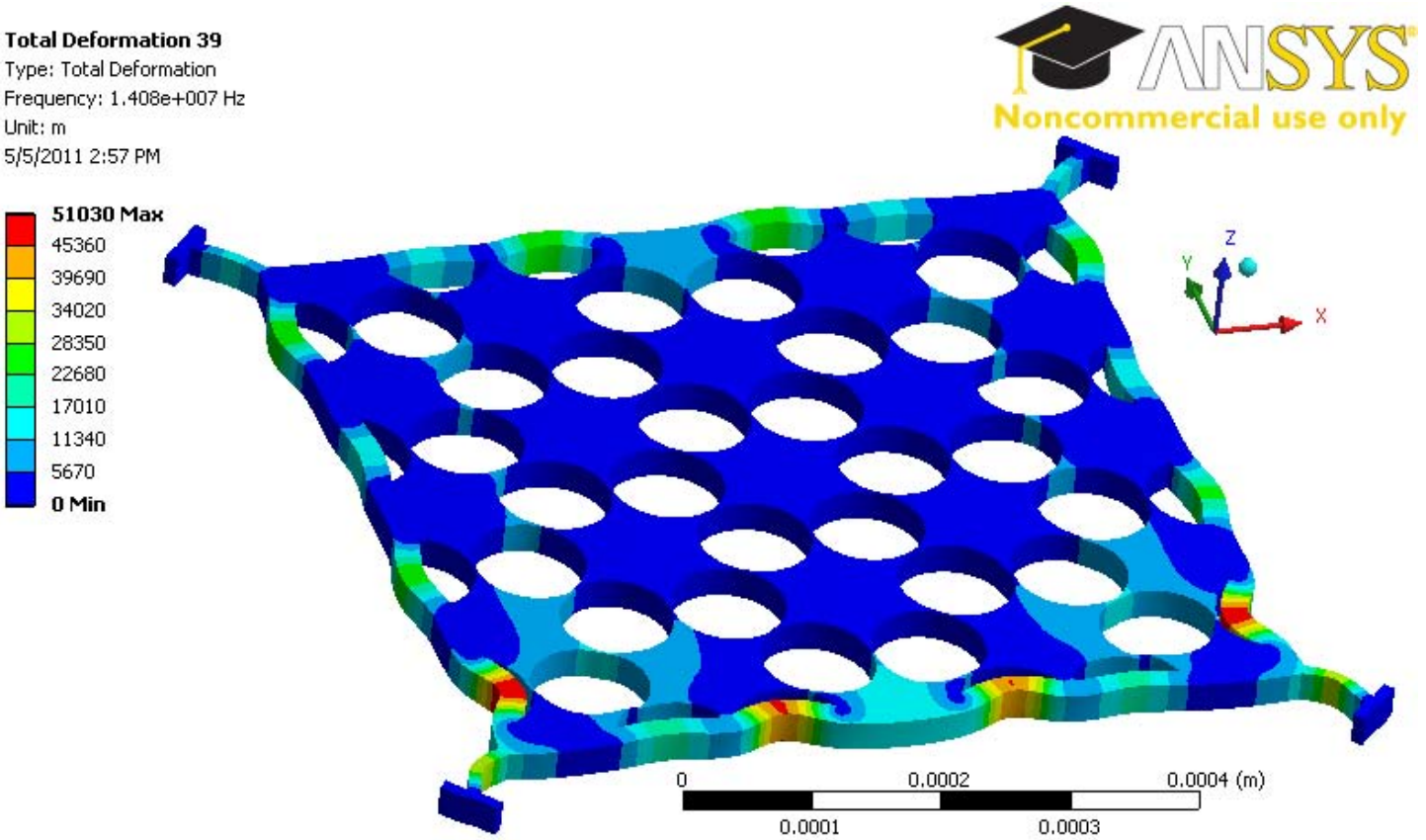

Figure 4.16: Resonance of the edges of the S4 phononic band gap quasi-crystal that has flat edges (instead of serrated edges). The edge resonances occur at in-gap frequencies and so produce defect states within the band gap.

4.2.4 Semi-Analytical Lumped Element Structural and Vibration Model

Figure 4.17 illustrates the patterns of vibration that occur versus mode number in the S2 P^{n}BG QC; similar vibration patterns are observed in the S1, S3, C1, C2 and C3 P^{n}BG QCs. As may be observed in Figure 4.17, at sub-band gap frequencies the P^{n}BG QC displays both in-plane and out-of-plane modes, while at hyper-band gap frequencies the P^{n}BG QC displays primarily out-of-plane modes (with the exception of in-plane tether resonances such as that illustrated in Figure 4.15).

Figures 4.7 and 4.8 indicate that the total width of behavioral zones I and II for square and circular truncated devices are 2.036 MHz and 2.535 MHz, respectively, which are the location of the inflection points at the upper boundary of behavioral zone II. At such inflection points, the effective wavelength may be computed for elastic waves within a homogeneous medium comprised of an average elastic wave velocity equal to that of the P^{n}BG QC primitive cell. These effective wavelengths may then be compared to the feature sizes of the P^{n}BG QC to deduce if there may be a physically insightful relation between effective wavelength within the various behavioral zones and the size of the structure. For the square truncated S1, S2, S3 P^{n}BG QCs (utilizing the material properties for silicon and air from Appendix A and Equation 2.6 for c_{avg}) the effective wavelengths for transverse and longitudinal waves at the upper edge of behavioral zone II ($f = 2.036MHz$) and the ratio of this effective wavelength to the truncation diameter,

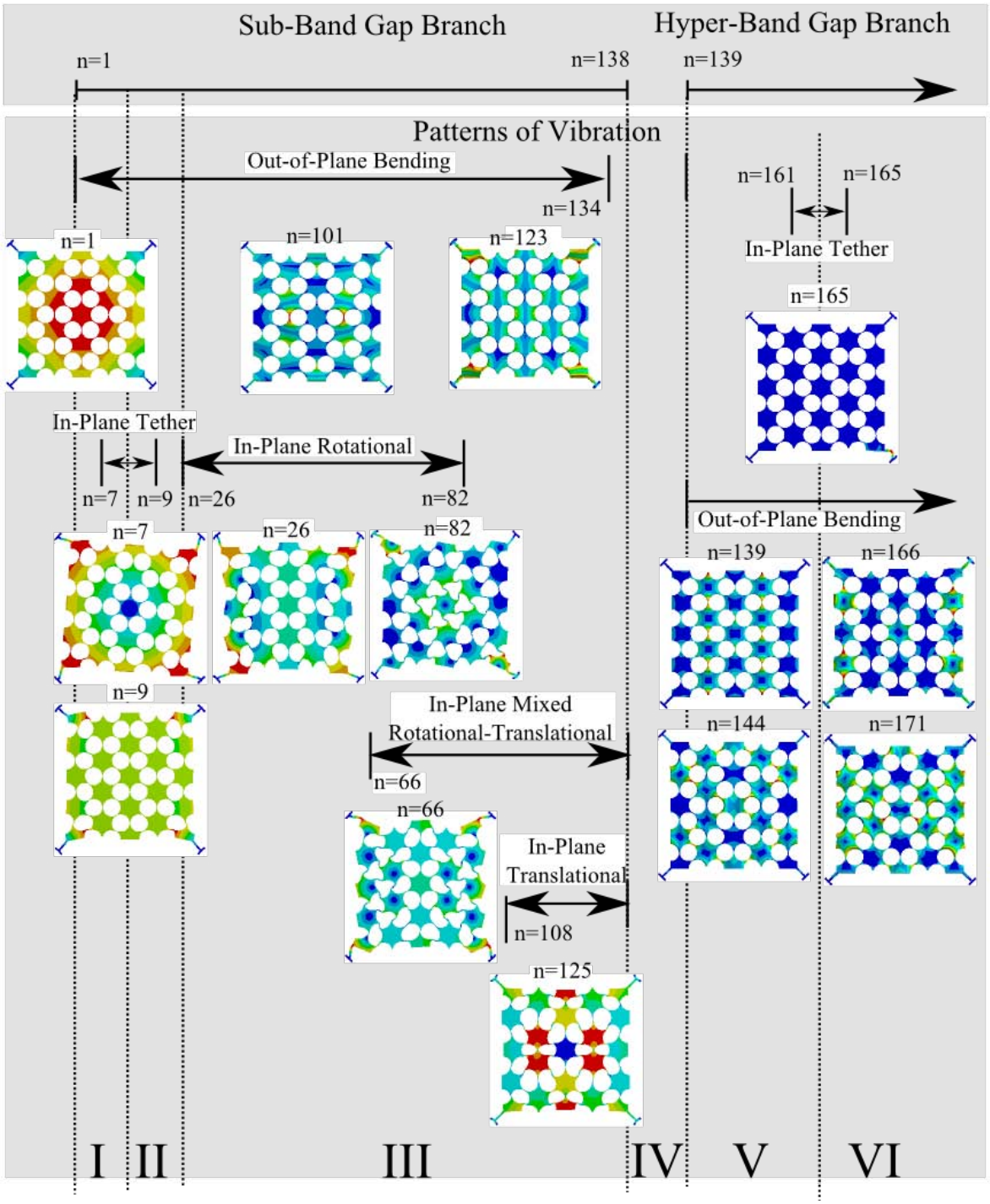

Figure 4.17: Vibration patterns of the S2 phononic band gap quasi-crystal versus mode number. The mode numbers, n, of the boundaries of each behavioral zones are noted.

$d = 650\mu m$, is typically:

$$
\begin{aligned}
&Transverse \\
c_{avg,transverse,typical} &= 2324.346 \quad m/s \\
\lambda &= c_{avg,transverse,typical}/f = 1141.6235 \quad \mu m \\
\lambda/d &= 1.756
\end{aligned}
\tag{4.11}
$$

$$
\begin{aligned}
&Longitudinal \\
c_{avg,longitudinal,typical} &= 4051.043 \quad m/s \\
\lambda &= c_{avg,longitudinal,typical}/f = 1989.707 \quad \mu m \\
\lambda/d &= 3.061
\end{aligned}
\tag{4.12}
$$

and for the circular truncated C1, C2, C3 P^{n}BG QCs with $d = 575\mu m$ is typically (the upper edge of behavioral zone II occurs at $f = 2.535MHz$):

$$
\begin{aligned}
&Transverse \\
c_{avg,transverse,typical} &= 2348.501 \quad m/s \\
\lambda &= c_{avg,transverse,typical}/f = 926.431 \quad \mu m \\
\lambda/d &= 1.6112
\end{aligned}
\tag{4.13}
$$

$$
\begin{aligned}
&Longitudinal \\
c_{avg,longitudinal,typical} &= 4090.026 \quad m/s \\
\lambda &= c_{avg,longitudinal,typical}/f = 1613.422 \quad \mu m \\
\lambda/d &= 2.806.
\end{aligned}
\tag{4.14}
$$

The upper boundary of behavioral zone II then occurs when wavelength is approxi-

mately 1.5× (for the average transverse elastic wave velocity) to 3× (for the average longitudinal elastic wave velocity) the P^{n}BG QC truncation diameter. If the edge of the behavioral zone II boundary is dependent on the ratio of effective wavelength to truncation diameter, then the frequency of the behavioral zone II boundary may be reduced to low frequencies by increasing the P^{n}BG QC truncation diameter; such a trend appears to be observed in the sensitivity analysis of Section 4.2.6 and Figure 4.36, however, may be present due to other mechanisms and may be investigated further.

As frequency increases to 20 MHz above behavioral zone II, for both square and circular truncated P^{n}BG QCs, the effective wavelength for typical average transverse, $c_{avg,transverse,typical}$, and longitudinal, $c_{avg,longitudinal,typical}$, elastic wave velocities reduces to approximately $115\mu m$ and $200\mu m$, respectively. For these transverse, and longitudinal, effective wavelengths, the ratio of plate truncation diameter, d, to wavelength is approximately 5, and 3, respectively. Hence, at the maximum operating frequency the minimum effective wavelength is approximately 3 to 5 times smaller than the P^{n}BG QC truncation diameters; at higher frequencies the P^{n}BG QC may start to display distributed system [116] behavior.

Mass-Spring Network Approximation

While at high frequencies the P^{n}BG QC may begin to display distributed system behavior, the vibration patterns in Figure 4.17 and the modal analysis presented in Section 4.2.3 indicate that at a given frequency specific physical regions of the P^{n}BG QC appear to predominantly behave either approximately as a mass element or a spring element. For sub-band gap modes, the host regions between the closet spacing of the inclusion holes often appear to approximately behave as spring elements, while the host regions between the most distant spacing of the inclusion holes often appear to approximately behave as mass elements. The converse behavior appears for the out-of-plane

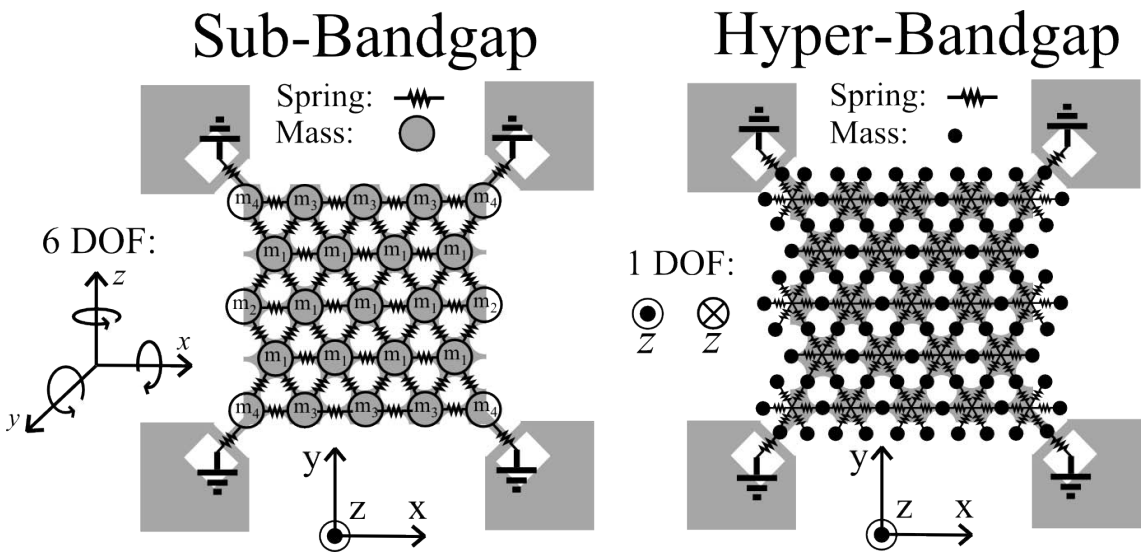

Figure 4.18: Approximation of a lumped element mass-spring network model of the phononic band gap quasi-crystal architecture illustrated for square truncation. Sub-band gap modes appear to display vibration patterns where the large masses, denoted by the grey filled circles in the mass-spring network on the left, behave as a mass element. The the mass, and number, of these large masses is denoted as m_{large}, and $N_{large\_masses} = 23$, respectively. Hyper-band gap modes appear to display vibration patterns where the small masses, denoted by the black dots in the mass-spring network on the right, behave as a mass element. The mass, and number, of these small masses will be denoted as m_{small} and $N_{small\_masses} = 88$, respectively.

hyper-band gap modes. The P^{n}BG QC may then potentially be approximated as a mass-spring network, where the distribution of the mass and spring elements may be different for sub-band gap and hyper-band gap modes. One approximation of the distribution of mass and spring elements for sub-band gap and hyper-band gap modes may be as shown in Figure 4.18.

Number of Sub-Band Gap Modes

The number of normal modes of a mass-spring system is equal to the total degrees of freedom (DOF) of the system. Behavioral zone III of the sub-band gap branch (see Figure 4.9) is comprised of in-plane and out-of-plane modes (see Figure 4.17) at which the

P^{n}BG QC behaves approximately as a mass-spring network with the masses and springs, of the sub-band gap mass-spring network of Figure 4.18, translating away from their equilibrium positions in the $\hat{x}, \hat{y}, \hat{z}$-directions (which requires 3 DOF) or rotating about virtual mechanical nodes either in-plane or out-of-plane (which requires 3 rotational DOF). The total number of DOFs per mass element for sub-band gap modes then appears to be six, as illustrated in Figure 4.19, which is the maximum DOFs for a rigid body in three dimensions ($dimensionality = 3, \quad DOF_{max} = dimensionality \times (dimensionality + 1)/2 = 6$). According to this model, the square (S1, S2, S3), and circular (C1, C2, C3), truncated P^{n}BG QCs may be approximated to be comprised of 23, and 19, large masses (see Figure 4.18), respectively. The total DOF for the sub-band gap modes for square and circular truncated P^{n}BG crystals may then be approximated to be $6DOF/mass\ element \times 23masses = 138$, and $6DOF/mass\ element \times 14masses = 114$, respectively, which displays the observed trend that $N_{SBGM,square} > N_{SBGM,circle}$. The FEM model of Figure 4.10 also predicts $N_{SBGM,square} = 138$ and $N_{SBGM,circle} = 114$, hence the analytical model corresponds precisely to the FEM model and may be formalized as:

$$\begin{aligned} N_{SBGM} &= DOF_{max} \times N_{large\_masses} \\ &= \frac{dimensionality \times (dimensionality + 1)}{2} N_{large\_masses} \end{aligned} \tag{4.15}$$

where N_{large_masses} is the number of large masses in the sub-band gap mass-spring network of Figure 4.18, $DOF_{max} = dimensionality \times (dimensionality + 1)/2$ and in three-dimensional space $dimensionality = 3$. Hence, for 3-dimensional space $N_{SBGM} = 6N_{large\_masses}$. Figure I.4 indicates that for a mass-spring network comprised of 17 large and and 16 small masses, the number of sub-band gap modes is equal to the number of large masses, 17. Hence, the P^{n}BG QC architecture proposed in the body of this thesis

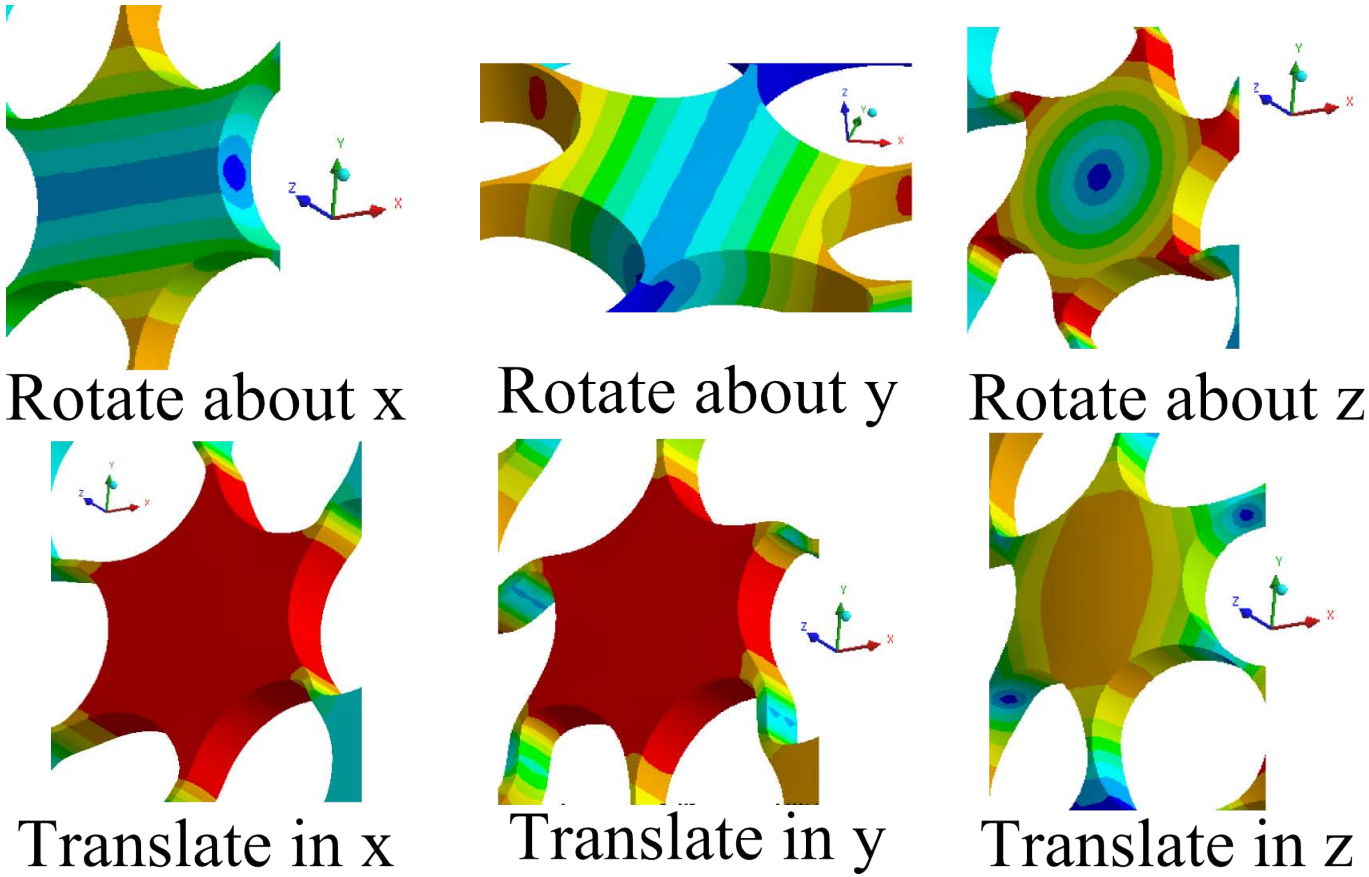

Figure 4.19: Close up of the physical region that is approximated by the lumped mass element, m_{large}, (in Figure 4.18) in the finite element method models of the phononic band gap quasi-crystal sub-band gap modes shapes. Each image illustrates one of the six degrees of freedom of each lumped mass element: (i) rotate about $\hat{x}$ (from mode 48), (ii) rotate about $\hat{y}$ (from mode 25), (iii) rotate about $\hat{z}$ (from mode 52), (iv) translate in $\hat{x}$ (from mode 89), (v) translate in $\hat{y}$ (from mode 87) and (vi) translate in $\hat{z}$ (from mode 62). Hence, each mass appears to have three translational and three rotational degrees of freedom.

displays behavior similar to the discretized diatomic phononic band gap quasi-crystals of Appendix I and [86].

Number of Hyper-Band Gap Modes

Due to the relatively short effective wavelength of the vibrations (quantified to be approximately 115 μm to 200 μm in Section 4.2.4 which is approximately 3 to 5 times smaller than the truncation width of the square and circular P$^{\text{n}}$BG QCs) of the hyper-band gap modes and the intricacy of the mode shapes, it is more difficult to count the number of mass elements for a mass-spring network model of the hyper-band gap modes as compared to the mass-spring network model of sub-band gap modes. According to the approximation of Figure 4.18, one approximate value for the number of small mass elements in the square truncated P$^{\text{n}}$BG QCs mass-spring network model for hyper-band gap modes may be $N_{small\_masses} = 88$. Figure 4.20 illustrates that the physical region of the P$^{\text{n}}$BG QC that is approximated by the small lumped element mass, m_{small}, appears to display one translational DOF in the $\hat{z}$-direction and potentially some rotational degrees of freedom. From Figure 4.18 it is not clear how many rotational degrees of freedom each lumped element mass, m_{small}, displays or about which axis the rotation occurs, so these potential rotational DOFs will not be accounted for in the following approximation. Recognizing that this model may not be accounting form some rotational DOFs of the hyper-band gap mass elements, the approximate number of hyper-band gap normal modes may be lower bounded by utilizing one DOF per mass element, m_{small}:

$$\begin{aligned} N_{HBGM} &= 1DOF \times N_{small\_masses} \\ &= 1 \times N_{small\_masses} \\ &= N_{small\_masses}. \end{aligned} \tag{4.16}$$

where N_{small_masses} is the number of small mass elements in the hyper-band gap mass-

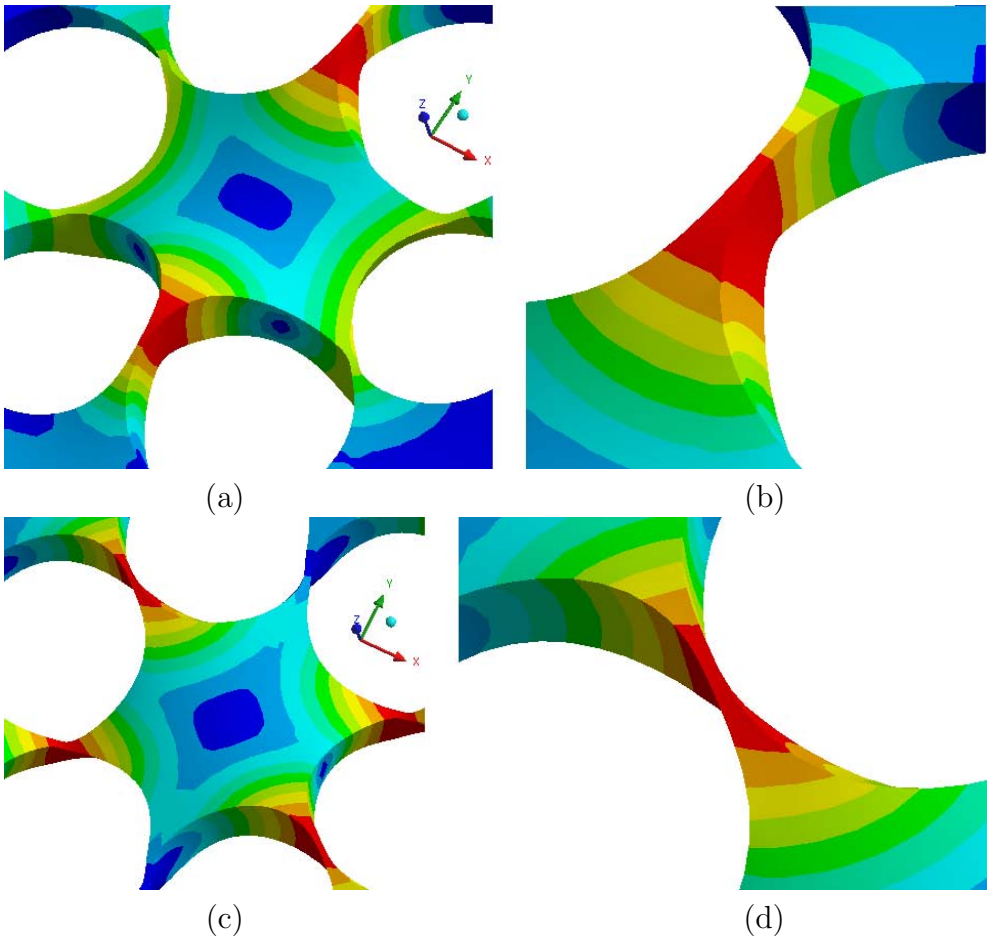

Figure 4.20: Close up of the finite element method models of the phononic band gap quasi-crystal modes for the hyper-band gap branch in the physical region that is approximated by the lumped mass element, m_{small}, of the hyper-band gap mass-spring model of Figure 4.18. The physical region that is approximated by the lumped mass element, m_{small}, appears to display a translational degree of freedom in the $\hat{z}$-direction (as may be seen in (a) and the corresponding close up in (b) for mode 149, 15.852 MHz, of the S2 phononic band-gap quasi-crystal) and a vibration pattern that may indicate rotational degrees of freedom (as may be seen in (c) and the corresponding close up in (d) for mode 140, 14.553 MHz, of the S2 phononic band-gap quasi-crystal).

spring network of Figure 4.18, which contains 88 small masses so $N_{HBGM} = 88$ modes. From Figure 4.7, the number of modes in behavioral zones V and VI of the square truncated devices is approximately 75, which is in reasonable agreement with the analytical model of $N_{HBGM} = 88$. The discrepancies between the analytical model of Equation 4.16 and the FEM model of Figure 4.7 may in-part be accounted for by the uncertainty in the number of hyper-band gap masses, N_{small_masses}, that should be included in Figure 4.18, which displays just one approximation of the number of hyper-band gap masses, N_{small_masses}. There is also uncertainty in the number of DOF that each hyper-band gap mass, m_{small}, should have in the hyper-band gap mass-spring network of Figure 4.18. That said, if each hyper-band gap mass, m_{small_masses}, was granted one more DOF, the number of hyper-band gap masses, N_{HBGM}, would be twice that predicted by Equation 4.16 leading to a larger discrepancy with the FEM model of Figure 4.7. Lastly, there is also uncertainty in how to define the extent of the hyper-band gap branch in the FEM model of Figure 4.7. If the extent of the hyper-band gap branch is larger than behavioral zones V and VI of Figure 4.7, which contain 75 modes, then the number of modes in the hyper-band gap branch should be greater than 75 and there may potentially be a closer match with the analytical model of 88 hyper-band gap modes given by Equation 4.16. Further investigation is required.

Slope of Frequency versus Mode Number Characteristic

The FEM model suggests that the sub-band gap branch is approximately linear, as described in Figure 4.17, with a slope equal to the rise in frequency divided by a run equal to the number of sub-band gap modes. The run of the sub-band gap branch is precisely equal to the number of sub-band gap modes given by Equation 4.15. If the location of the band gap in Figures 4.7 and 4.8 may be deduced utilizing P^{n}BG theory, the rise of the sub-band gap branch would be approximately equal to the first Bragg

frequency of the hexagonal lattice and so the slope of the sub-band gap branch of the P^{n}BG QC architecture would then be analytically approximated as:

$$\begin{aligned} m_{SBG} &= \frac{rise}{run} \\ &= \frac{f_{\Gamma M}}{N_{SBGM}} \\ &= \frac{\frac{c_{avg,transverse}}{\sqrt{3}a}}{6N_{lumped\_masses}} \\ &= \frac{c_{avg,transverse}}{6\sqrt{3}aN_{lumped\_masses}}. \end{aligned} \tag{4.17}$$

where $f_{\Gamma M}$ is given by Equation 2.5 and N_{SBGM} is given by Equation 4.15. Equation 4.17 approximates the slope of the frequency versus mode number curve and may then be utilized to provide the following approximation of the relation between frequency and mode number:

$$f_{sub-bandgap}(n) = m_{SBG} \times n + f_{offset} \qquad n \in [1, 2, 3...N_{SBGM}] \tag{4.18}$$

where f_{offset} is a frequency offset that may account for a potentially non-zero f-intercept in the frequency versus mode number characteristic. From the frequency versus mode number characteristics of Figures 4.7 and 4.8 the absolute value of f_{offset} appears to be very close to zero, relative to the extent of the frequency range examined, and will be approximated as such, $f_{offset} \approx 0$. Substituting Equation 4.17 into Equation 4.18, with $f_{offset} = 0$, yields:

$$f_{sub-bandgap}(n) = \frac{nc_{avg,transverse}}{6\sqrt{3}aN_{lumped\_masses}} \qquad n \in [1, 2, 3...N_{SBGM}], \tag{4.19}$$

where it may be observed that the frequency versus mode number characteristic in-

creases in slope with material velocity, $c_{avg,transverse}$, and decreases in slope with the lattice constant, a, and number of lumped mass elements, N_{lumped_masses}; this behavior is consistent with that predicted by the numerical sensitivity analysis of Section 4.2.6. The analytical model of Equation 4.19 suggests that the frequency versus mode number characteristic of the sub-band gap branch of the P^{n}BG QC architecture appears to be analytically approximated without accounting for, or including, the tether structures in the analysis. This may indicate that the tether design methodology described in Section 3.2 yields a tether that displays a relatively low order effect on the location of the sub-band gap frequency versus mode number characteristic of the P^{n}BG QCs and this may be an indication of a well designed tether element.

Linear Shape of the Frequency versus Mode Number Characteristic

For a mass-spring network, the frequency of each mode of the system may be obtained by solving the Eigenvalue problem utilizing a computer program as described in [86]. The frequency versus mode number characteristic may then be generated by assigning the mode number $n = 1$ to the first mode frequency and enumerating higher modes up to the total DOF of the mass-spring network as has been done for the discretized diatomic mass-spring P^{n}BG QC of Figure I.4 of Appendix I. Following this procedure, in Figure I.4, the frequency versus mode number characteristics of the discretized diatomic mass-spring P^{n}BG QC, which has 33 mass elements ($N_{masses} = 33$) with each mass element given one DOF (let $DOF = 1$), has been generated and contains a total of 33 modes ($N_{modes} = DOF \times N_{masses} = 33$). The frequency versus mode number characteristic of Figure I.4 may be approximated as piecewise linear by lines of differing slope for the sub- and hyper-band gap branches. In addition, mass-spring approximations of continuous systems have been illustrated to display linear frequency versus mode number relations where mode frequencies are integer multiples of the fundamental frequency [123]. Hence,

linear mode frequency versus mode number characteristics may often be observed for mass-spring systems.

Some of the properties of the frequency versus mode number characteristic observed in the FEM model (for example, Figure 4.10) of the proposed P$^{\mathrm{n}}$BG QC architecture have been approximated relatively accurately (for example, for the number of sub-band gap modes given by Equation 4.15) based on analytical models of the lumped element mass-spring network of Figure 4.18. The P$^{\mathrm{n}}$BG QC architecture may then also be expected to display an approximately linear frequency versus mode number characteristic. The analytical frequency versus mode number characteristic of the P$^{\mathrm{n}}$BG QC may be compared with those of strings and boxes which have simple analytical relations between frequency and mode number [122]:

$$\begin{aligned} f(n) &= \frac{nc}{2L} \qquad (string \quad or \quad open-ended \quad tube) \\ f(l,m,n) &= \frac{c}{2}\sqrt{\left(\frac{l}{L_x}\right)^2+\left(\frac{m}{L_y}\right)^2+\left(\frac{n}{L_z}\right)^2} \qquad (rectangular \quad box) \\ f_{sub-bandgap}(n) &= \frac{nc_{avg,transverse}}{6\sqrt{3}aN_{lumped\_masses}} \qquad (P^{\mathrm{n}}BG \quad QC \quad from \quad Equation \quad 4.19). \end{aligned} \tag{4.20}$$

where l, m and n are mode numbers, c is the speed of sound, L is the length of the string, and L_x, L_y, and L_z are the dimensions of the box in the $\hat{x}$, $\hat{y}$, and $\hat{z}$-directions, respectively. The frequency versus mode number characteristic given by Equation 4.19 for the P$^{\mathrm{n}}$BG QC and the similar relations given in Equation 4.20 for strings and boxes, are all proportional to elastic wave velocity and inversely proportional to the physical dimensions of the structure. The relations are also approximately linear as a result of the wavelength of higher order modes being multiples of the fundamental mode wavelength, which is controlled by the finite physical geometry between fixed boundaries.

Differences Between Sub- and Hyper-Band Gap Branches

Figure 4.10 indicates that the hyper-band gap branch displays a higher slope than the sub-band gap branch. Structurally speaking, the hyper-band gap modes bend the P^nBG QC in the out-of-plane direction in which the thickness is $25\mu m$, while many sub-band gap modes bend in the in-plane direction by flexing the relatively thin $2\mu m$ to $4\mu m$ wide regions between the inclusions. Spring stiffness tends to be proportional to the thickness in the dimension of bending. In addition, the hyper-band gap modes operate at smaller wavelengths and the length of the portion of the P^nBG QC that behaves as the spring may be smaller in the hyper-band gap mass-spring network than in the sub-band gap mass spring network of Figure 4.18. Spring stiffness tends to be inversely proportional to spring length.

Lastly, the mass element, m_{small}, in the mass-spring network model (Figure 4.18) of hyper-band gap modes may display a smaller mass than the mass element, m_{large}, in the mass-spring network of sub-band gap modes. This may be the result because the mass element of the hyper-band gap modes, m_{small}, is approximated by the region of the host that lies between the closest spacing of the inclusions, as shown in Figure 4.21, while the mass element of the sub-band gap modes, m_{large} is approximated by the region of the host that lies between the most distant spacing of the inclusions, as shown in Figure 4.21.

The aforementioned differences between the stiffness, and mass, of the sub- and hyper-band gap spring, and mass elements, respectively, of Figure 4.18 may relate to the differences between the slope of the sub- and hyper-band gap branches and requires further study. Next, structural analysis is utilized to investigate the quantity of the aforementioned stiffness and mass.

Semi-Analytical Structural Analysis

To construct a physical model, the physical regions that lie between nodes in the P^{n}BG QC mode shapes will be analyzed to form a semi-analytical model of their structural properties of mass and stiffness. These mass and stiffness values will then be utilized in a lumped element model of mode frequency. Scale factors will be applied to match the semi-analytical model to the FEM model of mode frequency to provide physical insight into what may be the effective mass and stiffness associated with the modes of the P^{n}BG QCs.

Sub-Band Gap Mass, m_{large}

First, the mass element of the sub-band gap mass-spring network of Figure 4.18 may be approximated as shown in Figure 4.21(a) and for the S2 P^{n}BG QC may be computed to have a mass of:

$$\begin{aligned} A_{hex} &= \frac{1}{2} \times 6 \times h \times b, \\ V_{hex} &= A_{hex} \times t, \\ m_{large} &= V_{hex} \times \rho_{Si} = 0.46491 \mu g, \end{aligned} \tag{4.21}$$

where $r = 45\mu m$, $s = 3\mu m$, $c = r + s$, $b = 2h \times tan(30^o) = 2h\sqrt{3}/3\mu m$, and $t = 25\mu m$ and $\rho_{Si} = 2300/m^3$ was taken from Table 4.1. The aforementioned value for the sub-band gap mass, m_{large}, has been listed in Table 4.6 for sub-band gap modes 62 and 87.

Sub-Band Gap Spring Stiffness for Mode 87

The mass element, m_{large}, appears to behave approximately as a rigid body, since the displacement field is uniform across the body as denoted by the uniform red coloration across this region in Figure 4.22(a). If this region behaves as a rigid body it may be

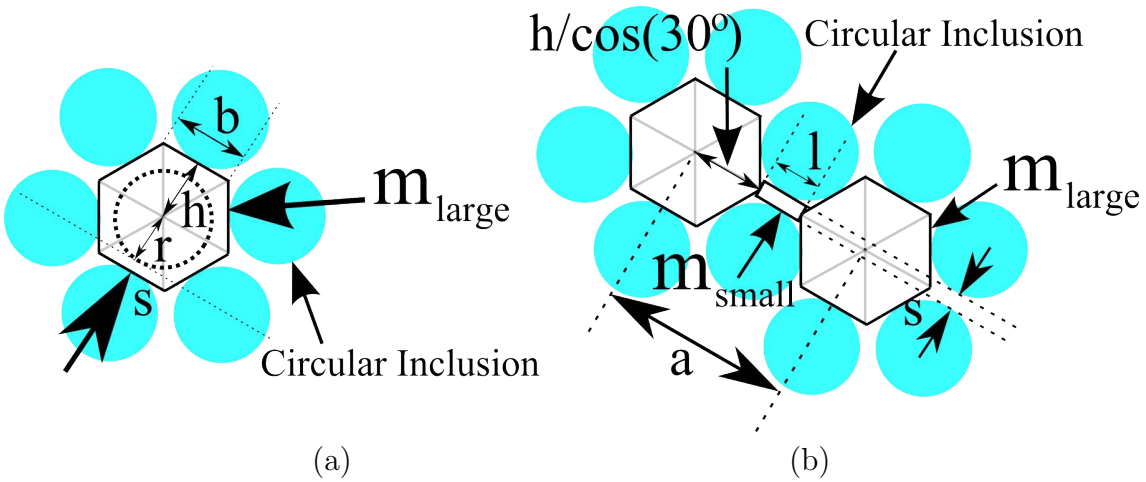

Figure 4.21: Dimensions of the physical region of the phononic band gap quasi-crystal that behaves as the dominant structural mass element for the (a) sub-band gap, m_{large}, and hyper-band gap, m_{small}, masses in the mass-spring networks of Figure 4.18. The inclusion radius, r, inclusion spacing, s and dimensions $h = r + s$, $b = 2h \times tan(30^o) = 2h\sqrt{3}/3$, and $l = a - 2h \times cos(30^o)$ are as shown.

lumped into a single point surrounded by four side flexure springs and a spring on either end as illustrated in Figure 4.22(c). The stiffness of the four side flexures of Figure 4.22(c) may be computed utilizing the equation for a fixed-fixed flexure from [124]:

$$k_{flexures,mode\ 87} = 4E \times t \left(\frac{s}{l_{SBG}}\right)^3 \tag{4.22}$$

where $l = a_{S2} - 2h/cos(30^o)$ is as shown in Figure 4.21, $l_{SBG} = \frac{l}{2}$ is denoted in Figure 4.22, $a_{S2} = 161.081\mu m$ is the lattice constant of the S2 P$^{\text{n}}$BG QC, $h = r + s$ as in Figure 4.21 and r and s are given in Table 3.2 for the S2 P$^{\text{n}}$BG QC, $t = 25\mu m$ as described in Figure 3.4 and listed in Table 3.1.

The end springs, k_{end}, in Figure 4.22 that are strained in the $\hat{y}$-direction of motion

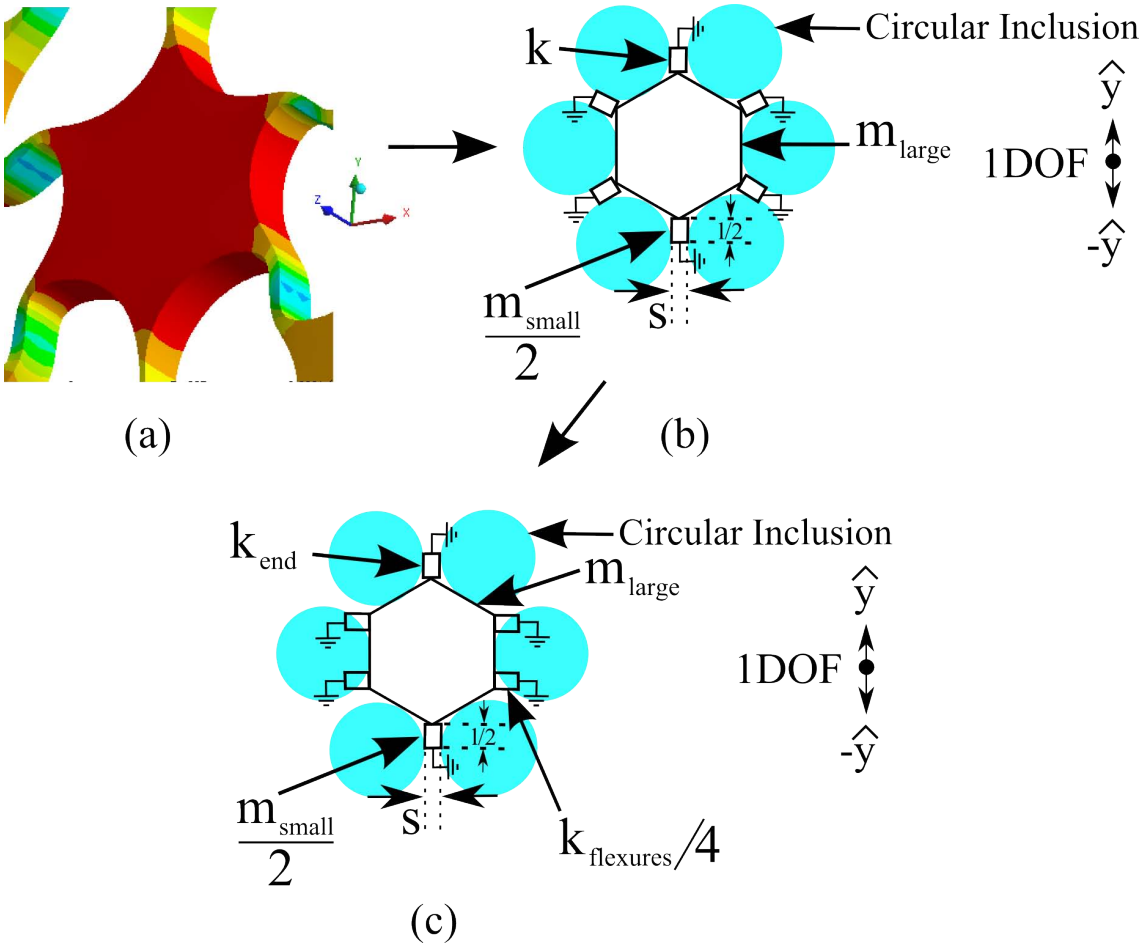

Figure 4.22: Dimensions of the physical regions of the phononic band gap quasi-crystal that approximate the lumped element springs, which are denoted above as k_{SBG}, of the sub-band gap mass-spring network of Figure 4.18. Virtual mechanical grounds are applied around the structure at the approximate locations of the anti-nodes displayed by the translational modes in Figure 4.20. The length of the spring elements is $l/2$ where l is given in Figure 4.21.

may be computed to have a spring constant of:

$$k_{end,mode\ 87} = \frac{E \times A}{l_{SBG}}, \tag{4.23}$$

where $A = t \times s$ is the cross-sectional area of the P$^{\text{n}}$BG QC in the region of minimum inclusion spacing. The total stiffness may be the parallel combination of $k_{flexures,mode\ 87}$ and two end springs $k_{end,mode\ 87}$:

$$k_{total,mode\ 87} = k_{flexures,mode\ 87} + 2k_{end,mode\ 87}, \tag{4.24}$$

and for the S2 P$^{\text{n}}$BG QC has the value of $k_{total,mode\ 87} = 1.1057MN/m$ as listed in Table 4.6 for the model of sub-band gap mode 87.

Sub-Band Gap Spring Stiffness for Mode 62

Similarly, for mode 62 of the S2 P$^{\text{n}}$BG QC with 1DOF in the $\hat{z}$-direction, as shown in Figure 4.23, the fixed-fixed flexure model may be utilized to compute the stiffness of the four flexures in the $\hat{z}$-direction $k_{flexures}$ [124]:

$$k_{flexures,mode\ 62} = 4E \times s \left(\frac{t}{l_{SBG}}\right)^3 \tag{4.25}$$

where $l = a_{S2} - 2h/cos(30^o)$ is as shown in Figure 4.21, $l_{SBG} = \frac{l}{2}$ is denoted in Figure 4.23, $a_{S2} = 161.081\mu m$ is the lattice constant of the S2 P$^{\text{n}}$BG QC, $h = r + s$ as in Figure 4.21 and r and s are given in Table 3.2 for the S2 P$^{\text{n}}$BG QC, $t = 25\mu m$ as described in Figure 3.4 and listed in Table 3.1.

The springs, k_{end}, in Figure 4.23 that are strained in the $\hat{z}$-direction of motion are essentially half of the fixed-fixed flexure, and so may be computed to have a spring

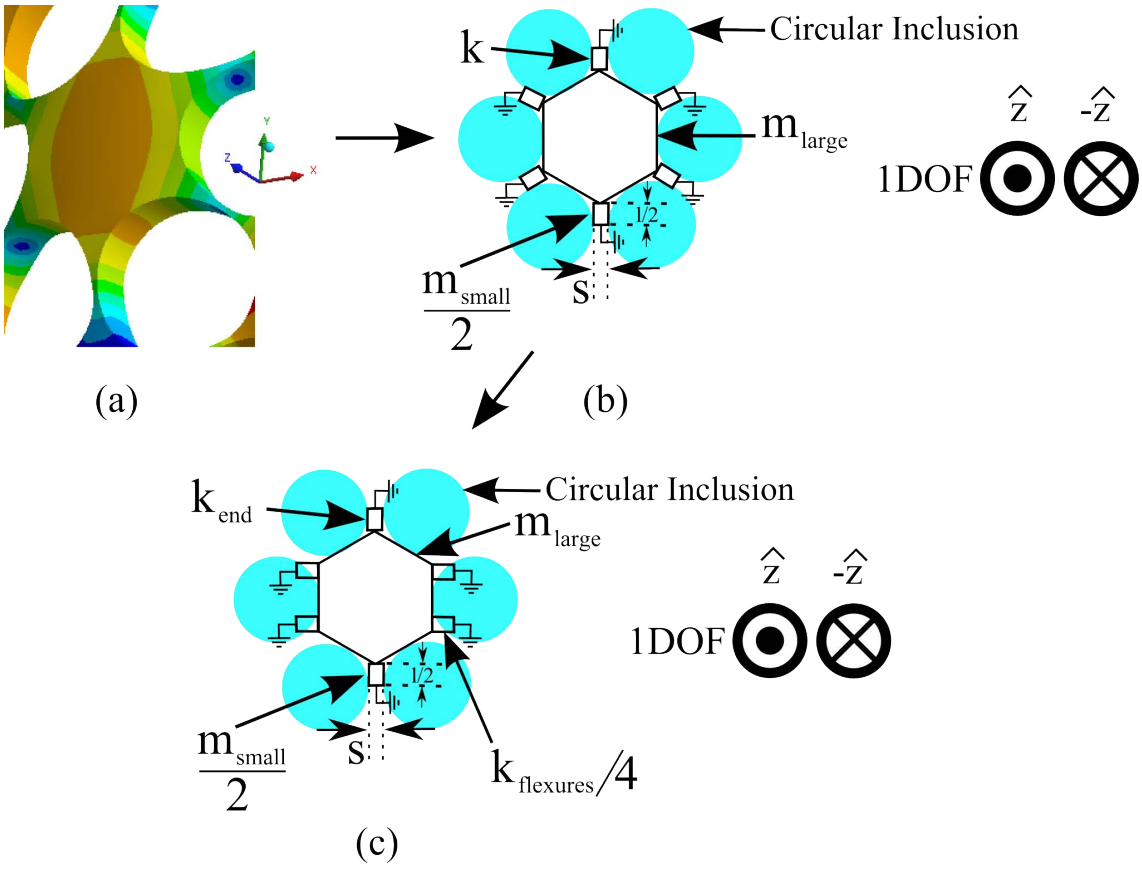

Figure 4.23: Dimensions of the physical regions of the phononic band gap quasi-crystal that approximate the lumped element springs, which are denoted above as k_{SBG}, of the sub-bandgap mass-spring network of Figure 4.18. Virtual mechanical grounds are applied around the structure at the approximate locations of the anti-nodes displayed by the translational modes in Figure 4.20. The length of the spring elements is $l/2$ where l is given in Figure 4.21.

constant of equal to half of $k_{flexures,mode\ 62}$:

$$k_{end,mode\ 62} = \frac{1}{2} k_{flexures,mode\ 62} \tag{4.26}$$

where $k_{flexures,mode\ 62}$ is given by Equation 4.25. The total stiffness is given by the parallel combination of $k_{flexures,mode\ 62}$ and $k_{end,mode\ 62}$:

$$k_{total,mode\ 62} = k_{flexures,mode\ 62} + k_{end,mode\ 62}\big|_{(k_{end,mode\ 62} = \frac{1}{2} k_{flexures,mode\ 62})}, \tag{4.27}$$

and for the S2 P$^{\text{n}}$BG QC has the value of $k_{total,mode\ 62} = 3.1957 MN/m$ which has been listed in Table 4.6 for sub-band gap mode 62.

Hyper-Band Gap Mass, m_{small}

Next, the mass of the lumped element mass, m_{small}, of the hyper-band gap mass-spring network of Figure 4.18, may be approximated to have the dimensions shown in Figure 4.21(b) and for the S2 P$^{\text{n}}$BG QC may be computed to have a mass of:

$$\begin{aligned} V_{hbg\_mass} &= l \times s \times t, \\ m_{small} &= V_{hbg\_mass} \times \rho_{Si} = 8.778 ng, \end{aligned} \tag{4.28}$$

where $s = 3\mu m$ is the hole spacing of the S2 P$^{\text{n}}$BG QC, $t = 25\mu m$, $l = a - 2 \times h/cos(30^o) = 50.230\mu m$, $a = 161.081\mu m$ is the lattice constant of the S2 P$^{\text{n}}$BG QC and h is as shown in Figure 4.21(b). It may be noted that $m_{large} = 0.465\mu g$ is approximately two orders of magnitude larger than $m_{small} = 8.778ng$, which may in-part account for the higher resonant frequencies of the hyper-band gap modes, since resonant frequency tends to increase with decreasing mass. The effective mass of the beam model may be upper bounded by Equation 4.28, since the inertia of the portion of the beam mass

nearer to the virtual mechanical grounds in Figure 4.21 may have less of an impact on the vibration of the beam. The computed mass of m_{small} is listed in Table 4.6 for the model mass of hyper-band gap mode 149.

Hyper-Band Gap Spring Stiffness

It may be observed that the physical region of the mode shape in Figure 4.20 that represents m_{small} (of Figure 4.21) is located between two nodes. If these nodes may be approximated as virtual mechanical grounds, then the physical region that represents m_{small} may be approximated as a fixed-fixed beam as shown in Figure 4.24. The computed stiffness of a fixed-fixed beam for a force concentrated at the center of the beam is given in [125], and using the same values as used in Equation 4.28 for m_{small}, yields the following stiffness for the hyper-band gap beam model:

$$\begin{aligned} k_{hbg} &= \frac{192 \times E \times I}{l^3} = 1.065 MN/m, \\ I &= \frac{s \times t^3}{12} = 3906.25 \mu m^4, \end{aligned} \tag{4.29}$$

where $E = 180GPa$ is Young's modulus for single-crystal-silicon from Table 4.1, $l = a - 2 \times h/cos(30^o)$ is the length of the beam (see Figure 4.21), I is the second moment of inertia for a beam with a rectangular cross section, s is the width of the beam and t is the thickness of the beam in the direction of deflection as shown in Figure 4.24. The stiffness k_{hbg} has been listed in Table 4.6 for the model of stiffness for hyper-band gap mode 149.

The stiffness given by Equation 4.29 has been computed for a force that is assumed to be located in the middle of the beam where the stiffness (compliance) is the minimum (maximum). Moreover, near the virtual mechanical grounds the P$^{\text{n}}$BG QC in Figure 4.24(a) is wider than the beam width s in the beam model of Figure 4.24(b); the ad-

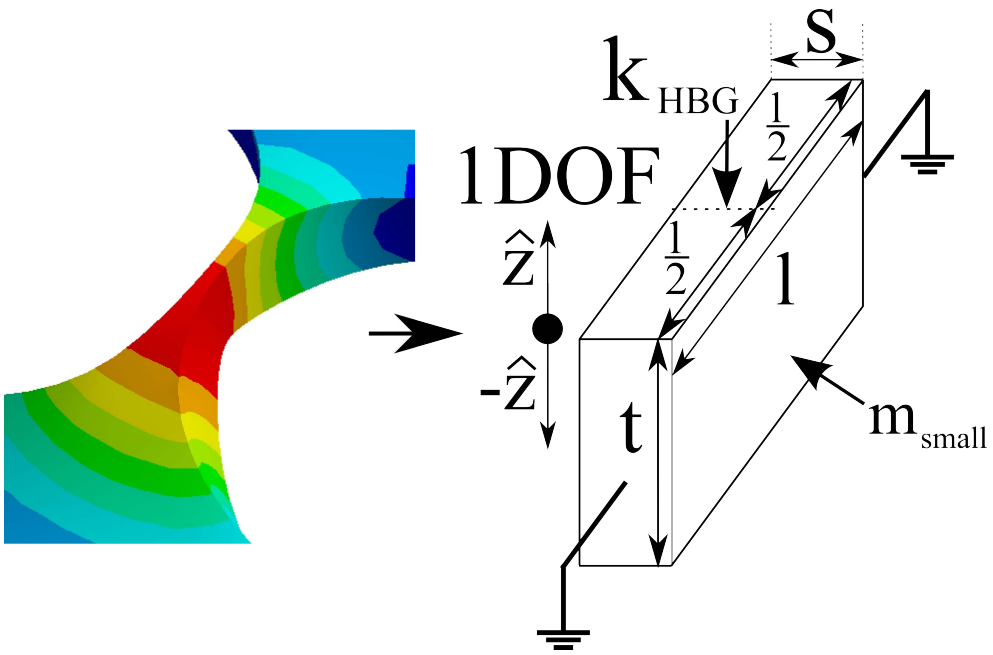

Figure 4.24: The nodes shown in (a) at each end of the physical region of the phononic band gap quasi-crystal (from Figure 4.20)(b) that is approximated by the m_{small} element of Figure 4.21 are approximated here as virtual mechanical grounds. In this fashion, the m_{small} element could be approximated as a beam that is bounded by virtual mechanical grounds as shown in (b).

ditional thickness near the virtual mechanical grounds will increase the stiffness above that of given by Equation 4.29. Hence, the value of the stiffness given by Equation 4.29 is a lower bound on the spring stiffness of hyper-band gap mode 149 of Figure 4.24.

Semi-Analytical Vibration Analysis

Within Appendix D the mass and stiffness values that have been computed in the preceding semi-analytical structural analysis and that are summarized in Table 4.6 are substituted into the analytical model of the resonant frequency of the first order harmonic oscillator shown in Figure 4.25. To assist in evaluating the semi-analytical structural models and the virtual mechanical ground methodology that was utilized to reduce the complexity of the complete P^{n}BG QC model down to relatively simple beam and flexural plate models, fitting parameters are applied in Appendix D to fit the first order harmonic oscillator resonant frequencies to the corresponding resonant frequencies of the FEM model of the complete P^{n}BG QC in Figure 4.10. The first order harmonic oscillator, fitted resonant frequencies and fitting values are summarized in Table 4.6. As an alternative to the first order harmonic oscillator model, an Eigenvalue approach to model the vibration of tether mode 161 is also presented in Appendix D and summarized in Table 4.6.

Discussion of Semi-Analytical Structural and Vibration Analysis

Despite the large percentage error in Table 4.6 (see Section D.2 for sources of error), the semi-analytical structural and vibration analysis appear to yield insight into the behavior of the P^{n}BG QC architecture. For example, the insensitivity of the hyper-band gap branch to changes in in-plane geometry may be accounted for in the semi-analytical model of Equation 4.29 by the linear dependence of beam stiffness on the beam dimension in the in-plane direction and third order dependence of beam stiffness on the beam dimension in the out-of-plane direction. In contrast, the semi-analytical model

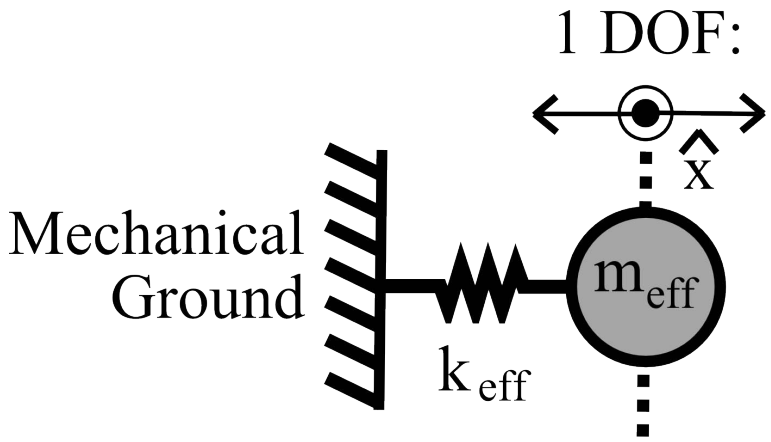

Figure 4.25: The first order harmonic oscillator model is comprised of a mass, which moves with one degree of freedom, that is connected to a fixed boundary via a spring.

suggests that the stiffness of sub-band gap modes displays a third order dependence on in-plane geometry and linear dependence on out-of-plane geometry, which is always held constant. This increased sensitivity of the spring stiffness for in-plane sub-band gap modes, as compared to out-of-plane hyper-band gap modes, may in-part explain why the sub-band gap branch, which includes many in-plane modes, may be observed in Figure 4.10 to be more sensitive than hyper-band gap modes to changes in in-plane geometry (such as, inclusion spacing, s). Both sub- and hyper-band gap mass elements would display a first order dependence to scaling in either a single in-plane or single out-of-plane dimension.

It may be noted in Table 4.6 that even after fitting the semi-analytical model for hyper-band gap mode 149 to the FEM model, the effective spring stiffness for mode 149 is still less than that for sub-band gap modes 62 and 87. However, both before and after fitting, the semi-analytical model does successfully predict that sub-band gap modes 62 and 87 should display lower resonant frequencies than hyper-band gap mode 149. This result occurs in-part due to the semi-analytical model of the sub-band gap mass, m_{large}, being approximately two orders of magnitude larger than the hyper-band gap mass,

m_{small}. Hence, any potentially large inaccuracy in predicting the spring constant of sub-band gap and hyper-band gap modes may be overshadowed by the potentially dominant variation between the mass that is estimated by the semi-analytical models for the sub-, and hyper-band gap, mass elements (of Figure 4.18), m_{large}, and m_{small}, respectively. While these results may be attributed to the sources of error discussed in Section D.2, alternatively, this trend may be reflective of the significant difference between sub- and hyper-band gap mode shapes, which indicate that the P^{n}BG QC reconfigures the region of the P^{n}BG QC that behaves as the mass and spring element. Each sub-band gap mass, m_{large}, appears to be attached to six springs, while each hyper-band gap mass, m_{small}, appears to be attached to only two springs. The difference between the sub-band gap and hyper-band gap mode frequencies may then not be due to a simple increase in stiffness and decrease in mass, but may rather be due to this reconfiguration of the mass and spring elements in a way that the mass element becomes significantly smaller for hyper-band gap modes, while the spring constant of hyper-band gap modes may not necessarily be significantly larger. Given the high percentage error listed in Table 4.6 for the semi-analytical model, sources of error in Section D.2, given that the choice of fitting parameters (discussed in Section D.1) for mass and spring constant do not follow a rigorous method and given that the lumped element approximations presented here do not represent the complete P^{n}BG QC structure, these observed trends are difficult to substantiate. The semi-analytical structural and vibration analysis have primarily been presented here for further consideration and to provide an insightful link between the FEM model to the physical parameters of the P^{n}BG QC structure.

A complete explanation of the behavior of the P^{n}BG QC architecture that is observed in the FEM model of Figure 4.10 may require a model that is more complete than the semi-analytical model presented here. More complete analytical modeling approaches

are discussed next.

Proposed Improvement to the Mass-Spring Network Model:

Periodic Mass-Spring Network

Each lumped element model presented in Figure 4.18 for the sub- and hyper-band gap modes is comprised of mass elements that have the same mass. The sub-, and hyper-band gap, mass-spring networks in Figure 4.18 would have to be analyzed separately to deduce the structural and vibration properties of the sub-, and hyper-band gap, branch, respectively. To create a single lumped element model that accounts for the periodicity in the mechanical properties of the honeycomb P^nBG QC architecture, and may simultaneously predict the behavior of both the sub- and hyper-band gap branches, a mass-spring network that consists of mass elements of contrasting mass may be suitable.

Such a mass-spring network may resemble the hybrid of the sub- and hyper-band gap mass-spring networks of Figure 4.18. A conceptualization of such a hybrid network is illustrated in Figure 4.26. Figures 4.19 and 4.20 may indicate that to more accurately characterize the vibration modes of the P^nBG QC architecture, each mass element may be assigned more than one DOF. Methods to analyze multi-degree-of-freedom systems are described in [126] and left for future work. CoventorWare® Architect may also assist with the analysis of multi-degree-of-freedom systems. Lastly, reduced order techniques, such as those described in [127], may be utilized by applying Taylor series expansions to differential equations and neglecting high order non-linearities to produce a small signal linear model.

A more easily analyzed hybrid mass-spring network may utilize a mass-spring network that is only a subset of the masses and springs within a network such as Figure 4.26. In theory, the smallest subset of a P^nBG crystal that should represent the behavior of the entire crystal, and that should display unique behavior at each mode frequency,

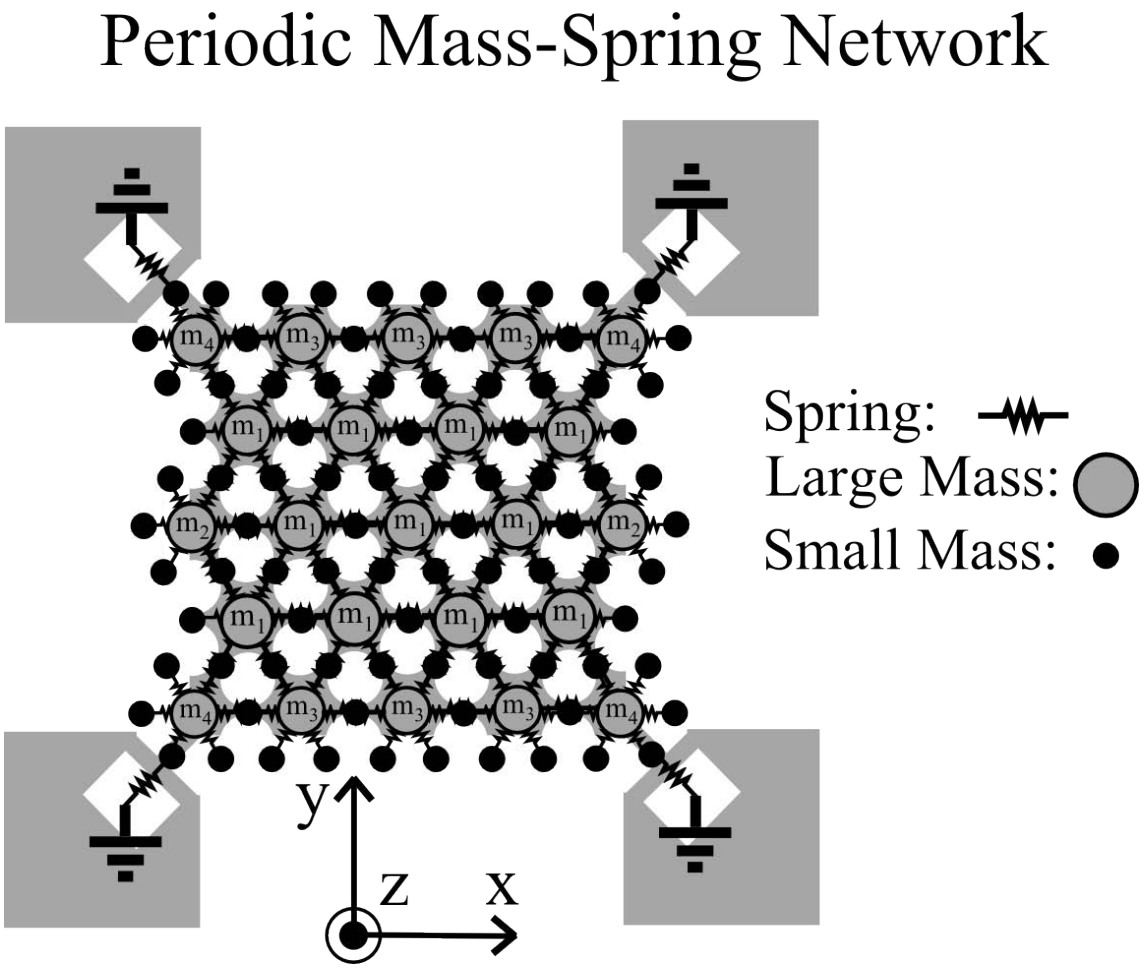

Figure 4.26: Conceptualization one possibility for a hybrid lumped element mass-spring network model of the phononic band gap quasi-crystal architecture with square truncation boundaries. The mass-spring networks of Figure 4.18 have been overlayed in a way the stiffness of mass elements and mass of spring elements are accounted for.

is the unit cell. To model the P^{n}BG QC utilizing just a unit cell may require the use of a periodic boundary condition [110], which may increase the complexity of the model. Without utilizing a periodic boundary condition, it may be possible that sufficient accuracy may be obtained by utilizing a lumped element model over a subset of the P^{n}BG QC where each mode displays a unique vibration pattern. This lumped element model may contain more than one lumped-element mass and spring in each coordinate direction, each mass may be assigned greater than or equal to 1DOF and different masses may have a different number of DOFs.

The simplified model may neglect features such as the stress-free boundary conditions at the free edges of the P^{n}BG QC architecture or the fixed boundary conditions at the anchored tethers. The absence of such features in the simplified model may assist in determining the importance of these features to the model. It may be observed that one dominant subset of the P^{n}BG QC architecture, for example the periodic structure, may account for the majority of the properties (such as the band gap or piecewise linear frequency versus mode number characteristic) of the P^{n}BG QC, while the tethers may for example display a lower order effect.

Simplified FEM models may be utilized to expedite the process of lumped-element model simplification by numerically determining which subsets of the P^{n}BG QC structure are most important to include in the lumped element model. For example, by removing the tethers from the FEM model, then performing a modal analysis on the simplified structure, the sensitivity of the frequency versus mode number characteristic to the removed component can be rapidly assessed. After simplification, if negligible changes in the FEM model results are observed, then the removed subsets, may not be as important to include in the lumped element model.

Lastly, if a periodic mass-spring network, which contains mass elements of contrasting

mass, similar to that of Figure 4.26, may be needed to form a more accurate lumped element model of the P^{n}BG QC architecture, this may highlight that the proposed P^{n}BG QC architecture is different from a homogeneous plate, for which a complete lumped element mass-spring model may contain only identical masses [126].

Table 4.6: Parameters of the semi-analytical models and associated results for the unfitted resonant frequency calculated by the semi-analytical models as well as the fitting parameters required to fit the semi-analytical model resonant frequencies to the FEM model resonant frequencies.

	Semi-Analytical Model Before Fitting			**Fit Parameters**		**Effective Values**			**Percentage Error Between Resonant Frequency and Fit**
	Total Mass	**Total Stiffness**	**Resonant Frequency**	**Mass Fitting Parameter**	**Stiffness Fitting Parameter**	**Effective Mass**	**Effective Spring Constant**	**Resonant Frequency Fitted to FEM Model**	
Model	m **[ng]**	k **[MN/m]**	f_o **[MHz]**	m_{factor}	k_{factor}	m_{eff} **[ng]**	k_{eff} **[MN/m]**	$f_{o,fit}$ **[MHz]**	$100\% \times (f_o - f_{o,fit})/f_{o,fit}$
SBG Out-Of-Plane Mode n=62	464.91	3.1957	0.41727	1	123.5	464.91	394.6744	4.6372	-91.0016%
SBG In-Plane Mode n=87	464.91	1.1057	0.24545	1	642	464.91	709.8846	6.2191	-96.053%
HBG Out-Of-Plane Mode n=149	8.778	1.0652	1.7533	2/3	54.494	5.852	58.0496	15.8517	-88.939%
Tether (Lumped Element) Mode n=161	34.658	0.32182	0.48498	2/3	893.2	23.105	287.4507	17.7519	-97.268%
Tether (Eigenvalue) Mode n=161	34.658	2716.680	44.5591	2/3	0.1058	23.105	287.4247	17.7511	151.022%

4.2.5 Dynamics Model over Wide and Narrow Frequency Band

A dynamics model examines the relation between the forces and motion of a system. This section presents an analytical linear (small displacement) first order dynamics model that may be utilized to model the dynamics of the P^{n}BG QC architecture over a narrow band of frequencies within the vicinity of each normal mode. Also presented is a FEM multi-mode dynamic numerical model of the P^{n}BG QCs over the wide band of frequencies from approximately 0 Hz to 20 MHz.

Analytical Narrow Band Linear (Small Displacement) Dynamics Model

The equation of motion for the 1DOF mass-spring harmonic oscillator system shown in Figure 4.25 is:

$$m_{eff}\frac{\partial^2 x}{\partial t^2} + \gamma\frac{\partial x}{\partial t} + k_{eff}x = F(t) \tag{4.30}$$

where m_{eff} is the effective mass, γ is the damping coefficient and k_{eff} is the effective spring constant. The forcing function, $F(t)$, and displacement, $x(t)$ are assumed to be time harmonic, $x(t) = Xe^{j\omega t}$ and $F(t) = Fe^{j\omega t}$ with amplitude X is and F, respectively, where $\omega = 2\pi f$ is the angular frequency and f is the temporal frequency. Reverse substitution of $x(t)$ and $F(t)$ into Equation 4.30 yields the displacement amplitude versus angular frequency:

$$|X| = \frac{F/k_{eff}}{\sqrt{(1-\frac{\omega^2}{\omega_o^2})^2 + (\frac{\omega}{\omega_o Q_{mech}})^2}} \tag{4.31}$$

where $\omega_o = \sqrt{k_{eff}/m_{eff}}$ is the normal mode frequency, and $Q_{mech} = \omega_o m_{eff}/\gamma$ is the mechanical quality factor.

For comparison with measured values, the displacement amplitude is often converted to a log scale. Utilizing Equations 6.1 and 6.2, the displacement amplitude, $|X|$, may be expressed on the log scale as $|X|(dBm) = 10log_{10}(\frac{[|X|/K_{vib}/\sqrt{2}]^2}{50\Omega}) + 30dBm = 20log_{10}(|X|) + X_{offset}$. As shown in Equation 6.1, $K_{vib} = 50nm/V$ is the conversion factor that the Laser doppler vibrometer applies to convert between voltage and displacement amplitude. Thus, $X_{offset} = 10log_{10}(1/(100K_{vib}^2)) + 30dBm = 156.021dBm$ accounts for conversion factors introduced by measurement equipment prior to displaying the value that corresponds to the measured displacement amplitude, $|X|$. The harmonic oscillator model of Figure 4.31 then has three fitting parameters: Q_{mech}, F/k_{eff} and ω_o. Figure 4.27 illustrates the effect of the fitting parameters, as well as X_{offset}, on Equation 4.31: the mechanical quality factor, Q_{mech} provides control of the shape and peak level, F/k_{eff} and X_{offset} provide control over the vertical level, while ω_o provides control of the horizontal position.

The fitting parameters may be determined by fitting Equation 4.31 to experimentally measured data. For Lamé and square extensional mode resonators, the mechanical quality factor parameter under specific configurations has be shown to be representative of the electrical quality factor [95]. Given a forcing function amplitude, F, effective mechanical parameters may be computed:

$$\begin{aligned} k_{eff} &= \frac{F}{(F/k_{eff})}, \\ m_{eff} &= \frac{F}{(F/k_{eff})\omega_o^2}, \\ \gamma &= \frac{F}{(F/k_{eff})\omega_o Q}, \end{aligned} \tag{4.32}$$

where it should be noted that (F/k_{eff}) is a single parameter obtained by fitting the model to measured data.

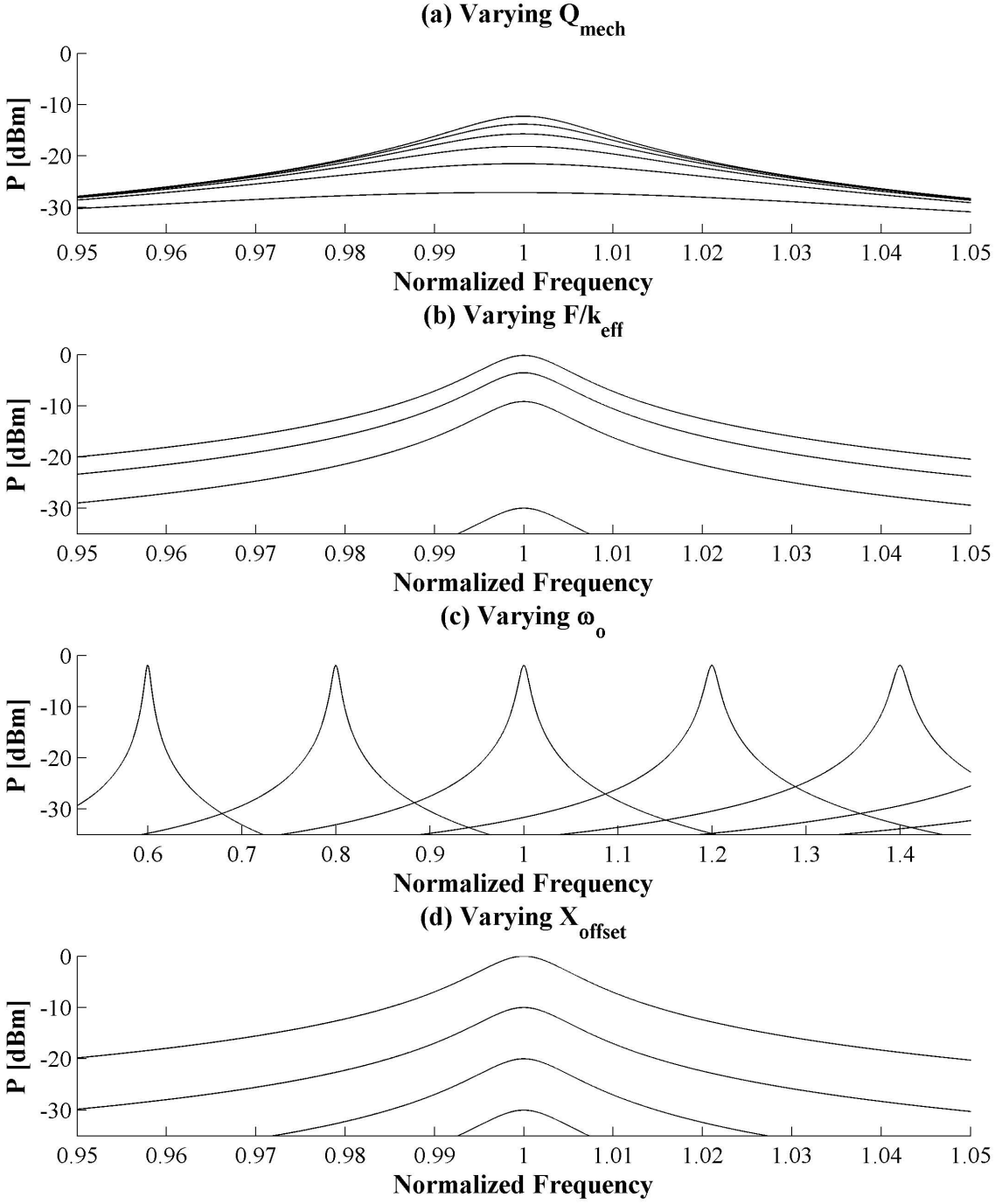

Figure 4.27: The first order harmonic oscillator model of Equation 4.31 versus the three fitting parameters as well as the conversion factor X_{offset}.

Wide Band Dynamics Model in the Finite Element Method

As shown in Figure 4.28 for the S2 P^{n}BG QC, a total harmonic force of $1\mu N$ is applied normal to each transducer electrode on the P^{n}BG QC. For the observation point depicted in Figure 4.28, the harmonic response over a frequency range from 0 Hz to 20 MHz is displayed in Figure 4.29 and Figure 4.30. The observation point is located on the transducer where electrical sensing may potentially be implemented for future work. The behavioral zone boundaries that are shown in Figure 4.7 are overlayed on Figure 4.29 where it may be observed that the $\hat{x}-$ and $\hat{y}-$ components of the displacement vector at the observation point display relatively small amplitude in zones I, II, V and VI and increased amplitude in zone III. The in-plane vibrational activity thus displays low and high cut-off frequencies.

In contrast, the $\hat{z}-$component of the displacement vector, which is the experimentally measured component, at the observation point displays resonant activity in zones I, II, III, IV and VI. This provides the first indication of how the band gap location may experimentally be measured, since the test equipment described in Chapter 6 can measure the $\hat{z}-$component of the displacement vector amplitude and the model suggests that the spectrum of the $\hat{z}-$component of the displacement vector contains the characteristic band gap signature: a lack of resonant peaks at band gap frequencies, while displaying resonant peaks at sub- and hyper-band gap branch frequencies.

The amplitude of the $\hat{x}-$ and $\hat{y}-$component of the displacement vector at hyper-band gap frequency zones V and VI is relatively small due to the FEM model result that many hyper-band gap modes are primarily composed of out-of-plane ($\hat{z}-$direction) vibration patterns as illustrated in Figure 4.17. While the harmonic response predicts a non-zero harmonic amplitude within the band gap zone IV, there is no resonant activity due to the absence of normal modes at band gap frequencies.

The Bode plot displayed in Figure 4.30 for the $\hat{z}-$component of the displacement vector at the observation point lacks phase changes at in-gap frequencies while 180^o phase changes are observed at each normal mode frequency. For the $1\mu N$ force amplitude the amplitude of the components of the displacement vectors are observed in Figure 4.30 to lie below $1nm$.

The relatively low amplitude of vibration observed in zones I and II for the $\hat{x}-$ and $\hat{y}-$ components, which are the components of the displacement vector which occur in the plane of periodicity of the P$^{\text{n}}$BG QC, displayed in Figure 4.29, resembles the low frequency cut-off that is observed for discretized P$^{\text{n}}$BG QCs in Figure I.3 of Appendix I and [86]. The locations of the low frequency cut-off in Figure 4.29 for the $\hat{x}-$ and $\hat{y}-$components of the displacement vector approximately coincide with the frequency in behavioral zone III where the P$^{\text{n}}$BG QCs start to display rotational modes, which are illustrated in Figure 4.17. Hence, the different behavioral zones appear to correspond to frequency regions where specific vibrational patterns occur in the mode shapes of the P$^{\text{n}}$BG QC and the behavioral zone boundaries may be identified in the harmonic response of the P$^{\text{n}}$BG QC.

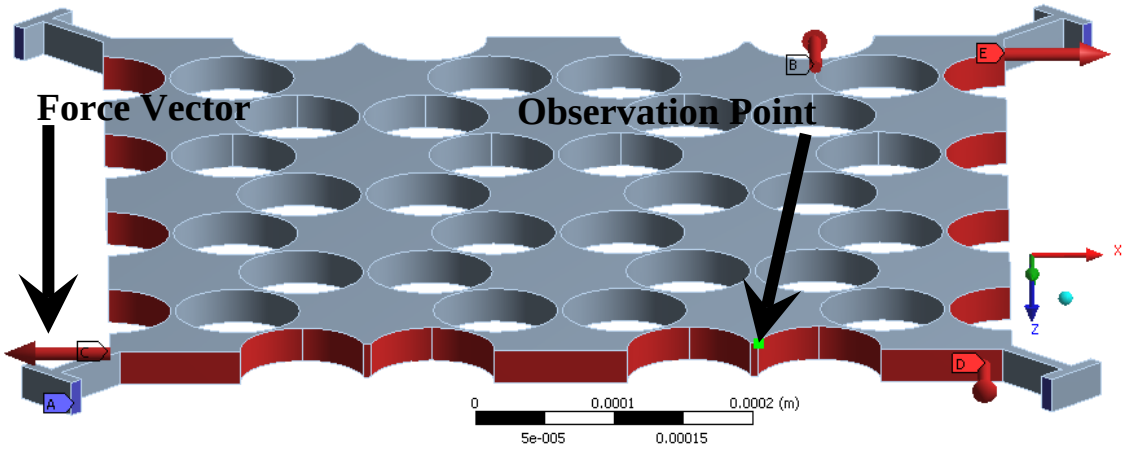

Figure 4.28: Point of observation for the harmonic response analysis conducted in this section on the S2 phononic band gap quasi-crystal. The harmonic response analysis is generated utilizing ANSYS® [121] with 2000 solution intervals and the mode superposition solution method. The finite element method mesh is comprised of 23188 nodes and 3362 elements.

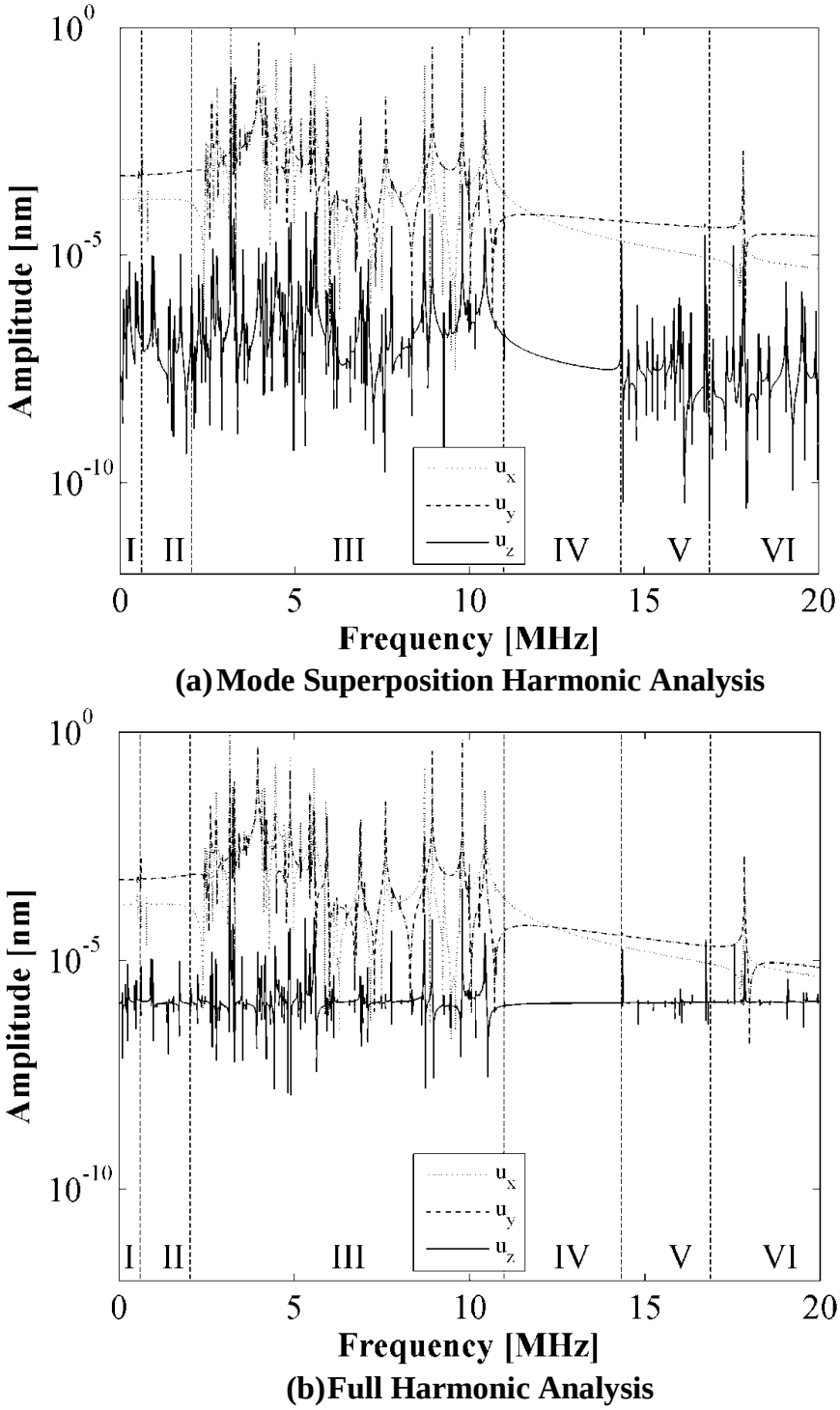

Figure 4.29: Harmonic response of the S2 phononic band gap quasi-crystal. The observation point is shown in Figure 4.28. Behavioral zones are labeled.

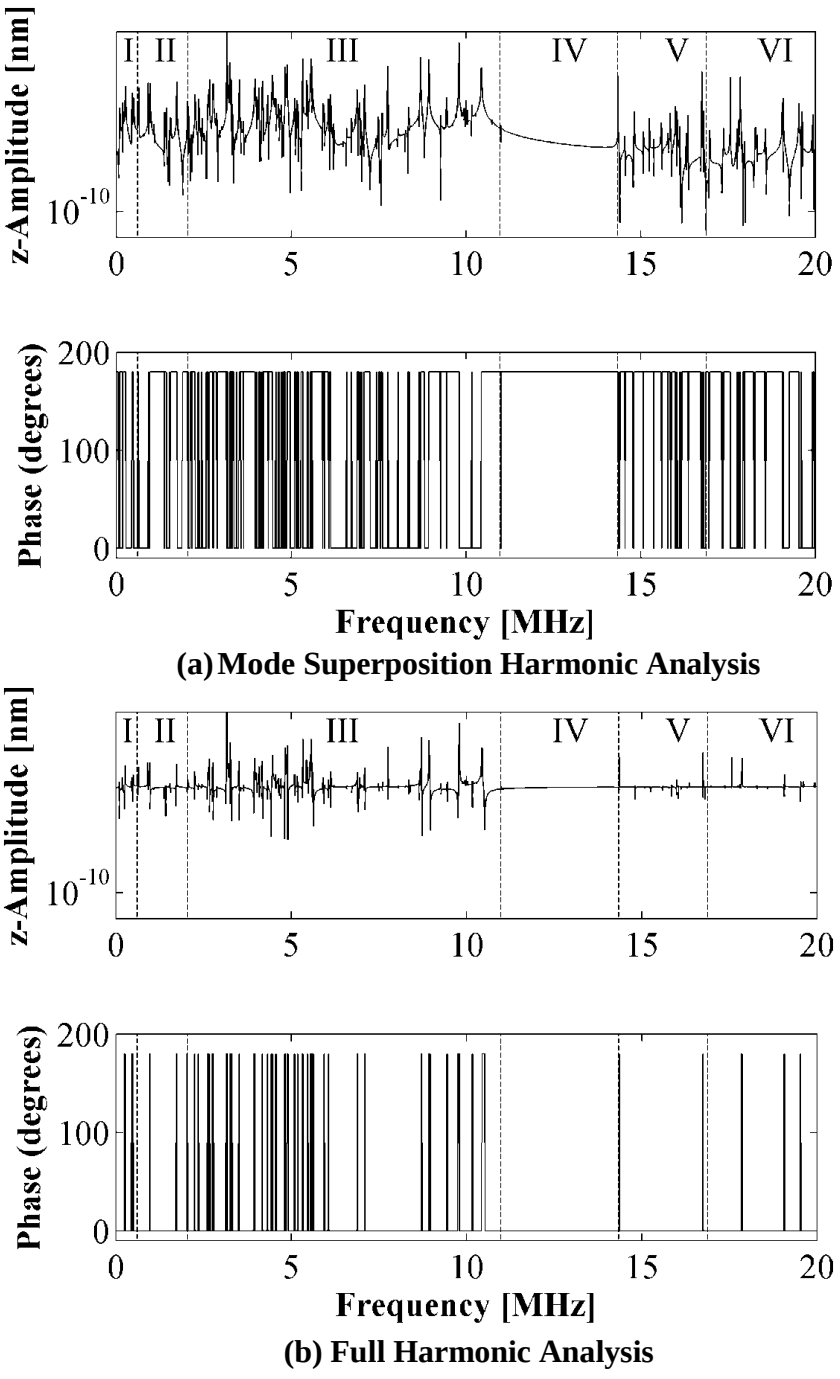

Figure 4.30: Bode plot of the S2 phononic band gap quasi-crystal. The observation point is shown in Figure 4.28. Behavioral zones are labeled.

4.2.6 Sensitivity Analysis

The lumped element semi-analytical analysis of Section 4.2.4 discussed the sensitivity of the P^{n}BG QC architecture to certain geometrical parameters such as lattice constant, a, and inclusion spacing, s. This section presents an exhaustive numerical sensitivity analysis with respect to geometrical parameters and material properties. This sensitivity analysis will serve to provide additional physical insight into the operation of the P^{n}BG QC architecture as well as insight regarding how the P^{n}BG QCs may respond to fabrication process variations. It will be observed in the FEM model of this section that hyper-band gap modes are more sensitive, relative to sub-band gap modes, to variations in material properties and geometrical parameters.

Material Properties

A sensitivity analysis for the S2 P^{n}BG QC is presented here versus the material properties of Poisson ratio, ν, Young's modulus, E, and mass density, ρ, which are varied about the a nominal value of $\nu = 0.29$, $E = 180GPa$ and $\rho = 2.330kg/m^3$, respectively. To investigate the worst case scenario, the material parameters are varied over a range that exceeds the range that may occur due to process variations in practice. The Poisson ratio is physically bounded between -1 and 0.5 and was varied from 0.09 to 0.49 and results are shown in Figure 4.31. Young's modulus is swept from 100 GPa to 260 GPa, results are displayed in Figure 4.32. The material density is varied from $1530kg/m^3$ to $3130kg/m^3$ with results shown in Figure 4.33.

As may be observed in Figure 4.32, increasing Young's modulus, E, increases the stiffness of the P^{n}BG QC and increases the band gap center frequency. From Figure 4.31, increasing the material density, ρ, appears to cause the mass of the P^{n}BG crystal to increase and the band gap center frequency to decrease. Figure 4.33 appears to

indicate that relative to hyper-band gap modes, sub-band gap modes appear less sensitive to variations in the Poisson ratio. Even for the extreme material property variations observed here, the band gap does not close and remains within the frequency range of 0 to 20 MHz which is measurable by the vibrometer.

Circular Inclusion Spacing and Radius and Truncation Geometry

Figure 4.34 displays the FEM model of band gap extent for square (solid line) and circular (dotted line) truncation geometries, where the inclusion spacing, s, is varied from $2\mu m$ to $4\mu m$, and the inclusion radius, r, is varied from $30\mu m$, to $60\mu m$. The square and circular truncation geometry diameters are $d = 650\mu m$ and $d = 575\mu m$, respectively. Plate thickness, t, is $25\mu m$ is held constant. Complete band gaps are observed within 5 to 30 MHz. Band gap center frequency and extent increase as circular inclusion radius and spacing decrease. The results illustrate that for wide variations in geometrical parameters, the band gap does not close and remains within the frequency range of 0 to 20 MHz which is measurable by the vibrometer.

Plate Thickness

P^{n}BG QC plate thickness, t, was varied from 15 to 35 about the nominal single-crystal-silicon layer thickness of 25. Fabrication process tolerances for the single-crystal-silicon layer thickness are ± 1 and so the range of thicknesses, t, examined here exceeds the worst case scenario that may occur due to process variations. As observed in Figure 4.35, the band gap is observed to close when plate thickness was reduced to 10; however, the band gap appears to remain open for the small thickness variations that may be produced by fabrication tolerances. As thickness is varied, the maximum sub-band gap mode frequency varies by approximately 2 MHz while the lower hyper-band gap mode

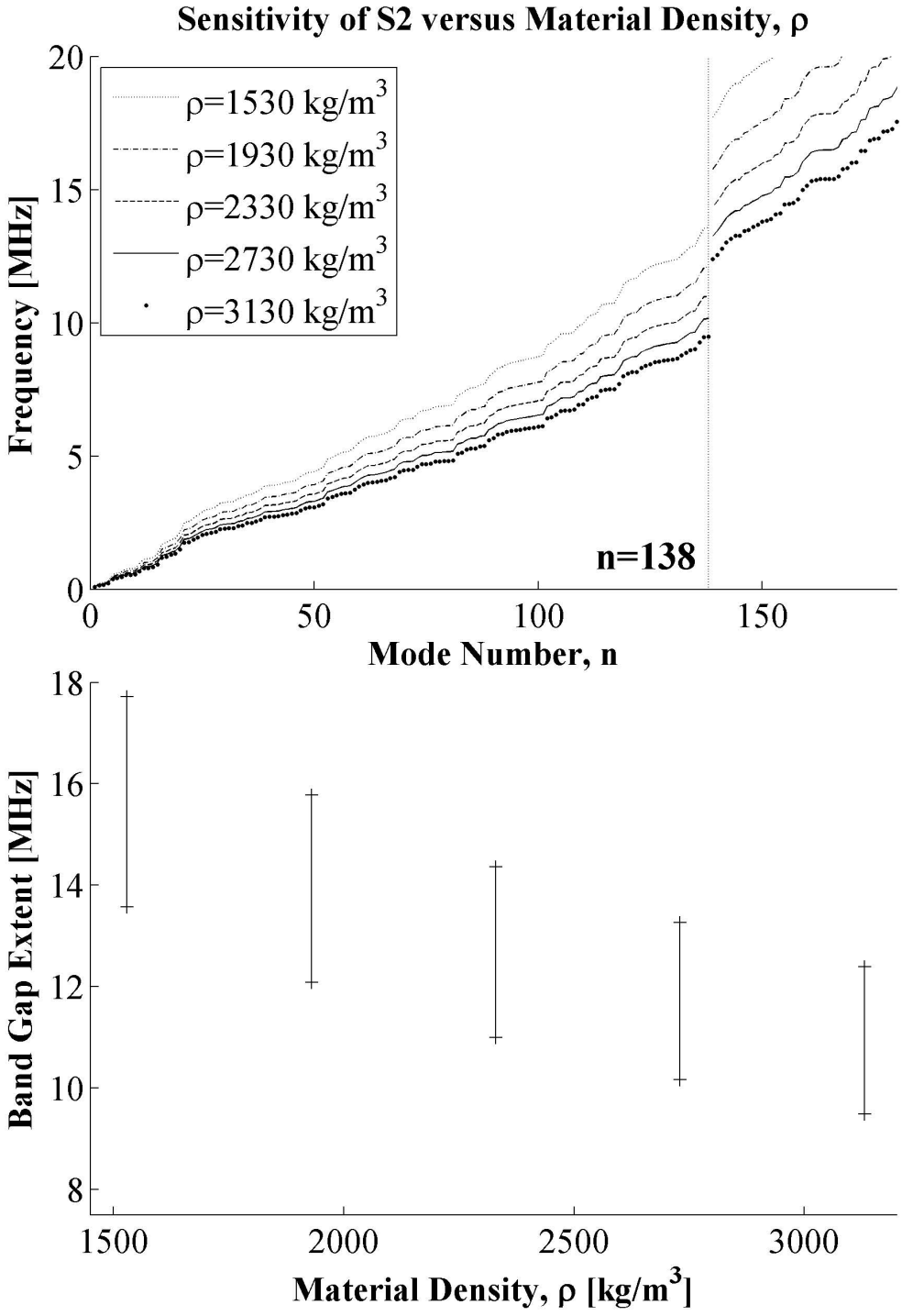

Figure 4.31: Sensitivity analysis of the S2 phononic band gap quasi-crystal versus material density, ρ. The finite element mesh contains 23,188 elements and 3,362 nodes. The geometrical parameters of the S2 phononic band gap quasi-crystal are contained in Table 3.1 and Table 3.2.

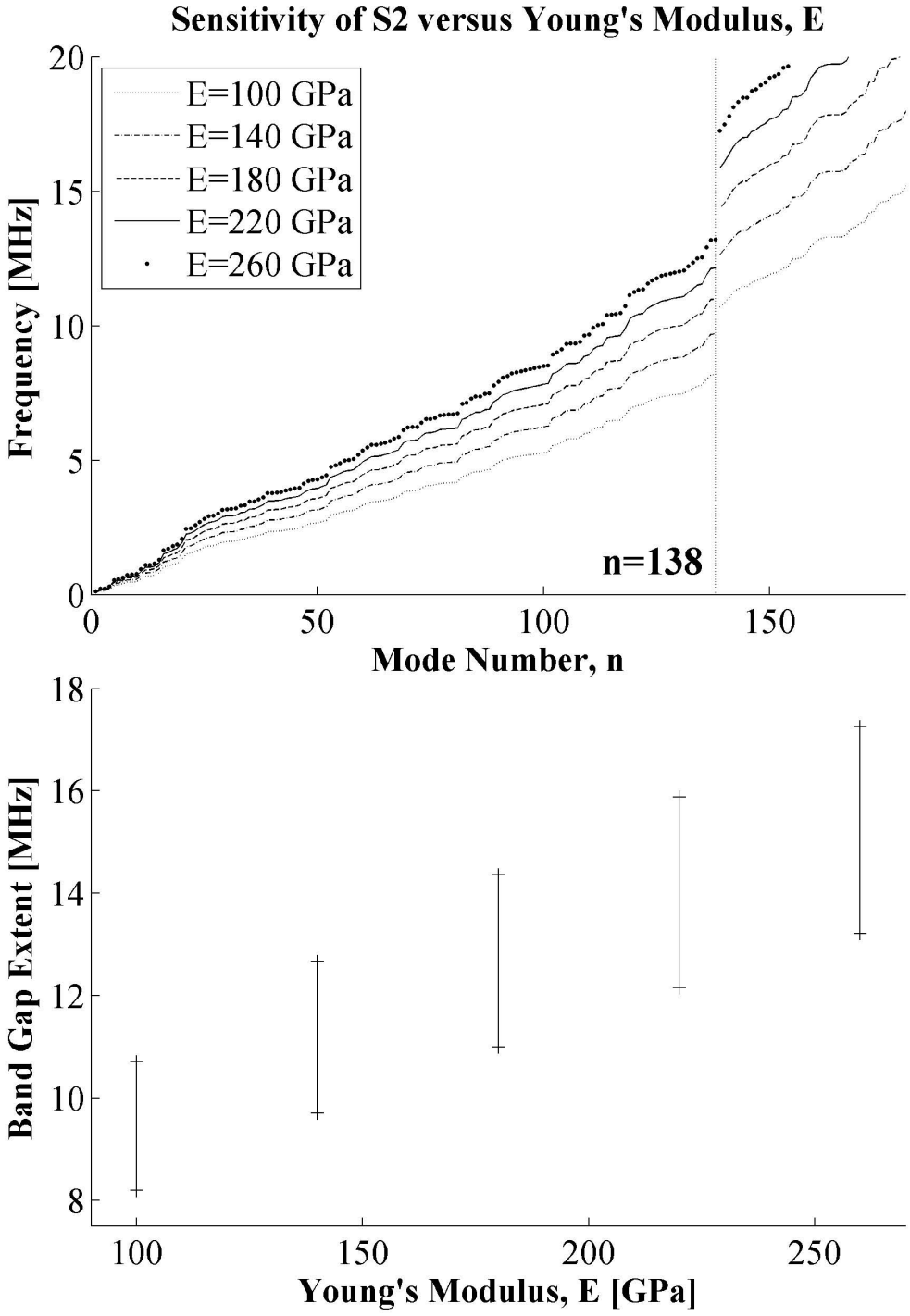

Figure 4.32: Sensitivity analysis of the S2 phononic band gap quasi-crystal versus Young's modulus, E. The finite element mesh contains 23,188 elements and 3,362 nodes. The geometrical parameters of the S2 phononic band gap quasi-crystal are contained in Table 3.1 and Table 3.2.

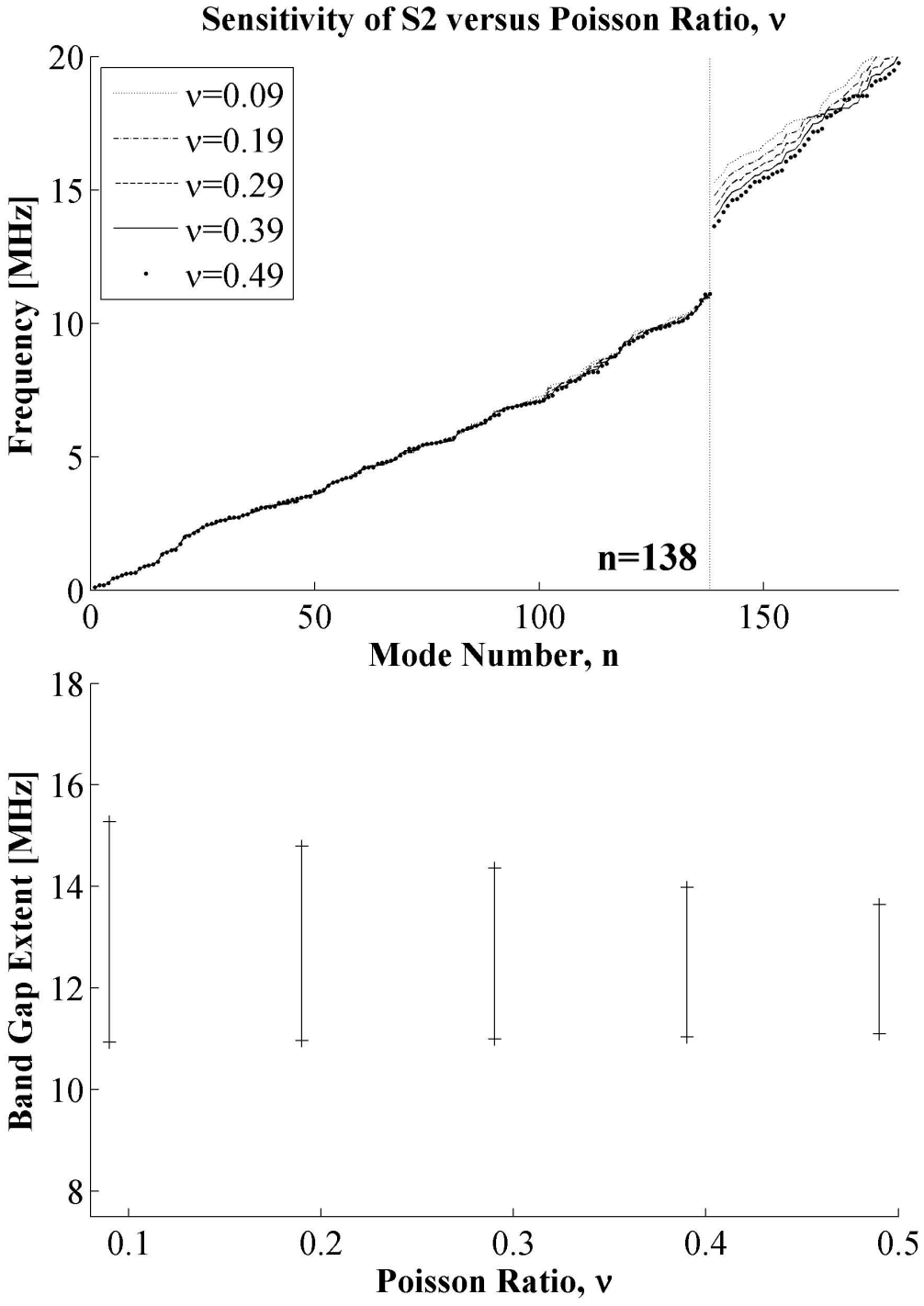

Figure 4.33: Sensitivity analysis of the S2 phononic band gap quasi-crystal versus Poisson ratio, ν. The finite element mesh contains 23,188 elements and 3,362 nodes. The geometrical parameters of the S2 phononic band gap quasi-crystal are contained in Table 3.1 and Table 3.2.

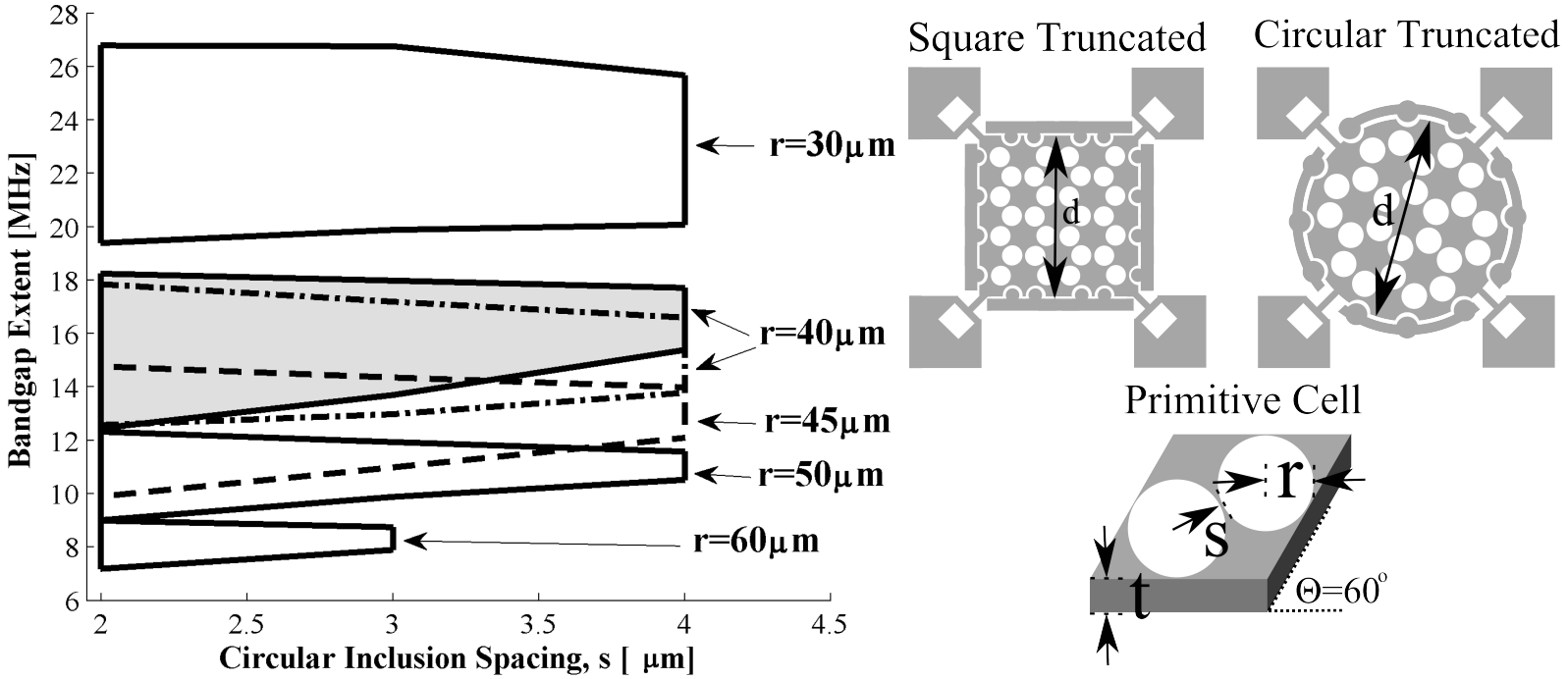

Figure 4.34: Sensitivity analysis of the phononic band gap quasi-crystal architecture band gap extent versus circular inclusion spacing and radius, s and r, and square and circular truncation boundary geometry. The finite element mesh contains 23,188 elements and 3,362 nodes. The square truncation (solid line) diameter is fixed at $d = 650\mu m$. The circular truncation (dotted line, shaded area) diameter is fixed at $d = 575\mu m$. Plate thickness, t, is fixed at $25\mu m$.

frequency varies by more than 6 MHz. Thus, relative to sub-band gap modes, hyper-band gap modes may be observed to be more sensitive to variations in thickness, t. This may be expected as the majority of hyper-band gap modes are out-of-plane modes whose out-of-plane compliance and thus frequency appear to be strongly dependent on plate thickness, t, in the out-of-plane direction (as discussed in Section 4.2.4).

Truncation Diameter

The truncation boundary diameter, d, was varied and results are displayed in Figure 4.37. As truncation diameter, d, increases the number of sub-band gap modes may be observed to increase approximately according to Equation 4.15 since the number of sub-band gap masses increases with d, while the band gap frequencies appear to remain approximately constant. Hence, the average density of sub-band gap modes, $\rho_{SBGM,avg}$, increases as the truncation diameter, d, increases. Figure 4.38 displays the density of states (DOS, refer to Appendix C for a definition) for each truncation diameter. It may be observed that up to a truncation diameter of $d = 880\mu m$ the average DOS increases for sub-band gap modes. However, the average DOS decreases for a truncation diameter of $d = 950\mu m$ which may be due to a change in the shape of the frequency versus mode number characteristic as the truncation diameter approaches larger values.

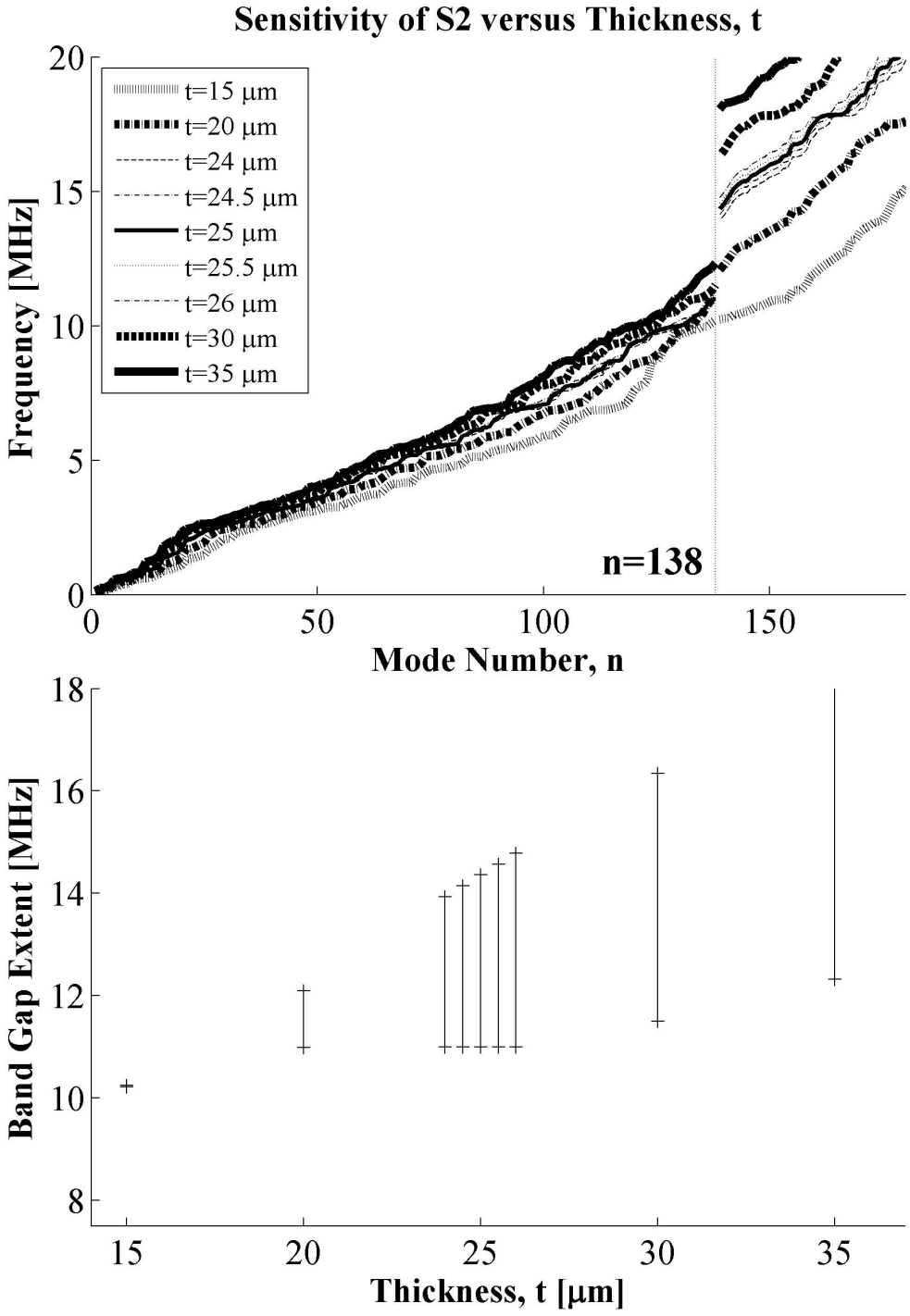

Figure 4.35: Sensitivity analysis of the S2 phononic band gap quasi-crystal (see Tables 3.1 and 3.2 for geometrical parameters) versus plate thickness, t. The finite element meshes contains approximately 30,000 elements.

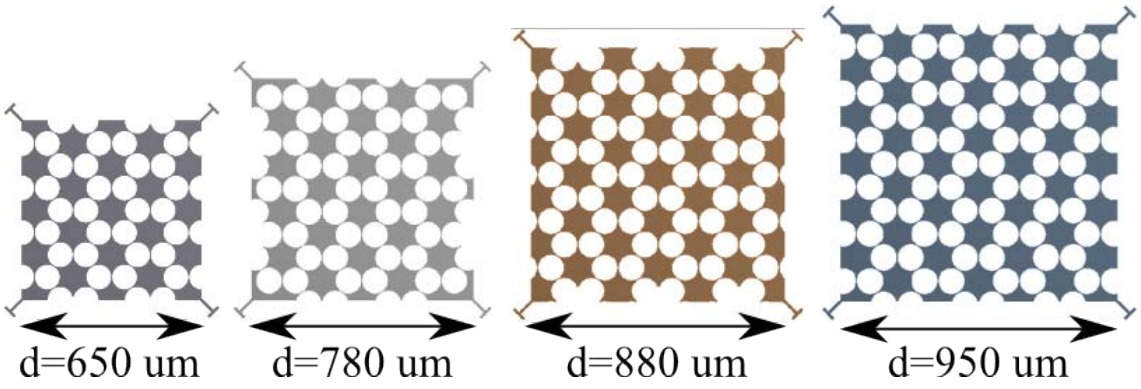

Figure 4.36: Solid models for the sensitivity analysis of the S2 phononic band gap quasi-crystal versus truncation diameter, d.

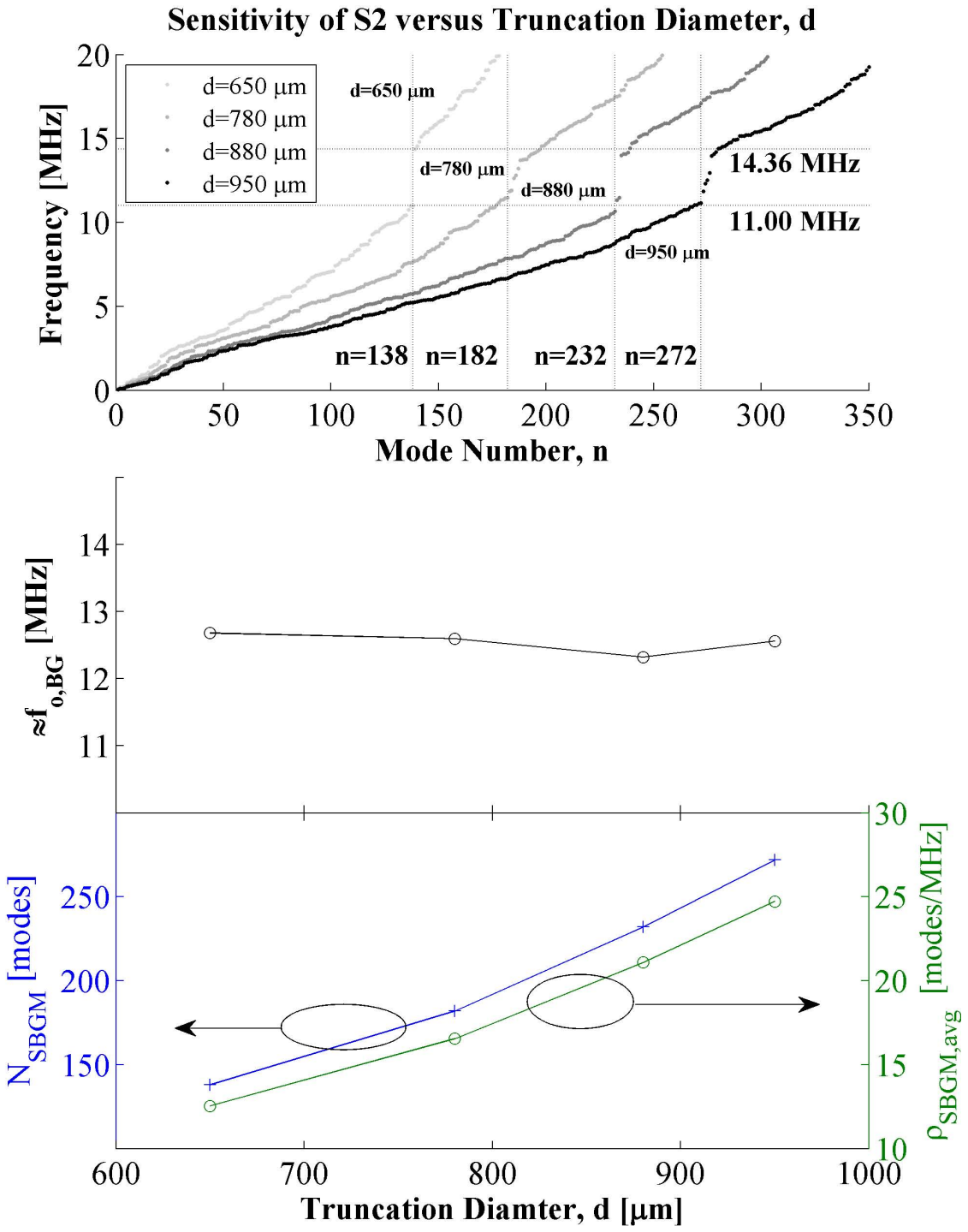

Figure 4.37: Sensitivity analysis of the S2 phononic band gap quasi-crystal versus truncation diameter, d (see solid models of Figure 4.36). The approximate band gap center frequency is denoted as $\approx f_{o,BG}$. The number and average density of sub-band gap modes are denoted as N_{SBGM} and $\rho_{SBGM,avg} = N_{SBGM}/11MHz$.

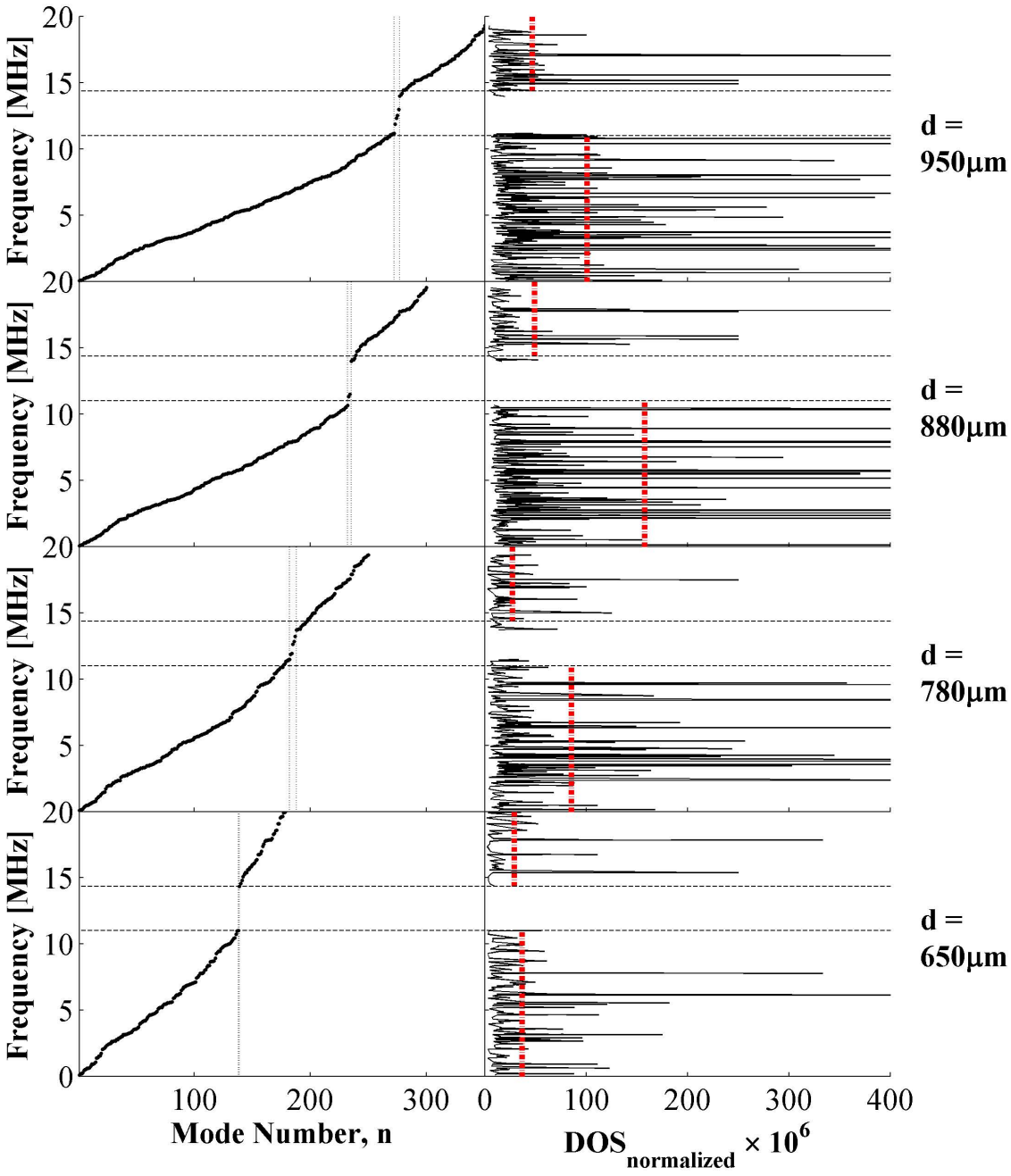

Figure 4.38: Sensitivity analysis of the S2 phononic band gap quasi-crystal density of states (DOS) versus truncation diameter, d. The phononic band gap quasi-crystal solid models are depicted in Figure 4.36. The average DOS in each branch is indicated by the thick vertical dotted line in the plot of $DOS_{normalized}$. The DOS is not computed within band gap frequencies (though some phononic band gap quasi-crystals display defect states and so could display a non-zero DOS at in-gap frequencies).

4.3 Electromechanical Coupling of Electrical and Phononic Band Gap Quasi-Crystal Model

Utilizing the MemMech^{TM} solver in CoventorWare® 2010, a coupled electrostatic-mechanical analysis is performed to determine the static displacement of the S2 P^{n}BG QC for a static transducer voltage. The intent to is quantify the ability of the electrostatic transducers to couple energy, between the electrical and mechanical energy domains, via a static electromechanical coupling coefficient. The static electromechanical coupling coefficient may, for low electrical signal frequencies, provide insight into the required electrical signal that is needed to generate a displacement that lies within the range that is measurable by the vibrometer test equipment (which is discussed within Section 6.1). The MemElectro^{TM} solver in CoventorWare® 2010 is then utilized to quantify the capacitance and electrostatic forces generated by the electrostatic transducers, which will be shown to display reasonable agreement with the analytical models of Section 4.1. Lastly, the utility of a coupled electrostatic-mechanical transient analysis is discussed to model the potential frequency dependency of the electromechanical coupling coefficient.

An FEM model was chosen in favor of an analytical or semi-analytical approach for determining the electromechanical coupling coefficient in part due to the uncertainty indicated by the relatively large error observed in Section 4.2.4 for one semi-analytical approach. Moreover, as shown in Section 4.2.4, when the P^{n}BG QC is modeled as a lumped element system, the mass elements appear to display six DOF, which may lead to a prohibitively complex analytical or semi-analytical model. A coupled electrostatic-mechanical and electrostatic FEM model can be readily implemented utilizing CoventorWare® 2010, while the ANSYS® Multi-Physics FEM implementation

could potentially also be utilized.

Within CoventorWare® 2010 the Young's modulus, Poisson ratio, and material density of the SOI layer out of which the P^{n}BG QCs are fabricated are $E = 169GPa$, $\nu = 0.290$, and $\rho = 0.0025kg/m^3$, respectively. For the SOI layer, the electrical conductivity is $2mS/\mu m^2$ and dielectric constant is $\epsilon = 11.9$. The medium surrounding the SOI layer and within the electrostatic transducer gap is assigned a dielectric constant of unity.

Within CoventorWare® 2010 a FEM mesh was created for the S2 P^{n}BG QC utilizing tetrahedron shaped elements, the order of the elements is parabolic, element size is $12.5\mu m$ and the resultant FEM mesh has 46,253 elements. The MemMech^{TM} solver was utilized to perform a static analysis to determine the magnitude of the mechanical displacement of the P^{n}BG QC for a DC voltage of 100 V, which is the typical DC bias voltage utilized during experiments. The static analysis provides the mechanical displacement at the equilibrium which occurs when the external electrostatic forces, encapsulated in the vector F, acting on each node in the FEM mesh are in balance with the internally generated forces, Ku, at each node in the FEM mesh resulting in a net force of zero [128]:

$$\begin{aligned} F_{net} &= F_{internal} - F_{external} \\ &= k\vec{u} - F_{external} \\ &= 0 \end{aligned} \tag{4.33}$$

where k is a square matrix containing the stiffness of each element in the FEM mesh and $\vec{u}$ is a vector containing the displacements at each node in the FEM mesh [128]. The result of the static analysis is contained in Figure 4.39. The FEM model indicates a maximum displacement magnitude in the $\hat{x}$, $\hat{y}$, and $\hat{z}$-directions of $22.810nm$, $35.057nm$,

and $1.361nm$, respectively, and a maximum total displacement magnitude of $35.474nm$. These values lie within the measurable range of $\pm 75nm$ [129] (as discussed within Section 6.1) for the vibrometer that will be utilized to experimentally characterize the out-of-plane ($\hat{z}$) component of the P^{n}BG QC device displacement amplitude. These values also indicate that for the S2 P^{n}BG QC, for a 100 V DC bias voltage, the electromechanical coupling coefficient between the four electrostatic transducers and the point at which the maximum $\hat{z}$-direction amplitude of $1.361nm$ occurs is $K_{elec-mech}(u_{z,max}, 100VDC) = 1.361m/100V = 13.61pm/V$.

With respect to the S2 P^{n}BG QC, for the electrode with widely spaced inclusions, the MemElectro^{TM} solver was utilized to determine the capacitance to be $91.134fF$, which is in reasonable agreement with the capacitance of $89.178pF$ from the analytical model in Table 4.2. For the same electrode, MemElecro^{TM} indicates the attractive force applied to the P^{n}BG QC side of the electrostatic transducer in the $\hat{x}$-direction (see Figure 4.39) to be $109.641\mu N$ which is in reasonable agreement with the attractive force of $110.779\mu N$ from the analytical model of Table 4.2. Similarly, MemElecro^{TM} indicates the electrostatic forces in the direction parallel to the length of the transducer (the $\hat{y}$ in Figure 4.39) and out-of plane direction ($\hat{z}$-direction in Figure 4.39) to be approximately $1.526\mu N$, and $0.090\mu N$, respectively. Hence, MemMech^{TM} indicates the electrostatic force is orders of magnitude larger in the $\hat{x}$-direction than in the $\hat{y}$-direction and four orders of magnitude larger in the $\hat{x}$-direction than in the $\hat{z}$-direction. Thus, the FEM model suggests that as desired for this electrode, despite the non-planar geometry of the transducer electrodes with widely spaced inclusions, the dominant electrostatic force is the force in the $\hat{x}$-direction (perpendicular to the edge of the P^{n}BG QC), which is also the assumed direction of the force in the dynamic harmonic model of Section 4.2.5. This analysis may be applied to the transducer with closely spaced inclusions on the square

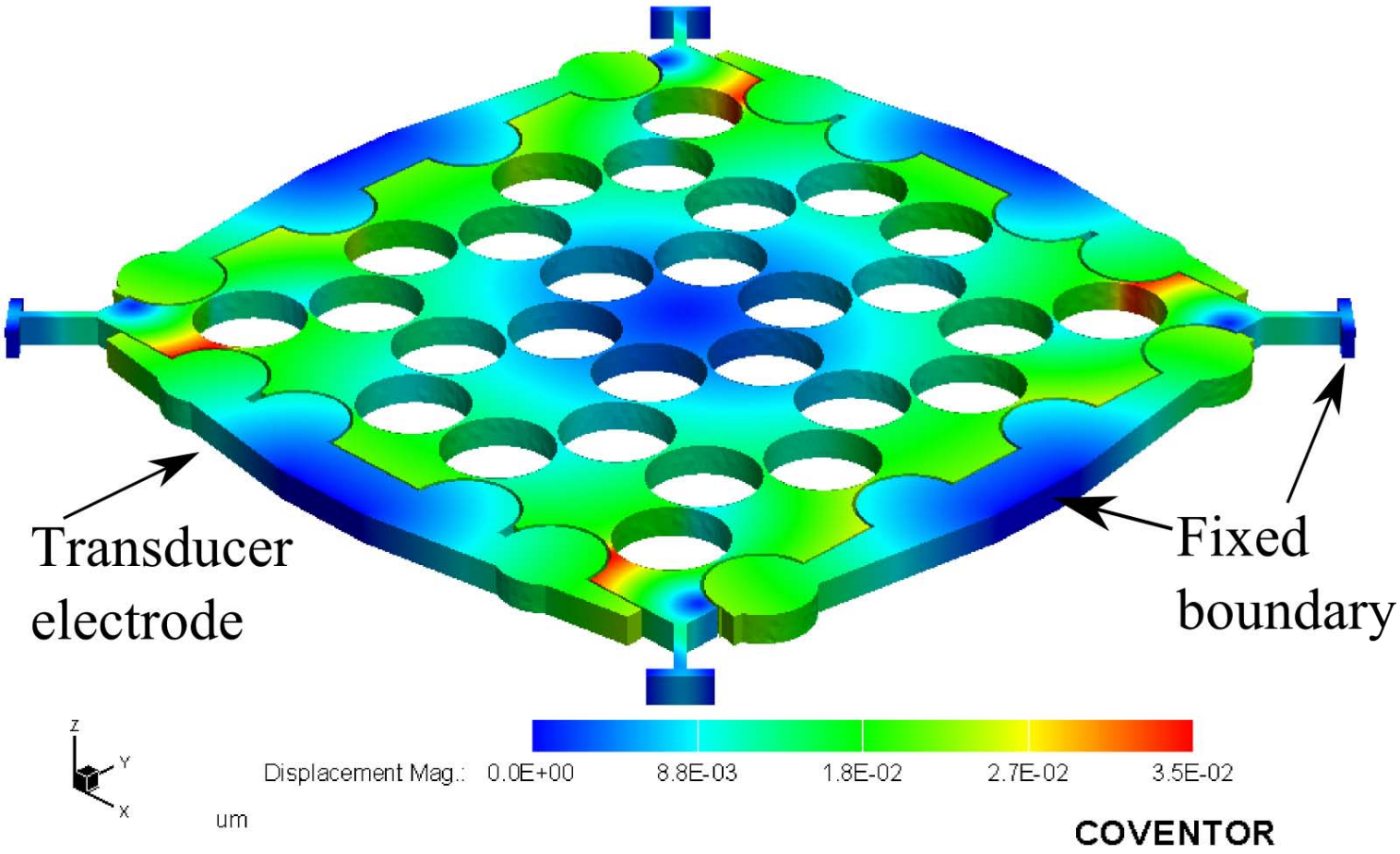

Figure 4.39: Coupled electrostatic-mechanical finite element method model of the static displacement of the S2 phononic band gap quasi-crystal for a DC bias of 100 V. The surface within each transducer gap has a potential surface boundary condition applied, with a DC voltage of 100 V, and 0 V, on the potential surface on the fixed electrode, and phononic band gap quasi-crystal-side electrode, respectively. The maximum, and minimum, magnitude of displacement is $0.035\mu m$ (red), and $0\mu m$ (blue), respectively.

truncated P^{n}BG QCs to determine whether the transducers with widely spaced and closely spaced inclusions impart electrostatic forces with relatively comparable magnitudes. A similar analysis may be performed for the circular truncated P^{n}BG QCs.

As mentioned above, the preceding static analysis assumes that sufficient time has elapsed to allow the P^{n}BG QC and transducers to settle into an equilibrium position where external and internal forces balance. When the external forces (in this case, the electrostatic forces generated by the transducers) vary with respect to time such that mechanical equilibrium does not occur before the transducer force changes, the motion of the P^{n}BG QC should be studied utilizing a transient analysis. In the transient analysis, the inertia ($m\frac{\partial^2 u}{\partial t^2}$) and internal damping of the P^{n}BG QC are included in the equation of motion [130]:

$$\begin{aligned} F_{net} &= m\frac{\partial^2 u}{\partial t^2} + F_{internal} - F_{external} \\ F_{net} &= m\frac{\partial^2 \vec{u}}{\partial t^2} + \gamma\frac{\partial \vec{u}}{\partial t} + k\vec{u} - F_{external} \\ &= 0 \end{aligned} \tag{4.34}$$

where m, γ, k, t, $\vec{u}$ represent mass, damping coefficients, stiffness, time, and displacement, respectively [130]. Under transient conditions, the electrostatic transducer forces interact with the adjacent edges of the P^{n}BG QC, which after some time delay will in turn be mechanically coupled to the regions internal to the P^{n}BG QC, and so forth. The coupling between the electrostatic force and displacement of the P^{n}BG QC will be a function of the time and the position at which the displacement is being observed within the P^{n}BG QC. The transient analysis may provide data regarding the potential dependency of the electromechanical coupling coefficient on frequency, DC bias voltage, inertia and damping within the P^{n}BG QC. Non-linear effects associated with the electrostatic forces generated by the transducers, which resemble parallel plate capacitors

[97], may also be observable.

The P^{n}BG QCs will be experimentally characterized over a frequency range from 5 kHz to 20 MHz. At frequencies near 20 MHz, the P^{n}BG QCs may have the greatest tendency to display distributed mechanical system behavior (see Section 4.2.4) for which a transient analysis may become necessary. If the predicted displacement is relatively small, the noise floor of the vibrometer and noise bandwidth of the spectrum analyzer may also be may also be considered in order to predict whether a measurable time harmonic displacement amplitude may be produced. Alternatively, time varying effects may provide a higher force, due to a higher rate of flux change, and potentially higher displacement than the static analysis predicts. Transient and noise floor analysis may be further investigated.

Prior to the development of the P^{n}BG QC architecture proposed within the body of this thesis, a prototype P^{n}BG QC was fabricated to develop insight into the electrostatic actuation of P^{n}BG QCs and models and measurements are presented in Section J.1 of Appendix J.

Chapter 5

Fabrication of Phononic Band Gap Quasi-Crystal Architecture in a 25 μm Silicon on Insulator Process and Test Fixture Assembly

The P^{n}BG QCs are fabricated in the three layer SOIMUMPs Silicon on Insulator (SOI) bulk micromachining process, which utilizes a $25\mu m$ thick single-crystal-silicon (also referred to as monocrystalline silicon) layer named Silicon, $1\mu m$ oxide layer named Oxide, metal layer named Metal and a $400\mu m$ substrate. A cross section of the three layers is depicted in Figure 5.1. With the exception of the Metal layer, the SOIMUMPs layers already exist on SOI wafers. The Metal layer is used for electrical contacts. The SOIMUMPs process first dopes, patterns and etches the silicon layer through to the oxide layer [115]. The substrate can be backside etched through to the oxide layer to release structures [115]. A shadow-masked metal process provides the course Metal

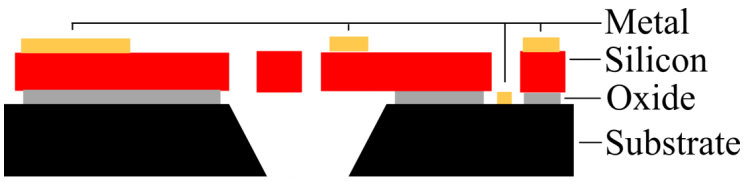

Figure 5.1: Cross sectional view showing three layers of the SOIMUMPs process [115].

features [115].

The top surface of the single-crystal-silicon layer is the (100) plane [131]. The $\langle 110 \rangle$ single-crystal-silicon-cubic crystal crystallographic axes align with the $\hat{x}$- and $\hat{y}$-axis of the P$^{\text{n}}$BG QC mask layout. The material properties of single-crystal-silicon are anisotropic. Young's modulus, E, and the Poisson ratio, $\nu_{\perp}$, are maximum in $\langle 110 \rangle$ directions and minimum in $\langle 100 \rangle$, $\langle 010 \rangle$ and $\langle 001 \rangle$ directions. The Poisson ratio, $\nu_{\parallel}$, is minimum in $\langle 110 \rangle$ directions and maximum in $\langle 100 \rangle$, $\langle 010 \rangle$ and $\langle 001 \rangle$ directions. Hence, the Young's modulus, E, and poisson ratio, $\nu_{\perp}$, display their maximum value in both the $\hat{x}$- and $\hat{y}$-directions of the P$^{\text{n}}$BG QC mask layout. The aforementioned anisotropy of single-crystal-silicon has the effect of extending the size of the first Brillouin zone of the P$^{\text{n}}$BG QC as described in Figure 5.2.

For traveling wave devices, the traveling wave should be directed in a minimum dispersion (velocity) direction, which is the direction for which $\frac{\delta c}{\delta \Theta} = 0$, where c is the anisotropic elastic wave velocity, since waves otherwise would naturally tend to redirect themselves into the lowest velocity direction [37]. The minimum dispersion directions for single-crystal-silicon include the [100] and [010] directions [132]. The [100] and [010] directions on the single-crystal-silicon layer in SOIMUMPs are oriented at 45^{o} to the $\hat{x}$- and $\hat{y}$ axes of the mask set [131]. Since the P$^{\text{n}}$BG QC architecture is utilized in a standing wave configuration, elastic waves are not launched in, or sensed from, a particular direction and so the minimum dispersion direction may be acknowledged for

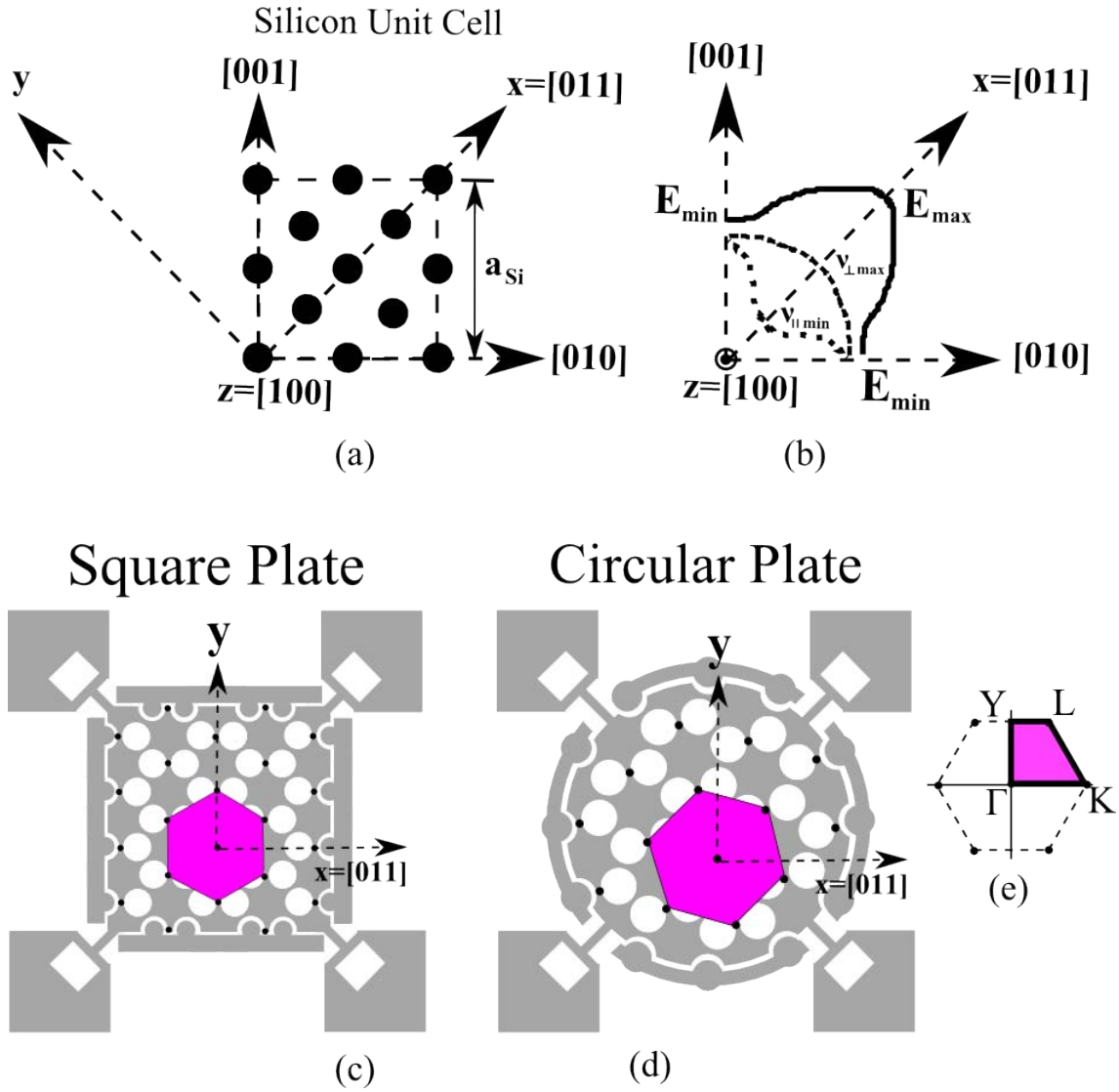

Figure 5.2: Mapping of the first Brillouin zone of the phononic band gap quasi-crystal architecture given the top surface is the (100) plane of single-crystal-silicon (SCS). (a) View of the SCS unit cell looking down at the (100) plane with crystallographic axes and $\hat{x}$- and $\hat{y}$-directions of the device layout. (b) Stylized illustration of the variation of Young's modulus, E, and poisson ratio, ν, versus direction within the SCS unit cell [132]. The hexagonal shape of the first Brillouin zone of the hexagonal lattice overlayed on the square (c) and circular (d) truncated architecture. The first irreducible Brillouin zone for an isotropic host material would be a wedge that is one-twelfth of the first Brillouin zone shown in (c) and (d). (e) The first irreducible Brillouin zone of the phononic band gap quasi-crystal architecture after accounting for the anisotropy of the SCS host material.

future implementations where traveling waves may be employed as the energy carrier within the P^{n}BG QC architecture.

In circuit design, often the response of a circuit can be designed to depend on the ratio of two device parameters, in which case if there is a systematic process error in either of these device parameters the ratio of these parameters will still remain approximately the same, and so the device response is desensitized to systematic process errors. In contrast, the P^{n}BG QC architecture may be based on the absolute value of device dimensions, as oppose to a ratio of device dimensions. Thus, the P^{n}BG QC architecture may be sensitive to process variations.

To account for the potential deviations between the model of Chapter 4 and experimental results of Chapter 6, the process errors that are present in the fabricated P^{n}BG QCs should be characterized. This chapter introduces the justification for the utilization of the SOIMUMPs process, characterization of process errors in the fabricated P^{n}BG QCs and the test fixturing of the chips that were fabricated utilizing the SOIMUMPs process.

5.1 SOIMUMPs Bulk Micromachining Fabrication Process

In this section, the primary motivation for choosing the SOIMUMPs process is provided and process design rule considerations and violations are presented. Due to the relatively unique structure of the P^{n}BG QCs, there was uncertainty in whether the P^{n}BG QC architecture would fabricate accurately.

Some of the features of the P^{n}BG QCs that were carefully considered before fabrication follow. The P^{n}BG QC architecture contains electrostatic transducer gaps between

surfaces that have multiple radii of curvature and need to be evaluated in the presence of photomask pixelation which may yield larger fabrication uncertainty between surfaces that have a smaller radii of curvature [115]. The P^{n}BG QC is several hundreds of microns in span, free standing, and comprised of relatively large regions that are interconnected by regions that have dimensions equal to the minimum feature size, so may appear relatively fragile. In addition, the tether geometry has to be tuned to ensure that no tether resonant defect states lie within the band gap while the tethers also meet the minimum anchor width requirements.

Moreover, to realize the P^{n}BG QC architecture requires a process that has a relatively high aspect ratio, which can be quantified as a low ratio of minimum feature size, s_{min}, to plate thickness, t, or low s_{min}/t. In Chapter 4, the P^{n}BG QC model indicated that to achieve the designed band gap location requires careful control over the plate thickness and inclusion (etch hole) spacing. As may be viewed in Table 3.1, the models of the P^{n}BG QC architecture fix the layer thickness at the design value of $25\mu m$ and in Table 3.2 the minimum, and maximum inclusion (etch hole) spacing are $2\mu m$, and $4\mu m$, respectively. Hence, for the devices listed in Table 3.1, the required minimum s_{min}/t is 2/25 or 0.08, while the maximum s_{max}/t is 4/25 or 0.16. Hence, the P^{n}BG QC architecture may not be realizable in an arbitrary fabrication process.

Table 5.1 list a few fabrication processes that are provided through CMC [114], and at the time were readily available to users at the University of Waterloo, along with their s_{min}/t ratios. As may be viewed in Table 5.1, the SOIMUMPs process with a single-crystal-silicon layer thickness of $25\mu m$ is the only process listed here that provides the required minimum s_{min}/t ratio of 0.08 needed for implementation of the P^{n}BG QCs that were designed in Chapter 4. Thus, there was motivation to fabricate the P^{n}BG QCs utilizing the SOIMUMPs process.

In addition, the SOIMUMPs process was also chosen for the natural properties, such as reduced substrate losses and parasitic capacitances, that SOI processes display. The single-crystal-silicon of the SOIMUMPs process may provide lower acoustic losses than polysilicon. The trench feature of the SOIMUMPs process provides a mechanism to eliminate loss due to air flow damping beneath the P^{n}BG QCs. The SOIMUMPs process is low cost for users at the University of Waterloo and high yield. Lastly, the elastic properties of the structural layers in SOIMUMPs have been well characterized [133] and provide a starting point for development.

Table 5.1: Available process options for the fabrication of the phononic band gap quasi-crystals. SOIMUMPs provides a single-crystal-silicon layer. PolyMUMPs provides polysilicon layers. The SOIMUMPs process with the $25\mu m$ thick single-crystal-silicon layer was chosen in-part since it appears to be the only process that provides a s_{min}/t ratio that is low enough to realize the phononic band gap quasi-crystal architecture.

Process	**Layer Thickness, t [μm] (Layer Name)**	**Minimum Feature Size, s_{min} [μm]**	**Ratio of s_{min}/t**
SOIMUMPs	25 (SOI)	2	0.08
SOIMUMPs	10 (SOI)	2	0.20
PolyMUMPs	1.5 (POLY1)	2	1.33
PolyMUMPs	2 (POLY2)	2	1.00

5.1.1 Intentional Process Design Rule Considerations and Violations

Many of the design rules of the SOIMUMPs process were followed to assist with successful fabrication. For example, due to photomask pixelation [115], in the relatively high curvature gaps of the electrostatic transducer, the suggested $3\mu m$ spacing was utilized instead of the minimum $2\mu m$ spacing, while for relatively low curvature gaps the $2\mu m$ spacing was utilized. Hence, SOIMUMPs was deemed suitable for fabrication of the unique electrostatic transducer geometry of the P^{n}BG QC architecture.

In addition, the minimum anchor width for the SOI layer is $10\mu m$. The tethers which were designed to display local resonance at hyper-band gap frequencies were further increased in width to approximately satisfy the minimum anchor size requirement by making the drawn width of the T-shaped anchors that contact the anchor pad approximately $9.899\mu m$.

To obtain sufficient in-gap attenuation, a two-dimensional P^{n}BG crystal should be a minimum of five lattice constants in length and width [11]. For the case of the P^{n}BG QC architecture proposed here, with an average lattice constant of $161\mu m$, a fabrication process is needed with the capability to produce a free-standing structure that is approximately $161\mu m \times 5 = 805\mu m$ in dimension, which may be satisfied by the SOIMUMPs process which provides an unlimited maximum feature length for structures that have a width greater than $6\mu m$.

The maximum feature length of the gold metal layer (named Metal) utilized in the SOIMUMPs process is $5000\mu m$, which exceeds the maximum size of the proposed P^{n}BG QC devices and so is more than suitable for fabricating the P^{n}BG QC devices.

The photomasks utilized in the SOIMUMPs process have a resolution of $0.25\mu m$ and the SOIMUMPs design handbook suggests that features and spaces that are non-orthogonal should be drawn with a size or spacing of $3\mu m$ instead of the minimum $2\mu m$ [115]. Since the inclusions in the P^{n}BG QC proposed here are circular and so non-orthogonal features, the SOIMUMPs design handbook appears to suggest to utilize a minimum spacing of $3\mu m$ between inclusions. This suggested practice was avoided for the P^{n}BG QC with a $2\mu m$ inclusion (etch hole) spacing and it was found that the SOIMUMPs process can successfully fabricate this structure. P^{n}BG QCs with a $3\mu m$ and $4\mu m$ inclusion (etch hole) spacing were also sent for fabrication, these structure don't appear to conflict with the SOIMUMPs design rules. The P^{n}BG QC architecture

may also potentially be fabricated in other high aspect ratio processes, such as the Micragem^{TM}[134] SOI process.

5.2 Wafer Level Characterization of Fabricated Phononic Band Gap Quasi-Crystals

The P^{n}BG QCs that were fabricated were characterized utilizing Scanning Electron Microscopy (SEM) and surface metrology characterization utilizing an optical profilometer.

5.2.1 Scanning Electron Microscopy Characterization

Utilizing the Hitachi S-3000N scanning electron microscope depicted in Figure 5.3, scanning electron micrograph images were obtained for the P^{n}BG QC and reference devices, described in Table 3.1, which were fabricated utilizing SOIMUMPs [47]. Figures 5.4 and 5.5 depict the S1 and C1 P^{n}BG QCs, respectively. Additional SEM images of the fabricated P^{n}BG QC and reference devices may be viewed in Appendix E.

The SEM images of Figures 5.4 and 5.5 and Appendix E indicate an overall successful fabrication of the proposed P^{n}BG QCs utilizing SOIMUMPs. Visual inspection of the SEM images suggest the electrostatic transducer gaps are present without any bridging of the electrodes and so the use of $3\mu m$ gap sizes in areas of high curvature appears to be successful. The $3\mu m$ gap sizes in the gaps of high curvature may potentially be reduced to $2\mu m$. The S1 and C1 P^{n}BG QCs, that have an inclusion (etch hole) spacing equal to the minimum feature size, are intact. Anchored tethers appear to be in tact and the P^{n}BG QCs appear to be free-standing. Further inspection of the fabricated devices was performed utilizing an optical profilometer, which allows for more

Figure 5.3: Hitachi S-3000N scanning electron microscope utilized to characterize the phononic band gap quasi-crystal and reference devices described in Table 3.1 fabricated in the SOIMUMPs [47].

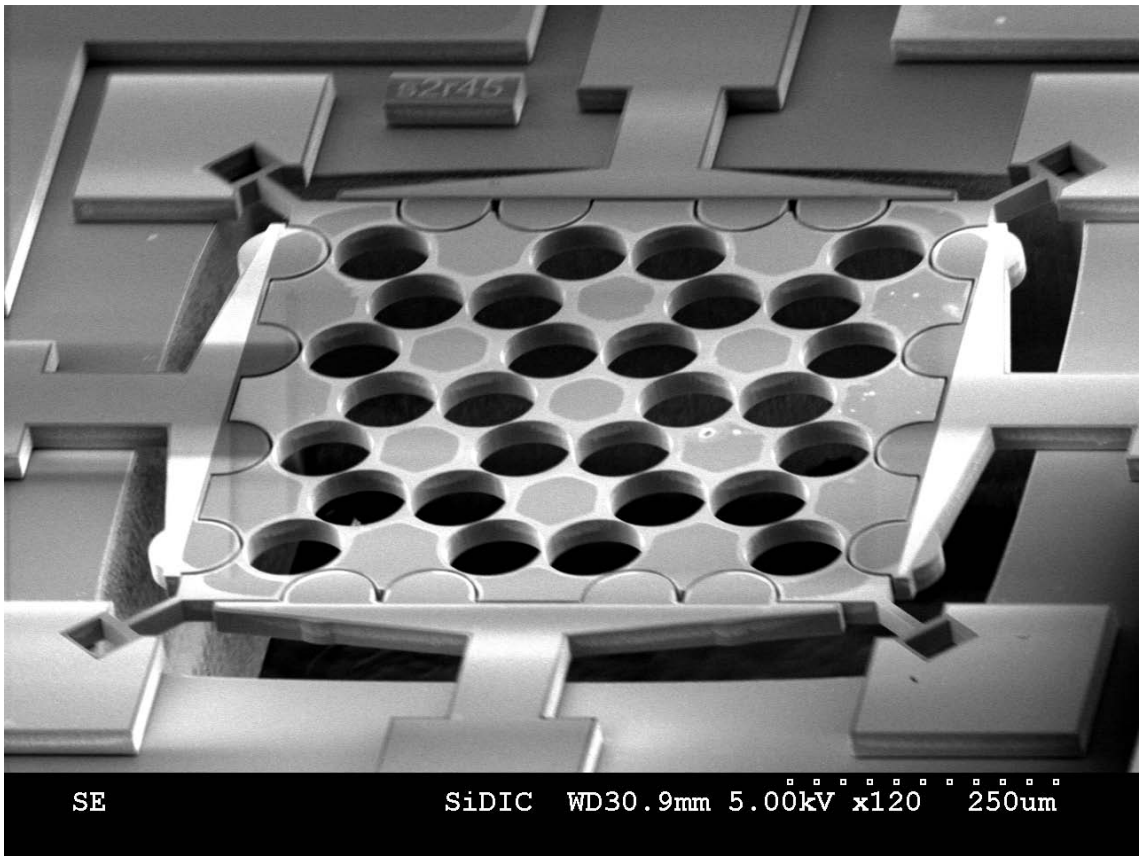

Figure 5.4: Scanning electron micrograph of the S1 phononic band gap quasi-crystal (see Table 3.1 and 3.2 for drawn dimensions).

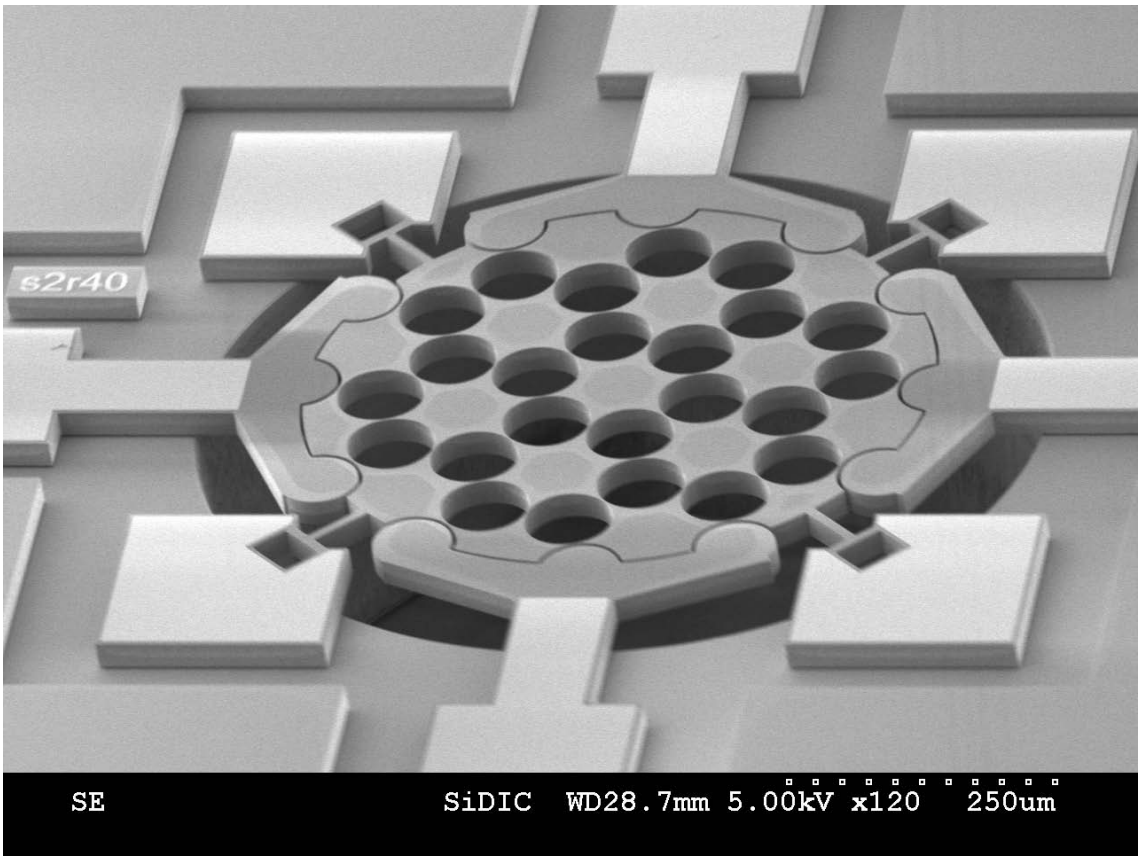

Figure 5.5: Scanning electron micrograph of the C1 phononic band gap quasi-crystal (see Table 3.1 and 3.2 for drawn dimensions).

quantitative characterization of the fabricated dimensions.

5.2.2 Surface Metrology Utilizing Optical Profilometer

The Wyko NT1100 optical profilometer, which utilizes optical phase-shifting and white light vertical scanning interferometry, provides sub-nanometer resolution in the vertical direction [135] and is depicted in Figure 5.6. Figure 5.7 displays a sample profilometer measurement of the physical region of the P^{n}BG QC that lies between the most distant spacing of the inclusions and was represented by m_{large} in Chapter 4. Additional profilometer measurements may be found in Appendix F.

Three significant fabrication errors were observed: (i) the trench location appears over etched by approximately $30\mu m$, and $20\mu m$, for the circular, and square, truncated devices, respectively, (ii) the $3\mu m$ gaps appear to be dramatically larger than drawn; however, the profilometer measurement accuracy is uncertain near edges and (iii) around curved features there appears to be a groove (as may be viewed in Figure 5.7 and Figure F.3) on top of the Silicon layer (see Figure 5.7) which may reduce the thickness of the Silicon layer in the region between inclusions. The semi-analytical model of Chapter 4 suggested that the hyper-band gap modes may display a third order dependence on the thickness of the Silicon layer in the region between inclusions. Hence, the aforementioned groove may be a significant source of error between the model and the measurement for hyper-band gap modes.

The profilometer measurements may be utilized to confirm that several device dimensions fabricated within the tolerances specified in the SOIMUMPs design hand book in [115] and the deflection at the center of the P^{n}BG QC may be utilized to quantify the residual stress in the single-crystal-silicon layer. Due to the large error in the fabricated trench location, profilometer measurements were utilized to obtain physical dimensions for the model of transducer pad substrate overlap area, $A_{sub,2}$, given in Table 4.3.

The optical profiler measurements may display increased error when measuring the

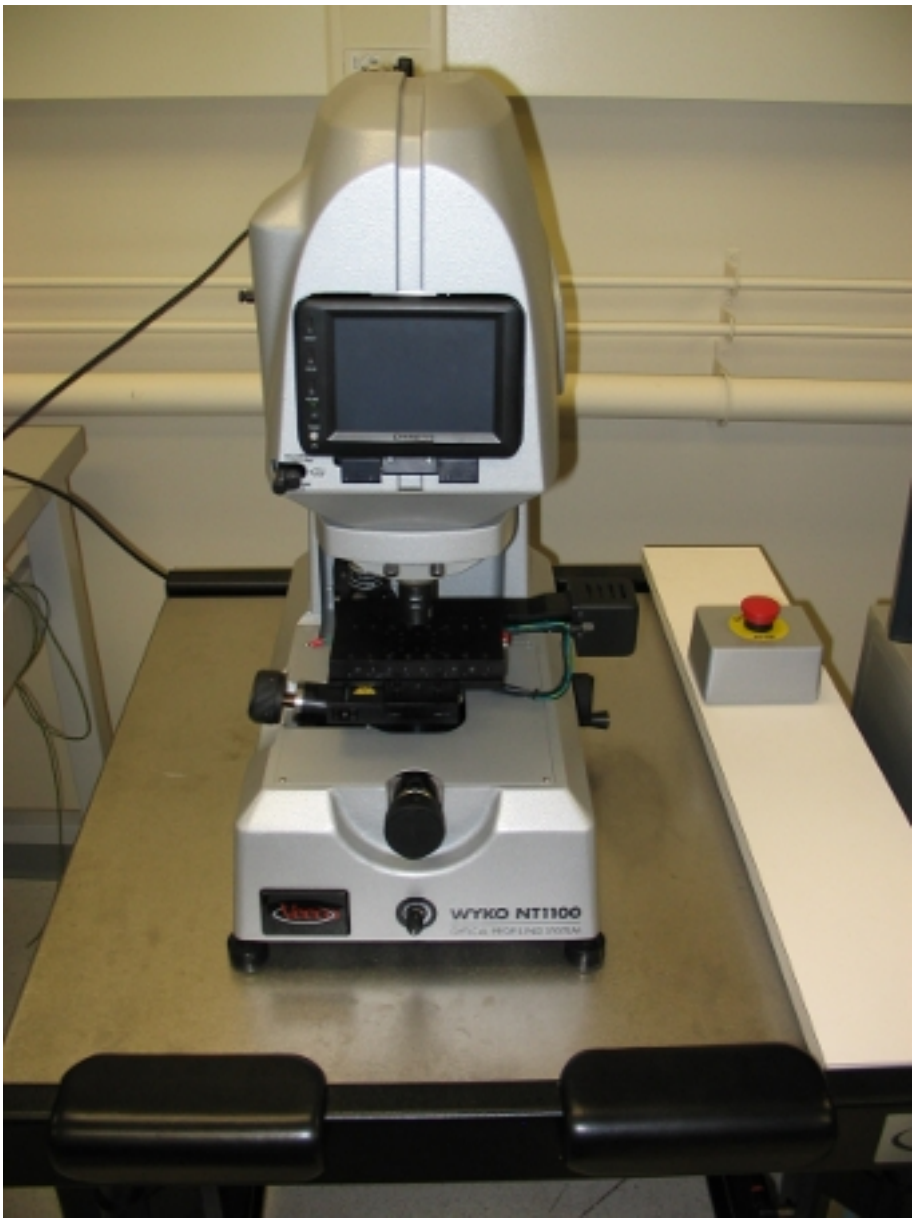

Figure 5.6: Wyko NT1100 optical profilometer that was utilized to characterize the surface of the fabrication devices.

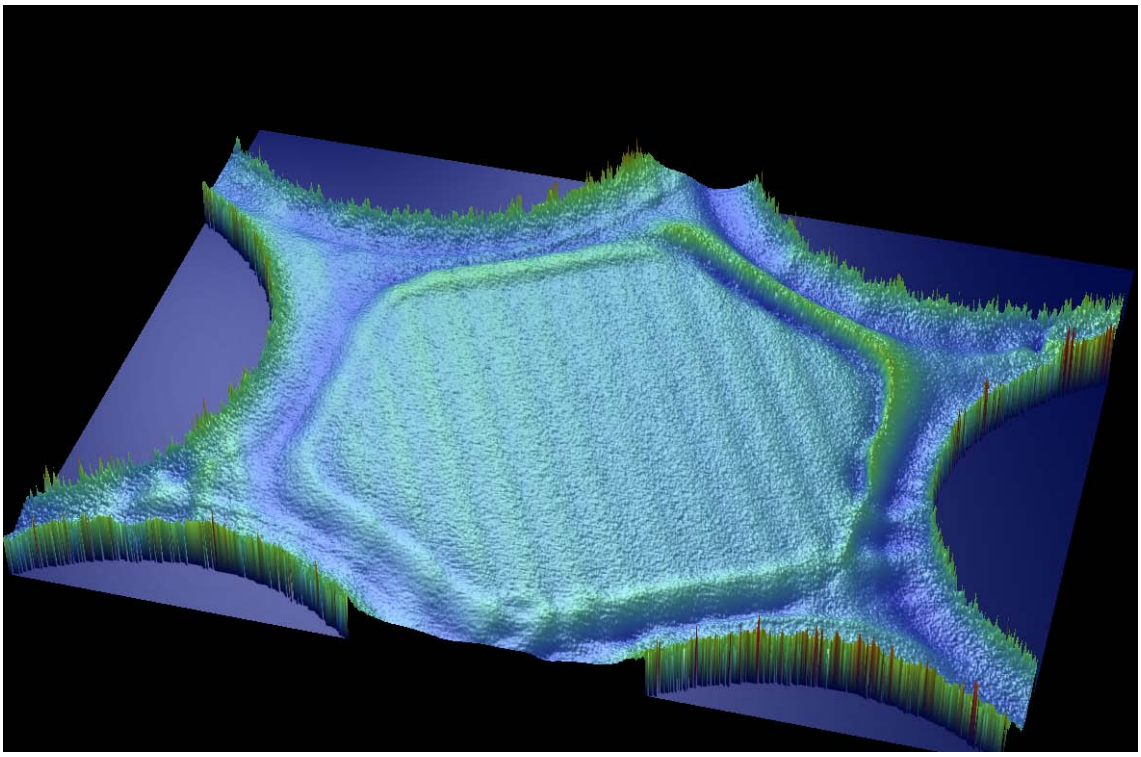

Figure 5.7: Profilometer 3D view of a portion of the host region of the S2 phononic band gap quasi-crystal.

distance between two closely spaced edges (possibly due to how the light is reflected at the edges and within the gap). This would yield low accuracy in measurement of gap size. A profiler such as the Veeco Dektak 8 stylus profiler [135] may potentially be utilized to perform more accurate measurements of the transducer gap size.

The profilometer images further support that the P^{n}BG QC architecture can be fabricated with reasonable accuracy utilizing SOIMUMPs. The profilometer measurements may be post-processed further to extract additional fabricated physical dimensions and built in stress data; physical dimensions may then be substituted for the drawn dimensions in the model to obtain a more accurate model of the fabricated P^{n}BG QCs.

5.3 Test Fixture Electrical Circuit Construction and Assembly Utilizing Surface Mount Printed Circuit Board Technology

Table 5.2 lists the components utilized to fabricate and assemble the test fixture depicted in Figure 5.8. This test fixture is designed to carry electrical Radio Frequency (RF) and DC signals to a maximum of eight out of the nine devices on the SOIMUMPs chip; which of the nine devices are electrically connected to the test fixture is determined by how the chip is bond-wired to the package. The bond-wire diagram for the SOIMUMPs chip tested for this thesis is shown in Figure 5.10, where it may be observed that signal and ground are connected to the eight devices on the perimeter of the SOIMUMPs chip. To apply signal to all four transducers of each device, the four transducer pads are bond stitched together as in Figure 5.10. The SOIMUMPs chip is electrically and mechanically bonded to a surface mount package which is left open to allow for optical access to the top surface of the SOIMUMPs chip. The Radio Frequency (RF) signal is delivered in-phase, via a bias-tee on the printed circuit board, to the four electrostatic transducers of each device. Two motorized stages, described in Table 5.2, set orthogonal to each other, allow for the motion of the text fixture to be automated in the $\hat{x}$- and $\hat{y}$-directions.

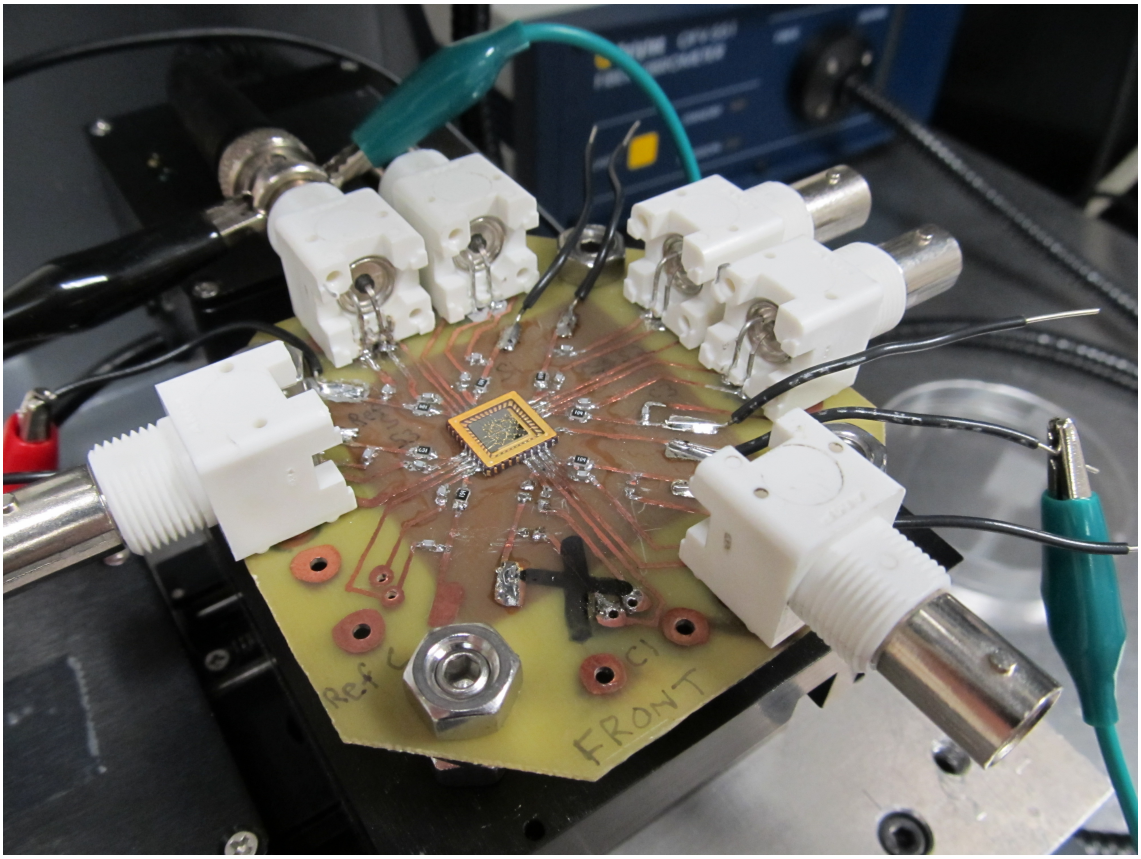

Figure 5.8: Assembled test fixture for the testing of the SOIMUMPs chip that contains the phononic band gap quasi-crystal devices.

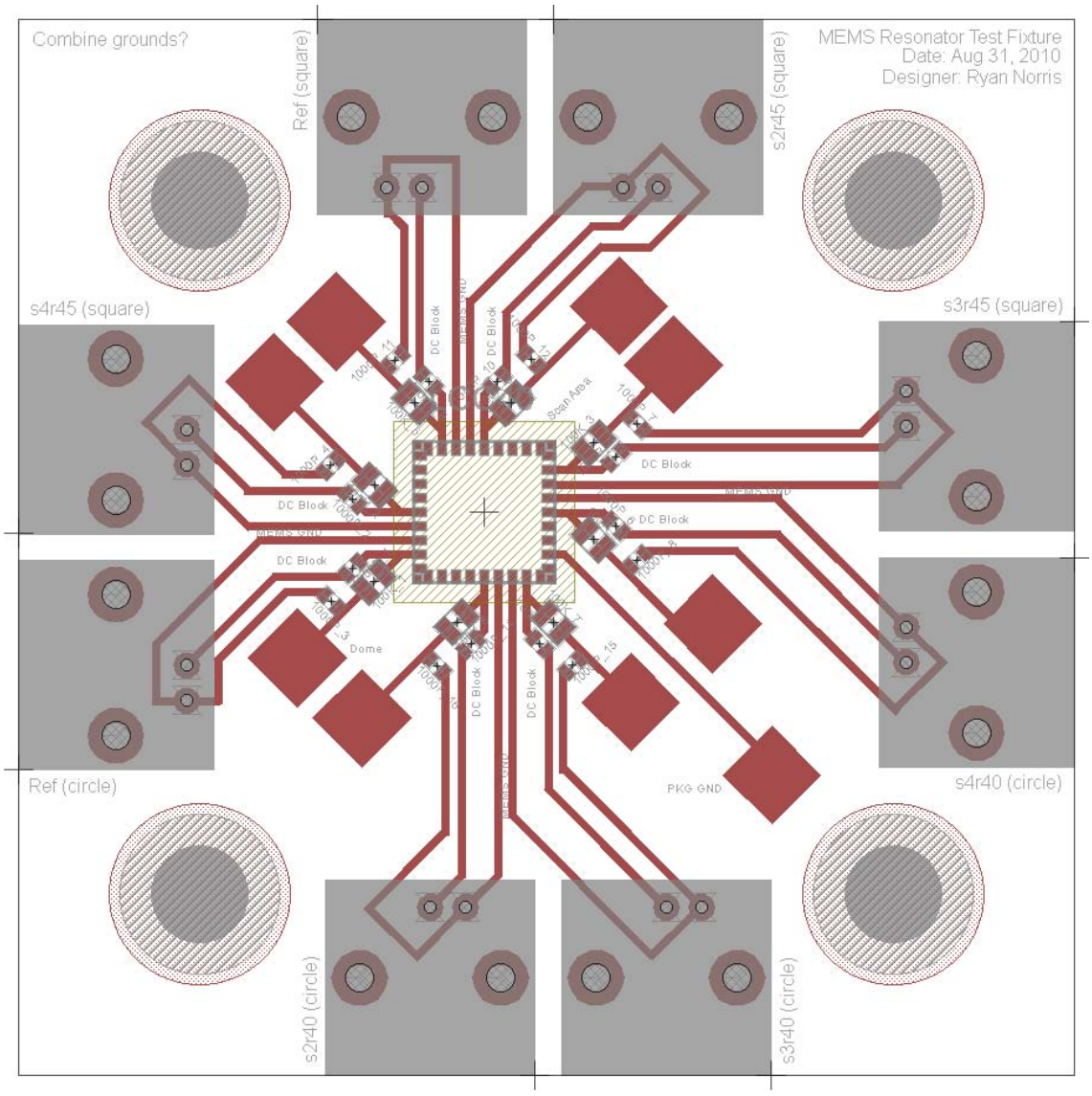

Figure 5.9: Layout of the printed circuit board designed for the text fixture that is shown in Figure 5.8.

Table 5.2: Components utilized in the assembly of the test fixture.

Component	Manufacturer	Model	Nominal	Tolerance	Temperature Coefficient	Notes
Copper clad board	MG Chemicals	Double Sided Copper Clad	1/32” thick 1 oz copper	-	-	Is masked, then etched, to create a printed circuit board
Etch Resist Ink Pen	GC Electronics	22-220	1/32” tip	-	-	Used to create an etch mask on the PCB before etching, course tip
Etch Resist Ink Pen	GC Electronics	22-222	1/64” tip	-	-	Used to create an etch mask on the PCB before etching, fine tip
Ferric Chloride	MG Chemicals	415-1L	$FeCl_3$ liquid solution	-	-	Copper etchant, etches copper clad board to create printed circuit board
Package	NTK (Distributor: Spectrum)	LCC04023	40 pin surface mount package, gold pads	-	-	Packages SOIMUMPs chip for electrical connection to printed circuit board
Bond wire	(unknown)	-	Gold 0.001" diameter	-	-	Electrically connects electrical pads on SOIMUMPs chip to LCC package
Silver epoxy	EPO-TEK®	H20E	Volume resistivity at 23°C: ≤ 0.0004 Ohm-cm	-	-	Electrically and mechanically connects SOIMUMPs chip to package
Solder	Chipquik	SMD 291AX	-	-	-	Utilized to solder all components
Resistor	Stackpole Electroics	RMCF0805JT 100K	100 kΩ	±5%	±200ppm/°C	RF Choke, 0805 SMD, Thick Film, 1/8 W, Maximum voltage of 150 V
Capacitor	Murata Electronics	GRM188R72 E102KW07D	1000 pF	±10%	X7R	DC Block, 0603 SMD, Ceramic, Maximum voltage of 250 V
BNC Connector	Amphenol	31-5431	50 Ω	-	-	Maximum frequency of 4GHz, allows electrical connection to RF signal
DC Wire	(unknown)	Poly-vinyl chloride jacket	24 AWG	-	-	Allows electrical connection to DC signal, Maximum 300 V
Motorized Stages	Zaber	T-LS13-M	Microstep resolution of 0.09921875 µm	-	-	Utilized to automate the motion of the text fixture for mode shape measurements

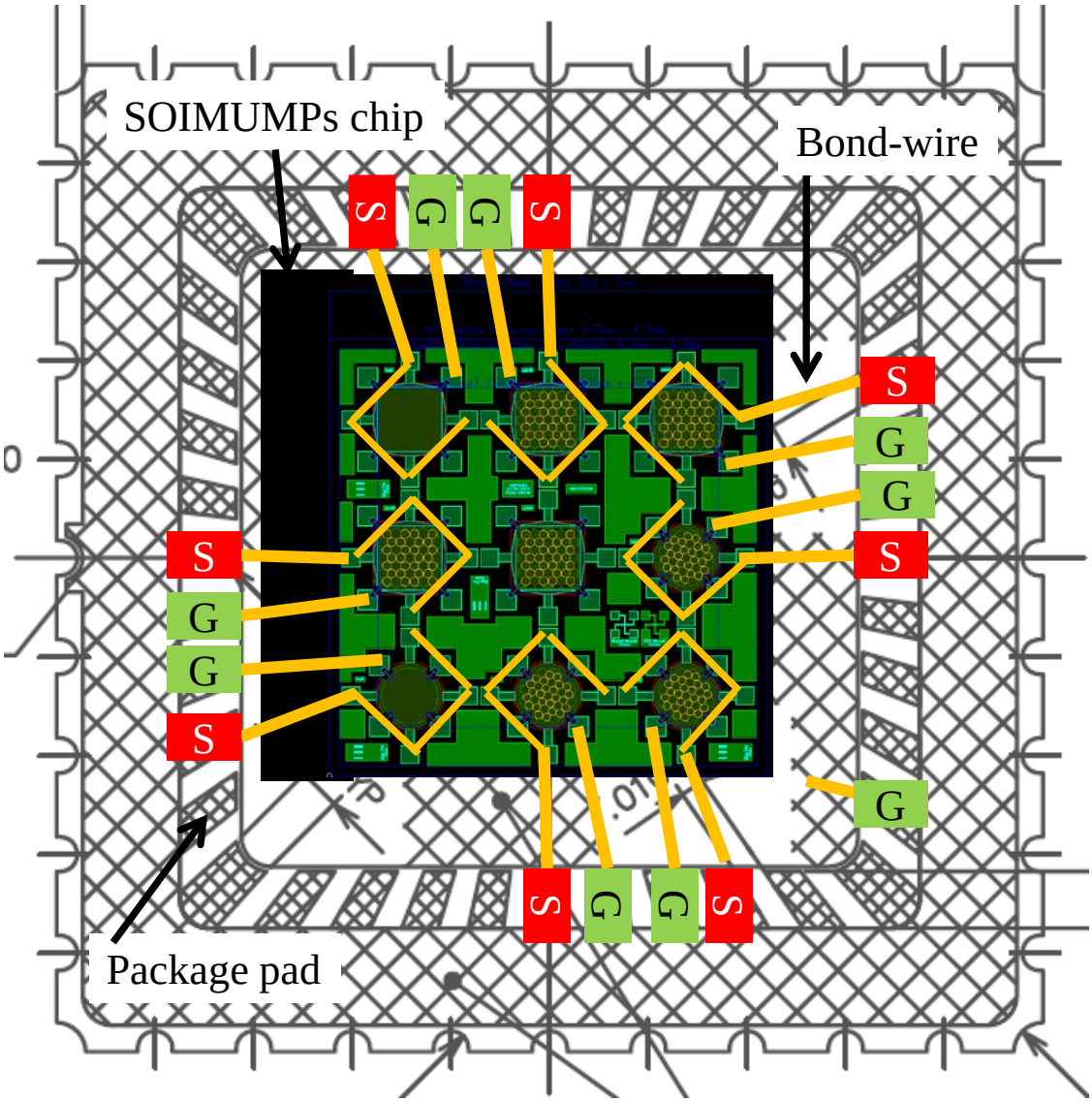

Figure 5.10: Bond wire diagram for the packaging of the SOIMUMPs chip.

Chapter 6

Experimental Measurement of Micro-Electro-Mechanical-System Implementation of Phononic Band Gap Quasi-Crystal Architecture

The six P^{n}BG QC devices and three reference devices listed in Table 3.1 were fabricated utilizing SOIMUMPs and characterized utilizing a scanning electron microscope and optical profilometer as discussed in Chapter 5. The characterization results presented in Chapter 5 and Appendices E and F provide qualitative and quantitative information that indicates that the six P^{n}BG QC devices and three reference devices could be fabricated with reasonable accuracy by utilizing the SOIMUMPs process.

This chapter presents measurement results of the dynamic harmonic response and mode shapes for the S1, S2 and C2 P^{n}BG QC devices as well as the Square homogeneous plate reference device, for which the geometrical parameters are illustrated in Figure 3.4

and quantified in Tables 3.1 and 3.2. The large amount of time required (discussed in Section 6.1) to perform spectrum and mode shape measurements did not permit the measurement of the S3, C1 and C3 P^{n}BG QCs or the Circle homogeneous plate and S4 reference devices. The measurement results provide reasonable support for several of the trends that were observed in the model of Chapter 4 for band gap location and mode shape behavior versus the parameters of P^{n}BG QC truncation geometry (square versus circular) and inclusion spacing, as well as band gap location versus DC bias voltage and the electromechanical coupling coefficient of the electrostatic transducers. Comparison of the measurements of the S1, S2 and C2 P^{n}BG QC devices with the Square reference device illustrate where the behavior of the P^{n}BG QC devices diverges from that of the Square reference. Where measurement results deviate from the model, data is established for model and device refinement.

6.1 Measurement Setup

The S1, S2 and C2 P^{n}BG QC devices and Square reference device are characterized in the frequency and spatial domains utilizing an optical laser-Doppler vibrometer as illustrated in the experimental setup of Figure 6.1. Each device is mechanically excited via the electrostatic transducers that are integrated into each device. The measurement of the mechanical response utilizing the optical laser-Doppler vibrometer provides a relatively non-invasive measurement. The vibrometer is manufactured by Polytec [136] and comprised of the Polytec OFV-551 fibre vibrometer, OFV-5000 vibrometer controller, and DD-330 displacement decoder and is displayed in Figure 6.2. The DD-300 displacement decoder has a measurement range of $\pm 75nm$, -3 dB bandpass frequency range from 30 kHz to 24 MHz, noise-limited resolution of $< 0.02pm/\sqrt{Hz}$ at 100% reflectivity, scaling factor of $50nm/V$ (for a load resistance of 50Ω) which may be utilized to convert

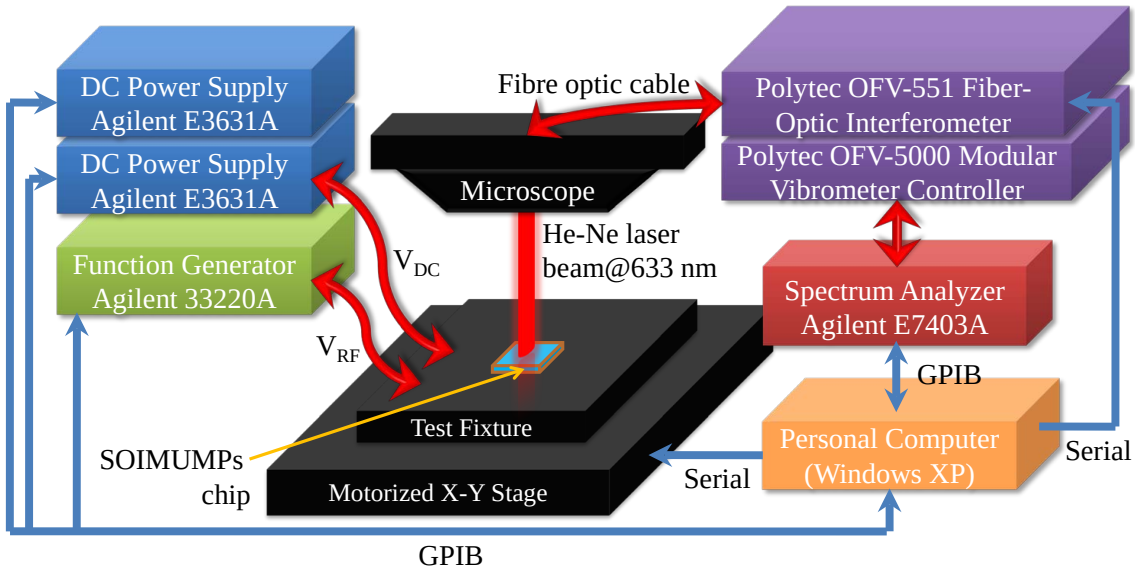

Figure 6.1: Block diagram of experimental setup. The devices rest on a motorized stage. The vibrometer laser is directed upon the upper surface of the phononic band gap quasi-crystal. Each instrument interfaces with the personal computer.

between voltage and displacement, output swing of $\pm 1.5V$ (for a load resistance of 50Ω) and output impedance of 50Ω [129]. The frequency response of the vibrometer is flat to within $\pm 1dB$ over the frequency range from 40 kHz to 20 MHz. On the surface of the device under test, the laser spot size that comes from the vibrometer is focused by the microscope objective lens to a diameter of approximately $10\mu m$.

The output of the vibrometer is a voltage with amplitude, V_{vib}, which is proportional to the measured displacement and may be expressed utilizing the vibrometer scaling factor, $K_{vib} = 50nm/V$ as:

$$V_{vib} = \frac{d_{vib}}{K_{vib}} \qquad K_{vib} = 50\ nm/V \tag{6.1}$$

where d_{vib} is the amplitude of the displacement measured by the vibrometer.

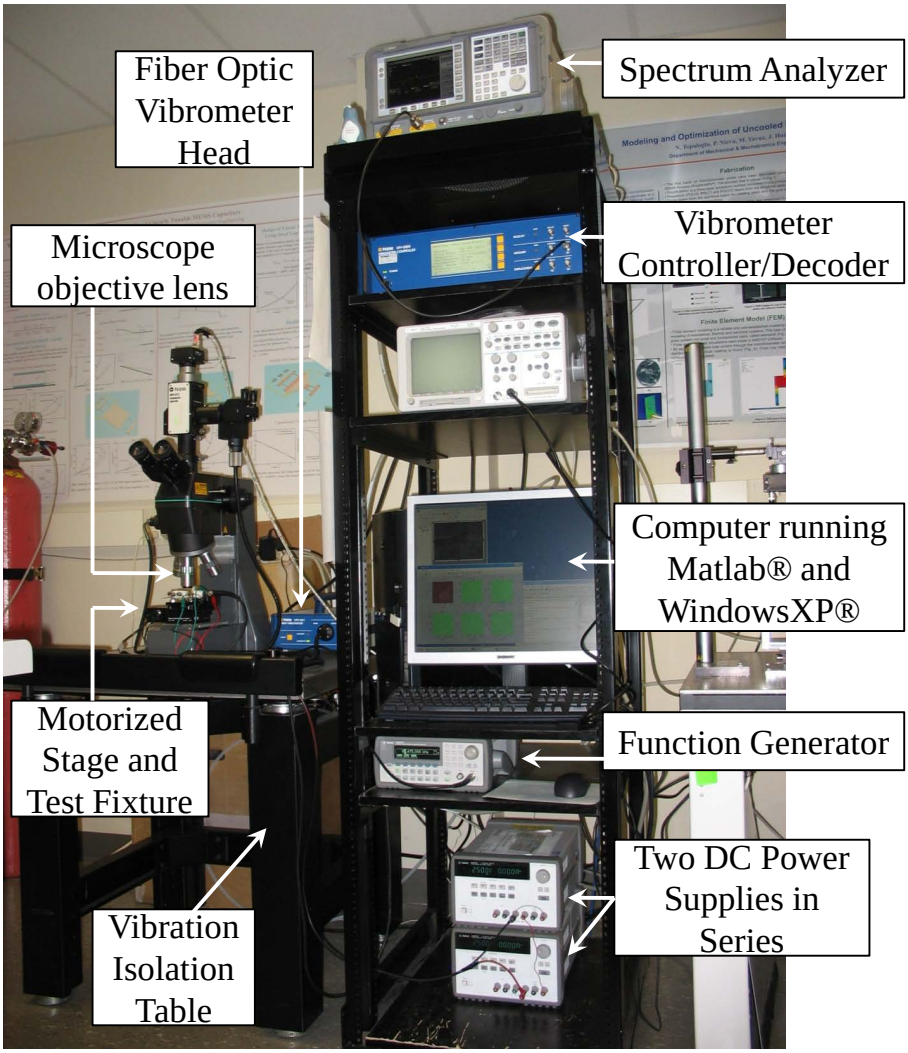

Figure 6.2: Physical setup of the experimental equipment.

The spectrum analyzer (which presents a 50 Ω load) was utilized to measure the vibrometer output voltage. The measurement of the spectrum analyzer is expressed in the units of power, decibel-milliwatt (dBm). The conversion between the power measured by the spectrum analyzer and the vibrometer output voltage amplitude is:

$$\begin{aligned} P &= 10log_{10}\left(P_{rms}\right) + 30 \quad (dBm) \\ P_{rms} &= \frac{V_{rms}^2}{50\Omega} \quad (root\ mean\ square\ watts) \\ V_{rms} &= V_{vib}/\sqrt{2} \end{aligned} \tag{6.2}$$

where the RMS voltage, V_{rms}, has been computed assuming the vibrometer signal is sinusoidal. Combining Equations 6.1 and 6.2 yields conversion equations between the power measured by the spectrum analyzer and the vibrometer output displacement amplitude:

$$\begin{aligned} P &= 10log_{10}\left(\frac{(V_{vib}/\sqrt{2})^2}{50\Omega}\right) + 30 \quad (dBm) \\ V_{vib} &= \sqrt{2}\sqrt{50\Omega \times 10^{(P-30)/10}} \quad (amplitude\ in\ volts) \\ d_{vib} &= K_{vib}\sqrt{2}\sqrt{50\Omega \times 10^{(P-30)/10}} \quad (amplitude\ in\ meters). \end{aligned} \tag{6.3}$$

These equations will be applied in Section 6.2.5 to produce measured displacement amplitude data that may be utilized to characterize the electromechanical coupling coefficient of the electrostatic transducers.

As shown in Figure 6.1 an Agilent 33220A function generator is utilized to create the sinusoidal electrical signal, V_{RF}, that is applied to the device under test via a bias-tee and transferred in-phase to all four transducers of the device as illustrated in Figure 6.3. The Agilent E7403A EMC analyzer is utilized to measure the spectrum of the electrical signal, V_{vib}, which is output from the Polytec vibrometer controller.

Two Agilent E3631A DC variable power supplies are wired in series to provide a DC voltage that is variable between 0 and 100 VDC, as shown in Figure 6.1. The use of a DC offset, V_{DC}, that is greater than or equal to the peak to peak value of V_{RF} is typically employed to ensure that frequency doubling, due to zero crossings and transducer voltage polarity changes, does not occur. This is achieved by forcing the polarity of the total voltage $V_{RF} + V_{DC}$ to always be positive, $V_{RF} + V_{DC} > 0|_{V_{RF,pp} \leq V_{DC}}$, given that V_{RF} is a sinusoidal voltage with zero DC offset and V_{DC} is a positive DC voltage. In this fashion, Equation 4.6 would predict that the electrostatic force is a minimum, and maximum, when V_{RF} is at the minimum, and maximum, respectively.

The test fixture and SOIMUMPs chip described in Chapter 5 rest upon two motorized linear translation stages which are oriented orthogonal to one another and so provide position control in the $\hat{x}$- and $\hat{y}$-directions. The vibrometer laser is incident upon the upper surface of the SOIMUMPs chip. Control of the laser spot location on the SOIMUMPs chip is automated utilizing the motorized stages. The spectrum analyzer, function generator, DC power supplies interface with the personal computer via a General Purpose Interface Bus (GPIB). The motorized stages and fiber optic interferometer interface with the personal computer via serial ports. The personal computer allows control of all instruments to be automated via MATLAB®.

The experimental setup of Figure 6.1 is schematically illustrated in Figure 6.3 and provides automated measurement of the (1) spectrum (displacement amplitude in the $\hat{z}$-direction versus frequency) of each device and (2) mode shape displacement in the $\hat{z}$-direction. The personal computer enables automation of the measurement of the spectrum via control of the DC voltage, V_{DC}, and frequency of the RF voltage, V_{RF}. Each spectrum measurement is typically performed over a bandwidth of $5kHz$ to $20MHz$, for a frequency spacing of 1 kHz, and a sense resolution bandwidth of $1Hz$ and takes

approximately 12 hours. For more detailed spectrum measurements with a lower noise floor, the frequency spacing, and sense resolution bandwidth, may be reduced to as low as $10Hz$, and $0.1Hz$, respectively. The personal computer enables automated measurement of the mode shape displacement in the $\hat{z}$-direction for a fixed DC voltage, V_{DC}, and fixed RF voltage, V_{RF}, through use of the motorized stage to automate control of the vibrometer laser spot location versus position on the device. Each mode shape measurement is performed over an area of approximately $800\mu m \times 800\mu m$, for a spatial sampling period of $5\mu m$, and sense resolution bandwidth of $0.1Hz$ and takes approximately 40 hours.

6.2 Experimental Results

This section presents the results for the measurement of the dynamic harmonic response (Section 6.2.1) and mode shape topography (Section 6.2.2) of the S1, S2, C2 P^{n}BG QCs and Square homogeneous plate reference device. The results of the dynamic harmonic response and mode shape topography measurements are post-processed to create the frequency versus FEM mode number characteristic in Section 6.2.3. Within Sections 6.2.4 and 6.2.5, the dynamic harmonic response measurements are post-processed into the displacement amplitude versus frequency characteristic to provide physical data regarding the electromechanical coupling coefficient of the electrostatic transducers on the S2 P^{n}BG QC. Lastly, the measurement results are discussed in Section 6.3.

6.2.1 Dynamic Harmonic Analysis

Measurement of the dynamic harmonic response, also referred to here as the vibrometer spectrum, was performed at room temperature and pressure at the University of

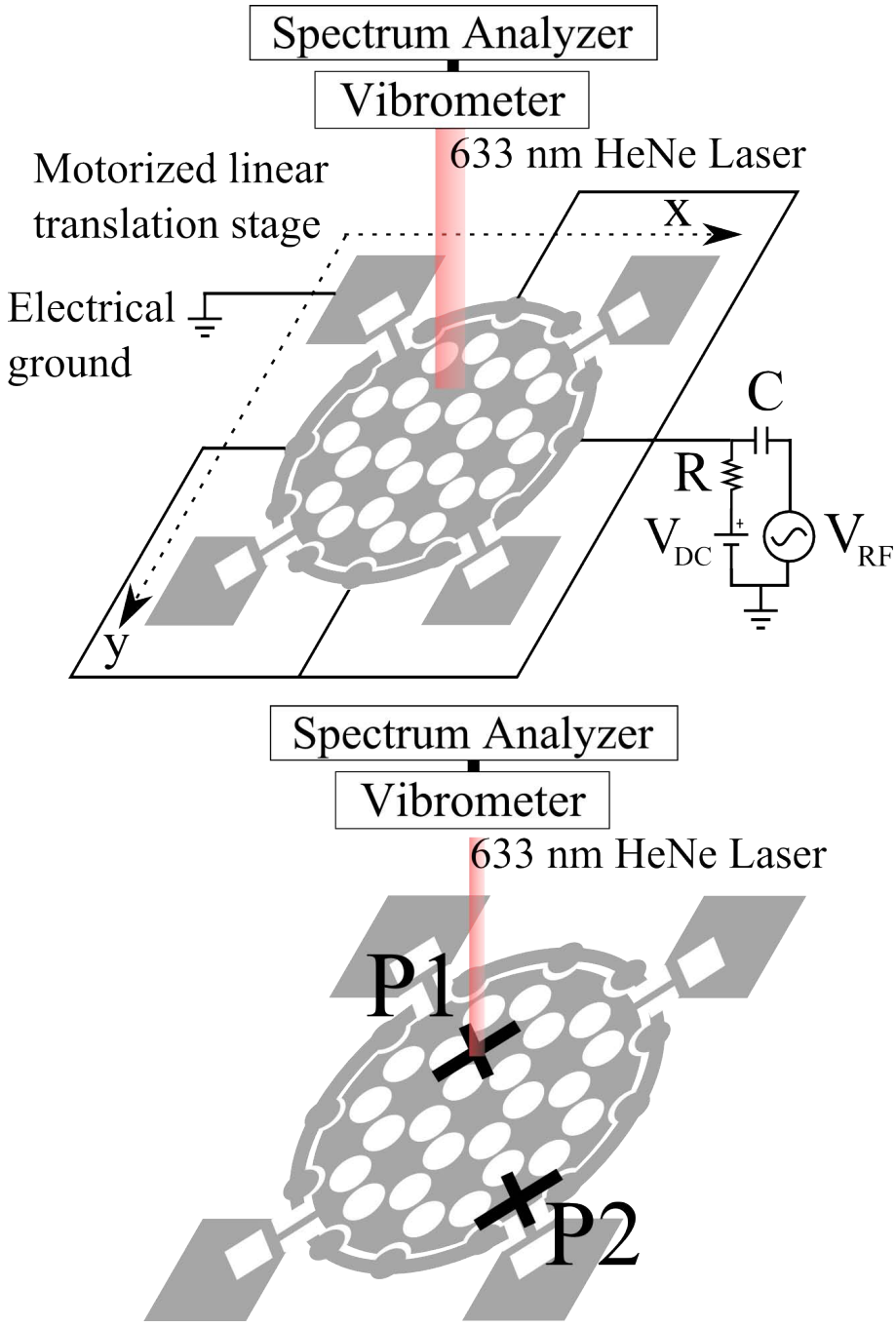

Figure 6.3: Experimental setup and device schematic. RF and DC signals are applied to four transducers. The phononic band gap quasi-crystal or reference device is grounded via the anchor. The device rests on a motorized stage. The vibrometer laser is directed upon the upper surface of the phononic band gap quasi-crystal or reference device.

Waterloo, Ontario, Canada. Figure 6.4 displays the measured vibrometer spectrum for the S1 and S2 P^{n}BG QC devices along side the measured vibrometer spectrum of the Square homogeneous reference plate device. In Figure 6.4 the measured vibrometer spectrum is presented at a single point where both sub- and hyper-band gap modes display anti-nodes so that both the sub- and hyper-band gap resonances can be observed in a single spectrum; measurement points are denoted in the insets of Figure 6.4. As may be observed in Figure 6.4, the vibrometer spectrums of the S1 and S2 P^{n}BG QCs do not appear to display resonant peaks (above the noise floor) within the frequency range from approximately 10 MHz to 13 MHz. Figure G.2 of Appendix G contains additional measurements of the vibrometer spectrum at different points on the surface of the S2 P^{n}BG QC. The spectrum at none of the measured points, on the P^{n}BG QCs, display resonant peaks within the approximate frequency range of 10 MHz to 13 MHz. The reason for performing the harmonic analysis at several points on the surface of the S2 P^{n}BG QC was to ensure that the observed absence of resonant peaks in the 10 to 13 MHz regime was not due to the laser spot being located at the a vibrational node. Hence, several points were measured, no points display resonant peaks in the approximate 10 MHz to 13 MHz frequency regime, and additional points may be measured to provide additional support for the potential absence of normal mode resonances and band gap location in this frequency range (additional points were not measured due to the large 12 hour measurement time).

The frequency ranges where the normal mode resonances are not observable may also in part be due to the displacement amplitude being below the experimental noise floor. However, identifying frequency regions where the (i) amplitude of vibration is not observable and which (ii) lie between frequency regions were the amplitude of vibration is observable and considerably larger, may still provide experimental evidence of physical

band gap behavior.

The absence of observable resonant peaks and corresponding normal modes for the S1 and S2 P^{n}BG QC devices over the frequency range from 10 MHz to 13 MHz may potentially be experimental evidence that the P^{n}BG QC devices display the characteristic band gap behavior of a P^{n}BG crystal for the $\hat{z}$-component of displacement. Figure G.1 of Appendix G displays additional harmonic analysis measurements at different points on the Square homogeneous plate reference device and resonant peaks are present over the entire measured frequency range (there is not a single frequency range of notably large extent where resonant peaks are not observed). This contrasting behavior between the S1 and S2 P^{n}BG QCs and the Square reference device appears to indicate that the behavior of the S1 and S2 P^{n}BG QC devices deviates significantly from that of a Square homogeneous plate.

As may be observed in Figure 6.4, the amplitude of the vibrometer spectrum of the S1 and S2 P^{n}BG QCs and the Square reference device decrease as frequency increases. This decrease in amplitude with frequency may in part be due to damping. Additionally, the electrostatic transducers generate electrostatic forces that may have the strongest component of the force in the in-plane ($\hat{x}$-$\hat{y}$) directions (according to the model of Section 4.3) while many modes display largely out-of-plane ($\hat{z}$-direction) motion, in particular at high frequency, and the transducer coupling coefficient may decrease as frequency increases. A third justification for the amplitude decrease with frequency may be accounted for in that, in the presence of damping, for a given force, higher frequency modes display a lower amplitude than lower frequency modes [137]. This concept may be understood in that higher frequency modes have a shorter wavelength and so more physical bends per unit length in the mode shape. To produce equal vibration amplitude in a higher frequency (shorter wavelength) and lower frequency (longer wavelength) mode

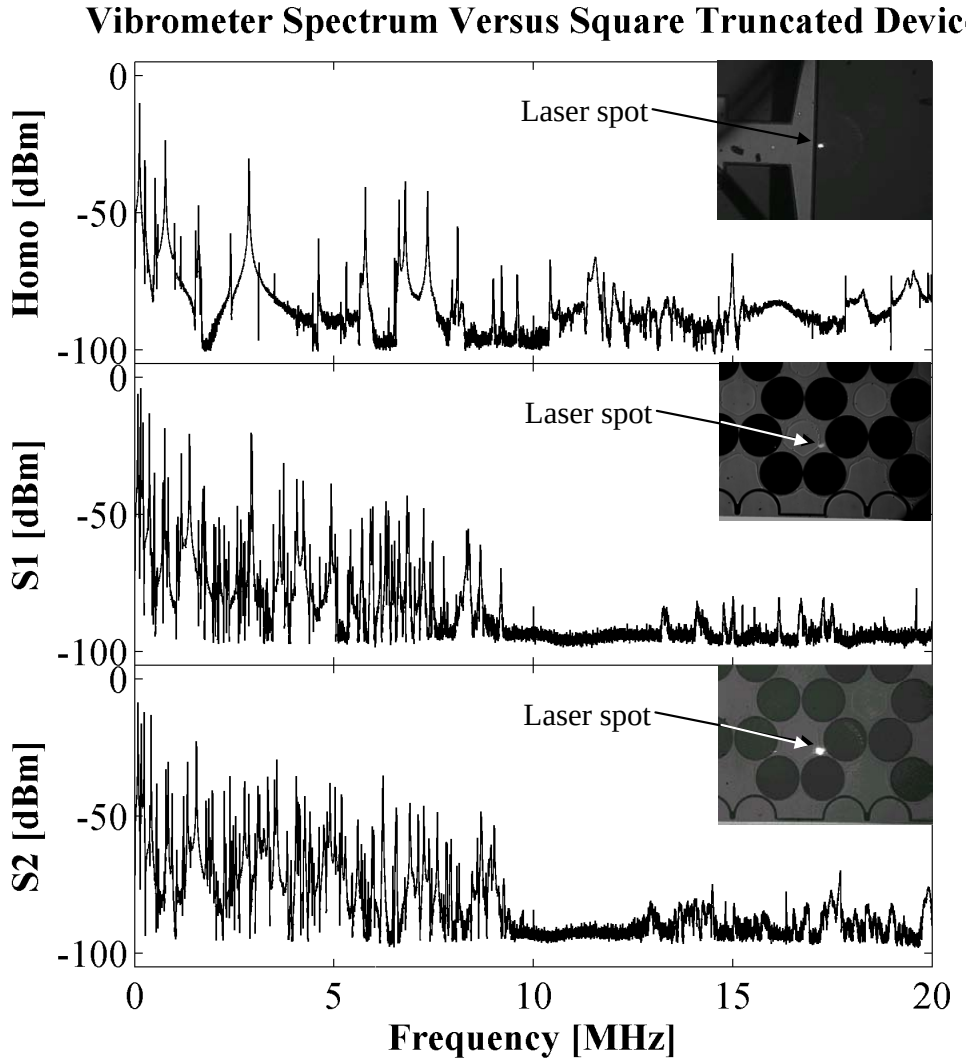

Figure 6.4: Comparison of the spectrum of Square homogeneous plate reference device and the S1 and S2 phononic band gap quasi-crystals. The spectrum is measured by the spectrum analyzer, using the measurement setup shown in Figure 6.1, as the power of the signal coming from the vibrometer controller and expressed in the units of dBm. The laser spot location is denoted in the figure and is held the same for the S1 and S2 phononic band gap quasi-crystals.

shape, would then require a larger stress gradient and larger force to provide the energy needed to create the higher stress field with the same overall displacement amplitude. It should also be noted that the potential frequency dependence of the electrostatic force

amplitude has not been de-embedded from these measurements.

To develop an approximation of the mechanical quality factor of the normal modes of the P^{n}BG QC device, the first-order harmonic oscillator model that was presented in Section 4.2.5 is fit to several of the normal mode resonant peaks in the harmonic response displayed in Figure 6.4 for the S2 P^{n}BG QC. Results of the fit for both sub-band gap and hyper-band gap modes are displayed in Figures 6.5, 6.6 and 6.7. The harmonic oscillator model is fit to both normal mode peaks that are relatively distant from one another as well as to closely grouped pairs of normal modes. If the shape of the normal mode peak is asymmetrical relative to the shape of the harmonic oscillator model, then the harmonic oscillator model is fit twice to the experimental normal mode peak, once for each skirt of the experimental normal peak. The set of fitting parameters that were utilized to fit the model to the measured data are displayed in the inset of Figures 6.5, 6.6 and 6.7 and listed in Table 6.1.

As may be observed in Figures 6.5, 6.6 and 6.7, the first order harmonic oscillator model of Section 4.2.5 fits relatively well to the measured normal mode peaks for modes 1, 42, 73, 105, and the sub-band gap mode at 9.016 MHz. In particular, the fit of the first order harmonic oscillator model to modes 1 and 73 and the mode at 9.016 MHz matches reasonably well to both skirts of the measured normal mode peaks in Figure 6.5. The measured normal mode peaks of modes 42 and 105 in Figures 6.5 and 6.6 display asymmetry relative to the shape of the first order harmonic oscillator model and so a given fit of the first order harmonic oscillator model fits closer to one skirt of the normal mode peak than the other. For the pairs of closely space normal modes in Figure 6.6 the superposition of two first order harmonic oscillator models is fit to the two measured peaks with reasonable accuracy close in to each of the two peaks and reduced accuracy near the outer skirts of the two peaks. The first order harmonic oscillator model displays

lower accuracy for the hyper-band gap modes at 14.487 MHz and 17.69 MHz, this may in part be due to the reduced signal to noise ratio which is provided by the reduced amplitude of displacement at higher frequencies and an associated potential increase in measurement error. From Table 6.1, the observed quality factors that result from this fitting of the first order harmonic oscillator model to the measured harmonic response are observed to lie within the range of 180 to 4000.

Utilizing Equation 4.32 normalized to the forcing function amplitude, F, along with the fitting parameters in Table 6.1, the normalized effective mechanical parameters, k_{eff}/F, m_{eff}/F and γ/F were computed and listed in Table 6.1. As may be viewed in Table 6.1, under this fit, the normalized effective spring constant, k_{eff}/F, varies over four orders of magnitude and tracks the large variations in the measured peak amplitude versus frequency. In contrast, the normalized effective mass, m_{eff}/F, depends on the product of measured peak amplitude and the square of angular resonant frequency, and varies by less than one order of magnitude for the fitting parameters and modes in Table 6.1, indicating that the variations in amplitude and square of angular frequency may offset one another. Lastly, the normalized damping coefficient, γ/F, depends on the product of the measured peak amplitude, resonant frequency and quality factor and for the fitting parameters in Table 6.1 appears to increase by approximately one order of magnitude between the low and high frequency modes. It is important to note that the normalized effective mechanical parameters, k_{eff}/F, m_{eff}/F and γ/F, were normalized to the forcing function amplitude, F, which may display its own frequency dependence. One approach to remove the normalization and obtain k_{eff}, m_{eff} and γ may require investigation of the forcing amplitude, F. Alternatively, if the physical bounds on k_{eff}, m_{eff} and γ may be obtained, it may be possible to utilize the data in Table 6.1 to estimate the forcing function amplitude, F. A possible relation between the

forcing function amplitude, F, of the harmonic oscillator model of Figure 4.25, which was applied in Figures 6.5, 6.6 and 6.7 to the spectrum of the out-of-plane motion of the S2 P^{n}BG QC, and the in-plane electrostatic forces generated by the electrostatic transducers may be investigated further.

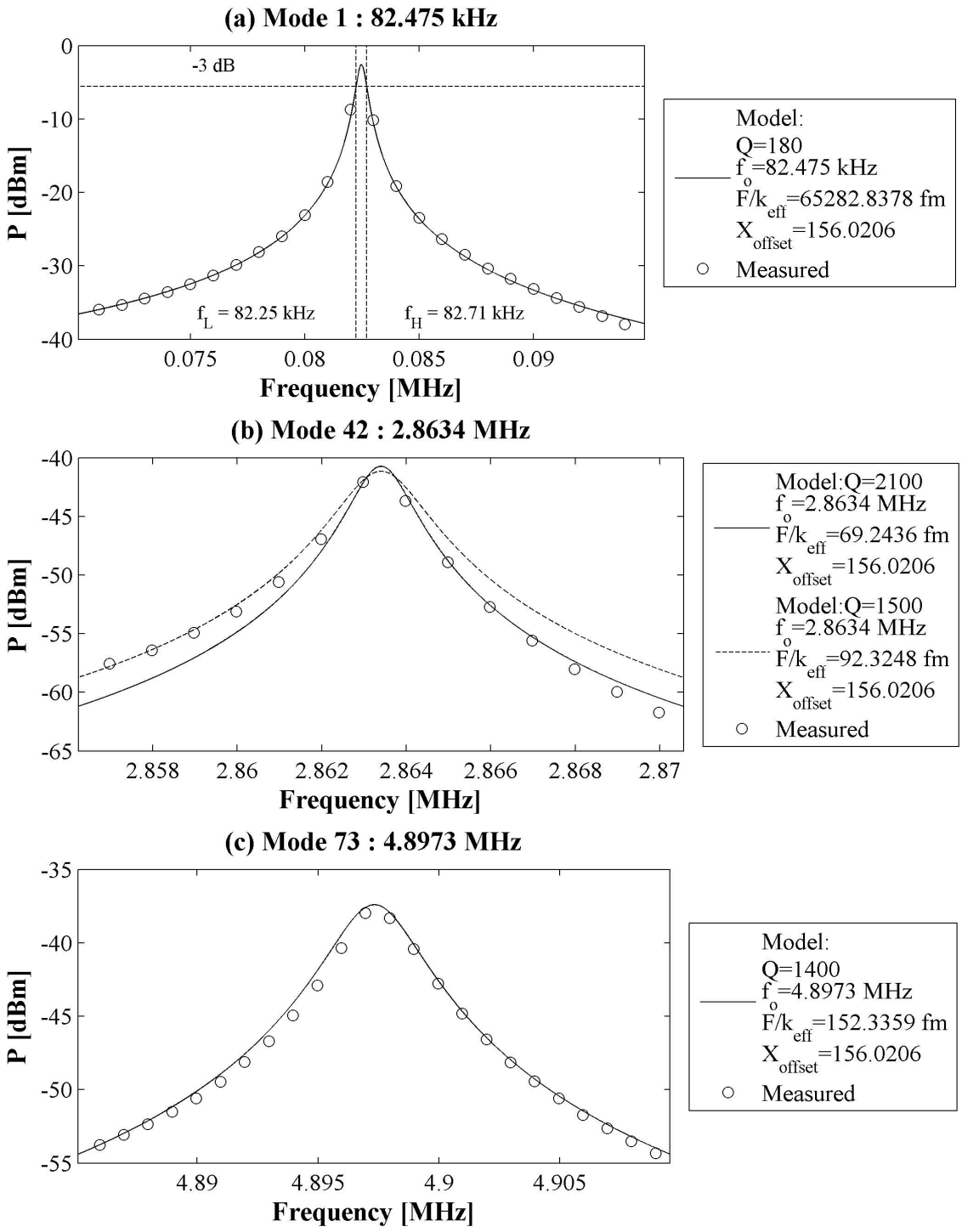

Figure 6.5: First order harmonic oscillator model fitted to experiment for sub-band gap modes 1, 42 and 73 of the S2 phononic band gap quasi-crystal device. For mode 1, the fit was performed within a normalized bandwidth ($\Delta f/f_o$) of 0.3 while other modes were fitted within a normalized bandwidth of 0.005.

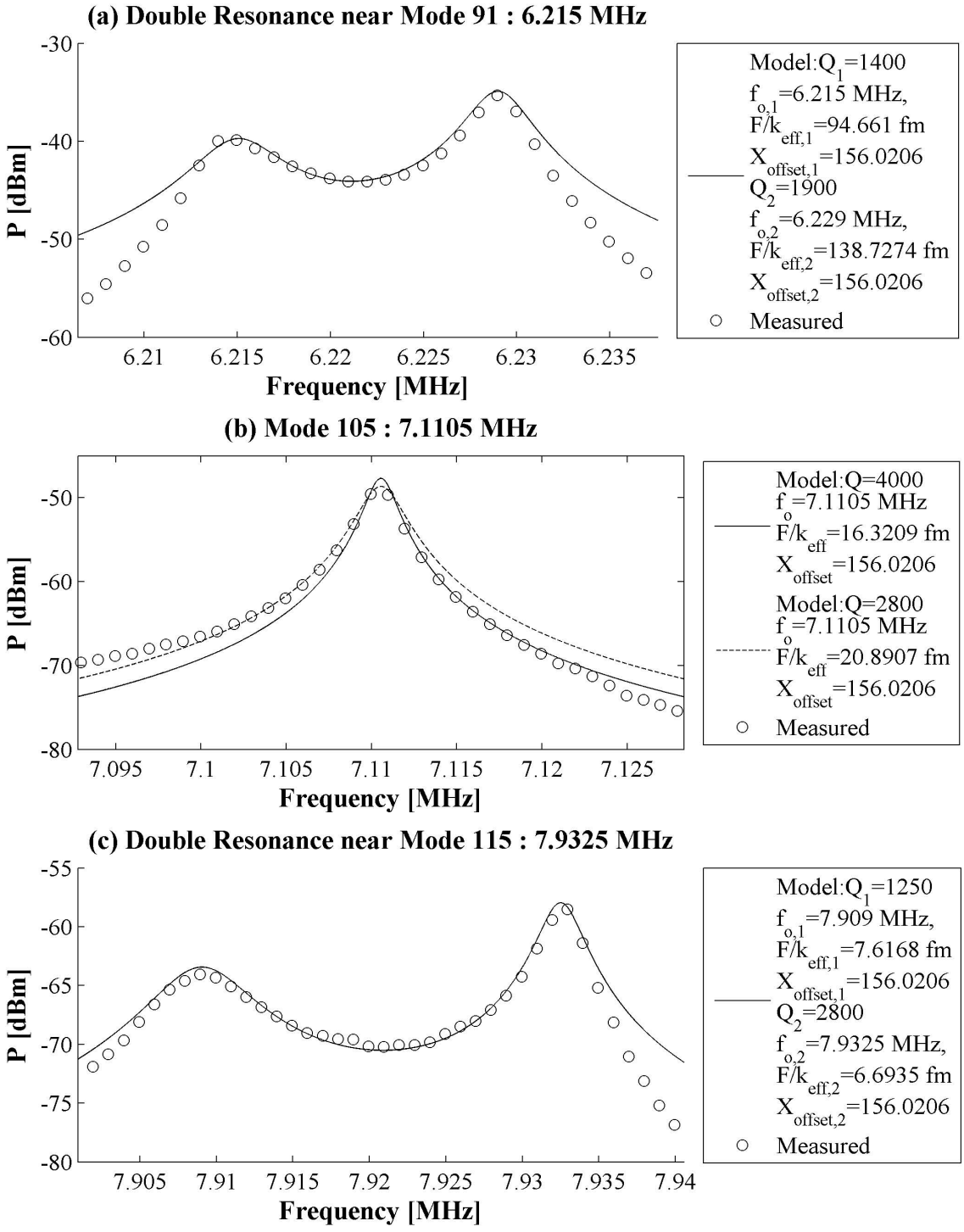

Figure 6.6: First order harmonic oscillator model fitted to experiment for sub-band gap modes 91, 105 and 115 of the S2 phononic band gap quasi-crystal device. The fit was performed within a normalized bandwidth ($\Delta f/f_o$) of 0.005.

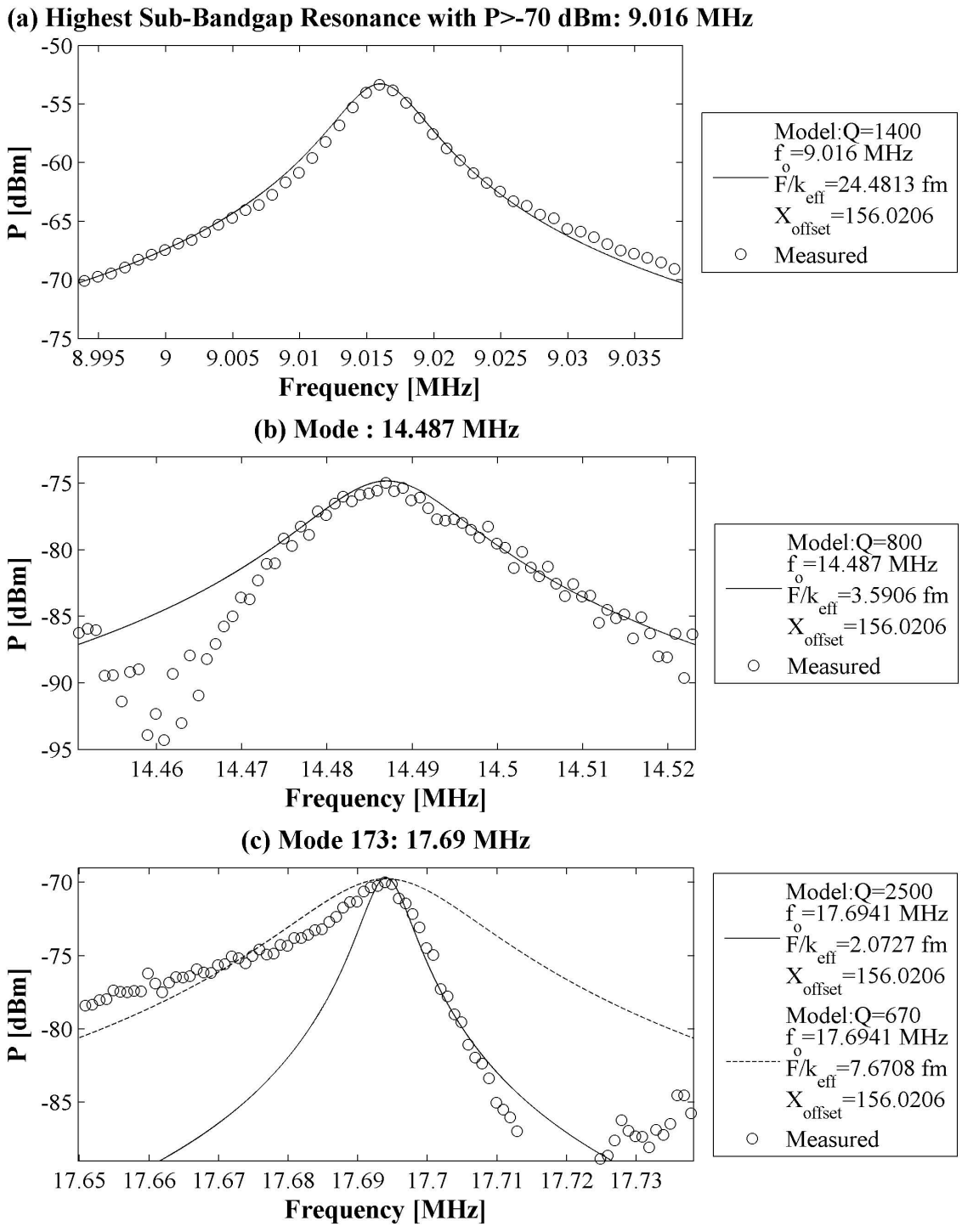

Figure 6.7: First order harmonic oscillator model fitted to experiment for the sub-band gap resonance at 9.016 MHz, hyper-band gap resonance at 14.487 MHz and mode 173 of S2 phononic band gap quasi-crystal device. The fit was performed within a normalized bandwidth ($\Delta f/f_o$) of 0.005.

Table 6.1: Parameters (from Figures 6.5, 6.6 and 6.7) for the fit of the first order harmonic oscillator model (of Section 4.2.5) to the experimental vibrometer spectrum centered at various normal modes of the S2 phononic band gap quasi-crystal. The listed effective normalized mechanical parameters were computed utilizing Equation 4.32 normalized to the forcing function, F, which was modeled in Sections 4.3 and 4.1.2 and represents and experimental unknown. The resonant frequency under damping may be expressed as $f_{undamped}\sqrt{1-\xi}$ where $\xi = \gamma/(2\sqrt{k_{eff}m_{eff}})$ is the critical damping fraction and $f_{undamped}$ is the undamped resonant frequency [138]. When $\xi < 0.1$ the resonant frequency of the damped system may be well approximated by the resonant frequency of the undamped system [138]. Mode 1 was fitted within a normalized bandwidth ($\Delta f/f_o$) of 0.3 while all other modes were fitted within a normalized bandwidth of 0.005.

			Fit Parameters			**Effective Values Normalized to Force Amplitude, *F***			
			Damped Resonant Frequency	**Force Amplitude Over Effective Spring Constant†**	**Quality Factor**	**Normalized Effective Spring Constant**	**Normalized Effective Mass**	**Normalized Damping Coefficient**	**Critical Damping Fraction**
Branch	**Mode Number**		**f_o (MHz)**	**F/k_{eff} (fm)**	**Q_{mech}**	**k_{eff}/F (GN/(m·N))**	**m_{eff}/F (μg/N)**	**γ/F (1/N)**	**ξ (1/(kg·N/m)$^{1/2}$)**
Sub-band gap	1		0.082475	$6.528\cdot10^{4}$	180	$1.532\cdot10^{1}$	$5.704\cdot10^{4}$	$1.642\cdot10^{2}$	$2.778\cdot10^{-3}$
	42	max Q:	2.8634	$6.924\cdot10^{1}$	2100	$1.444\cdot10^{4}$	$4.462\cdot10^{4}$	$3.822\cdot10^{2}$	$2.381\cdot10^{-4}$
		min Q:	2.8634	$9.232\cdot10^{1}$	1500	$1.083\cdot10^{4}$	$3.346\cdot10^{4}$	$4.014\cdot10^{2}$	$3.333\cdot10^{-4}$
	73		4.8973	$1.523\cdot10^{2}$	1400	$6.564\cdot10^{3}$	$6.933\cdot10^{3}$	$1.524\cdot10^{2}$	$3.571\cdot10^{-4}$
	91		6.2150	$9.466\cdot10^{1}$	1400	$1.056\cdot10^{4}$	$6.928\cdot10^{3}$	$1.932\cdot10^{2}$	$3.571\cdot10^{-4}$
	Unknown		6.2290	$1.387\cdot10^{2}$	1900	$7.208\cdot10^{3}$	$4.706\cdot10^{3}$	$9.694\cdot10^{1}$	$2.632\cdot10^{-4}$
	105	max Q:	7.1105	$1.632\cdot10^{1}$	4000	$6.127\cdot10^{4}$	$3.070\cdot10^{4}$	$3.429\cdot10^{2}$	$1.250\cdot10^{-4}$
		min Q:	7.1105	$2.089\cdot10^{1}$	2800	$4.787\cdot10^{4}$	$2.398\cdot10^{4}$	$3.827\cdot10^{2}$	$1.786\cdot10^{-4}$
	Unknown		7.9090	7.617	1250	$1.313\cdot10^{5}$	$5.316\cdot10^{4}$	$2.114\cdot10^{3}$	$4.000\cdot10^{-4}$
	115		7.9325	6.694	2800	$1.494\cdot10^{5}$	$6.014\cdot10^{4}$	$1.071\cdot10^{3}$	$1.786\cdot10^{-4}$
	Unknown		9.0160	$2.448\cdot10^{1}$	1400	$4.085\cdot10^{4}$	$1.273\cdot10^{4}$	$5.150\cdot10^{2}$	$3.571\cdot10^{-4}$
Hyper-band gap	Unknown		14.4870	3.591	800	$2.785\cdot10^{5}$	$3.361\cdot10^{4}$	$3.825\cdot10^{3}$	$6.250\cdot10^{-4}$
	173	max Q:	17.6941	2.073	2500	$4.825\cdot10^{5}$	$3.903\cdot10^{4}$	$1.736\cdot10^{3}$	$2.000\cdot10^{-4}$
		min Q:	17.6941	7.671	670	$1.304\cdot10^{5}$	$1.055\cdot10^{4}$	$1.750\cdot10^{3}$	$7.463\cdot10^{-4}$

† Fitted for the X_{offset} = 156.021 dBm provided in Section 4.2.5.

6.2.2 Mode Shape Topography

In order to assess the accuracy of the FEM model of the physical shape of P^{n}BG QC normal modes presented in Section 4.2.3, the normal mode shape displacement in the $\hat{z}$-direction is measured with respect to position. Reasonable agreement between the node and anti-node topography of the fourteen FEM model and measured mode shapes in Figure 6.8 illustrate confirmation of the characteristic out-of-plane sub- and hyper-band gap mode shapes for the S2 P^{n}BG QC. Time permitted for the measurement of eight sub-band gap modes of the C2 P^{n}BG QC, which are displayed along with the corresponding FEM model mode shape in Figure 6.9. For comparison, fifteen FEM model and measured mode for the Square reference are displayed in Figure 6.10.

By comparing the P^{n}BG QC mode shapes of Figures 6.8 and 6.9 with those of the Square reference in Figure 6.10, the influence of the P^{n}BG QC geometry is apparent on the confinement of vibrations within the periodically shaped host region of the P^{n}BG QC. Mode shape measurements for the S1 P^{n}BG QC may be found in Appendix H.

Distortion with respect to position in measured mode shape may be accounted for in part by stepper motor error, anchor loss, damping, material anisotropy and fabrication error. Deviation between the modeled and measured mode shape may also potentially be created if a non-linearity in the P^{n}BG QC architecture excites creates a harmonic in a way that the harmonic frequency corresponds with an adjacent mode frequency. In this way, a single excitation frequency may excite two modes, which may distort one another, leading to deviation between the measured and modeled mode shape. Even at low power levels, where the forces may be limited such that the device operates in the regime of the linear Hook's law and the linear region of the P^{n}BG QC, a potential source of non-linearity may be in the conversion between voltage and electrostatic force [97] in the electrostatic transducer which may behave as a parallel plate capacitor.

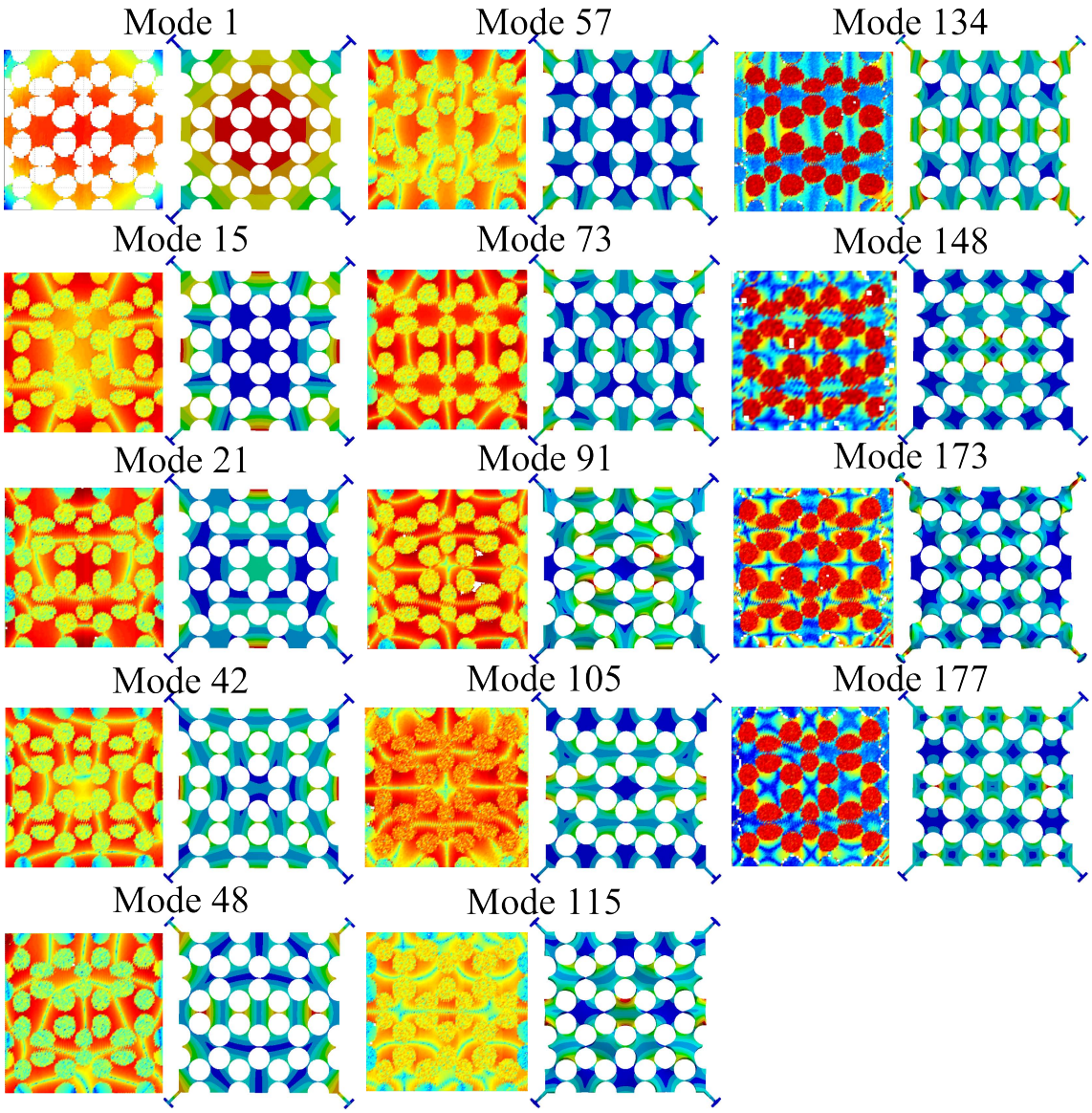

Figure 6.8: Measured normal mode surface topography for the S2 phononic band gap quasi-crystal versus the ANSYS® finite element method model. Sub-band gap modes are: (n=1 , 82.475 kHz), (n=15, 934.925 kHz), (n=21, 1.857500 MHz), (n=42, 2.863400 MHz), (n=48, 3.090175 MHz), (n=57, 3.918900 MHz), (n=73, 4.899325 MHz), (n=91, 6.216875 MHz), (n=105, 7.110550 MHz), (n=115, 7.933175 MHz), and (n=134, 9.254000 MHz). Hyper-band gap modes are: (148, 14.486350 MHz), (n=173, 17.694050 MHz) and (177, 19.903000 MHz).

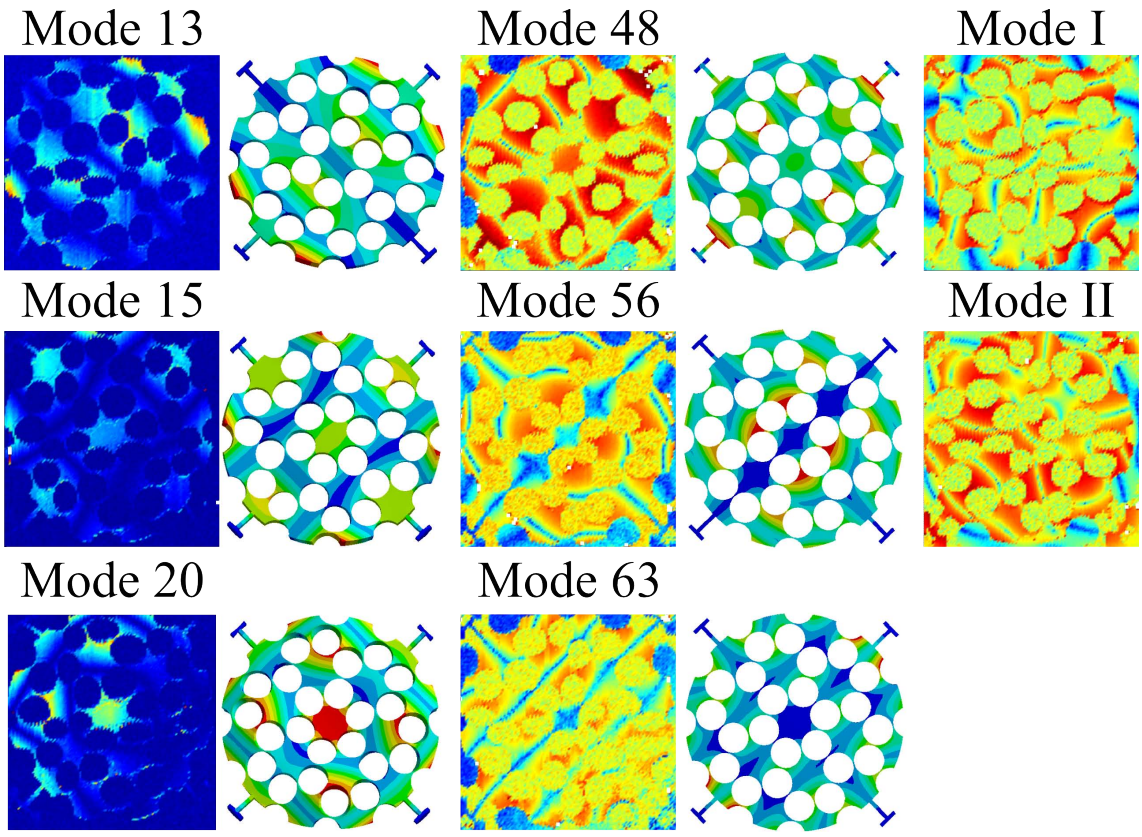

Figure 6.9: Measured normal mode surface topography for the C2 phononic band gap quasi-crystal versus the ANSYS® finite element method model. Sub-band gap modes are: (n=13, 1.344000 MHz), (n=15, 1.712000 MHz), (n=20, 2.567000 MHz), (n=48, 4.675000 MHz), (n=56, 5.700000 MHz), (n=63, 6.673000 MHz), (unidentifiable mode I, 7.415000 MHz) and (unidentifiable mode II, 9.385000 MHz).

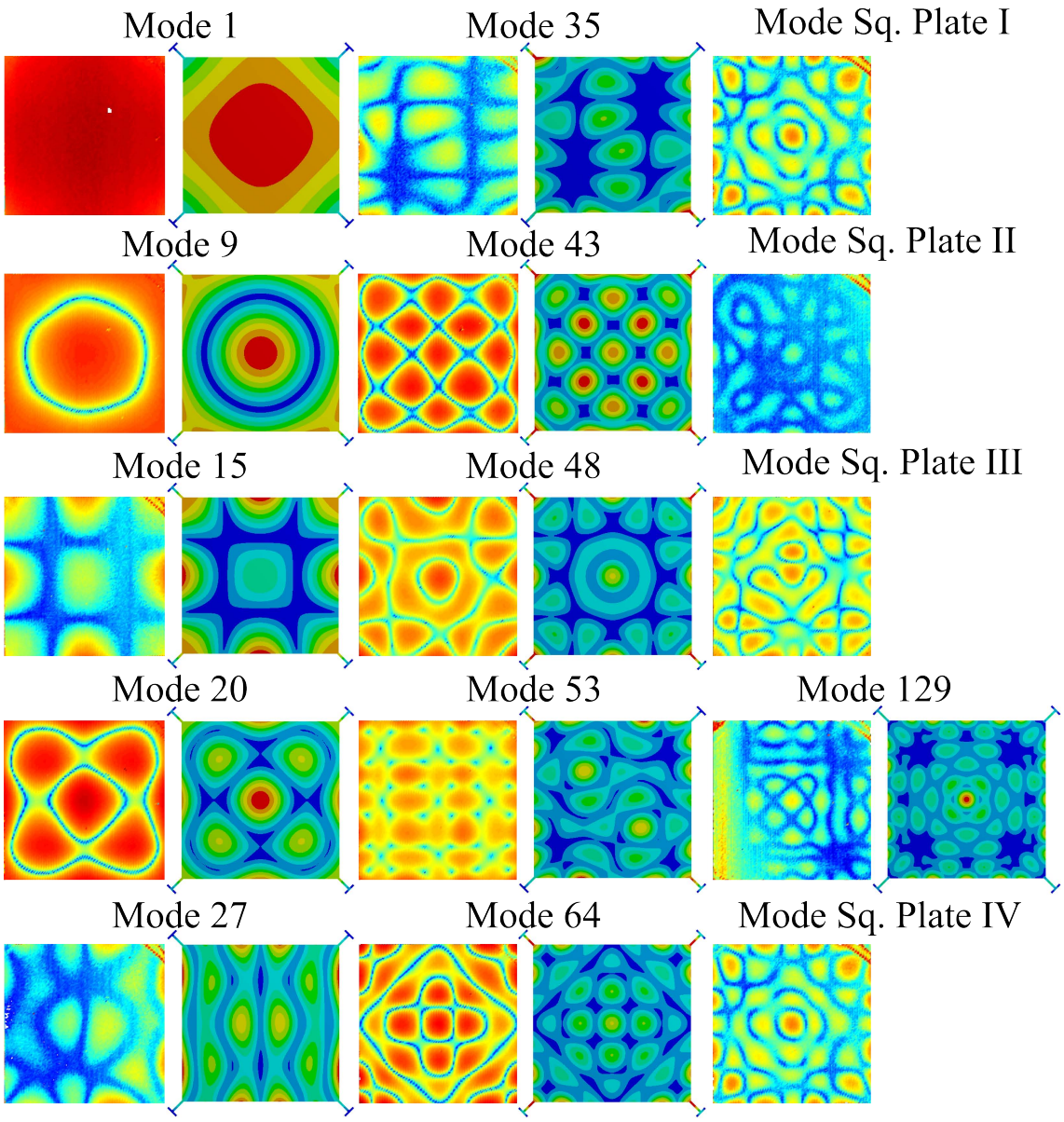

Figure 6.10: Measured normal mode surface topography for the homogeneous square plate phononic band gap quasi-crystal versus the ANSYS® finite element method model. Modes shapes are: (n = 1, 119.998 kHz), (n = 9, 767.993 kHz), (n = 15, 1.599986 MHz), (n = 20, 2.864977 MHz), (n = 27, 4.463965 MHz), (n = 35, 5.305959 MHz), (n = 43, 6.626948 MHz), (n = 48, 7.343942 MHz), (n = 53, 8.099935 MHz), (n = 64, 9.246926 MHz), (n = 129, 18.266852 MHz), (unidentifiable square plate mode I, 12435900 Hz), (unidentifiable square plate mode II, 13525892 Hz), (unidentifiable square plate mode III, 14988881 Hz) and (unidentifiable square plate mode IC, 19428842 Hz).

6.2.3 Frequency Versus Mode Number Characteristic

The measured frequencies of the FEM model mode shapes are combined with the FEM model mode number for square and circular truncated P^{n}BG QC in Figures 6.11 and 6.12. Reasonable support for an approximately piecewise linear relation between mode frequency and number may be observed in Figures 6.11, and 6.12, for the S1 and S2, and C2, P^{n}BG QC devices, respectively. A linear projection of the measured normal mode points for the C2 P^{n}BG QC in Figure 6.12 may provide insight into the experimental band gap location.

Measured and model results for S1, S2 and C2 P^{n}BG QC devices and Square reference device are superimposed in Figure 6.13. The measurements provide reasonable experimental support for the trend that band gap location increases as geometry is varied from the S1 to the S2 to the C2 P^{n}BG QC device. In addition, all frequency versus mode number characteristics originate at approximately the same point and diverge from one another as mode number and frequency increase. This experimentally supports the presence of the behavioral zones observed in the model of Section 4.2.1. For the square Reference device, the modes that were observed to be present in the harmonic response (of Figure 6.4) between approximately 12 MHz and 18 MHz could not be identified and so are not plotted in Figure 6.13. In Figure 6.13, the absence of modes between approximately 10 MHz and 13 MHz for the S1 and S2 P^{n}BG QC devices reflects the result that no normal mode resonances were observed in the measured spectrum (of Figure 6.4) within this frequency region and may provide support for the experimental band gap location. The error between the model and measured mode frequency increases as frequency increases.

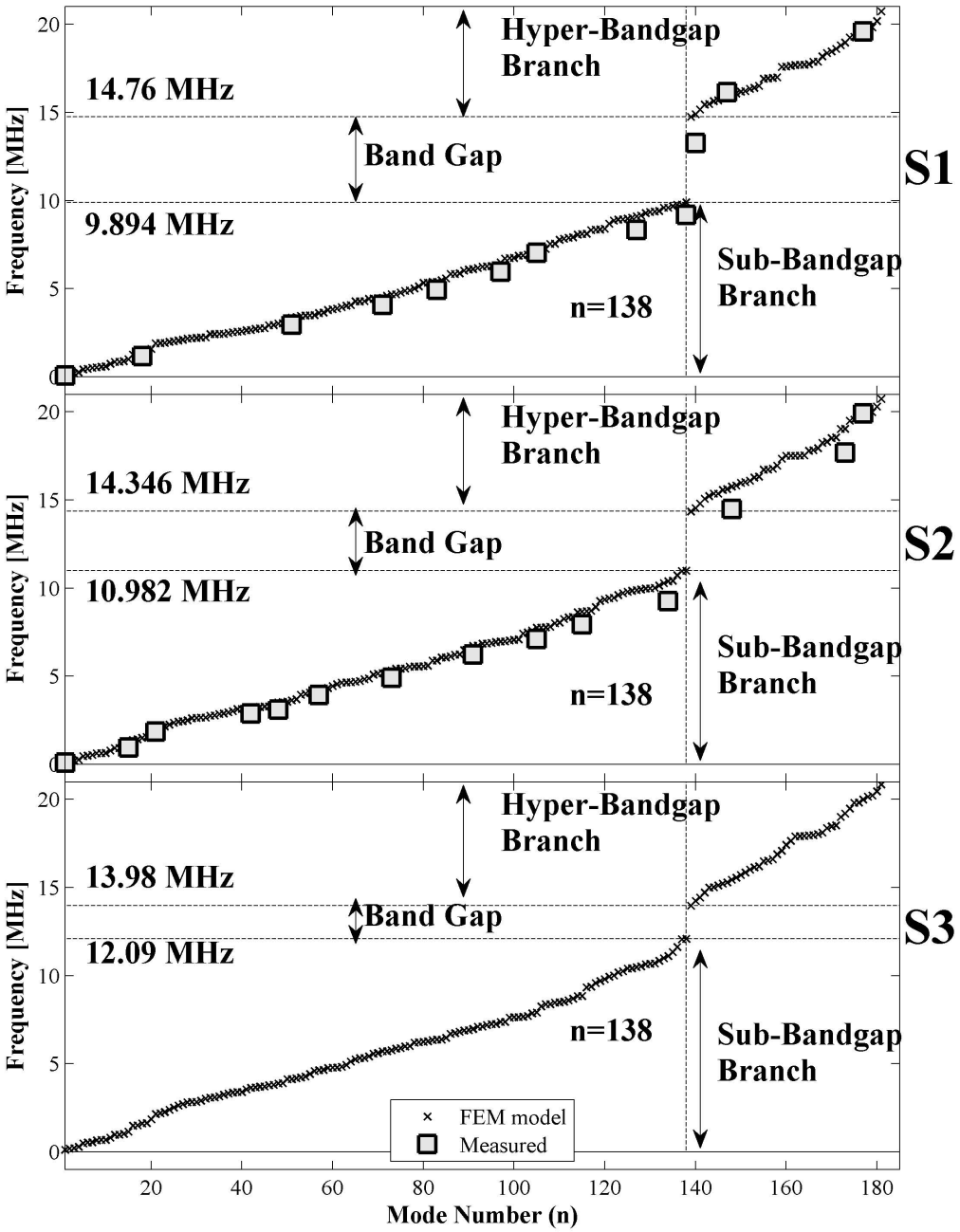

Figure 6.11: Measured frequencies of finite element method model mode numbers for the S1 and S2 phononic band gap quasi-crystals. The finite element method model is denoted the by 'x' while measurement points are denoted by the squares. Time did not permit measurement of the S3 phononic band gap quasi-crystal.

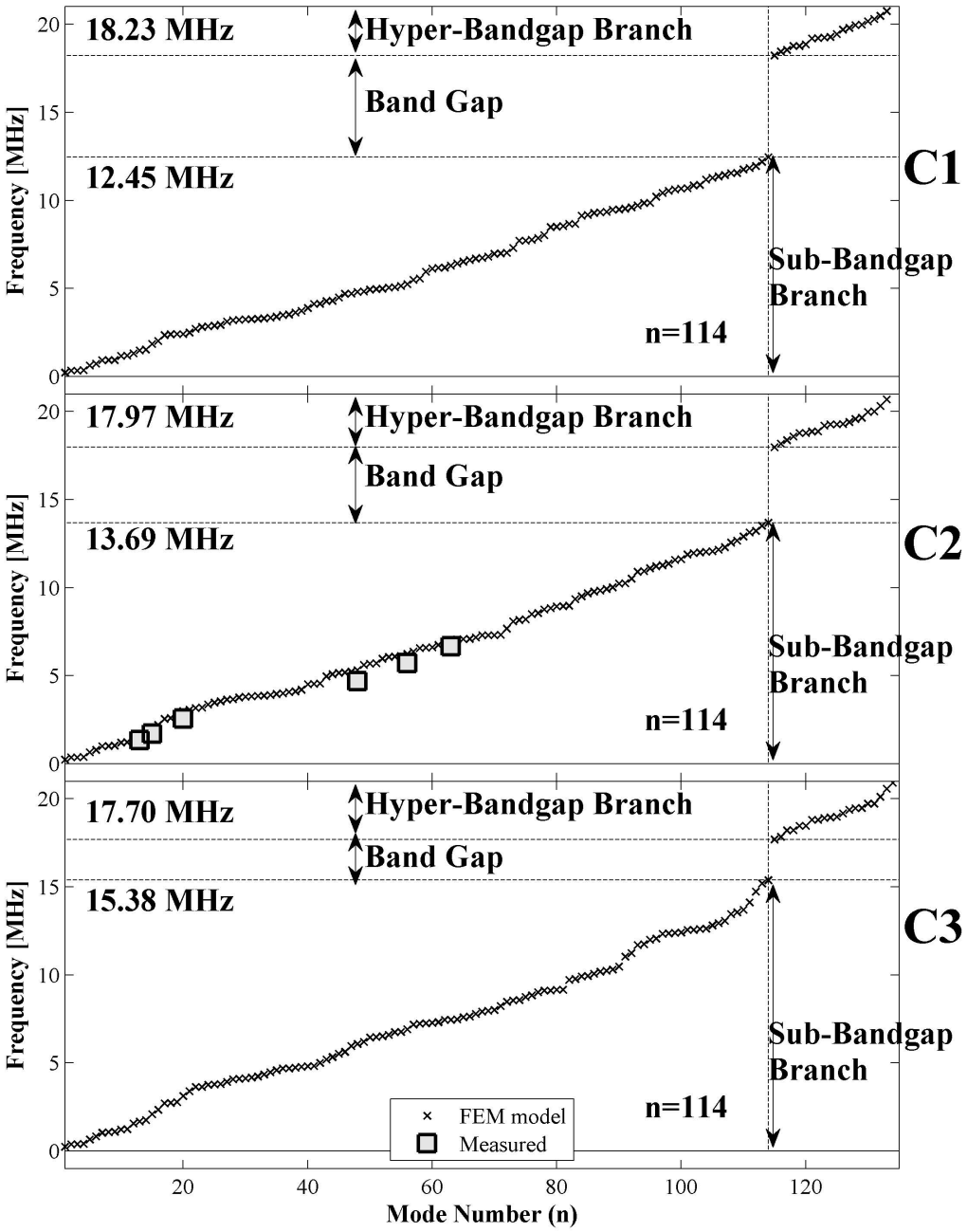

Figure 6.12: Measured frequencies of finite element method model mode numbers for the circular truncated phononic band gap crystals. The finite element method model is denoted the by 'x' while measurement points are denoted by the squares. Time did not permit measurement of the C1, C3, nor hyper-band gap modes of the C2 phononic band gap quasi-crystals.

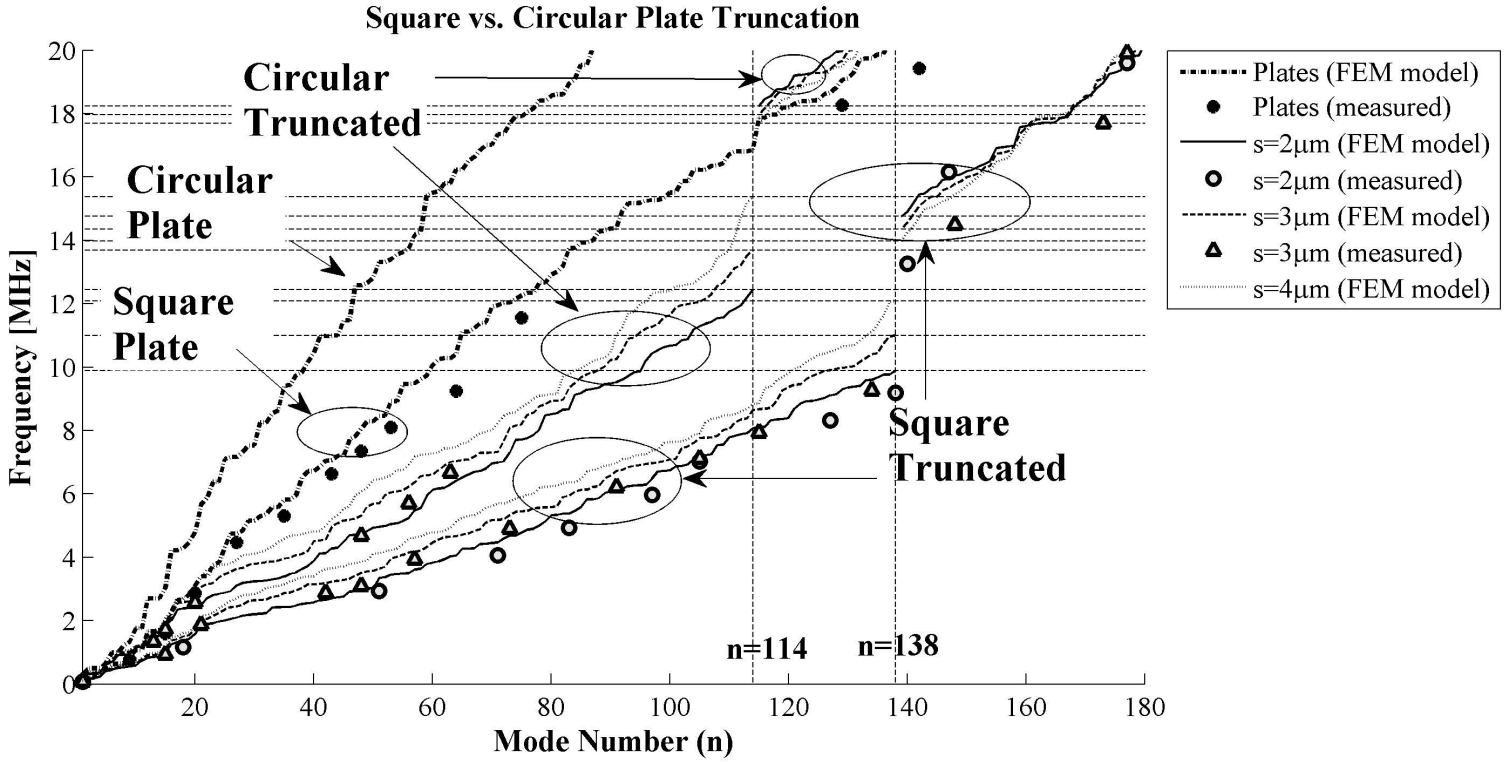

Figure 6.13: Measured versus finite element method model mode frequencies for square and circular truncated (S1, S2, C2) phononic band gap quasi-crystal devices and the homogeneous Square reference devices versus the finite element method mode numbers. For the square Reference device the mode numbers of the modes that were observed to be present in the harmonic response (of Figure 6.4) between approximately 12 MHz and 18 MHz could not be identified and so are not plotted here. The absence of modes between approximately 10 MHz and 13 MHz for the S1 and S2 phononic band gap quasi-crystal devices reflects the result that no normal mode resonances were observed in the measured spectrum (of Figure 6.4) within this frequency region and may provide support for the experimental band gap location.

6.2.4 Electrostatic Spring Softening

For an increased DC bias voltage, resonant frequency may be expected to decrease due to electrostatic spring softening [97]. For one measurement point, the spectrum of the S2 P^{n}BG QC versus DC voltage is displayed in Figure 6.14 and closeups are displayed in Figures 6.15 and 6.16. At this measurement point, the resonant peak and band gap location presented in Figure 6.14 display no observable (less than 50 Hz) change as DC bias voltage is varied. This may possibly be attributed to the application of balanced voltages to the relatively similar transducers of the S2 P^{n}BG QC device and possible generation of relatively balanced electrostatic forces that may oppose one another to counteract potential spring softening and stabilize band gap location with respect to DC bias voltage. The sensitivity of spring softening to electrode configuration of discussed next.

Relative to the case where only one electrostatic transducer is acting to displace the body of the P^{n}BG QC in a given direction and reduce the electrostatic gap in a way that leads to pull-in and spring softening, the utilization of the four balanced electrode configuration, presented in Section 3.4, may change the pull-in voltage and affect spring softening. To justify this, assume that the fixed (anchored) electrode of the electrostatic transducer is anchored in a way that the fixed electrode undergoes zero displacement (note that, as discussed Section J.2 of Appendix J, the fixed electrode moves considerably and this should be accounted for in a complete analysis). Next observe that in the P^{n}BG QC architecture, approximately equal but opposite (balanced) forces are present on diametrically oppose transducers. These balanced forces may counteract one another in a way that the center of the P^{n}BG QC displays no net displacement and so acts as a virtual mechanical ground or fixed boundary (as was observed in the electromechanical model presented in Section 4.3) which may counter act pull-in. Pull-in would then have

to occur by stretching the P^{n}BG QC pseudo-extensionally from all four edges until the stress on the edges would produce enough strain that the electrostatic transducer gap would be reduced enough to increase the electrostatic force to exceed the restoring force of the edges. In contrast, if a single transducer acted upon the P^{n}BG QC, pull-in may occur via a different mechanism and so may occur at a different voltage. Hence, pull-in and spring softening may be a function of the transducer electrode configuration. The observed insensitivity of the P^{n}BG QC to DC bias may then in part be a feature of the balanced transducer configuration. In addition, electrostatic spring softening is larger near pull-in [97]. The bias voltage may be too far from the pull-in voltage to allow spring softening to be observable. Numerical and experimental characterizations of pull-in voltage and spring softening versus electrode configuration may be investigated further.

Alternatively, the absence of observable spring softening may potentially be due to the measurement of the out-of-plane component of vibration that was presented in Figure 6.14. Spring softening may be more observable in the in-plane (which is the plane in which the model of Section 4.3 suggests that the dominant component of the electrostatic force is generated) component of vibration.

Moreover, the P^{n}BG QC is a relatively complex structure that is subject to electrostatic forces that are applied primarily to the edges of the P^{n}BG QC in four different directions. These complexities may potentially result in electrostatic spring softening being a function of position within the P^{n}BG QC. Hence, spring softening may potentially be more observable at positions other than the point measured in Figure 6.14. For example, it may be possible that spring softening is more observable in the vicinity of the electrostatic transducers, near the edges of the P^{n}BG QCs, and less observable near the center of the P^{n}BG QC. The potential position sensitivity of electrostatic spring

softening in the P^nBG QC may be investigated further.

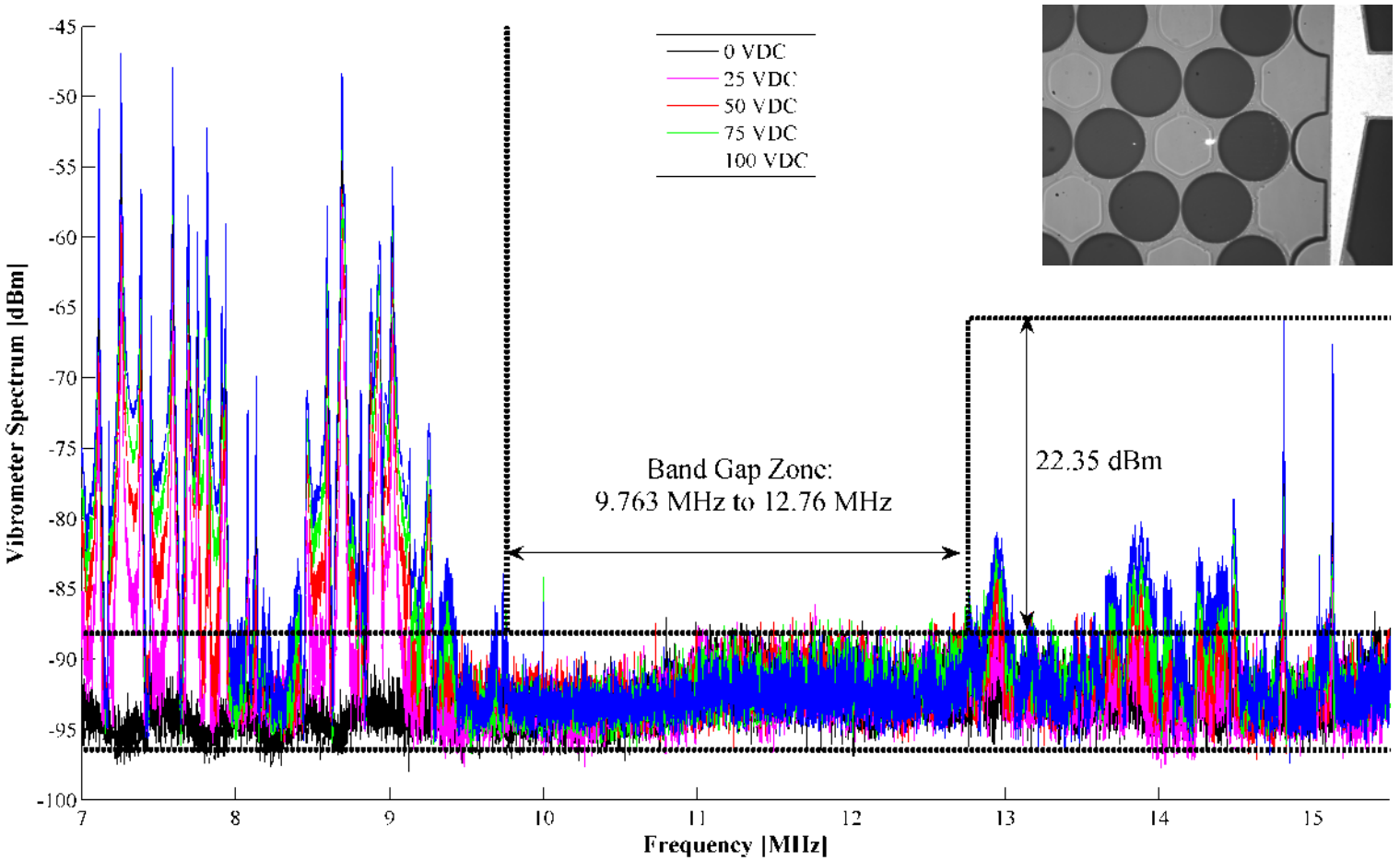

Figure 6.14: Harmonic analysis of S2 phononic band gap quasi-crystal versus DC bias voltage, V_{DC}. Negligible (less than the 50 Hz measured frequency resolution) change in the band gap location is observed as DC bias is varied.

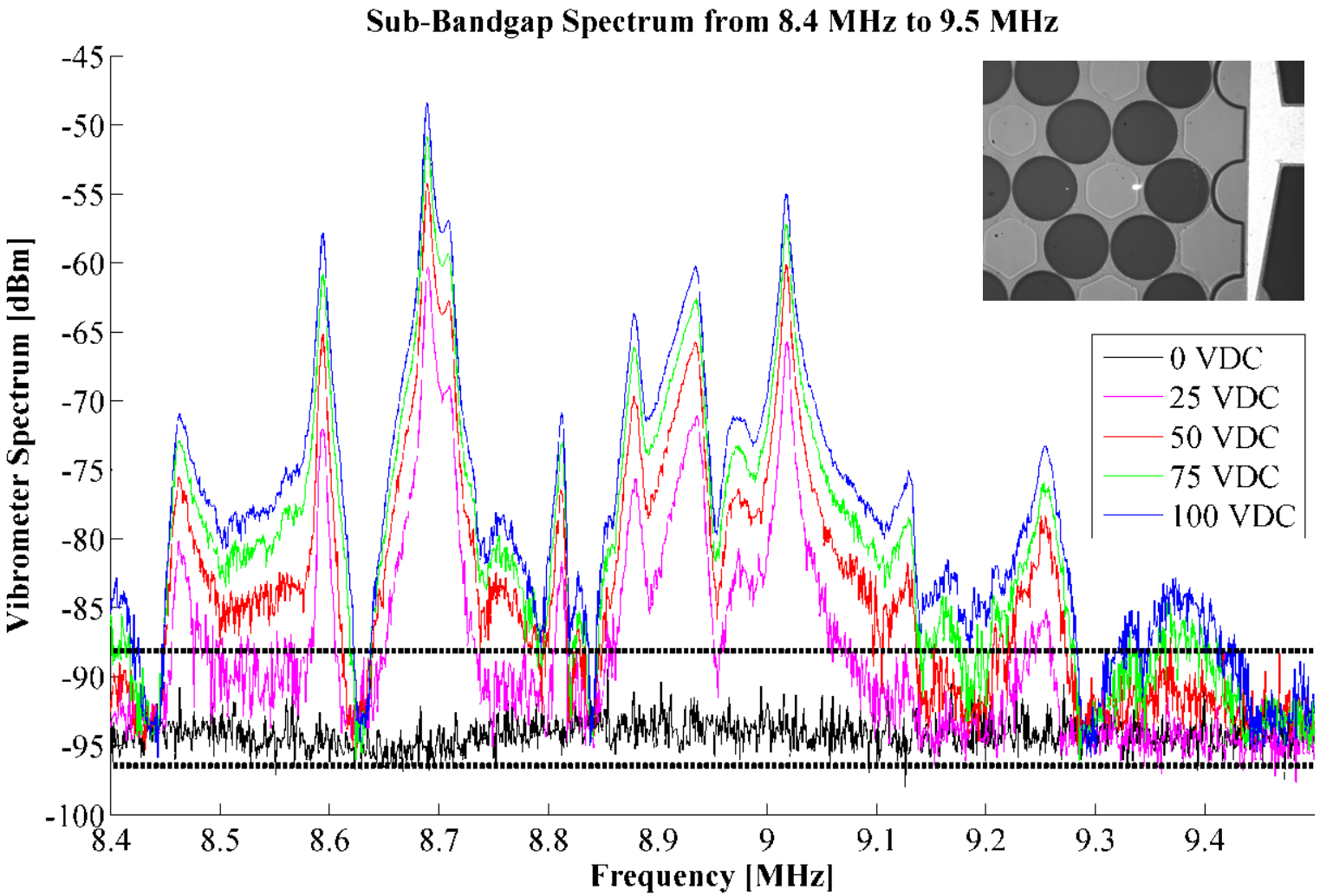

Figure 6.15: Harmonic analysis of a portion of the sub-band gap branch of the S2 phononic band gap quasi-crystal versus DC bias voltage, V_{DC}.

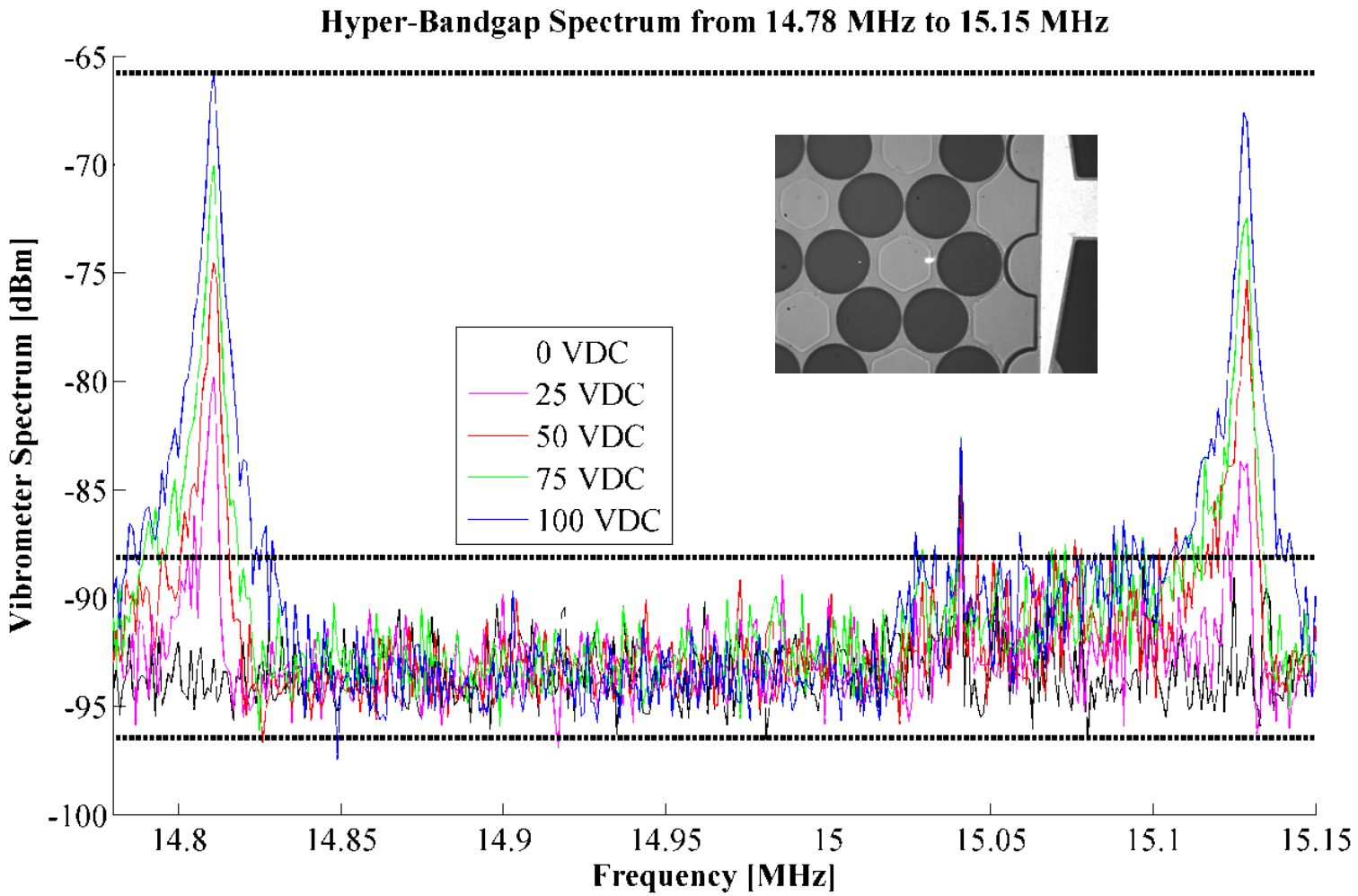

Figure 6.16: Harmonic analysis of a portion of the hyper-band gap branch of the S2 phononic band gap quasi-crystal versus DC bias voltage, V_{DC}.

6.2.5 Electro-Mechanical Coupling

The measured vibrometer spectra of the S1, S2, C2 P^{n}BG QCs and Square reference device have been presented in the units of power, or dBm, versus frequency. In this section, Equation 6.3 is utilized to convert the units of the vibrometer spectrum from power to the displacement amplitude in meters. This conversion will reveal the mechanical displacement amplitudes in the $\hat{z}$-direction that are physically generated by the electrostatic transducers.

The spectrum for the S2 P^{n}BG QC that was displayed in Figure 6.4 has been converted from the units of power to amplitude in meters and is displayed in Figure 6.17. The displacement amplitudes in the $\hat{z}$-direction at sub-, and hyper-, band gap frequencies may be observed to vary from approximately $10nm$ to $10^{-4}nm$, and $10^{-2}nm$ to $10^{-4}nm$, respectively. The DD-300 displacement decoder has a measurement range of $\pm 75nm$ and a non-linear error of approximately 2% at displacement amplitudes of 5 nm, 0% at displacement amplitudes of 50 nm and 7% at displacement amplitudes of 75 nm [129]. The measured displacement amplitudes of the spectrum at very low frequencies (approximately 50 kHz to 500 kHz) where the displacement amplitude is between 2 nm and 10 nm may then have an error of 2%. Above approximately 500 kHz the displacement amplitude is less than 1 nm which is below the documented range of the non-linear error curve of the vibrometer and so the measured amplitudes may contain an unknown percentage error.

Let F be some electrostatic force, generated by the electrostatic transducers, produced by a voltage, V_{RF}, and acting within the x, y-plane on the P^{n}BG QC. Let the displacement amplitude in the $\hat{z}$-direction, at a position $\vec{r} = (x_i, y_i)$ on the top surface of the P^{n}BG QC, for an arbitrary frequency, f, be $u_z(x_i, y_i, f)$. During measurements, the amplitude of the RF voltage was fixed at $V_{RF} = 10V_{pp}$ for all frequencies.

The electromechanical coupling coefficient between the voltage, V_{RF}, and displacement amplitude $u_z(x_i, y_i)$, versus frequency, f, may be expressed as $K_{elec-mech}(x_i, y_i, f) = u_z(x_i, y_i, f)/V_{RF}$.

For the maximum, and minimum, observed displacement amplitudes of approximately $10nm$, and $10^{-4}nm$, in Figure 6.17, the maximum, and minimum, dynamic coupling coefficient to the point (x_1, y_1) measured in Figure 6.17 (denoted by the laser spot location in Figure 6.4 for the S2 P$^{\text{n}}$BG QC) are:

$$\begin{aligned} K_{elec-mech,max}(x_1, y_1, f_1) &= u_z(x_1, y_1, f_1)/V_{RF} \\ &= 10nm/10V_{pp} \\ &= 1nm/V_{pp}, \end{aligned} \tag{6.4}$$

and

$$\begin{aligned} K_{elec-mech,min}(x_1, y_1, f_2) &= u_z(x_1, y_1, f_2)/V_{RF} \\ &= 10^{-4}nm/10V_{pp} \\ &= 10fm/V_{pp}, \end{aligned} \tag{6.5}$$

respectively. Unlike the static coupling coefficient of the model in Section 4.3, the aforementioned coupling coefficients include the experimental dynamics of the P$^{\text{n}}$BG QC devices.

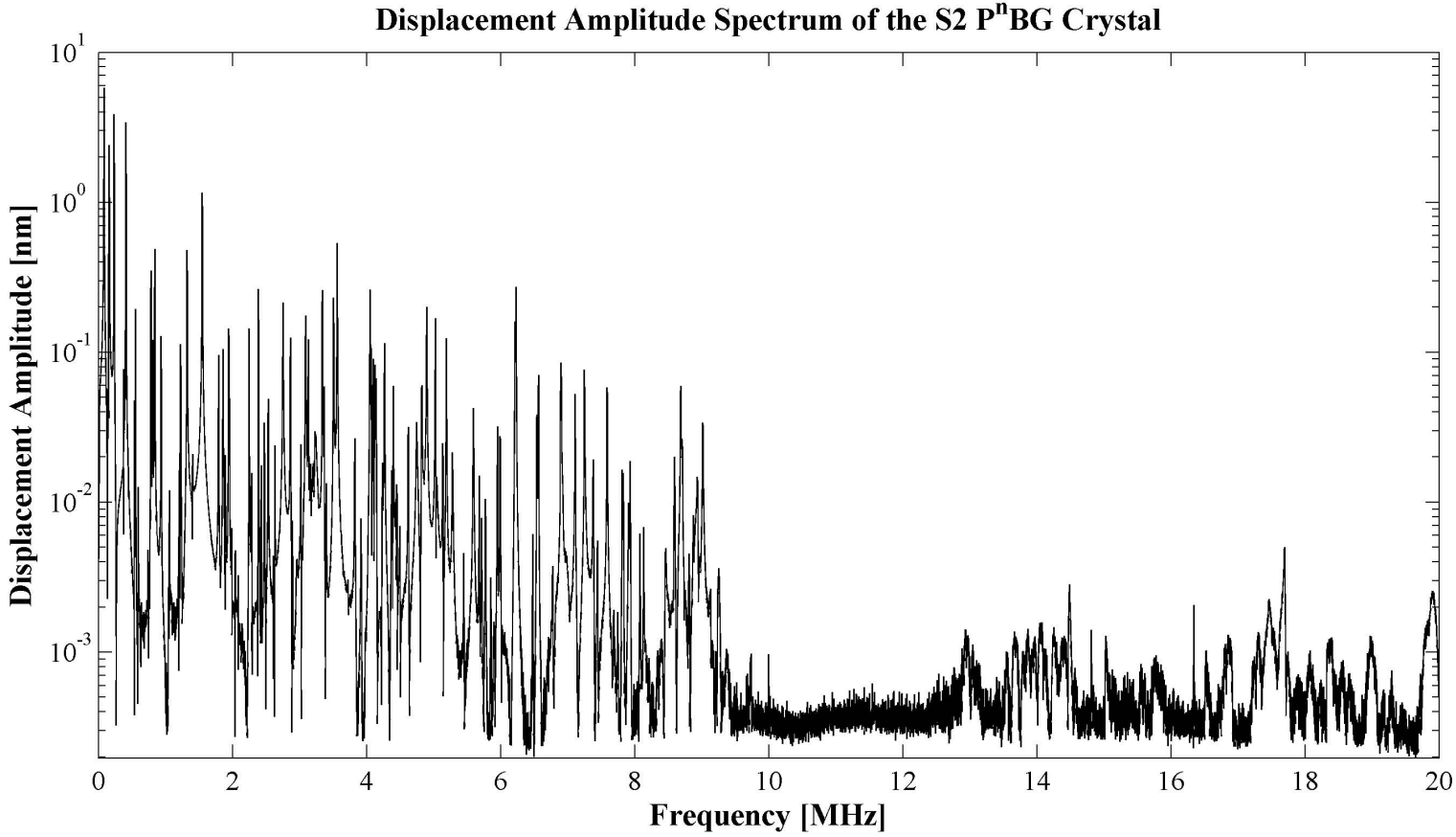

Figure 6.17: Displacement spectrum of the S2 phononic band gap quasi-crystal The dynamic range of the measured displacement amplitude is from approximately $10nm$ to approximately $10^{-4}nm = 0.1pm$.

6.3 Discussion of Experimental Results

The measurements of P^{n}BG QCs and reference devices presented in this chapter display reasonable agreement with the dynamic harmonic, mode shape and frequency versus mode shape models that were presented in Chapter 4. The dynamic harmonic spectrum of the P^{n}BG QCs displays a range of frequencies within which there appears be an absence of resonant peaks in the $\hat{z}$-component of displacement at several points on the surface of the P^{n}BG QCs. The P^{n}BG QC mode shapes, display characteristic shapes at sub- and hyper-band gap frequencies. The piecewise linear shape of the FEM model mode number versus frequency was also experimentally supported. Further identification of the experimental band gap location requires measurement of in-plane modes and a higher signal to noise ratio to measure potential defect state modes that may exist at the frequencies where the experimental band gap appears to exist. Lastly, though the electrostatic transducers were modeled to generate primarily in-plane forces (see Section 4.3), the electrostatic transducers were observed to successfully excite the out-of-plane modes of the P^{n}BG QCs with a measurable displacement amplitude, which is also consistent with the model behavior (of Section 4.2.5).

The dynamic harmonic analysis measurements presented in this chapter were not de-embedded from the potential frequency dependence of the excitation circuitry or electrostatic force; while the electrical models of Chapter 4 indicate a relatively uniform excitation voltage should be presented with respect to frequency on each electrostatic transducer, electrostatic force may still vary with frequency. The Square reference device, which was excited utilizing the same measurement circuit as the P^{n}BG QCs, was observed to be successfully excited at frequencies from 50 kHz to 20 MHz. Though the unique transducer geometry of the P^{n}BG QCs may present an input impedance that is slightly different from the Square reference device or have slightly different electrostatic

forces, the successful actuation of the Square reference suggests that the P^{n}BG QCs could potentially also have received electrostatic actuation over the 50 kHz to 20 MHz range. The observed absence of modes in the frequency response of the S1, S2 and C2 P^{n}BG QCs for wide frequency ranges may then be due to an absence of mechanical resonant modes within these frequency ranges, as oppose to poor electrostatic excitation. Non-ideal experimental behavior of the electrostatic transducers is presented in Section J.2 of Appendix J; the potential impact of this non-ideal behavior may be investigated further.

To measure the potential frequency dependence of the electrical excitation circuitry, the node that interfaces the electrical excitation circuit with the electrostatic transducer may be probed utilizing a high input impedance probe and frequency could be swept from 50 kHz to 20 MHz to characterize the potential frequency dependence in the transference of the electrical signal from the function generator to the electrostatic transducer. Once the electrical signal that is physically applied to the transducer has been measured, the amplitude of the dynamic harmonic analysis (spectrum) measurements can be adjusted to de-embedded any amplitude variations that may be produced by the electrical excitation circuit. The result will be a spectrum that contains only the amplitude variations, with respect to frequency, that are produced by the frequency dependence of the electrostatic force and mechanical frequency selectivity of the P^{n}BG QC or reference devices.

Dynamic harmonic and mode shape measurements provide data concerning the discrepancies between the model and fabricated devices. These discrepancies may be produced by damping, anchor loss, electrical or mechanical parasitic elements, fabrication process errors, errors in the material properties utilized in the models, non-linearities that weren't accounted for in the model, and so forth, and may be characterized versus

frequency or on a mode by mode basis.

Model refinement was not presented in this thesis in part because a sufficient level of agreement between the measurements and model was observed to meet the objective of the thesis. As mentioned, accurate model refinement would require the investigation of the actual source of the discrepancy between the model and the fabricated device. A more rapid approach to model refinement may be to attempt to utilize effective material parameters to account for all discrepancies, and fit the model to the measured data utilizing these effective material parameters. These effective material parameters would attempt to account for all discrepancies, however, may not in all cases enable a fit of the model to the measurement, for example, an effective material parameter may not always be able to account for a structural difference. In some cases, multiple model refinements may be required in parallel. For example, a simple set of diagnostic test structures may be utilized to investigate the physical material properties, while scanning electron micrograph and profilometer measurements such as those of Section 5.2 may be utilized to quantify error in the geometry of the models.

A material property characterization was not performed due to the large area of the P^nBG QCs and the corresponding lack of available die space for a set of diagnostic test structures. In addition, a reasonable amount of material property data for SOIMUMPs was found in the literature (see Table 4.1) to provide sufficient data, for a first iteration design, into the expected range of material properties in SOIMUMPs. Lastly, the results of the sensitivity analysis of Section 4.2.6 illustrated a relatively low sensitivity of the band gap location to the ranges of material property variations that occur in practice. Material property characterization may be investigated further.

Chapter 7

Applicability of the Phononic Band Gap Quasi-Crystal Architecture to Temperature Sensors and Vibration Stabilization in Micro-Electro-Mechanical-Systems

Within this chapter the applicability of the P^{n}BG QC architecture to physical temperature sensors and localized or vibration stabilized resonators is developed. First, the temperature dependence of the band gap is investigated utilizing thermomechanical models and measurement of P^{n}BG QC mode frequency versus temperature. Second, the utility of the P^{n}BG QC architecture to create increasingly complex frequency selective characteristics, vibration stabilized or localized resonators, reduced anchor loss and potentially improved mechanical systems is developed through the introduction of defect

states into the P^{n}BG QC architecture.

7.1 Temperature Dependence of Band Gap

The temperature dependence of the normal mode frequencies of the S1 P^{n}BG QC was investigated numerically and experimentally. The experimental temperature dependence of the Square reference device was characterized under similar conditions to provide a reference for comparison with the temperature dependence of the S1 P^{n}BG QC device.

7.1.1 Thermomechanical Model

The FEM implementation in ANSYS® Workbench^{TM} 11.0 was utilized to perform a steady state thermal analysis which was used as the initial condition for a steady state structural analysis, which yields the internal stress generated by a temperature change. The stress field generated at a temperature of 60^oC is displayed in Figure 7.1 and was utilized as the initial condition for a modal analysis to determine the effect of temperature on the frequencies of the normal modes. The thermal expansion coefficient of single-crystal-silicon was set to $2.6 \times 10^{-6} \frac{1}{^oC}$ [139].

The result of the modal analysis for the S1 P^{n}BG QC at room temperature, 23^oC, and 60^oC is presented in Figure 7.2. The FEM model indicates that above behavioral zone II (see Figure 4.7 for the location of behavioral zone II) the sub-band gap resonant frequencies decrease (negative temperature coefficient) while hyper-band gap resonant frequencies increase (positive temperature coefficient). For the temperatures and normal mode frequencies studied here some sub-band gap normal mode frequencies, as compared to hyper-band gap frequencies, tend to display a larger change in frequency.

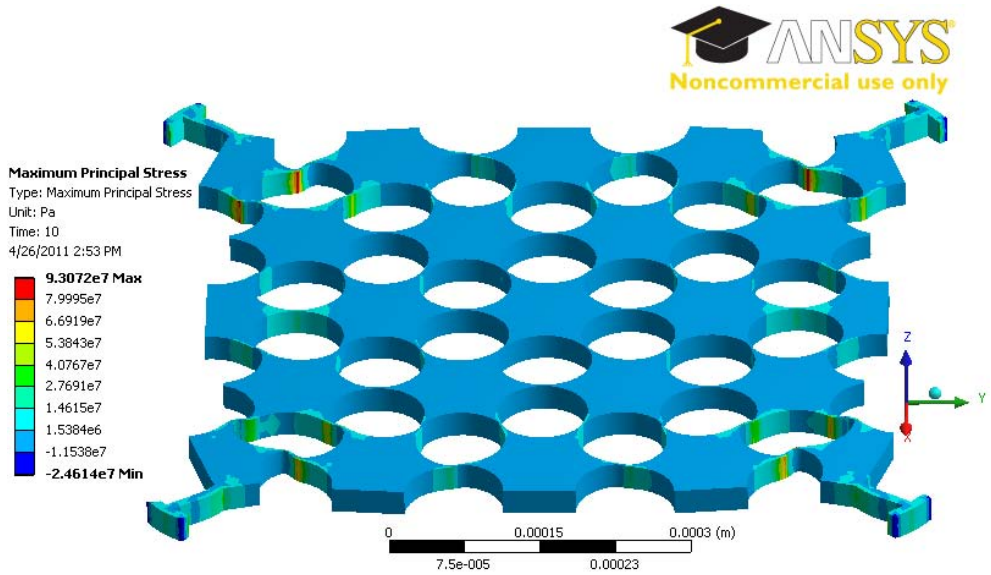

(a)

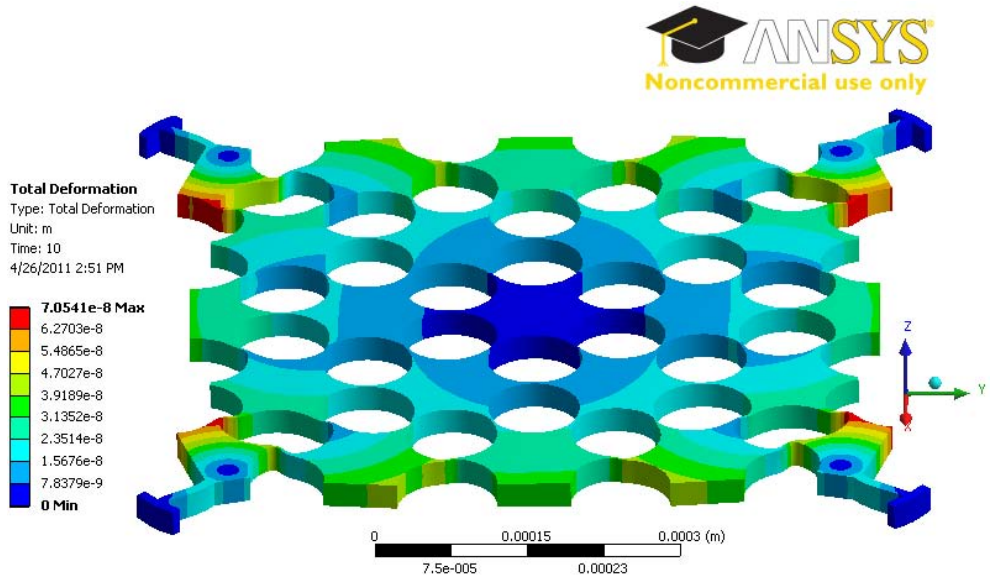

(b)

Figure 7.1: Finite element method thermomechanical model of the S1 phononic band gap quasi-crystal. The figure displays, for a temperature of 60^oC, (a) the maximum stress and (b) the deformation.

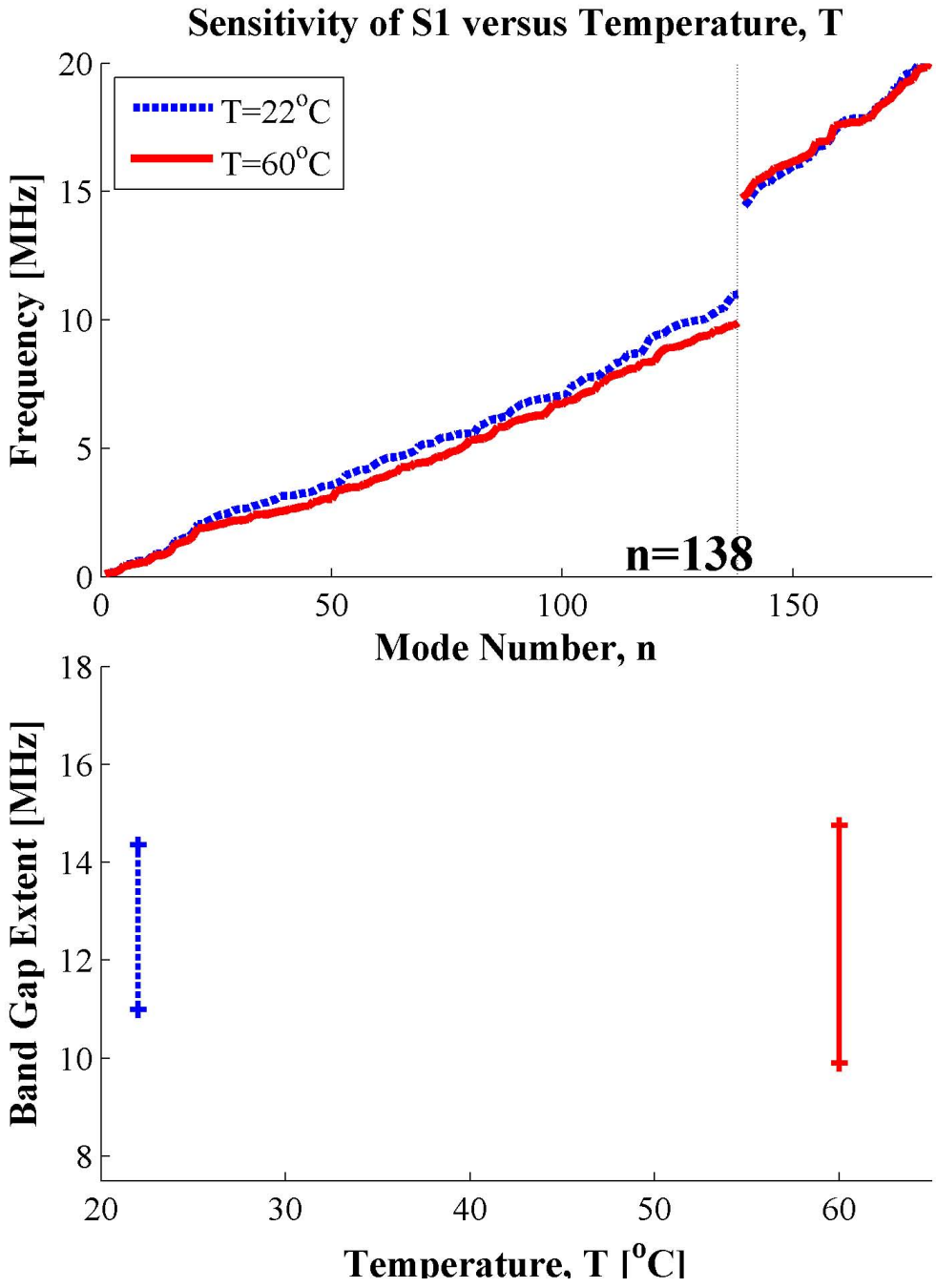

Figure 7.2: Finite element method model of the variation of normal mode frequency and band gap extent, versus temperature, for the S1 phononic band gap quasi-crystal. Above behavioral zone II (see Figure 4.7 for the location of behavioral zone II) the sub-band gap resonant frequencies dramatically decrease while hyper-band gap resonant frequencies increase.

7.1.2 Experimental Results

Dynamic harmonic analysis experiments were conducted at elevated temperatures on the S1 P^{n}BG QC. The experimental setup is illustrated in the schematic of Figure 7.3. The physical experimental setup is photographed in Figure 7.4. The infrared radiation source is a 500 W halogen lamp. The tip of the thermal couple is placed approximately $5mm$ away from the device under test. In this configuration the maximum temperature that can be generated at the tip of the thermal couple (the approximate location of the device under test) is $65^{o}C$. The junction where the thermal couple is plugged into the readout circuit is placed behind thermal shielding and remains at room temperature to provide a cold junction.

The device under test moves during thermal expansion and during the experiment the motorized stages were utilized to manually adjust the position of the device under test to ensure the laser spot remained on the same position on the surface of each device. This allowed for the vibration amplitude to be compared at different temperatures, since any amplitude variations will be primarily due to temperature variations as oppose to due to a change in the position of the device.

For each temperature measurement, thermal steady state was considered to occur when the device stopped moving relative to the laser spot (indicating a relatively stable position in the $\hat{x} - \hat{y}$-plane) and objective lens (that is, when the view of the device through the microscope stops going out of focus, indicating a relatively stable position in the $\hat{z}$-direction). These steady state conditions were observed to occur in approximately 1 hour.

Measurement results are displayed in Figure 7.5 and indicate that as temperature increases from $24^{o}C$ to $60^{o}C$ the center frequency of the measured modes decreases for both the S1 P^{n}BG QC and the Square reference device. This measured reduction

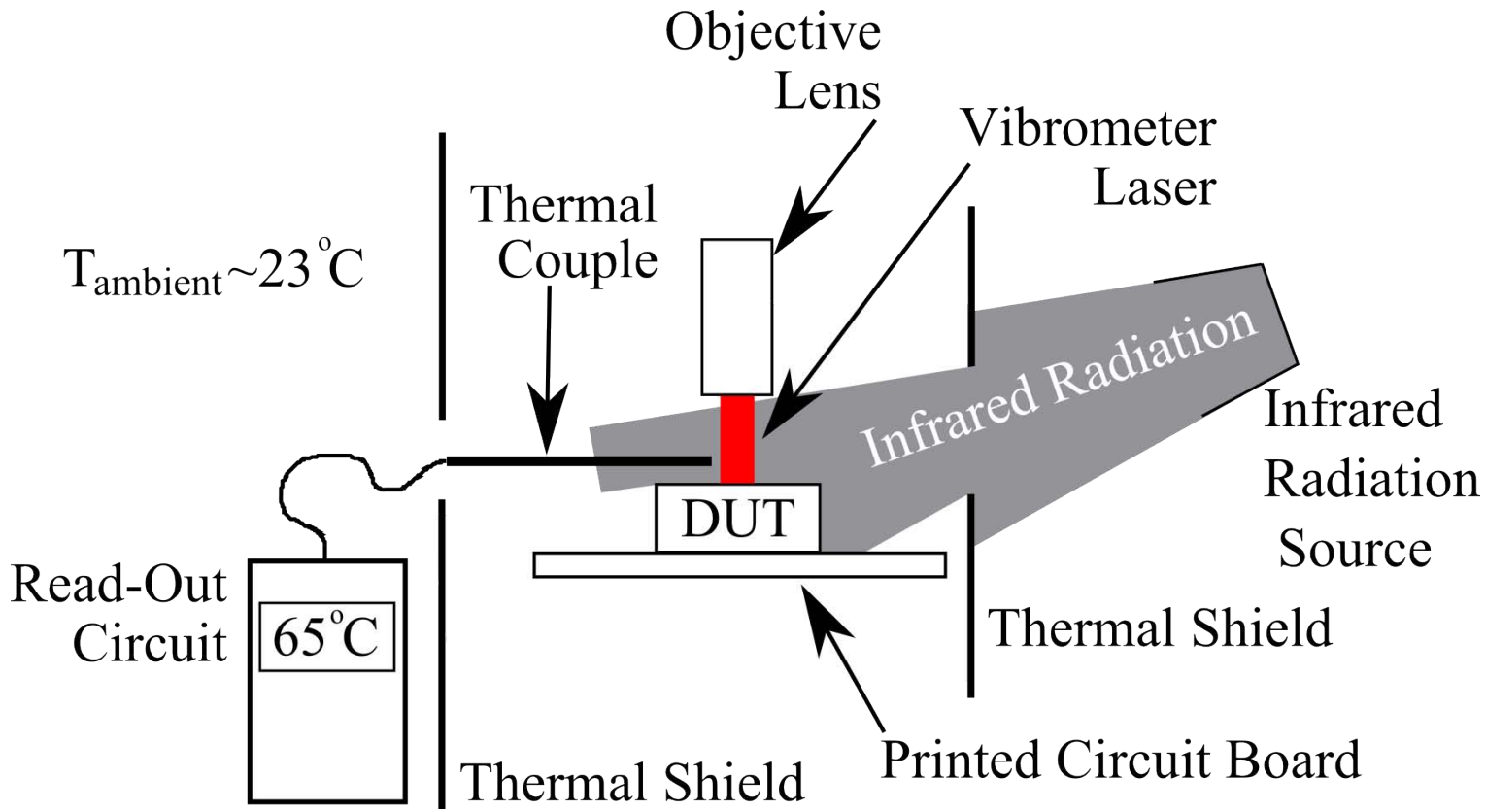

Figure 7.3: Schematic of the measurement setup for the measurement of the S1 phononic band gap quasi-crystal and Square reference device. A 500 W halogen lamp is utilized as an infrared radiation source which is incident upon the device under test (DUT). Thermal shields are utilized to help prevent infrared radiation from impinging on the objective lens, vibrometer system and thermal couple read-out circuit so that these components of the measurement system are held at approximately room temperature. The thermal couple lies approximately 5 mm above the DUT. This setup yields a maximum thermal couple temperature of approximately 65^oC.

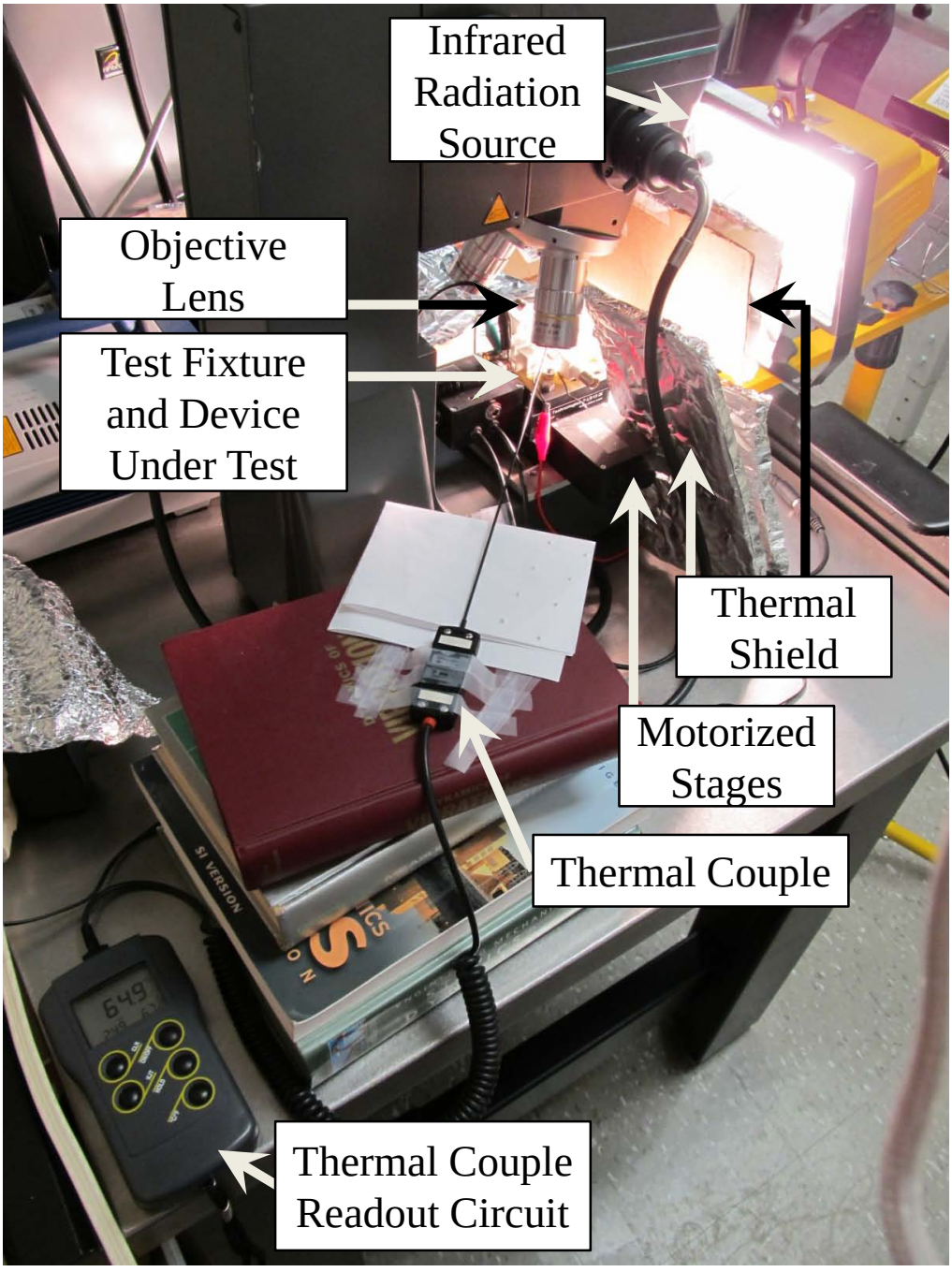

Figure 7.4: Physical setup of the dynamic harmonic analysis experiments. The figure depicts the infrared radiation source (a 500 W halogen lamp), thermal shield, thermal couple, test fixture and device under test, motorized stage, microscope objective lens and thermal couple readout circuit. The remaining equipment in the system is displayed in Figure 6.2.

in the hyper-band gap mode frequency contrasts the modeled increase in hyper-band gap mode frequency near the band gap edge. This discrepancy may in-part be due to the substrate not being included in the FEM model. In the experiment there may be thermally induced variations in the substrate to which the P^{n}BG QC is anchored, so in the experiment the anchors of the P^{n}BG QC may not be held at fixed locations. If the substrate were to thermally expand, the anchors may diverge from one another so as to counter act any tensile stress that may be created due to thermal expansion of the P^{n}BG QC. Such an alleviation of tensile stress may provide a mechanism for the experimental measurements to deviate from the FEM model.

An increase in tensile stress may be expected to increase normal mode frequency, while a decrease in Young's modulus due to softening of the material at elevated temperature may reduced normal mode frequency. In the model of Figure 7.2, some modes appear to increase in frequency while other modes appear to decrease in frequency as temperature is increased; this indicates that structural properties of the P^{n}BG QC may also control wether normal mode frequency increases or decreases with temperature. Due to the elaborate thermomechanical behavior of the P^{n}BG QC, and the unknown variations in the thermal expansion of the substrate, further investigation may be performed to conclude what is responsible for the reduced normal mode frequency observed in experiments.

The amplitude, frequency and temperature values for the S1 P^{n}BG QC and Square reference devices are compared in Table 7.1. The trend in the presented experimental results is that normal mode frequency and amplitude decrease at the elevated temperature. Experimental band gap frequency may then also reduce with respect to temperature (display a negative temperature coefficient) for the S1 P^{n}BG QC; however, to accurately deduce whether band gap location displays a positive or negative temperature

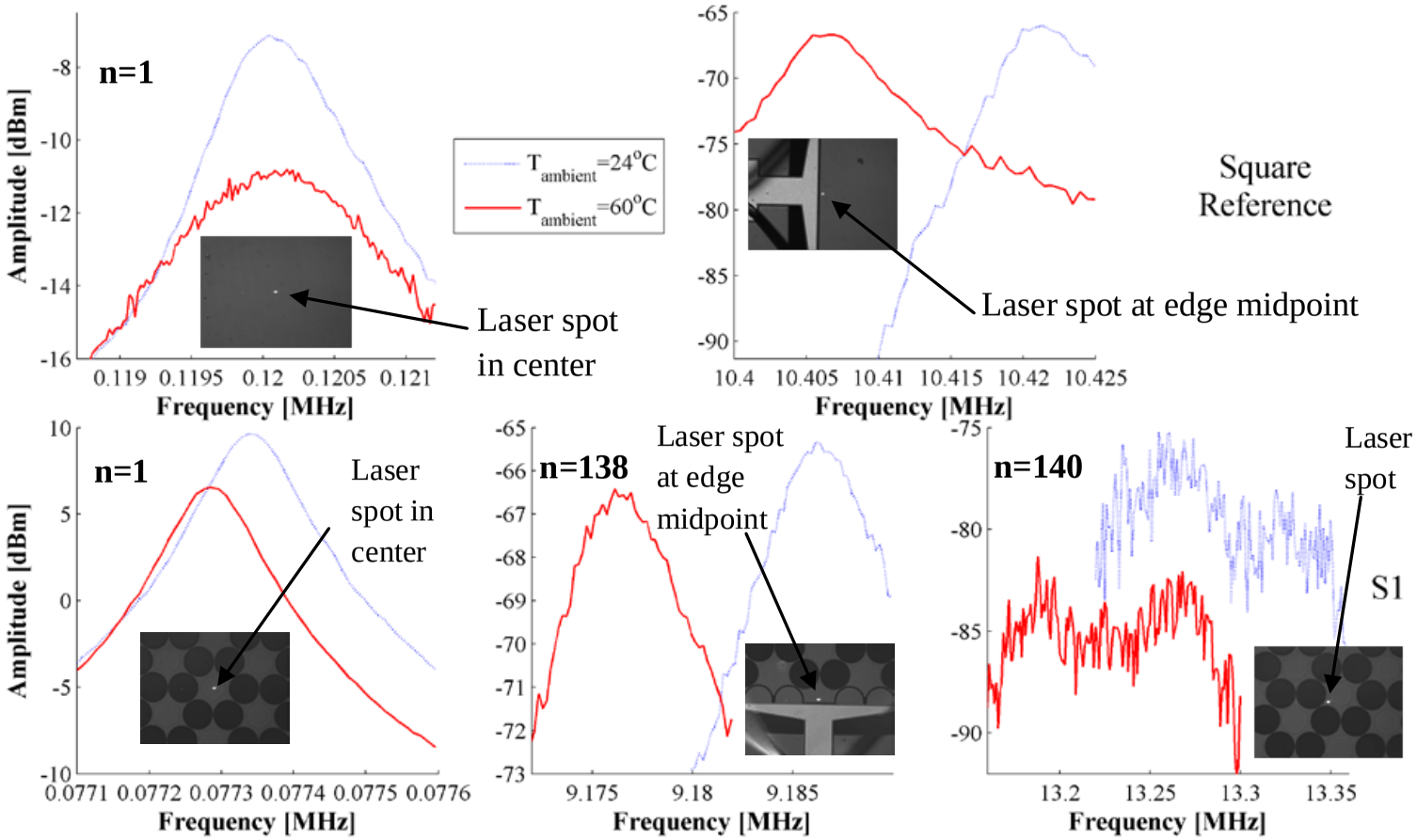

Figure 7.5: Harmonic response versus temperature for normal modes 1, 138 and 140 of the S1 phononic band gap quasi-crystal device compared with normal mode 1 and a mode at 10.42 MHz for the Square homogeneous plate reference device. The laser spot location on the surface of the device is denoted by the white dot in the microscope image in the inset. The harmonic response of each mode is measured at 24^oC (blue line) and 60^oC (red line).

coefficient, measurement of the center frequency of the normal mode peaks that upper and lower bound the band gap would need to be performed versus temperature. It may also be observed in Table 7.1 that the percentage change in the normal mode frequencies appears to increase with frequency. The percentage change in the normal mode frequencies in Table 7.1 do not appear to indicate that there is a dramatic difference between the temperature dependence of the S1 P^nBG QC and the Square reference device.

Table 7.1: Frequency versus temperature for the S1 phononic band gap quasi-crystal and Square reference device. The equation utilized for percent change is $Percent\ Change = 100\% \frac{final - initial}{initial}$.

Mode	Square Reference				S1 PnBG QC			
	Frequency (Amplitude)		Absolute Change	Percent Change	Frequency (Amplitude)		Absolute Change	Percent Change
	~23°C	~65°C			~23°C	~65°C		
1	120.048 kHz (-7.119 dBm)	119.968 kHz (-10.867 dBm)	-80 Hz (-3.748 dBm)	-0.067% (52.648%)	77.34 kHz (9.6 dBm)	77.29 kHz (6.642 dBm)	-50 Hz (2.958 dBm)	-0.0646% (-30.813%)
138	-	-	-	-	9.186 MHz (-65.335 dBm)	9.176 MHz (-66.415 dBm)	-10 kHz (-1.08 dBm)	-0.1089% (1.653%)
10.42 MHz	10.422 MHz (-66.036 dBm)	10.407 MHz (-66.701 dBm)	-15 kHz (-0.665 dBm)	-0.1439% (1.007%)	-	-	-	-
140	-	-	-	-	13.26 MHz (-75.25 dBm)	13.19 MHz (-81.34 dBm)	-70 kHz (-6.06 dBm)	-0.5279% (8.093%)

7.2 Vibration Stabilized Resonator within a Phononic Band Gap Quasi-Crystal

Last, the applicability of the P^{n}BG QC architecture to signal processing elements is developed numerically by interrupting the periodicity of the C1 P^{n}BG QC, this interruption will be referred to as a defect state. The defect state is comprised of a circular inclusion (of the same $40\mu m$ diameter as the other inclusions) placed in host region at the center of the C1 P^{n}BG QC. Modal analysis was performed following the methodology detailed in Section 4.2.3. The shape of modes 58, and 120, of the defected C1 P^{n}BG QC are displayed in Figures 7.6, and 7.7, respectively, where the circular defect state that was introduced into the middle of the P^{n}BG QC may be observed. Modes 58, and 120, are modes of the sub-band gap, and hyper-band gap, branches, respectively, and display the characteristic mode shapes, and vibration patterns, that were observed in the corresponding branches of the original P^{n}BG QCs discussed in Section 4.2.3, and displayed in Figure 4.17, respectively.

As may be observed in Figure 7.8, the new feature observed in the model of the defected C1 P^{n}BG QC is the presence of normal modes that lie within the frequency range of the band gap (referred to as in-gap frequencies) of the original C1 P^{n}BG QC, which was presented in Chapter 3. The normal modes that are present at in-gap frequencies are also referred to as defect states, six of which may be observed in Figure 7.8. The FEM model of the mode shape of one of these defect states is illustrated in Figure 7.9, where it may be observed that the deformation of the mode shape primarily occurs in the vicinity of the defect state that was introduced in the center of the C1 P^{n}BG QC. The magnitude of the displacement field in the region surrounding the defect state inclusion is relatively small. The vibrations of the defect state may then be considered

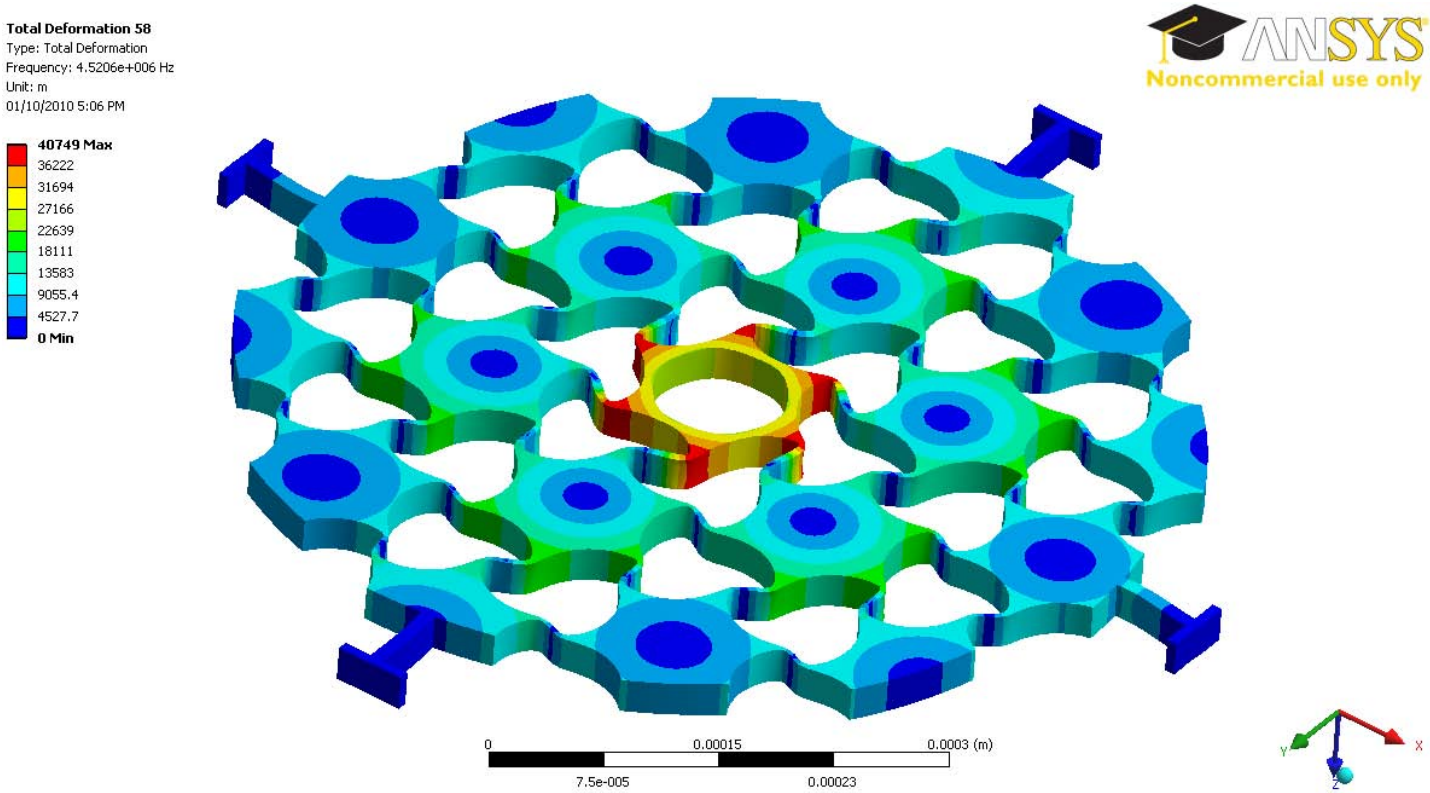

Figure 7.6: Finite element method model of the shape of sub-band gap branch mode 58 of the defected C1 phononic band gap quasi-crystal. The defected C1 phononic band gap quasi-crystal is created by introducing a circular inclusion (with a diameter of $40\mu m$) into the host region directly in the middle of the phononic band gap quasi-crystal. A similarly shaped sub-band gap mode of the original C1 phononic band gap quasi-crystal is depicted in Figure 4.13.

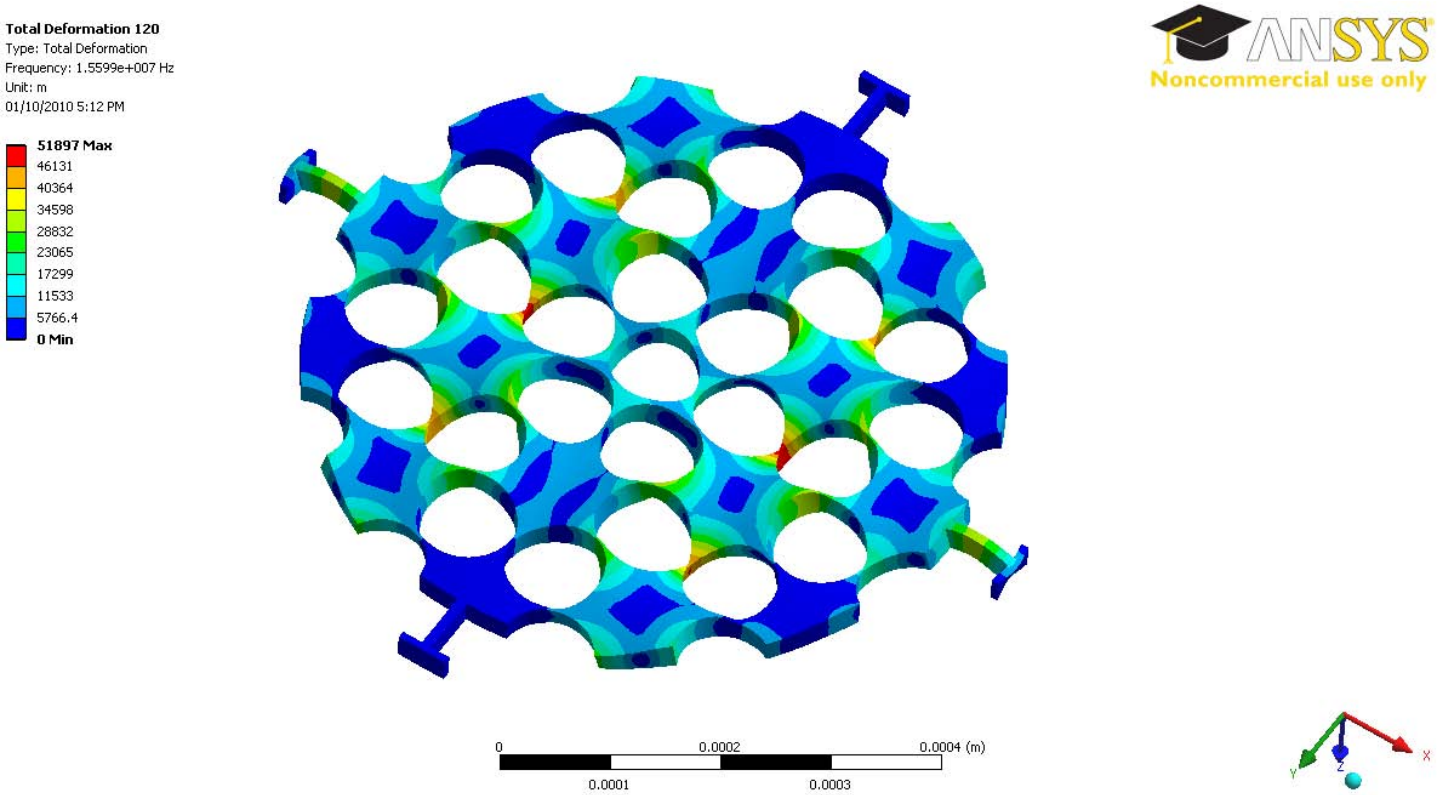

Figure 7.7: Finite element method model of the shape of hyper-band gap branch mode 120 of the defected C1 phononic band gap quasi-crystal. The defected C1 phononic band gap quasi-crystal is created by introducing a circular inclusion (with a diameter of $40\mu m$) into the host region directly in the middle of the phononic band gap quasi-crystal. A similarly shaped sub-band gap mode of the original C1 phononic band gap quasi-crystal is depicted in Figure 4.14.

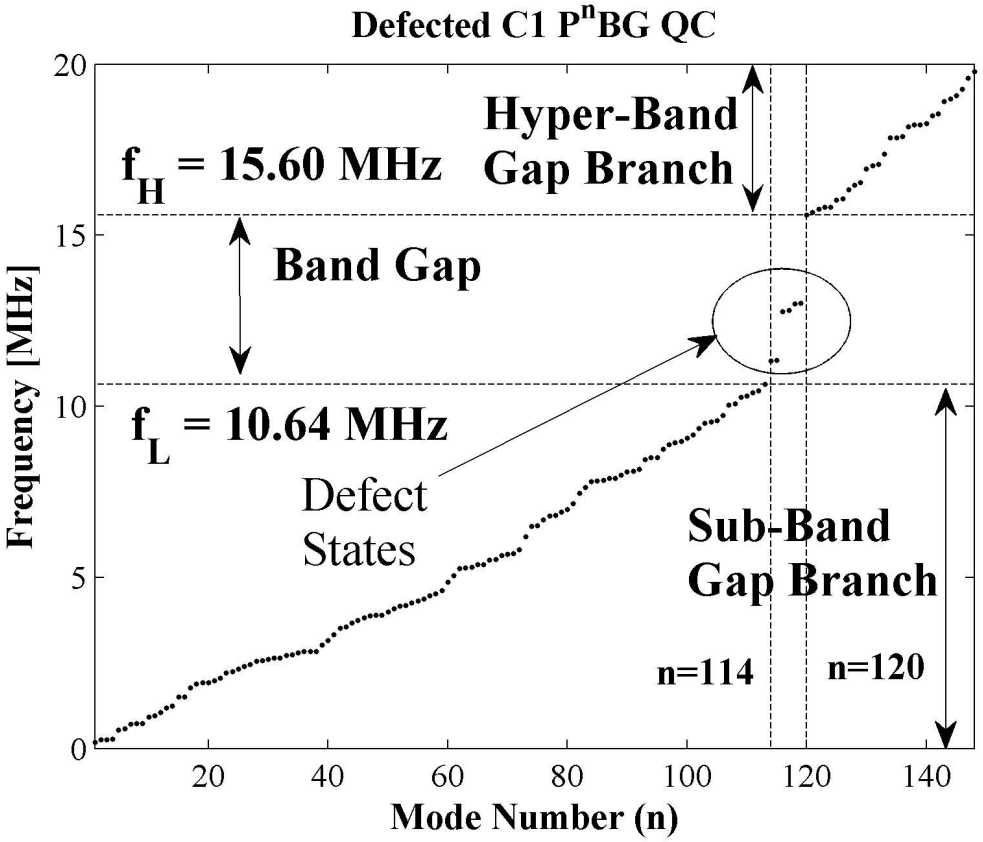

Figure 7.8: Finite element method model of the frequency versus mode number characteristic of the defected C1 phononic band gap quasi-crystal structure that is depicted in Figure 7.6. Within the band gap, normal modes, referred to as defect states, may be observed.

to be localized within the P^{n}BG QC. Further investigation may determine if vibrations, at in-gap frequencies, originating from the substrate or electrostatic transducers may be strongly attenuated before reaching the defect state, so as to make the defect state immune to, or protected from, substrate vibrations and transducer forces that may be present at band gap frequencies. This property may also have applicability to anchor loss reduction in that the region surrounding the localized resonator (defect state) may inhibit the propagation, or loss of, vibrations away from from the defect state.

Some defect state modes observed in Figure 7.8 for the defected C1 P^{n}BG QC are

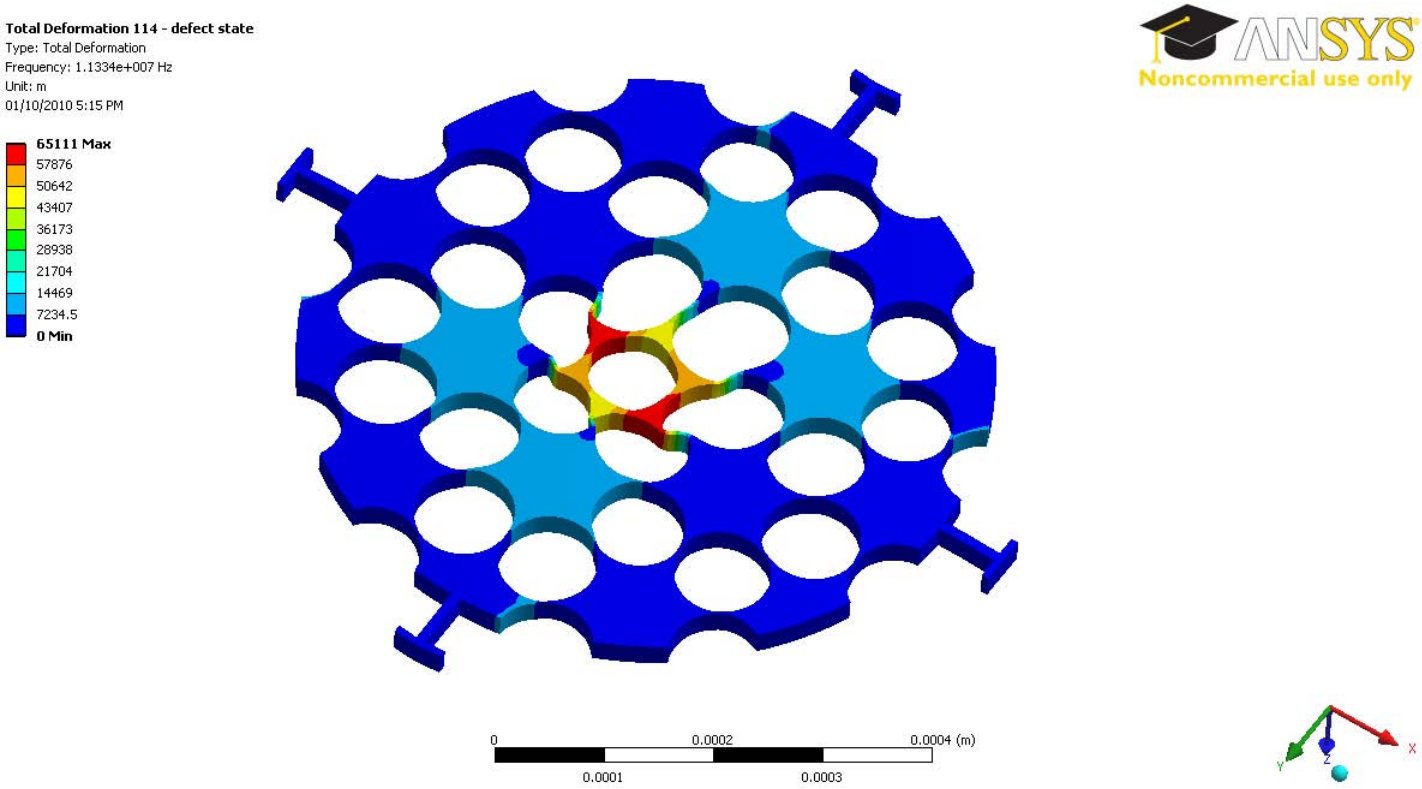

Figure 7.9: Finite element method model of mode 114, one of the six intentionally induced defect states of the defected C1 phononic band gap quasi-crystal.

also relatively distant from adjacent modes in frequency, due to the presence of the defect state within the band gap region where there is a relatively low density of normal modes with respect to frequency. As a result of the frequency separation, the defect state modes may display improved immunity to interference from vibrations at adjacent frequencies. In addition, the isolation of defect state modes in frequency provides narrow band-pass filter functionality, while the sub-band gap branch may be developed to provide relatively wide-band low pass filter functionality. Thus, the defect states are useful for creating a more complex frequency selective response.

The defect state introduced here may be considered to be a point defect that is isolated at the center of the defected C1 P^nBG QC. This point defect state may be moved to a different position in the C1 P^nBG QC. Following the theory in [57], line defects may also be introduced into the P^nBG QC architecture presented in Chapter 3. Line defects may create a localized waveguide through the P^nBG QC. In this way, for example, vibrations at line defect state frequencies may be permitted to transfer from one edge of the P^nBG QC to the other.

The properties that have been illustrated here for the defected C1 P^nBG QC may be further investigated to develop their applicability to vibration stabilization, anchor loss reduction, signal processing element construction and auxiliary functions in MEMS and mechanical systems.

Chapter 8

Conclusions

A new architecture, referred to as the P^{n}BG QC architecture, was developed for the integration of P^{n}BG crystal-like structures into silicon processes, methodologies were developed to provide P^{n}BG crystal-like behavior and electrostatic actuating transducers were leveraged. The presented methodologies may be scaled to additional frequency regimes and were investigated for micron-sized structures. Preliminary operation of the proposed P^{n}BG QC architecture was illustrated experimentally for P^{n}BG QC devices fabricated in the SOIMUMPs process. Experimental evidence of band gap behavior (absence of normal modes) was observed for several P^{n}BG QC devices in the 10 to 13 MHz frequency regime. Comparison with reference models and devices supports that the observed band gap behavior is a specific property of the P^{n}BG QC geometry. Reasonable agreement between models and experiments provides some confirmation that the crystal truncation, and edge and tether tuning design methodologies provide the desired band gap operation. The applicability to physical temperature sensors of the P^{n}BG QC architecture was investigated numerically and experimentally and the tested P^{n}BG QC structure displayed a percentage change in normal mode frequency versus temperature

that was comparable to the reference structure, with a higher percentage change in normal mode frequency observed for higher order modes. The P^{n}BG QC architecture was also demonstrated to have applicability to the development of localized resonators and potentially vibration stabilization and anchor loss reduction.

8.1 Contributions

This thesis developed the design methodologies, numerical and analytical model, realization and experimental characterization of a new device architecture, referred to as the P^{n}BG QC architecture, by leveraging the science of P^{n}BG crystals coupled with MEMS modeling and fabrication technologies. The applicability of the P^{n}BG QC architecture was investigated numerically and experimentally for temperature sensors and numerically for signal processing element construction. The main contributions of this research may be grouped into five areas which are summarized below.

1. Development of the Phononic Band Gap Quasi-Crystal Architecture and Design Methodologies: The development of the P^{n}BG QC architecture in this thesis appears to present several studies that are the first of their kind, including (i) the development of the novel P^{n}BG QC architecture which was shown to be compatible with SOI multiuser bulk micromachining MEMS fabrication technologies, (ii) the utilization of free standing serrated edges along the truncation boundary of the P^{n}BG QC, (iii) boundary tuning to provide a mechanism to eliminate edge effect defect states and enable complete band gap formation, (iii) the implementation of electrostatic (as oppose to piezoelectric) transduction for actuation of P^{n}BG crystal-like structures and novel electrostatic transducer geometries, (iv) the utilization of circular and square crystal truncation boundary geometries, as well as (v) the development of a tuning methodology

for tethers to enable complete band gap formation in the presence of the non-idealities of finite periodicity of the P^{n}BG QC lattice and attachment of anchored tethers to the P^{n}BG QC. The P^{n}BG QC architecture was developed to ensure compatibility with local experimental characterization equipment which required the band gap behavior to lie within the 0 to 20 MHz frequency range.

The unique crystal truncation and anchor tuning methodology systematically removes edge effect defect states and shifts tether defect states to hyper-band gap branch frequencies. Band gap behavior is achieved with P^{n}BG QCs that are approximately six lattice constants in dimension. Electrostatic transducers mitigate the need for piezoelectric materials thereby improving silicon-compatibility and provide action at a distance type forces so that the edges of the P^{n}BG QC may be free standing for reduced anchor loss. The primary energy carrying waves in the P^{n}BG QCs appear to be standing waves, in contrast to traditional traveling waves that are generated in piezoelectrically actuated P^{n}BG crystals. The circular truncation boundary geometry was shown to provide more symmetrical electrostatic transducer electrodes than square truncation.

The P^{n}BG QC architecture described here displays the geometry and behavior of a two-dimensional distributed (as oppose to discrete) mechanical system of mechanically coupled resonators designed utilizing P^{n}BG crystal geometry to realize the band stop frequency selectivity that is characteristic of a P^{n}BG crystal. In contrast, typically coupled resonator MEMS couple together discrete mass-spring resonator elements to approximate bandpass filter functions [30, 98]. The order of (number of mass-elements in) the proposed P^{n}BG QC may be controlled relatively easily by adjusting the P^{n}BG crystal truncation boundary location. The P^{n}BG QC architecture may have application to the design of coupled mass-spring resonators.

2. Numerical and Analytical Model and Theory of Operation: The unique

geometry of the proposed P^{n}BG QC architecture, namely truncation of the P^{n}BG crystal by free boundaries and the attachment of the P^{n}BG QC to mechanically grounded tethers, introduces a unique set of boundary conditions on the elastic wave equation. Thus, generic models of infinitely periodic P^{n}BG crystals do not provide a complete model of the proposed P^{n}BG QC architecture and unique models of the P^{n}BG QC architecture were developed. Electrical, mechanical, and coupled electromechanical models were presented. Numerical models employ the FEM and analytical and semi-analytical models were also developed.

The mechanical model illustrated that the proposed P^{n}BG QC architecture appears to display some of the characteristic behavior of a P^{n}BG crystal. Namely, the shape of the modes above and below the band gap of the proposed P^{n}BG QC display different characteristic shapes, similar to differing mode shapes of the acoustical and optical branch modes of a P^{n}BG crystal. The model differentiated between the behavior of a P^{n}BG QC and a plate with an arbitrary array of periodically placed etch holes. The model illustrated that a plate with periodically spaced etch holes does not necessarily display a band gap. The model also characterized the non-obvious outcome that careful choice of inclusion geometry and the implementation of the proposed P^{n}BG QC architecture design methodologies yields a structure that displays the band gap characteristic of an ideal infinitely periodic P^{n}BG crystal. Lastly, comparison with the model of homogeneous plate resonators and flat edged P^{n}BG QC structures of comparable geometry illustrated that the modal and band gap characteristics of the P^{n}BG QC architecture are specific to the serrated edge P^{n}BG QC and not just generic properties of comparable devices. The P^{n}BG QC architecture provides a methodology to increase the density of normal modes in sub- and hyper-band gap branch frequency regions, and simultaneously decrease the density of modes (to zero) in band gap frequency regions to provide a broad-

band absence of normal modes modes, which is analogous to the characteristic behavior of a P^{n}BG crystal. The wide band harmonic analysis implemented with the FEM model indicated that the harmonic spectrum of the $\hat{z}$-component of displacement does display an abundance of normal mode peaks over sub- and hyper-band gap branches and an absence of normal mode peaks at band gap frequencies, this was identified to provide a means for identifying the band gap activity by measuring the out-of-plane harmonic spectrum of P^{n}BG QC devices.

The mechanical model also illustrated the unique properties, and behavioral zones, in the frequency versus mode number characteristic of the P^{n}BG QCs: (i) at low frequencies the P^{n}BG QCs displays similar characteristics to a homogeneous plate, while (ii) at intermediate frequencies the P^{n}BG QC behavior dramatically deviates away from homogeneous plate behavior, then (iii) at high frequencies the behavior of the P^{n}BG QC and homogeneous plate appear to converge. The boundaries of these behavioral zones are often denoted by modes in which tether resonance occurs. This may indicate that the tethers perturb the behavior of the P^{n}BG QC and may in part be responsible for, and may be utilized to mitigate or control, the division of the frequency versus mode number characteristic into different behavioral zones. The model contrasted the effect of circular and square truncation boundary geometry on the properties of the band gap.

The FEM models appear to have indicated that for the structures studied in this thesis, the implementation of the design methodologies of Chapter 3 and use of serrated edges in association with the P^{n}BG QC geometry is mandatory to produce a structure that displays the band gap behavior of a P^{n}BG crystal. This supports the significance of the P^{n}BG QC architecture.

Comparison of numerical models of P^{n}BG QC band gap location with the analytical models of the Bragg frequencies of infinitely periodic honeycomb P^{n}BG crystals indi-

cated relatively comparable band gap locations and trends in band gap location versus geometry. The similarities between the P^{n}BG QC band gap model and the analytical Bragg frequency model of infinitely periodic P^{n}BG crystals may support the notion that the proposed P^{n}BG QC architecture may adhere to some infinitely periodic P^{n}BG crystal theory.

Utilizing the FEM model, multiple sensitivity analysis were performed on the S2 P^{n}BG QC. Band gap location was observed to change by less than 1% when the fixed boundary conditions, which are attached to the tethers, are removed indicating a relatively low sensitivity. A complete band gap remains present for extreme variations about the nominal material density, Young's modulus and Poisson ratio, with the hyper-band gap branch displays a higher sensitivity to material property variations than the sub-band gap branch. For a given inclusion radius, band gap width was observed to decrease as hole spacing decreased. For a given inclusion radius, band gap width was observed to increase as inclusion radius decreased. Band gap width was observed to be sensitive to plate thickness, and for low plate thicknesses the band gap was observed to close. Hence the band gap occurs for only specific combinations of P^{n}BG QC geometry. Lastly, band gap location was observed to be relatively insensitive to truncation diameter; however, the number of sub-band gap modes was observed to be sensitive to truncation diameter.

The electrical model produced insight into the operation of the unique electrostatic transducer geometries. Square truncation was shown to produce more asymmetrical transducer geometries relative to circular truncation, namely for square truncation the transducers with widely spaced inclusions have smaller overlap areas than the transducers with closely spaced inclusions. However, the electrical model indicated that the asymmetries in the electrostatic force, which depends on transducer gap size as well as surface area, were less than $5\mu N$ or 5% of the total force. Hence, despite being gener-

ated by transducer electrodes that have asymmetrical geometry, approximately balanced forces are applied to the four edges of square truncated P^{n}BG QCs. By symmetry, the electrical model predicted that balanced forces would be generated by the electrostatic transducers of circular truncated P^{n}BG QCs. Per unit die area, square truncation yields larger transducer overlap areas and larger electrostatic forces than circular truncation. Due to the serrated edges, the P^{n}BG QCs display larger transducer electrode overlap areas than the corresponding flat transducers of the Square and Circular reference devices; however, the flat transducers of the Square and Circular reference devices display larger electrostatic forces due to having a smaller gap size. The electrical model indicated that the test fixture circuit will apply a relatively uniform voltage to the electrostatic transducers from approximately DC to 20 MHz. For a uniform electrostatic force, the time harmonic models indicate mechanical actuation of in-plane and out-of-plane modes from approximately DC to 20 MHz suggesting that the novel electrostatic transducer geometries would produce the desired wide band excitation of the P^{n}BG QCs.

The semi-analytical models identified that at a given frequency specific physical regions of the P^{n}BG QC appear to predominantly behave either approximately as a mass element or a spring element. Each mass element appeared to display six degrees of freedom. The P^{n}BG QCs were then approximated as mass-spring systems. From these observations, a semi-analytical model of the number of sub-band gap modes was derived. Analogies to analytical models of mass-spring systems and infinitely periodic P^{n}BG crystals were utilized to explain the slope and piecewise linear frequency versus mode number characteristics of the P^{n}BG QCs. Next, the concept of virtual mechanical ground was applied to reduce the complexity of the FEM model down to a subset that could be approximated as a mass-spring system with a single mass. Semi-analytical flexural plate and beam models of these simplified mass-spring systems were developed to predict

their structural properties of stiffness and mass, from which a lumped element vibration model was developed, for select normal modes of the P^{n}BG QCs. The percentage error is approximately $\pm 100\%$ between the semi-analytical flexural plate and beam models and the numerical FEM model. It was observed from the large error in the semi-analytical virtual mechanical ground mass-spring models of the sub- and hyper-band gap branch modes, that improved analytical or semi-analytical models are needed. A more complete model may employ a periodic mass-spring network; this observation may support the notion that the P^{n}BG QCs are fundamentally mechanically periodic structures.

Lastly, the mechanical and electric models were combined to model the coupled electromechanical behavior of the P^{n}BG QC architecture. A steady state electromechanical model illustrated the shape of the P^{n}BG QCs deformation that is produced by the electrostatic transducers and indicated the magnitude of displacement under a static voltage. The electromechanical FEM model displayed reasonable agreement with the analytical model for the magnitude of the capacitance and electrostatic force and indicated that the dominant component of the force generated by each electrostatic transducer is as desired in the in-plane direction orthogonal to the length of the transducer. Lastly, the free-standing portion of the fixed electrode of the electrostatic transducer was observed to undergo considerable deformation suggesting that an improved fixed electrode may be developed.

3. Realization: Due to the relatively unique structure of the P^{n}BG QCs, there was uncertainty in whether the P^{n}BG QC architecture would fabricate accurately. The sensitivity analysis of the FEM models indicated that complete band gaps would only form for specific ratios of feature size to plate thickness and SOIMUMPs with a $25\mu m$ thick single-crystal-silicon layer was found to achieve the required ratio of minimum feature size to plate thickness. In addition, with relatively few design rule violations,

SOIMUMPs was hypothesized to enable the realization of the unique electrostatic transducer electrode geometry (comprised of surfaces of multiple radii of curvature) and realization of anchors that support the relatively large P^{n}BG QC which is free standing and comprised of relatively massive regions interconnected by slender regions. Scanning electron microscope images and optical profilometer images provided reasonable evidence for the successful demonstration of the realization of the P^{n}BG QC architecture utilizing SOIMUMPs with a $25\mu m$ thick single-crystal-silicon layer. The gap between the electrodes of the electrostatic transducers, upon visual inspection of the SEM images, appear to have been fabricated larger than the drawn value of $3\mu m$ in the areas of high radius of curvature, and may be reduced to $2\mu m$ in future designs to yield higher electrostatic force. Profilometer measurements indicate that around curved features, on the top of the Silicon layer, there appears to be a groove which may reduce the thickness of the Silicon layer between inclusions. The models indicate that the hyper-band gap branch may be strongly dependent (third order dependence) on the geometry between the inclusions and so the aforementioned groove may be the source of significant error between the model and measurements of hyper-band gap modes.

4. Experimental Characterization: The results of the vibrometer measurement of the harmonic spectrum for the out-of-plane component ($\hat{z}$-component) of the S1 and S2 P^{n}BG QCs provides reasonable experimental support that the S1 and S2 P^{n}BG QCs may display band gap behavior from approximately 10 MHz to 13 MHz. This experimental result was reasonably anticipated by the FEM model. The appearance of a band gap (a single frequency region, of significant width, where normal mode resonances were not observable) in the spectrum of the aforementioned P^{n}BG QCs was not observed to be present in the spectrum of the Square reference device. The behavior of the S1 and S2 P^{n}BG QC devices was thus shown to differ significantly from that of a homogeneous

plate.

An approximation of the mechanical quality factor of the P^{n}BG QC device normal mode resonances was obtained by fitting a first-order harmonic oscillator model to several of the normal mode resonant peaks in the measured harmonic response of the S2 P^{n}BG QC. Quality factor was observed to vary from 180 to 4000. The fit of the first order harmonic oscillator model to the measured normal mode peaks appeared to provide an approximate experimental means to measure the mass of the S2 P^{n}BG QC device, potentially material density and hence perform material property characterization. Approximations of the effective spring stiffness and damping coefficient were also obtained.

Reasonable agreement between the node and anti-node topography of the fourteen FEM model and measured mode shapes illustrated confirmation of the characteristic out-of-plane sub- and hyper-band gap mode shapes for the S1 and S2 P^{n}BG QC and sub-band gap mode shapes for the C2 P^{n}BG QC. Some of the experimentally measured mode shapes were absent from the FEM model and may be produced by error in fabrication, FEM model, measurement or electrostatic actuation. By comparing the P^{n}BG QC mode shapes with those of the Square homogeneous plate reference devices, the influence of the P^{n}BG QC geometry on the mode shape was apparent due to the confinement of vibrations within the periodically shaped host region of the P^{n}BG QC.

The experimentally assembled frequency versus mode number characteristic provides reasonable support for an approximately piecewise linear relation between mode frequency and number. The measured frequency versus mode number characteristic provides reasonable support for the observed behavioral zones and the observations that band gap location increases as geometry is varied from the S1 to the S2 to the C2 P^{n}BG QC devices (that is, as the inclusion spacing increases for a fixed inclusion ra-

dius and truncation geometry) and the frequency versus mode number characteristics diverge from the origin and one another as frequency increases then converge at higher frequencies.

The harmonic analysis versus DC bias voltage indicate a negligible (less than 50 Hz) change in band gap location versus DC bias voltages from 0 to 100 VDC. As a result, the application of balanced voltage to the relatively similar transducers of the S2 P^{n}BG QC device may assist in stabilizing the band gap location with respect to DC bias voltage.

The measured displacement amplitudes in the $\hat{z}$-direction for the sub-band gap appear to range from approximately $10nm$ to $10^{-4}nm$ and for the hyper-band gap range from approximately $10^{-2}nm$ to $10^{-4}nm$. For the S2 P^{n}BG QC, the maximum and minimum dynamic electromechanical coupling coefficients for the electrostatic transducers, with a 100 V DC bias voltage, and peak-to-peak RF voltage of 10 V, for one measurement point were observed to be $1nm/V_{pp}$ and $10fm/V_{pp}$. The unique electrostatic transducers successfully excite the out-of-plane modes of the P^{n}BG QCs with a measurable displacement amplitude.

5. Applicability: Next, the performance of the P^{n}BG QC architecture was investigated for application to physical temperature sensors, localized resonators, vibration stabilization, anchor loss reduction and auxiliary applications in MEMS and mechanical systems.

First, the temperature dependence of the band gap was investigated utilizing numerical FEM thermomechanical models and measurement of the dynamic harmonic response, versus temperature, for the S1 P^{n}BG QC device. The FEM model indicated that sub-band gap resonant frequencies decrease (negative temperature coefficient) while some hyper-band gap resonant frequencies increase (positive temperature coefficient). For the temperatures and frequencies modeled here, the models indicate that sub-band gap fre-

quencies, as compared to hyper-band gap frequencies, would tend to display a higher percentage change in normal mode frequency for a given temperature change.

Dynamic harmonic analysis experiments were conducted at elevated temperatures on the S1 P^{n}BG QC. Measurement results indicated that as temperature increased from $24^{o}C$ to $60^{o}C$ the center frequency and amplitude of the measured modes decrease for both the S1 P^{n}BG QC and the Square reference device. The measured reduction in the hyper-band gap mode frequency contrasts the modeled increase in hyper-band gap mode frequency. Experimentally, band gap frequency may then also reduce with respect to temperature (display a negative temperature coefficient) for the S1 P^{n}BG QC and requires further investigation. Experimentally the percentage change of the normal mode center frequencies appears to increase with frequency, which contrasts the FEM model. In the experiment, thermally induced variations in the substrate (anchors) may in-part account for the observed discrepancies between measurement and model, which has a fixed anchor locations. The experimentally observed percentage change in the normal mode frequencies do not indicate that there is a dramatic difference between the temperature coefficient of the S1 P^{n}BG QC and the Square reference device.

Second, the utility of the P^{n}BG QC architecture to create increasingly complex frequency selective characteristics, vibration stabilized or localized resonators, reduced anchor loss and potentially improved mechanical systems was developed through the introduction of defect states into the P^{n}BG QC architecture. The mode shape of the defect state appears to be localized within the center of the P^{n}BG QC and this behavior may have application to vibration stabilization and anchor loss reduction. Some defect state modes are also relatively distant from adjacent modes in frequency and so the defect state modes may display improved immunity to interference from vibrations at adjacent frequencies. In addition, the isolation of defect state modes in frequency

provides narrow band-pass filter functionality, while the sub-band gap branch may be developed to provide relatively wide band low pass filter functionality. Thus, the defect states are useful for creating a more complex frequency selective response.

The experimental data supports the development of new knowledge into the integration of phononic band gap phenomenon in silicon-based MEMS utilizing a novel electrostatic transduction mechanism utilized to excite P^{n}BG QC devices. With approximately 130 modes in the sub-band gap branches, the P^{n}BG QC architecture may be one of the most multi-mode two-dimensional MEMS coupled-mass resonator created. The P^{n}BG QC architecture presented here may provide insight into the design of two-dimensional mechanically coupled resonators by providing a relatively easy method to interconnect large arrays of mass-spring resonator elements.

Lastly, many of the phenomenon studied here may be scalable to additional frequency regimes. For example, if the P^{n}BG QC architecture presented here were scaled from a $25\mu m$ thick layer to a $2\mu m$ thick layer (a scale factor of $25/2 = 12.5$), which is obtainable utilizing a surface micromachining fabrication process, by the scalability of the elastic wave equation, the band gap location may scale from approximately 13 MHz to 162.5 MHz ($\because 13MHz \times 12.5 = 162.5MHz$).

8.2 Future Research

The measured data provides reasonable experimental support for the modeled behavior of the P^{n}BG QC architecture, and the investigation into the applicability of the P^{n}BG QC architecture to sensors and signal processing elements supports several applications. Future work may then be fruitful and is discussed here.

Phononic Band Gap Quasi-Crystal Development: The P^{n}BG QC architecture

may be adapted to other material systems, inclusion geometry, defect states (move the position of point defects, introduce a line defect, and so forth), crystal truncation geometry (diamond, and so forth), fill factors, tether types and geometry and crystal lattices. This may further enable the realization of increasingly complex functionalities. It may be possible that for P^{n}BG QCs that are a relatively large numbers of lattice constants in dimension, or through very careful design, the edge effect defect states may be mitigated without the use of a serrated or periodic edge. Hence, additional P^{n}BG crystal truncation mechanisms may continue to be examined. A more elaborate investigation of tether tuning may be performed, tethers may be tuned to sub-band gap branch frequencies (as oppose to hyper-band gap frequencies, as investigated here) for increased compliance, and other tether geometries may be utilized. The utilization of (111) silicon for the fabrication of P^{n}BG QCs may mitigate the effects of the silicon anisotropy since the Young's modulus, Poisson ratio and shear modulus are isotropic on (111) silicon [140]. Tension control and the effects of residual and in-plane stress on the behavior of the P^{n}BG QC may be investigated. Laser trimming may potentially be employed to tune and create defect states in the fabricated P^{n}BG QC so as to obtain additional experimental data from the fabricated devices.

Decreasing the ratio of lattice constant to plate thickness for the P^{n}BG QC architecture will increase the stiffness in the out-of-plane direction and shift both the out-of-plane sub- and hyper-band gap modes to higher frequencies. This may potentially create a sub-band gap branch that displays only in-plane modes. If this is possible, it may then be feasible to further develop the geometry of the P^{n}BG QCs to create two branches of in-plane modes: one branch of in-plane modes that, for example, mimic the acoustical branch modes of a P^{n}BG crystal and one branch of in-plane modes that, for example, mimic the optical branch of a P^{n}BG crystal. Each of the two branches of in-plane modes

would have to display distinct mode shapes (vibration patterns) so that they occur in separate frequencies ranges. The in-plane sub-band gap vibration patterns presented in this thesis may provide insight into how to achieve two branches of in-plane modes that display distinct mode shapes, since for example, distinct in-plane mode shapes comprised of purely rotational, mixed rotational-translational, and purely translational vibration patters were observed. Through careful scaling of the P^{n}BG QC geometry, two branches of distinct in-plane mode shapes may be designed to occur in frequency ranges that are separated from one another by a range of frequencies where normal modes are absent to produce band gap phenomenon with purely in-plane modes. Such a development of band gap behavior for branches consisting of purely in-plane modes may assist energy transmission and retrieval to and from the P^{n}BG QC at branch mode frequencies since the electrostatic transducers of the P^{n}BG QC architecture appear to operate primarily on in-plane motion. Alternatively, transducers that are optimized for out-of-plane motion may be developed to leverage out-of-plane vibrations modes.

Anchor Optimization: A complete study of an anchor design space may be performed. The P^{n}BG QCs may be supported at their center or at a single edge for reduced anchor loses. Though the current set of anchors appear to be tuned to mitigate defect state creation, the current tethers do not reflect the periodicity of the P^{n}BG QC and may have been observed in the vibration pattern analysis of Figure 4.17 to resonate at the boundaries of the behavioral zone and thus perturb the behavior of the P^{n}BG QC away from ideal behavior. Other tether geometries, such as tethers that are a natural extension of the P^{n}BG QC geometry, may be investigated for the control or mitigation of behavioral zone boundaries. For example, a slender portion of the host region of the P^{n}BG QC may form a tether while a larger portion of the host region of the P^{n}BG QC may be directly anchored to the substrate.

Electrostatic Transducer Development: It may be recommended to reduce the $3\mu m$ gap between the regions of high curvature in the electrodes of the electrostatic transducer to $2\mu m$ to increase the magnitude of the electrostatic force. Self-aligned electrode techniques may also be applied to produce a smaller electrostatic transducer gap. The geometry of the fixed electrode may be optimized to place its mechanical resonant modes away from the frequency regions where actuation is desired to occur; this may improve transducer efficiency and thereby improve accuracy in the measurement of the band gap location by ensuring that the electrostatic transducer behaves more uniformly (does not resonate) at all frequencies of interest. The electrical signal that is applied to the transducers should be measured so that any frequency selectivity in the electrical excitation circuit can be de-embedded from measurements. The capacitance of the electrostatic transducer may be more accurately modeled to account for the curvature of the electrodes and fringe fields. Matching networks may be implemented to optimize power transfer to the electrostatic transducers. An electrical read-out circuit may be developed to electrically sense the motion of the P^{n}BG QC via the electrostatic transducers. The existing transducers may be reconfigured, for example, not all four transducers need to be shorted together, to more efficiently excite other modes, for example using differential signals. Phased array transducers may be developed to more efficiently excite the higher order modes of the P^{n}BG QC. Through a modification of the P^{n}BG QC architecture, capacitive MEMS ultrasonic traveling wave transducers or piezoresistive transducers may be utilized. The P^{n}BG QC may also be placed in a feedback loop to assist in the excitation of the P^{n}BG QC.

Measurement: Mechanical measurement of the in-plane modes of the P^{n}BG QC may be performed by developing an optical or electrical measurement system. Thermal measurements may be improved through the development of an apparatus that can be

utilized to guard the (electrical and optical) components of the test fixture and measurement system from the thermal source. Such an apparatus may take the form of a thermal chamber that has a window through which optical characterization may be performed, a more localized heat source, lenses that direct the infrared radiation directly at the device or additional thermal shields (for example, a cylindrical thermal shield around the objective lens of a microscope). The P^{n}BG QC may be characterized at higher temperatures to test the behavior in harsh environments and potential plastic deformation that may ensue. Higher temperature solder may be needed to perform high temperature measurements. Optical mode shape topology measurement may be performed at elevated temperatures (this may require a thermal chamber with an optical window, for laser access, to maintain a constant temperature over long periods of time since the present mode shape topology measurements take approximately 40 hours per mode). A network analyzer or lock-in amplifier may be utilized to increase the rate at which measurements may be obtained. The use of a network analyzer would also enable phase information to be measured, so that the relative phase of different physical regions within each normal mode shape may be obtained. An infrared thermometer, or thermal couple on the surface of the test fixture, may be implemented to track the temperature of the P^{n}BG QC more accurately during temperature measurements. To decrease measurement time, instead of performing harmonic analysis, a chirped pulse may be utilized to excite the P^{n}BG QCs so that more frequency information may potentially be obtained in a single measurement. Characterization may be performed for the reference device with flat edges and other P^{n}BG QCs that were not able to be measured due to time constraints. The capacitance of the electrostatic transducers, including the feed-through capacitance of a device, may be measured to quantify their physical capacitance and assist in modeling. S-parameters measurement of the P^{n}BG QC devices may assist in the characterization of the electrical circuit and electrical parasitic elements.

The harmonic spectrum of the fixed electrode may be measured to experimentally determine the non-ideal behavior of the fixed electrode. To accurately deduce whether the band gap frequencies of the P^{n}BG QC devices have positive or negative temperature coefficients, measurement of the center frequency of the normal mode peaks that upper and lower bound the band gap may be performed versus temperature. Loss mechanisms such as thermoelastic and Akhiezer dissipation may be investigated as a part of the determination of whether the P^{n}BG QC may be utilized for anchor loss reduction. Raman spectroscopy may assist in the characterization of loss. Damping and anchor losses may also be experimentally investigated utilizing optical techniques.

Modeling: The temperature, mode shape topography (spatial domain) and time and frequency domain (dynamic harmonic analysis) measurement data may be utilized to refine the electrical, thermal and mechanical material property data utilized in models. The electrical resistance of the P^{n}BG QC can be modeled and measured (possibly in CoventorWare® MemHenry^{TM}) and incorporated into the electrical models. The electrical circuit model of the P^{n}BG QC can be developed further. Models should be developed to account for the anisotropy of silicon. P^{n}BG crystals that have a comparable crystal structure to the P^{n}BG QCs may be investigated. Periodic two-dimensional mass-spring network and thermomechanical models should be refined. The thesis contained a sensitivity analysis for the square truncated P^{n}BG QCs, a similar sensitivity analysis may be performed for circularly truncated P^{n}BG QCs. A transient analysis model should be developed to build insight into the time and frequency dependence of the electromechanical coupling coefficient on transducer voltage, electrostatic force, and inertia and damping within the P^{n}BG QC. An electromechanical model of the output-current generation capability of the electrostatic transducers may be developed. The mechanism that controls the polarity of the temperature coefficient of the P^{n}BG QC

may be modeled further.

Nanoacoustics: Through the scalability of the elastic wave equation, the P^{n}BG QC architecture presented here may be scaled to nanometer dimensions to provide phonon control at hyper-sonic frequencies. The P^{n}BG QC architecture may have applicability in nano-electro-mechanical-systems and high quality factor and high linearity graphine may be a suitable material.

Discretized Phononics: The presented continuous elastic wave P^{n}BG QC architecture appears to be a distributed mechanical system and may be discretized into an array of mechanically coupled lumped element resonators.

Simultaneous Photonic-Phononic Integrated Circuits: The P^{n}BG QC architecture presented here may be compatible with integration into planar photonic integrated circuits to assist in enhanced photon-phonon control and interaction.

Applicability: The applicability of the P^{n}BG QC architecture may be further investigated for physical, chemical and bio-sensors, vibration stabilization, anchor loss reduction, sensor and signal processing element construction, coupled mass-spring resonator arrays, energy harvesters and the design of distributed mechanical systems in general. The vibration stabilized local resonator design that was presented in Chapter 7 may be developed and fabricated.

Appendix A

Mechanical Properties of Materials

The mechanical material properties and elastic wave velocities for air and the [100] direction in silicon are listed in Table A.1.

Table A.1: Mechanical material properties for air and the [100] direction in silicon. The velocity of the longitudinal, and transverse, components of the elastic wave are denoted as, c_l, and c_t, respectively.

Material Name	Density $[g/cm^3]$	c_l $[cm/s]$	c_t $[cm/s]$
Air	0.001225	30000	0
Silicon	2.33	895000	536000

Appendix B

Finite Element Method Mesh Convergence Study for Phononic Band Gap Quasi-Crystal Model

The modal analysis extraction method in ANSYS® utilizes the Block Lanczos calculation of eigenvectors and the FEM meshes utilize SOLID186 elements (unless otherwise specified) [141]. A convergence study was performed for the S1 P^{n}BG QC since it displays the minimum feature size of $2um$ (the minimum inclusion spacing), and so may be represented by the finest mesh, to develop insight into the degree of mesh refinement that should be utilized to represent the P^{n}BG QCs. The FEM mesh was refined three times as quantified in Table B.1 and illustrated in Figure B.1. These FEM meshes display one element across the features of minimum feature size and an increasing number of elements in the $\hat{z}$-direction.

The mesh refinement study indicates the band gap location, mode frequencies and the overall shape of the frequency versus mode number characteristic display relatively

small variations as the mesh is varied between the three FEM meshes of Table B.1 and Figure B.1. Close inspection indicates that two adjacent modes that have very similar frequencies may swap mode numbers as the mesh is refined; however, the mode shape of both modes would typically be present for each mesh and the presence of the band gap and the overall shape of the frequency versus mode number characteristic would remain relatively constant as the mesh is varied.

Since the P^{n}BG QCs are comprised of regions that are relatively large in comparison to the dimensions of the region between the inclusions, a mesh refinement which implements smaller (larger) element sizes in the regions of smaller (larger) feature size may be more computationally efficient and accurate. Such a mesh refinement was performed in ANSYS® utilizing SOLID187 elements and implemented meshes with two, three and four (for which the corresponding mesh is referred to as mesh 4) elements, across the region of minimum inclusion spacing. Mesh 4 is shown in Figure B.3.

As shown in Figure B.2, the frequency versus mode number characteristic computed utilizing mesh 4 (displayed in Figure B.3), which implements four elements across the region of minimum inclusion spacing, is relatively consistent with the result obtained for the unrefined mesh 3 (displayed in Figure B.1), which implements one element across the region of minimum inclusion spacing. Often course meshes yield sufficient accuracy for the overall mode shape and relative mechanical displacements (as long as absolute values are not required) [138] and in some cases perhaps mode frequency. In addition, according to Section 4.2.4, the minimum effective wavelength, λ, may be on the order of approximately $1000\mu m$; thus, even mesh 1, with an element size of $2\mu m$, provides approximately 500 elements (sample points) per wavelength, which is more than the Nyquist sampling theorem requires. Calculations of mechanical stress or absolute value of displacement may tend to display a higher sensitivity to mesh density [138]. The ab-

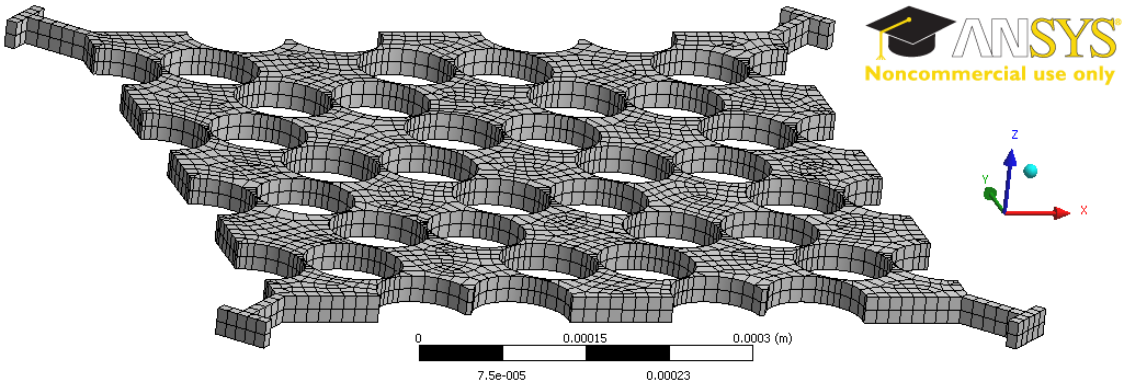

Mesh 1: mesh generated for an ANSYS® element size parameter of 12.5 um.

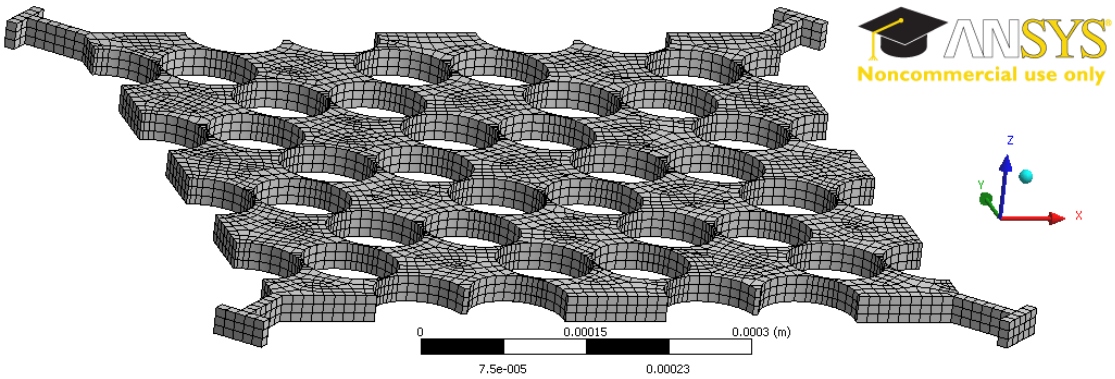

Mesh 2: mesh generated for an ANSYS® element size parameter of 10.25 µm.

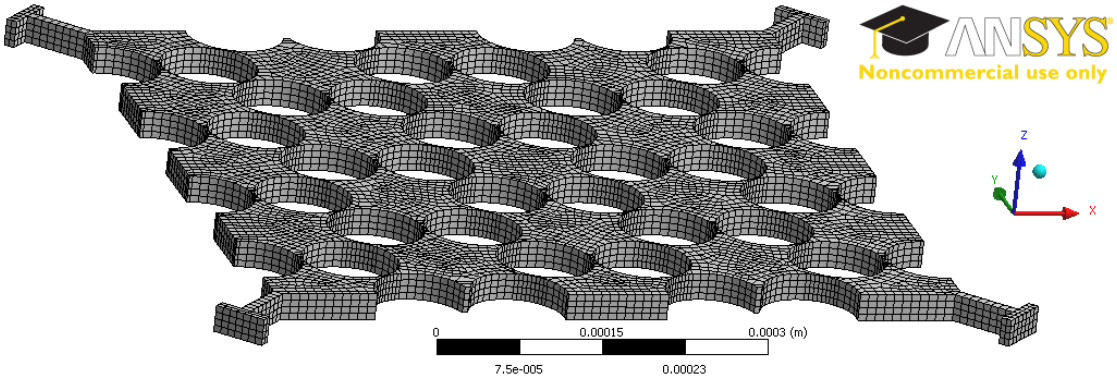

Mesh 3: mesh generated for an ANSYS® element size parameter of 8.25 um.

Figure B.1: Image of the meshes utilized in the finite element method method convergence study.

solute value of mode frequency, mechanical stress and the absolute value of displacement may be primarily relevant to future work, while the current work is primarily interest in overall trends and relative behavior. Figure B.4 displays a closeup of the region where the frequency versus mode number characteristic of the S1 P^nBG QC displays the greatest sensitivity to the mesh; it may be observed that mesh 3 and the refined mesh 4 display comparable results, however, as described in Figure B.4, the duration of time required to obtain this result utilizing mesh 4 was more than 10 times the duration of time required utilizing mesh 3.

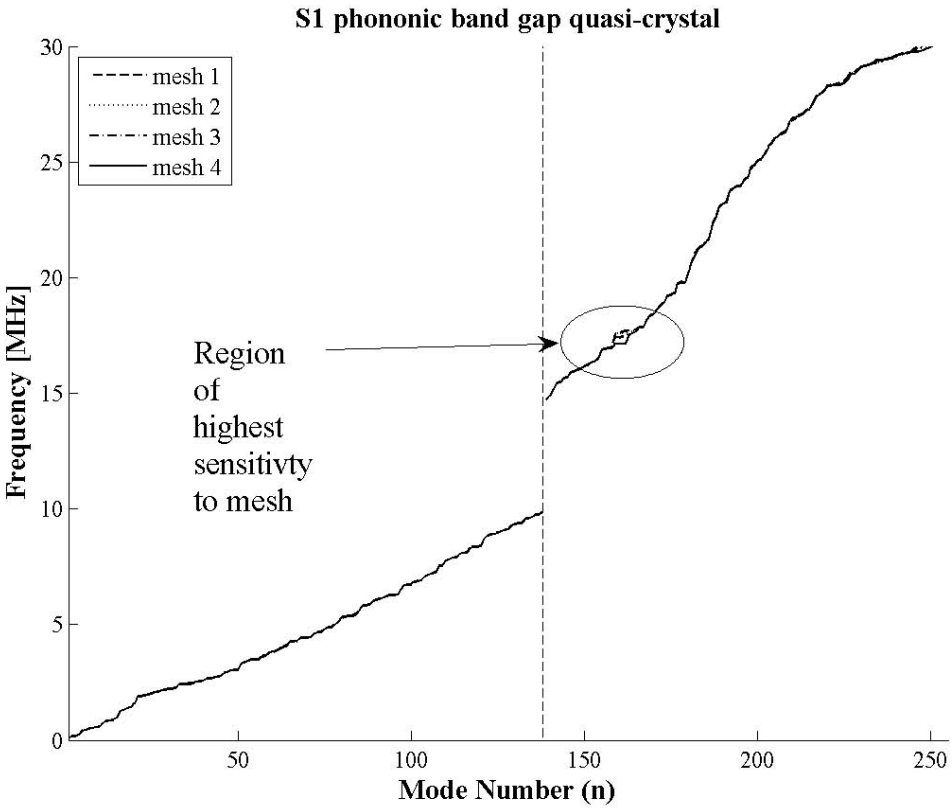

Figure B.2: Frequency versus mode number characteristic, for the S1 phononic band gap quasi-crystal, generated utilizing modal analysis in ANYSYS® and the finite element meshes, of Table B.1 and Figure B.1 and Figure B.3, which were utilized to perform a convergence study. The convergence study indicates that the band gap location and overall shape of the mode frequency versus mode number characteristic is relatively insensitive to the mesh utilized in the convergence study, since all four frequency versus mode number characteristics lie approximately on top of one another. One region, displayed in detail in Figure B.4, of the frequency versus of the mode number characteristic displays an increased sensitivity to the mesh; this region appears to be within the vicinity of where in-plane tether resonances are observed to occur on the boundary of behavioral zones V and VI as illustrated in Figure 4.17 and may indicate that the tether resonant modes, or nearby modes, are relatively sensitive to the mesh.

Table B.1: Description of the meshes, utilized in the finite element method mesh convergence study, and sample simulation times to perform modal analysis.

Device	Mesh #1				Mesh # 2				Mesh # 3			
	Element Size (μm)	Nodes	Elements	Time‡ (s)	Element Size (μm)	Nodes	Elements	Time‡ (s)	Element Size (μm)	Nodes	Elements	Time‡ (s)
Square		31834	5582	437/1133		-	-	-		-	-	-
S1		25900	3746	198/360		47516	7869	527/1046		86210	15436	1060/3649
S2		23188	3362	201/354		-	-	-		-	-	-
S3		23272	3402	212/361		-	-	-		-	-	-
S4	12.50	28111	4132	245/565	10.25	-	-	-	8.25	-	-	-
Circle		25274	4430	244/481		-	-	-		-	-	-
C1		17813	2560	120/240		-	-	-		-	-	-
C2		17273	2472	205/226		-	-	-		-	-	-
C3		17365	2512	93/201		-	-	-		-	-	-

‡Time is the CPU Time/Elapsed Time to perform a modal analysis with the search range limited to 255 modes for square truncated devices and 180 modes for circular truncated devices.

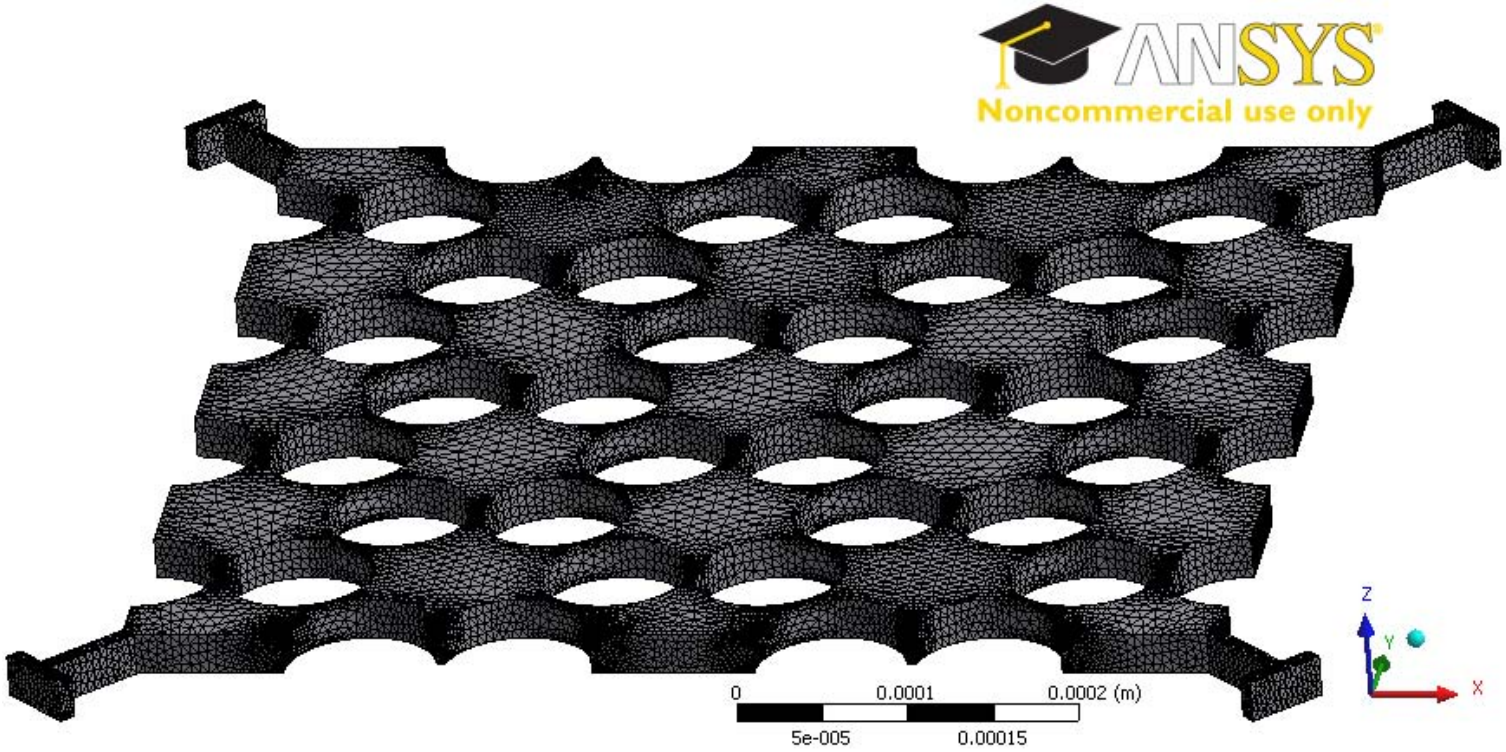

Figure B.3: Image of a refined mesh, referred to as mesh 4, utilized in the finite element method method convergence study for the S2 phononic band gap quasi-crystal. The element size is initially set to $25\mu m$. The maximum mesh refinement was performed on the top and bottom surface of the S2 phononic band gap quasi-crystal and resulted in the mesh having 367,300 nodes and 221,451 elements. The CPU time, and elapsed time, to perform a modal analysis with the search range limited to 170 modes is approximately 30 minutes, and 3.5 hours, which is approximately 10, and 35, respectively, times longer than the modal analysis of 255 modes utilizing mesh 3 of Table B.1 and Figure B.1.

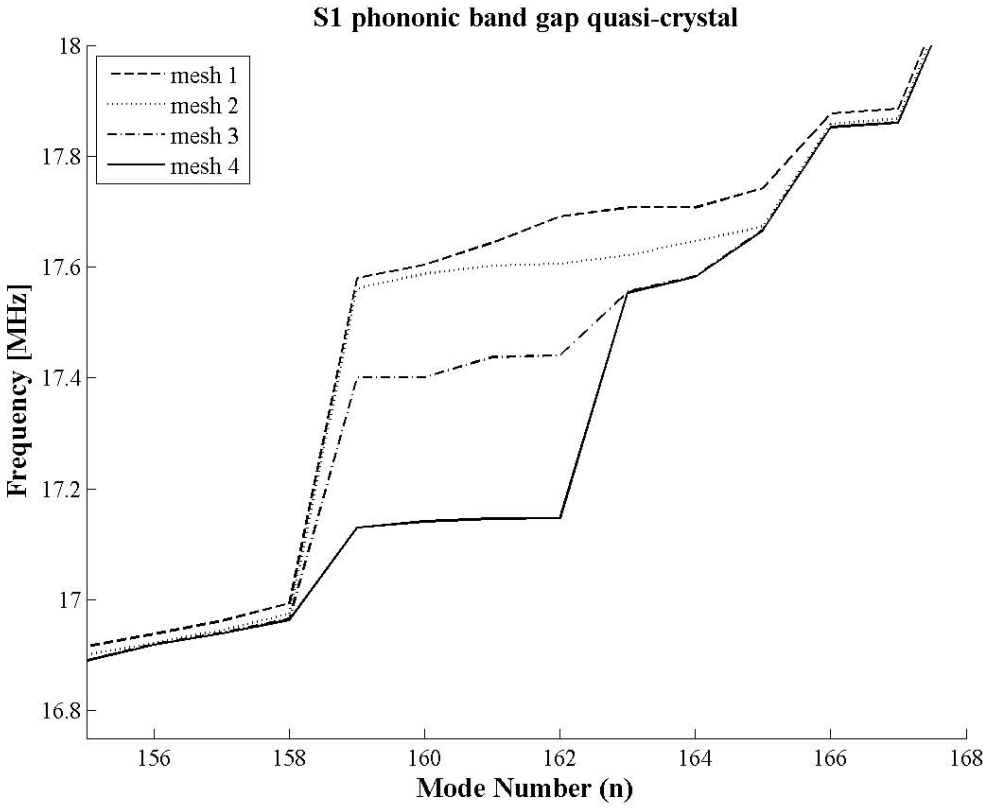

Figure B.4: Closeup of the region of Figure B.2 where the frequency versus mode number characteristic of the S1 phononic band gap quasi-crystal displays the highest sensitivity to the finite element method mesh.

Appendix C

Density of States Calculation for Phononic Band Gap Quasi-Crystals

A Density of States (DOS) calculation provides information regarding the frequency spacing of the modes of a P^{n}BG QC. A higher DOS implies more closely spaced modes. For application to the frequency versus mode number characteristics presented in this thesis, the DOS will be defined as:

$$DOS_{normalized} \triangleq \frac{1}{\frac{\Delta f}{\Delta n}}, \tag{C.1}$$

where Δf is frequency difference between adjacent normal modes and Δn the difference between the mode numbers of the corresponding modes of the frequency versus mode number characteristic. In the vicinity of adjacent degenerate modes (adjacent modes that

have the same frequency) the DOS is infinity. When the modes are evenly distributed, and there are not too many closely spaced modes, the average DOS of two structures may be compared; however, when a structure displays a few modes that are more closely spaced than the majority of modes, the average DOS can misleadingly become large. At band gap frequencies the DOS is not defined.

The DOS is computed for each of the S1, S2 and S3 P^nBG QCs and plotted in Figure C.1. It may be observed that there is no significant change in DOS between the square truncated P^nBG QCs; however, the average DOS of sub-band gap branches appears to be consistently larger than the average DOS of hyper-band gap branches.

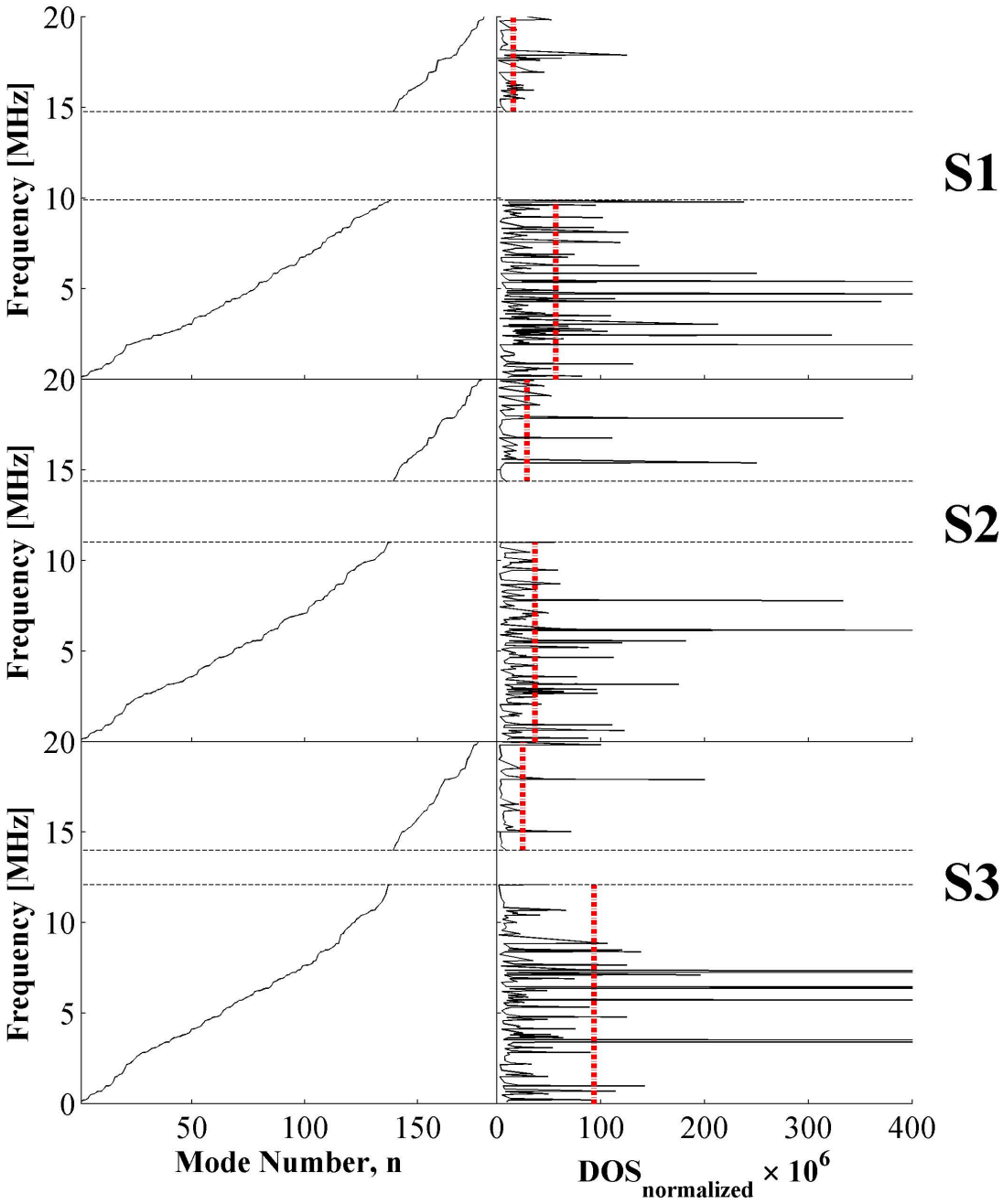

Figure C.1: Comparison of the frequency versus mode number characteristics and corresponding density of states calculated for the square truncated P^{n}BG QCs. The average density of states over each branch is indicate by the thick vertical dotted line that is superimposed upon the plot of $DOS_{normalized}$.

Appendix D

Semi-Analytic Vibration Model Calculations

The mass and stiffness values computed by the semi-analytical structural analysis performed in Section 4.2.4 and summarized in Table 4.6 for the S2 P^{n}BG QC will now be substituted into the analytical model of the resonant frequency of the first order harmonic oscillator shown in Figure 4.25. To resultant resonant frequencies are fitted to the corresponding resonant frequencies of the FEM model for the complete P^{n}BG QC. The resonant frequencies and fitting values are summarized in Table 4.6.

Sub-Band Gap Modes 62 and 87

The resonant frequency of the 1DOF models displayed in Figures 4.22, and 4.23, for the sub-band gap modes 62, and 87, respectively, for the S2 P^{n}BG QC may be approximated utilizing the model for the resonant frequency of the 1DOF lumped element harmonic oscillator shown in Figure 4.25:

$$f_{o,SBG,mode\ 62} = \frac{1}{2\pi}\sqrt{\frac{k_{total,mode\ 62}}{m_{large}}} = 0.417MHz \tag{D.1}$$

$$f_{o,SBG,mode\ 87} = \frac{1}{2\pi}\sqrt{\frac{k_{total,mode\ 87}}{m_{large}}} = 0.245MHz. \tag{D.2}$$

These resonant frequency values may be fit to the FEM model frequencies for mode 62, and 87, of 4.637 MHz, and 6.219 MHz, utilizing the fitting parameters shown in Table 4.6. As seen in Table 4.6, the percentage error between the 1DOF lumped element mass-spring harmonic oscillator model and the FEM model for modes 62, and 87, are -91%, and -96%, respectively.

Before fitting, the total stiffness, k, for mode 62 is larger than that for mode 87, while the effective mass is the same for both modes and so the first order harmonic oscillator model inaccurately predicts the resonant frequency to be larger for mode 62 than for mode 87. As may be seen in Table 4.6, after fitting occurs the total spring constants for modes 62 and 87 do increase as frequency increases for a given mass, as may be expected for the first order harmonic oscillator model.

Hyper-Band Gap Mode 149

The resonant frequency of the 1DOF beam model shown in Figure 4.24 for the hyper-band gap mode 149 of the S2 P^{n}BG QC may be approximated utilizing the model for the resonant frequency of the 1DOF lumped element harmonic oscillator shown in Figure 4.25:

$$f_{o,HBG,mode\ 149} = \frac{1}{2\pi}\sqrt{\frac{k_{HBG}}{m_{small}}} = 1.753MHz. \tag{D.3}$$

Equation D.3 indicates that the resonant frequency predicted by the beam model would be 1.753 MHz, which lies below the minimum hyper-band gap frequency of 14.346 MHz from Table 4.5. However, as mentioned in the structural analysis of Section 4.2.4, the hyper-band gap mass, m_{small}, of Figure 4.18 is an upper bound on the effective mass, and the spring constant k_{hbg} is a lower bound on the effective spring constant. Equation D.3 for the resonant frequency of mode 149 of the S2 P^{n}BG QC may be fit the to the FEM model (Figure 4.24) frequency of 15.852 MHz utilizing the fitting parameters in Table 4.6. As seen in Table 4.6, the percentage error between the FEM model and 1DOF lumped element mass-spring harmonic oscillator model for mode 149 is -88.939%.

If instead of computing an effective spring constant to fit the fixed-fixed beam model of Figure 4.24 and Equation D.3 to the FEM model frequency of 15.852 MHz for mode 149 of the S2 P^{n}BG QC, alternatively, the fit may be performed by scaling the beam length, l in Figure 4.21 and Figure 4.24 to an effective length of $l_{eff} = 0.368l$ (or 37% of the original length) for the same effective mass, $m_{eff} = \frac{2}{3}m_{small}$.

Hyper-Band Gap Tether Mode 161

The preceding vibration models utilized semi-analytical models of mass and stiffness in a lumped element 1DOF harmonic oscillator model to compute the resonant frequency the S2 P^{n}BG QC modes. For the tether mode 161 of Figure 4.15, an alternative approach may be to directly compute resonant frequency by solving the Eigenvalue problem for the fundamental mode of a uniform hinged-hinged beam [142]:

$$f_{o,TETHER,mode\ 161} = \frac{\pi}{2}\sqrt{\frac{EI}{ml_1^4}} = 44.5591MHz,$$
$$I = \frac{t \times w_1^3}{12}, \tag{D.4}$$

where $w_1 = 9.9\mu m$, $l_1 = 60.1\mu m$, and $t = 25\mu m$ are as denoted in Figure 3.4 and Table 3.1. The analytical model of Equation D.4 may be fit to the FEM model of the tether resonant frequency of $17.752MHz$ using the fitting parameters listed in Table 4.6. The Eigenvalue approach for mode 161 displays an error of 151.022%.

If the semi-analytical models of mass and stiffness were utilized in the lumped element 1DOF harmonic oscillator model shown in Figure 4.25 and fit to the FEM model of the tether mode 161 the percentage error would have been -97.268%. The semi-analytical structural analysis predicts an overly soft spring stiffness, while the Eigenvalue approach of Equation D.4 predicts an overly stiff spring stiffness. The analytical model parameters and fitted parameters for tether mode 161 computed utilizing the Eigenvalue and lumped element approaches are summarized in Table 4.6.

The Eigenvalue approach of Equation D.4 utilizes a hinged boundary while the 1DOF lumped element model of Figure 4.25 utilizes a fixed boundary condition, so there may not be equal grounds for comparison of the Eigenvalue and lumped-element models presented here. The Eigenvalue approach described in [142] along with a fixed boundary may be studied further.

D.1 Discussion of the Fitting Parameters

The results of the semi-analytical structural and vibration model and fitting parameters are summarized in Table 4.6. As may be viewed in Table 4.6, for the sub-band gap modes 62 and 87 the effective mass is not scaled during the fitting of the semi-analytical model to the FEM model. The reason for not scaling these sub-band gap mass values may be observed in Figures 4.22 and 4.23 where the physical region of the mode shape that represents the hexagonal mass element may be observed to display an approximately uniform displacement fields. Hence, it may be reasonable to assume that this hexagonal mass element may be approximated as a rigid body mass element for which the entire inertia of the mass element is concentrated at a single point the vibration model. Under these conditions, the effective mass may be very similar to the actual mass of the mass element and so no scale factor was applied to scale the mass of this mass element for modes 62 and 87.

In contrast, for the hyper-band gap modes 149 and 161, a scale factor of 2/3 was chosen to scale the mass of the beam models. The reason for doing so may be observed in Figure 4.24 where the mass of the beam is distributed over the entire length of the beam, with the portion of the mass near the ends of the beam undergoing less displacement than the portion of the mass near the center of the beam. Hence, it may be reasonable to assume that to have the same inertia a lumped mass located at the center of the beam should have a mass less than the physical mass of the entire beam. Typically a scale factor of 0.24 is applied to compute the effective mass of rectangular cantilevers [143]; thus, the scaling factor of 2/3 that was applied to the mass of hyper-band gap modes 149 and 161 may be considered well within an order of magnitude of the scaling factors typically used for rectangular cantilever structures. That said, during fitting, the individual scaling factors that were applied to the mass and spring stiffness in Table

4.6 are immediately divided by one another to produce just one scaling factor; the two scaling factors that were applied to mass and spring stiffness have been presented here just to illustrate a possible factorization of this one scaling factor.

D.2 Sources of Error

As may be viewed in Table 4.6 the semi-analytical model of resonant frequency displays percentage errors ranging from approximately -100% to 150%. This section provides possible sources of error.

Error may be attributed to the initial choice of geometrical parameters utilized in the semi-analytical model. The initial geometrical parameters were the geometrical parameters, such as inclusion spacing, s, and lattice constant, a, of the S2 P^{n}BG QC. As described within the semi-analytical structural analysis of Section 4.2.4, the geometrical parameters of the S2 P^{n}BG QC did not, in most cases, accurately represent the geometry of the simplified beams and flexural plate geometries. Rather, the geometrical parameters of the S2 P^{n}BG QC provided a relatively unbiased initial geometry. As a result, it was expected that scaling factors would have to be applied to the initial geometrical parameters of Table 4.6. This methodology of choosing the initial geometrical parameters for the semi-analytical model in a way that is clearly based on the existing geometrical parameters of the P^{n}BG QC was chosen in favor of an alternative approach where the initial geometrical parameters could have been chosen in a way that would introduce immediate scaling and fitting of the semi-analytical model parameters so as to produce expected results prior to the application of fitting parameters.

The percentage error in Table 4.6 between the semi-analytical vibration model and FEM model is relatively large independent of whether the one degree of freedom lumped

element harmonic oscillator or Eigenvalue approach to vibration modeling is utilized. The percentage error is 150% even for tether mode 161 where the geometry of the beam model approximation is very comparable to the FEM model. Thus, in the absence of other sources or error, the error in the beam model may not be due to a poor choice of beam geometry, and may be attributed an in accurate analytical model. That said, other sources of error may be present; for example, the Eigenvalue approach utilizes a hinged boundary condition approximation of what in Figure 4.15 may more accurately be described as a fixed, pinned, or elastic boundary.

Error also arises in the semi-analytical model since different modes, that have different mode frequencies in the FEM model, may in one subset of the FEM model display the same local vibration pattern and so possibly the same lumped element approximation, which would result in the same semi-analytical resonant frequency for modes that have different frequencies. A more accurate semi-analytical model should describe a subset of the P^{n}BG QC that displays a unique vibration pattern for each mode.

Lastly, as the inclusion spacing, s, is reduced, hyper-band gap spring stiffness may be expected to decrease which may in turn be expected to reduce hyper-band gap resonant frequencies; however, some frequency regions of the hyper-band gap branches in Figure 4.10 may be observed to increase in frequency as inclusion spacing, s, is reduced. To account for such complex behavior may require a more complex analytical model, for example, that accounts for more than one DOF. For instance, Figure 4.20 illustrates that the physical region of the P^{n}BG QC that is approximated by the small lumped element mass, m_{small}, of the hyper-band gap mass-spring network of Figure 4.18 appears to display one translational DOF in the $\hat{z}$-direction and potentially some rotational degrees of freedom so may be more accurately modeled utilizing more than one DOF. Due to the many sources of error discussed within this section, the trends in the semi-analytical

structural and vibration model are primarily presented here for further development.

Appendix E

Library of Scanning Electron Micrograph Images of the Fabricated Phononic Band Gap Quasi-Crystal Devices

This appendix presents scanning electron micrograph images of the remaining devices, that were not presented in the body of the thesis, on the IMOWTRF2 chip, which was fabricated in SOIMUMPs [47]. The Square, S1 P^nBG QC, S4 P^nBG QC, S3 P^nBG QC, Circular, C1 P^nBG QC and C3 P^nBG QC devices are displayed.

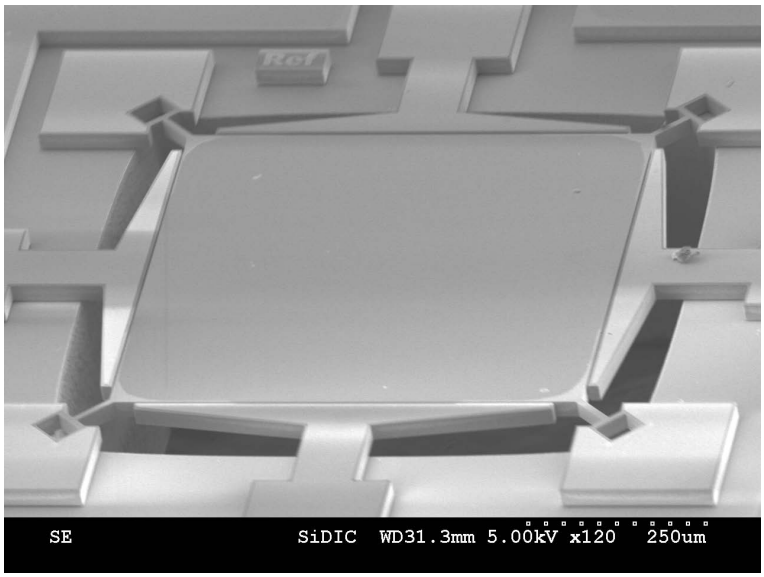

Figure E.1: Scanning electron micrograph of the Square homogeneous plate.

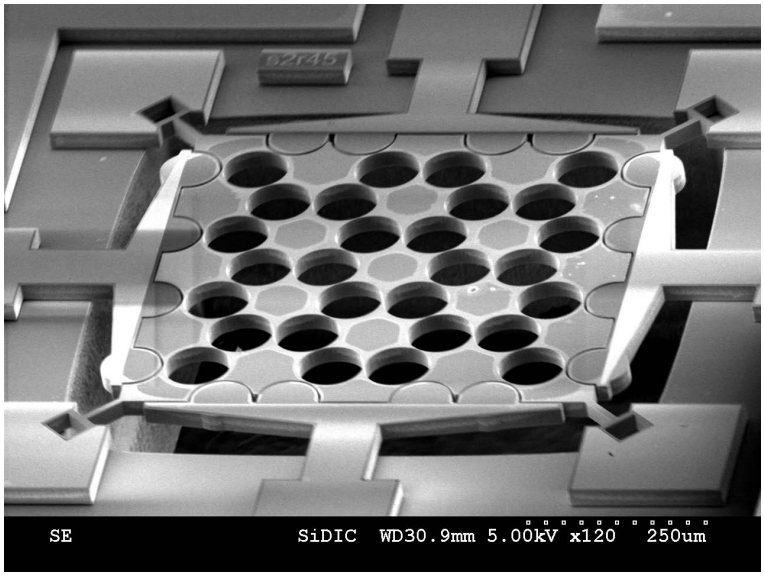

Figure E.2: Scanning electron micrograph of the S1 phononic band gap quasi-crystal.

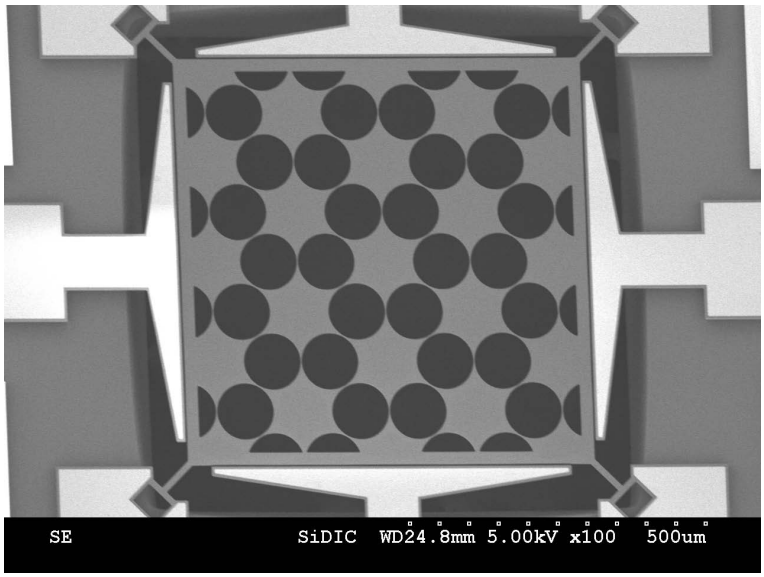

Figure E.3: Scanning electron micrograph of the S4 phononic band gap quasi-crystal.

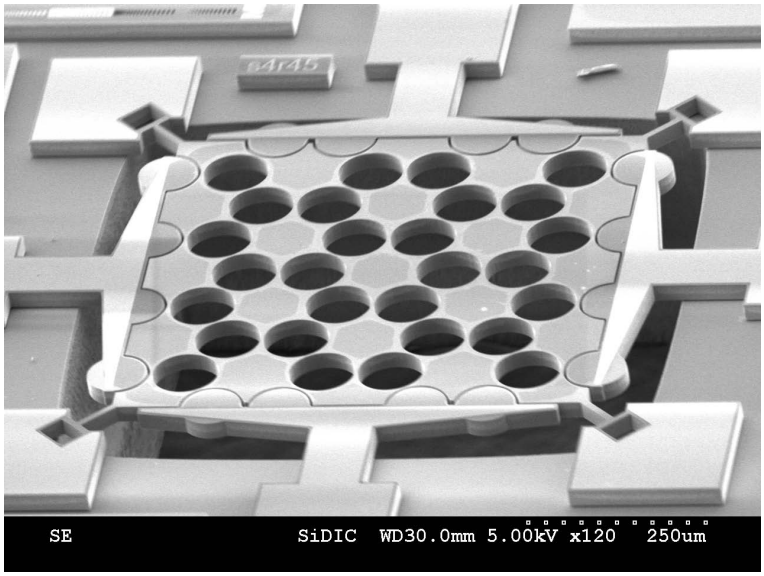

Figure E.4: Scanning electron micrograph of the S3 phononic band gap quasi-crystal.

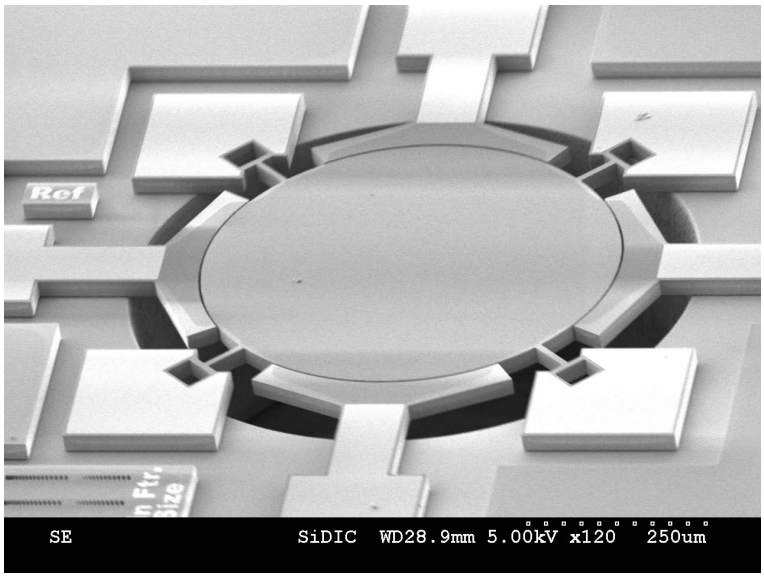

Figure E.5: Scanning electron micrograph of the Circular homogeneous plate.

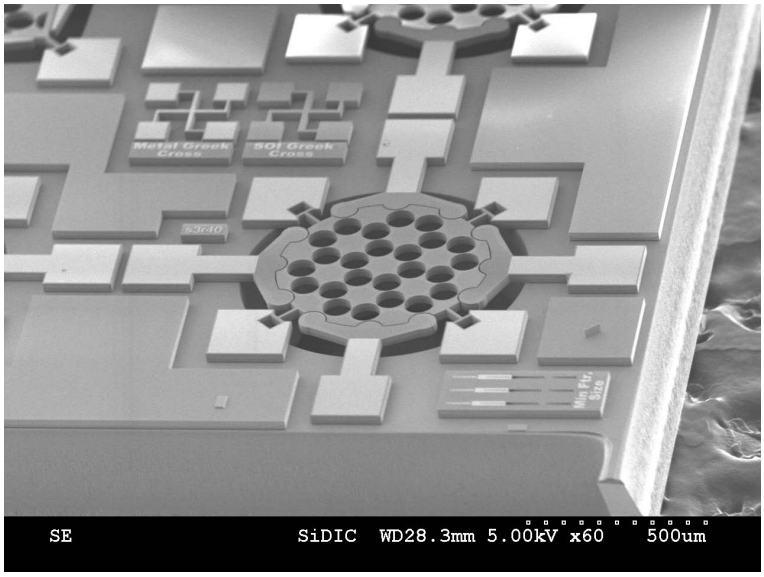

Figure E.6: Scanning electron micrograph of the C2 phononic band gap quasi-crystal.

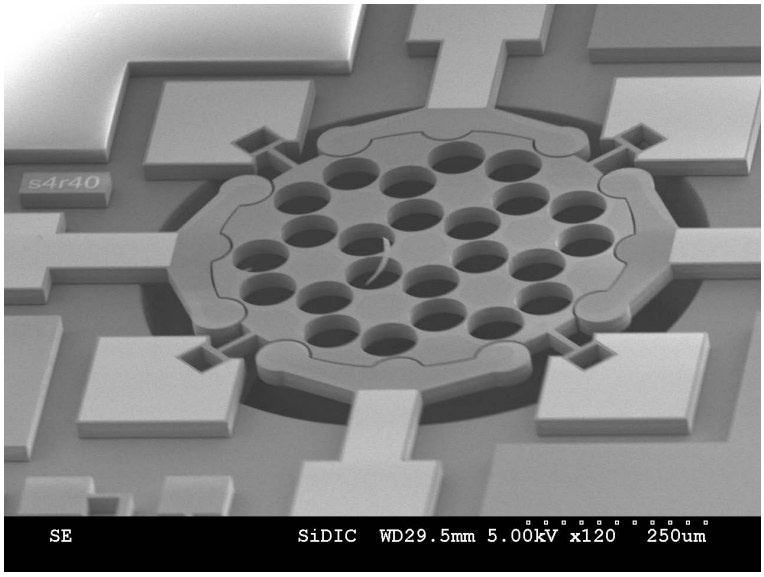

Figure E.7: Scanning electron micrograph of the C3 phononic band gap quasi-crystal.

Appendix F

Library of Surface Metrology Measurements of the Fabricated Phononic Band Gap Quasi-Crystal Devices

This appendix presents surface metrology measurements, taken utilizing the profilometer shown in Figure 5.6, of the S2 P^nBG QC. A 3D view of the tether region is displayed in Figure F.1 and tether widths were measured in Figure F.2 to be greater than $10\mu m$; however, profilometer measurements may display relatively large error near the edges of a device. The profilometer measurement of the entire S2 P^nBG QC device is displayed in Figure F.3, where the groove that was discussed in Section 5.2.2 may be observed to be present across the surface of the S2 P^nBG QC.

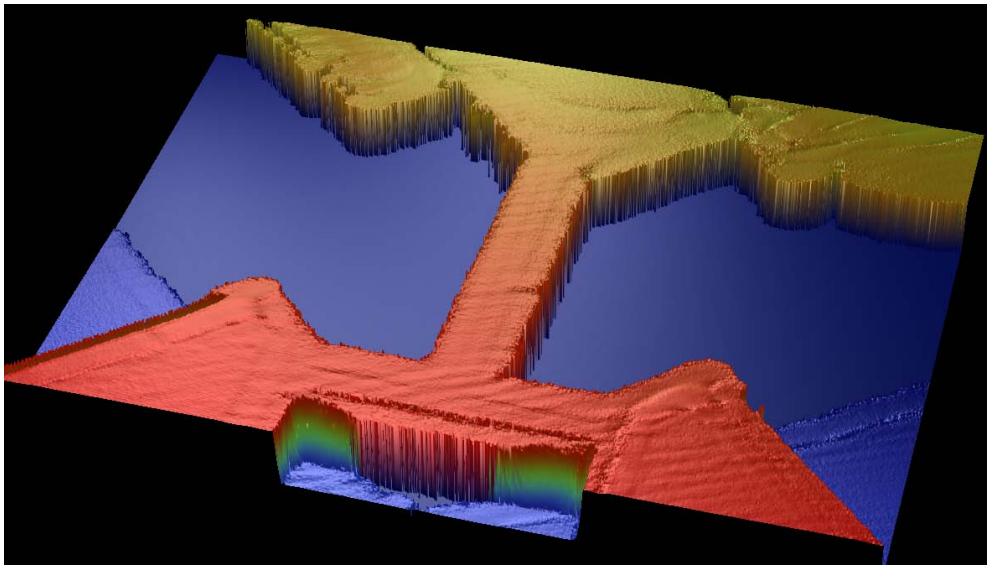

Figure F.1: 3D view of the profilometer measurement of the tether of the S2 phononic band gap quasi-crystal device.

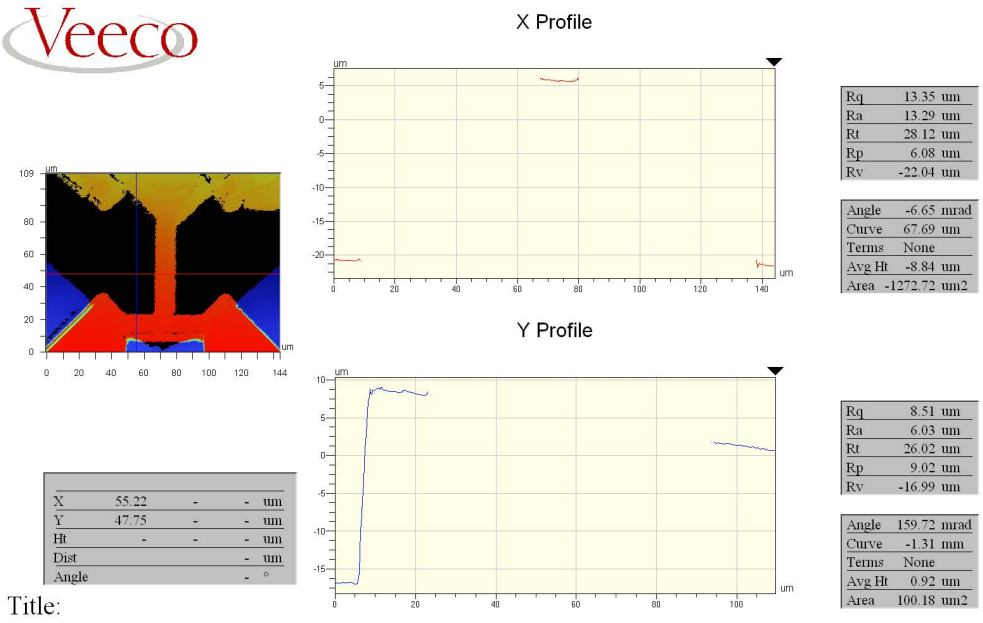

Figure F.2: Profilometer measurement of the tether widths of the S2 phononic band gap quasi-crystal device.

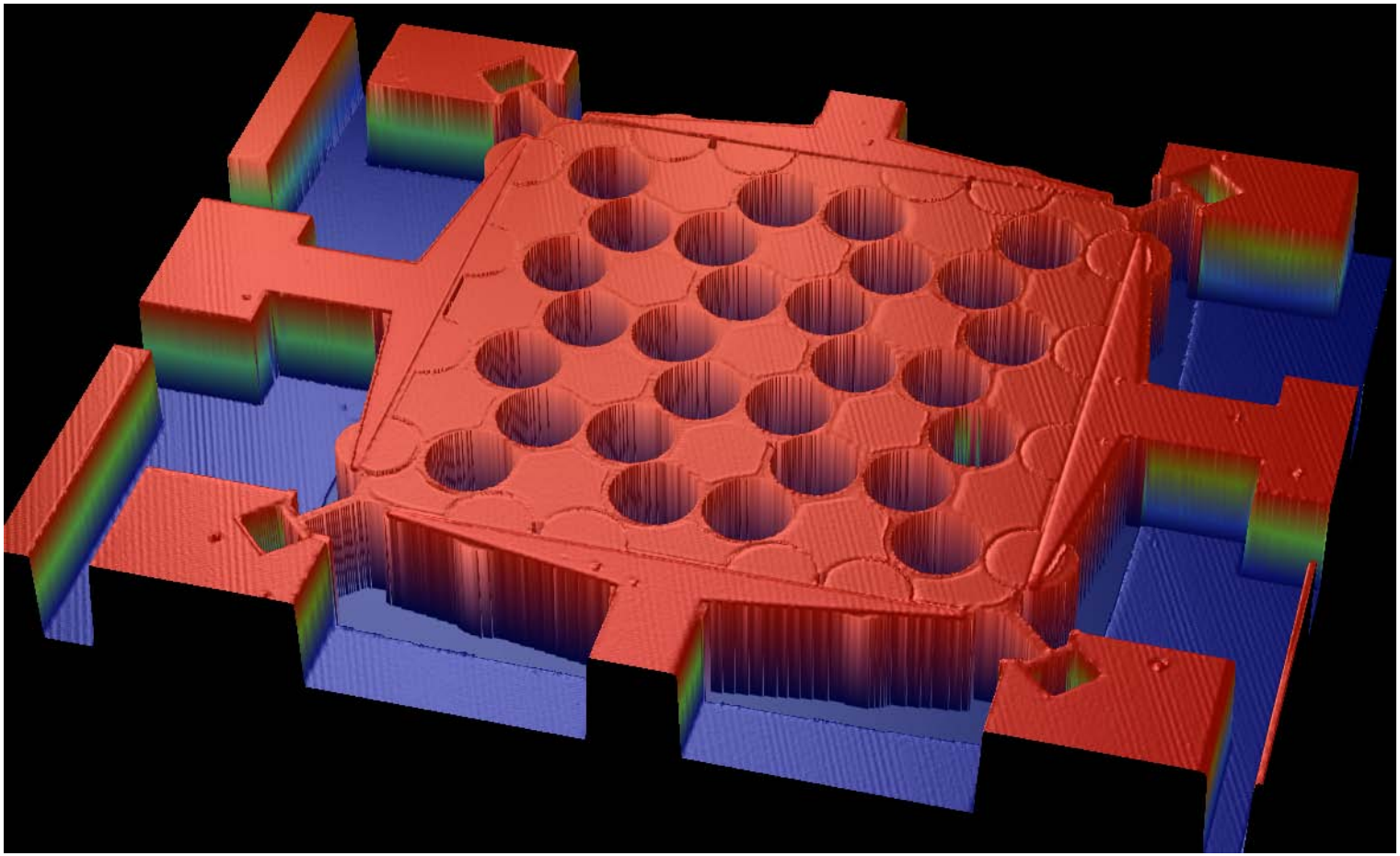

Figure F.3: 3D view of the profilometer measurement of the S2 phononic band gap quasi-crystal device.

Appendix G

Library of Harmonic Analysis of the Fabricated Phononic Band Gap Quasi-Crystal Devices

This appendix contains harmonic analysis measurements for the Square reference and S2 P^nBG QC devices on the IMOWTRF2 chip which was fabricated in SOIMUMPs [47]. Each harmonic measurement is taken over a 5 kHz to 20 MHz frequency range utilizing the spectrum analyzer (shown in Figure 6.2) set to a 1 Hz sense resolution bandwidth. It is notable that the vibrometer spectrum for Point 3 in Figure G.2 does not appear to display resonant peaks above 13 MHz; this may in part be due to the laser spot being located on or near the node location that was observed in Section 4.2.3 in this physical region for the majority of the hyper-band gap mode shapes that are present in this frequency region.

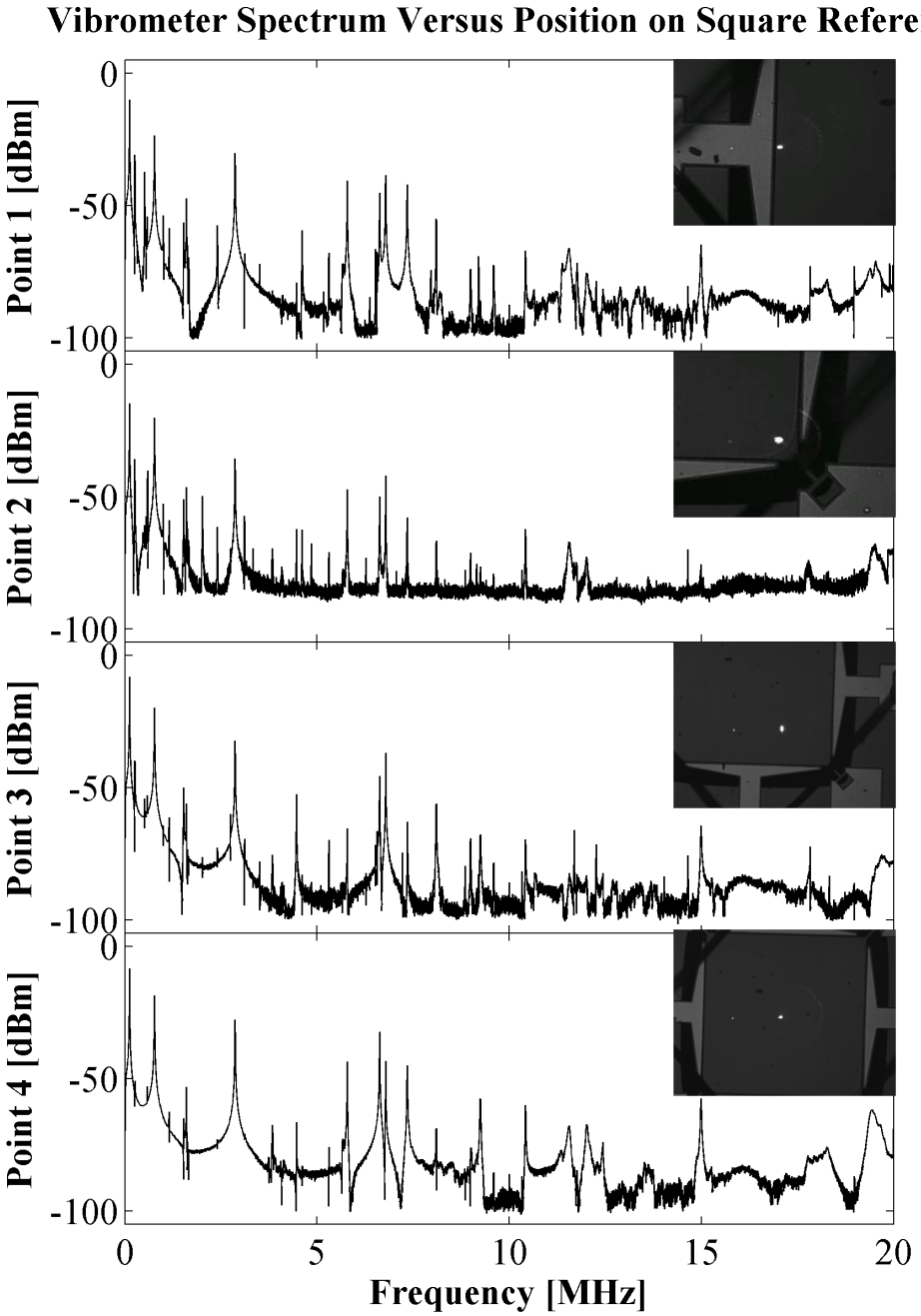

Figure G.1: Spectrum of the homogeneous Square reference device taken at the points denoted by the white spot in each inset.

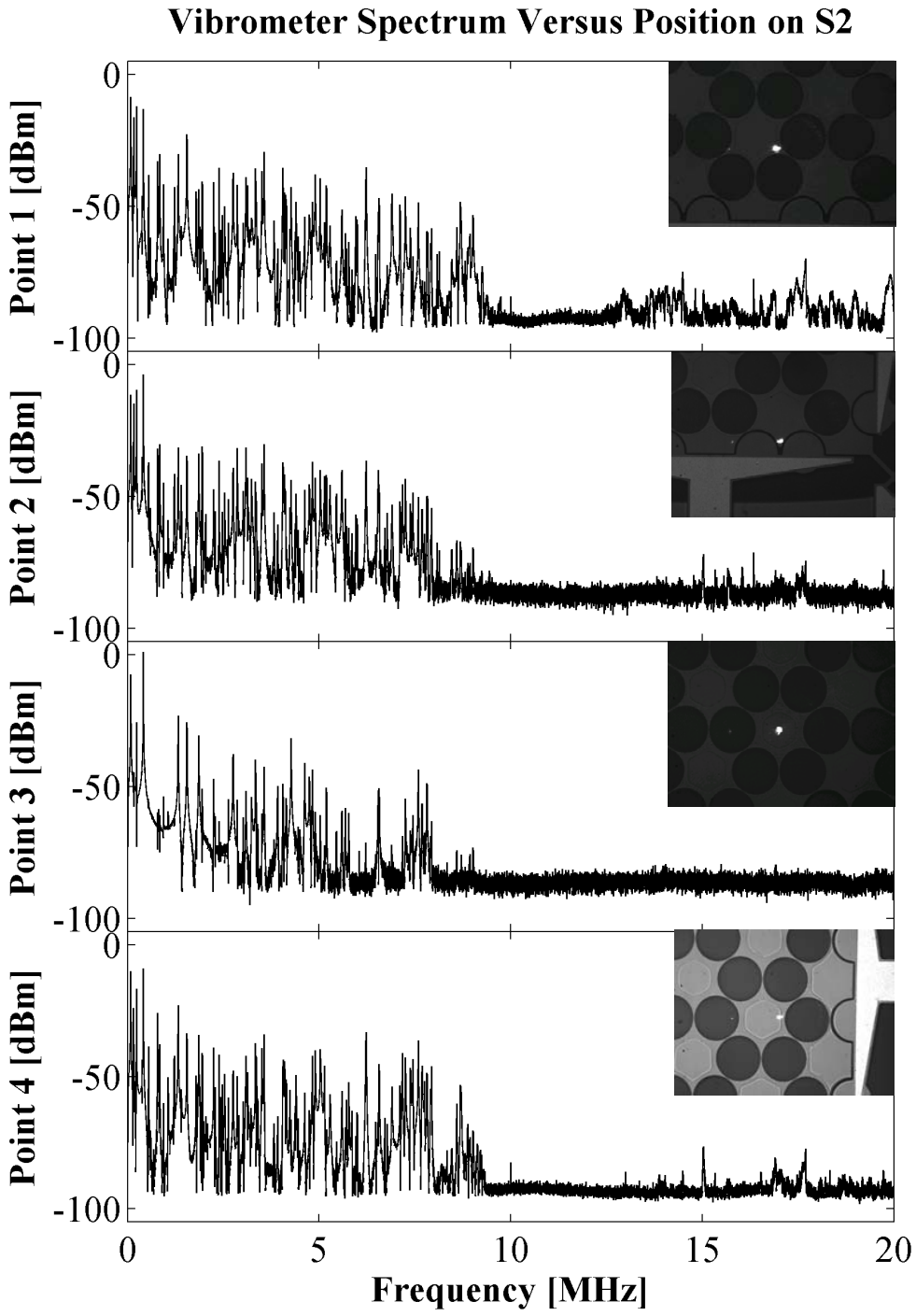

Figure G.2: Spectrum of the S2 phononic band gap quasi-crystal device taken at the points denoted by the white spot in each inset.

Appendix H

Library of Mode Shape Topology Measurements of the Fabricated Phononic Band Gap Quasi-Crystal Devices

This appendix contains mode shape topography measurements for the S1 P^nBG QC on the IMOWTRF2 chip which was fabricated in SOIMUMPs [47]. Each mode shape measurement takes approximately 40 hours utilizing the spectrum analyzer (shown in Figure 6.2) set to a 0.1 Hz sense resolution bandwidth.

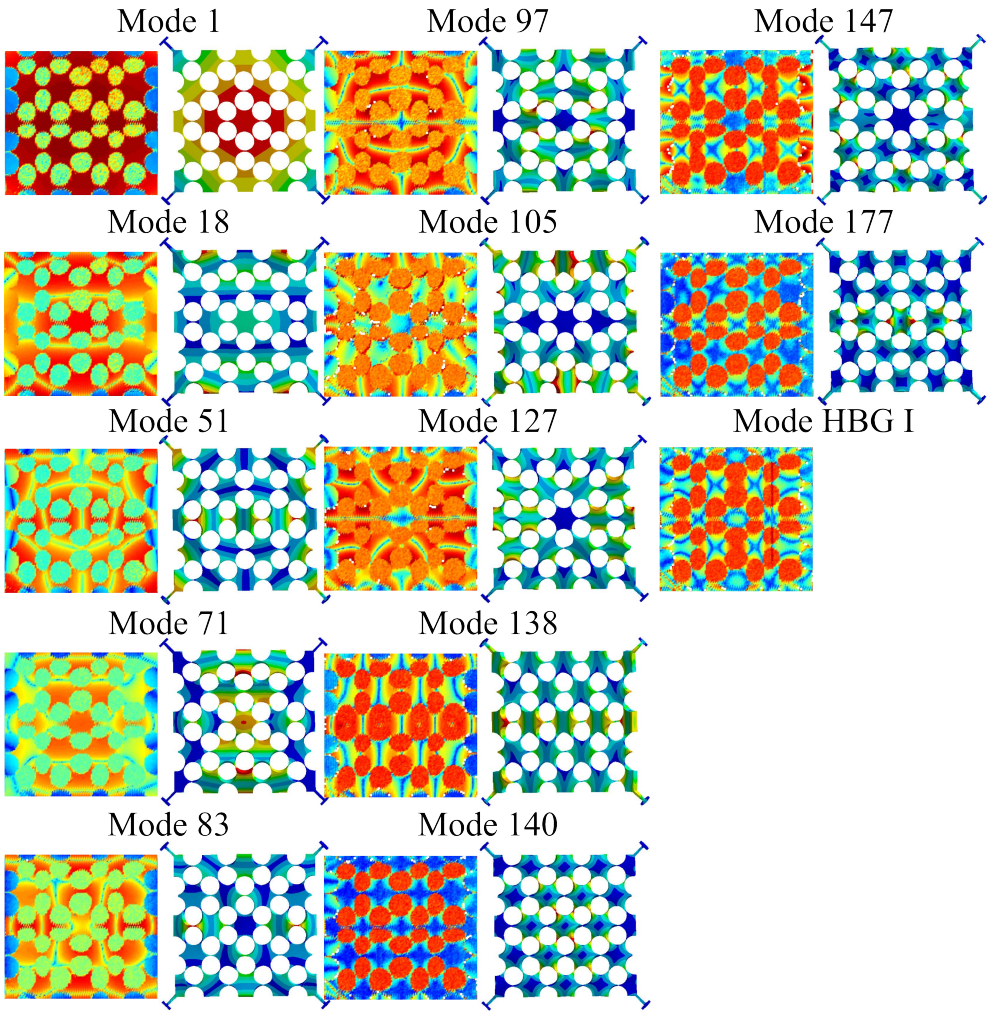

Figure H.1: Measured normal mode surface topography for the S1 phononic band gap quasi-crystal. Sub-Bandgap modes are: (n=1, 720.00 kHz), (n=18, 1.168350 MHz), (n=51, 2.938000 MHz), (n=71, 4.067200 MHz), (n=83, 4.929200 MHz), (n=97, 5.966350 MHz), (n=105, 7.019700 MHz), (n=127, 8.327800 MHz) and (n=138, 9.184400 MHz). Hyper-Bandgap modes are: (n=140, 13.270550 MHz), (n=147, 16.157050 MHz), (n=177, 19.606400 MHz), (n=188, 17.281250 MHz) and (unknown hyper-bandgap I, 17.281250 MHz).

Appendix I

Discretized Phononic Band Gap Quasi-Crystals

This appendix utilizes the analytical model presented in [86] to design mass-spring networks according to P^{n}BG crystal theory. A discretized P^{n}BG QC will be defined as a periodic mass-spring network that is truncated to a finite periodicity. Discretized P^{n}BG QCs approximate the frequency selectivity of P^{n}BG crystals (see Chapter 1). The behavior of the discretized P^{n}BG QC will be compared with that of infinitely periodic mass-spring networks. Section I.1 presents the dispersion curve of infinitely periodic mass-spring networks, while Section I.2 presents the spectrum and frequency versus mode number characteristic for a discretized P^{n}BG QC.

I.1 Infinitely Periodic Mass-Spring Networks

An Infinitely Periodic Mass-Spring (IPMS) network is displayed in Figure I.1(a). Employing the analytical model presented in [86] (noting that in [86], the expression below

Equation 9 should read $C_i = 2C_c + C_s - m_n\omega^2$), the dispersion curve of the IMPS may be computed for various conditions as displayed in Figure I.2. It may be noted in Figure I.2 that only the IPMSs that have contrasting mass elements, $m_1 \neq m_2$, display a band gap between the Longitudinal Acoustical (LA) and Longitudinal Optical (LO) branches. Further analysis is presented in [86].

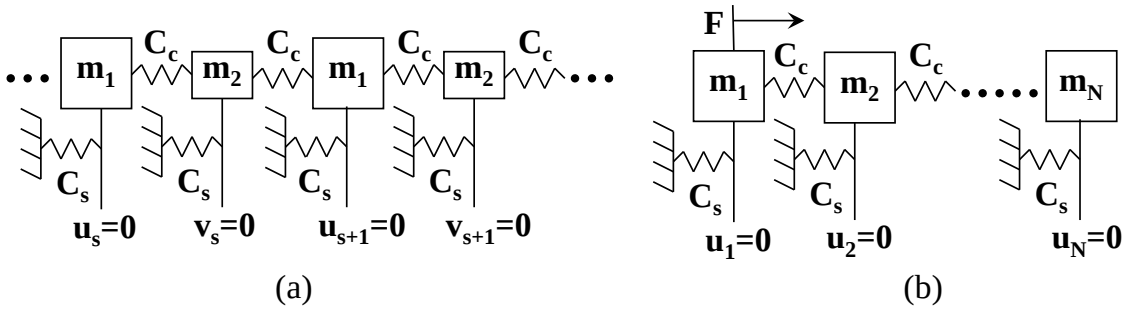

Figure I.1: (a) Infinitely periodic mass-spring network with displacement of large masses, m_1, denoted as u_s, and displacement of small masses, m_2, denoted as v_s. (b) Truncated periodic mass-spring network comprised of N masses, with time harmonic force, and displacement, amplitudes of F, and u_n, respectively. Coupling and suspension spring constants are denoted as C_c and C_s. Each mass element is anchored to mechanical ground via a suspension spring. [86]

I.2 Discretized Phononic Band Gap Quasi-Crystal Mass-Spring Networks

An truncated periodic mass-spring network, or discretized P$^{\text{n}}$BG QC, is displayed in Figure I.1(b). Employing the analytical model presented in [86], Figure I.3 displays the harmonic response result for a 33-mass discretized P$^{\text{n}}$BG QC, which has the parameters listed in Table I.1. The band gap location in the harmonic response of Figure I.3 approximates the equivalent IPMS band gap location which is denoted by f_L and f_H. The frequency versus mode number characteristic of the 33-mass discretized P$^{\text{n}}$BG QC

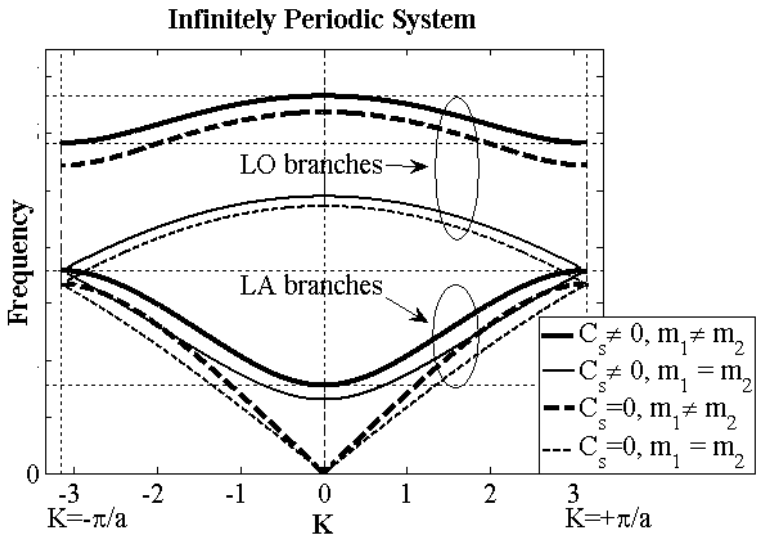

Figure I.2: Dispersion relations for diatomic ($m_1 \neq m_2$) and monatomic ($m_1 = m_2$) IPMS networks. Longitudinal Acoustical (LA) and Longitudinal Optical (LO) branches are displayed over the first Brillouin zone for $Cs \neq 0$ and $C_s = 0$. K is the wave vector in the longitudinal direction. The lattice constant is $a = 1$ m. This figure represents a correction to that presented in [86].

Table I.1: Geometrical parameters of the 33-mass discretized phononic band gap quasi-crystal.

Large mass	m_1	32 ng
Small mass	m_2	12 ng
Suspension spring constant	C_s	70 N/m
Coupling spring constant	C_c	10 N/m

is displayed in Figure I.4.

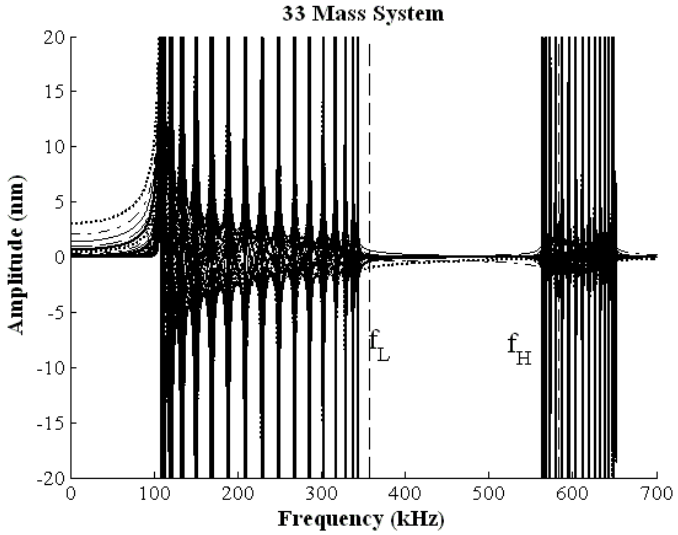

Figure I.3: Time harmonic amplitude versus frequency for each mass in a 33-mass discretized phononic band gap quasi-crystal.

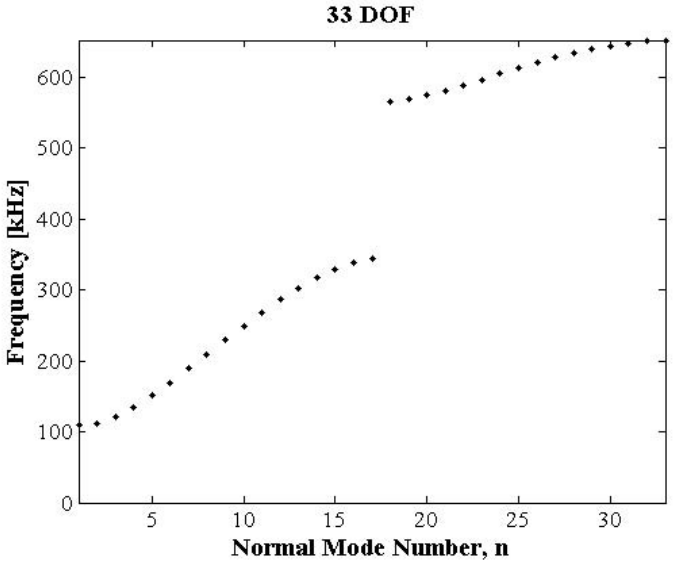

Figure I.4: Frequency versus mode number characteristic of a 33-mass discretized phononic band gap quasi-crystal. The slope of a line that passes through the branch below the band gap is slightly larger than the slope of a line that passes through the branch above the band gap.

Appendix J

Measurement of the Transducers of the Phononic Band Gap Quasi-Crystal Architecture

Section J.1 of this appendix presents harmonic analysis measurements of an electrostatically actuated prototype P^{n}BG QC, which was fabricated prior to the development of the P^{n}BG QC architecture that was presented in the body of this thesis, and was utilized to demonstrate wide band actuation up to approximately 8 MHz, with a measurable amplitude. This provided preliminary data for the electrostatic actuation of P^{n}BG QCs. Section J.2 of this appendix presents dynamic harmonic measurements of the fixed transducer electrodes of the S2 P^{n}BG QC.

J.1 Preliminary Investigation of Electrostatic Actuation of Phononic Band Gap Quasi-Crystals

To test the ability of electrostatic transducers to actuate P^{n}BG QCs, a prototype P^{n}BG QC design that is comprised of a honeycomb crystal that is approximately nine lattice constants square in dimension, suspended by straight tethers and bounded by flat edges was designed and fabricated. A SEM image of the prototype P^{n}BG QC is depicted in Figure J.1.

The P^{n}BG QC prototype was modeled utilizing the FEM implementation in ANSYS® [121] utilizing a mesh with 204,427 nodes, 34,470 elements and the approximate simulation time for modes within a 0 to 100 MHz frequency range was 1.5 days.

The FEM model results are displayed in Figure J.2 and suggests band gap activity from approximately $f_1 = 63.435$ MHz to $f_2 = 87.183$ MHz. Evidence of band gap activity is also displayed in Figure J.3, in the FEM model of mode shape, obtained utilizing CoventorWare® , in the form of reduced vibrational amplitude within the center region of the prototype P^{n}BG QC for modes above approximately 60 MHz and below approximately 90 MHz. The FEM model of mode shape in Figure J.3 suggests that complete band gap formation does not occur due to the presence of in-gap defect states that are composed parasitic edge or anchor resonances.

Mode shape measurements, of the prototype P^{n}BG QC of Figure J.1, are displayed in Figure J.4 which indicates that electrostatic actuation occurs up to 8.204 MHz; higher frequency modes may also be measurable. The prototype P^{n}BG QC is less compliant than the P^{n}BG QCs presented in the body of this thesis. The actuation of the prototype P^{n}BG QC may then provide some support that electrostatic actuation may be applied to the more compliant P^{n}BG QCs that are developed within the body of this thesis (though

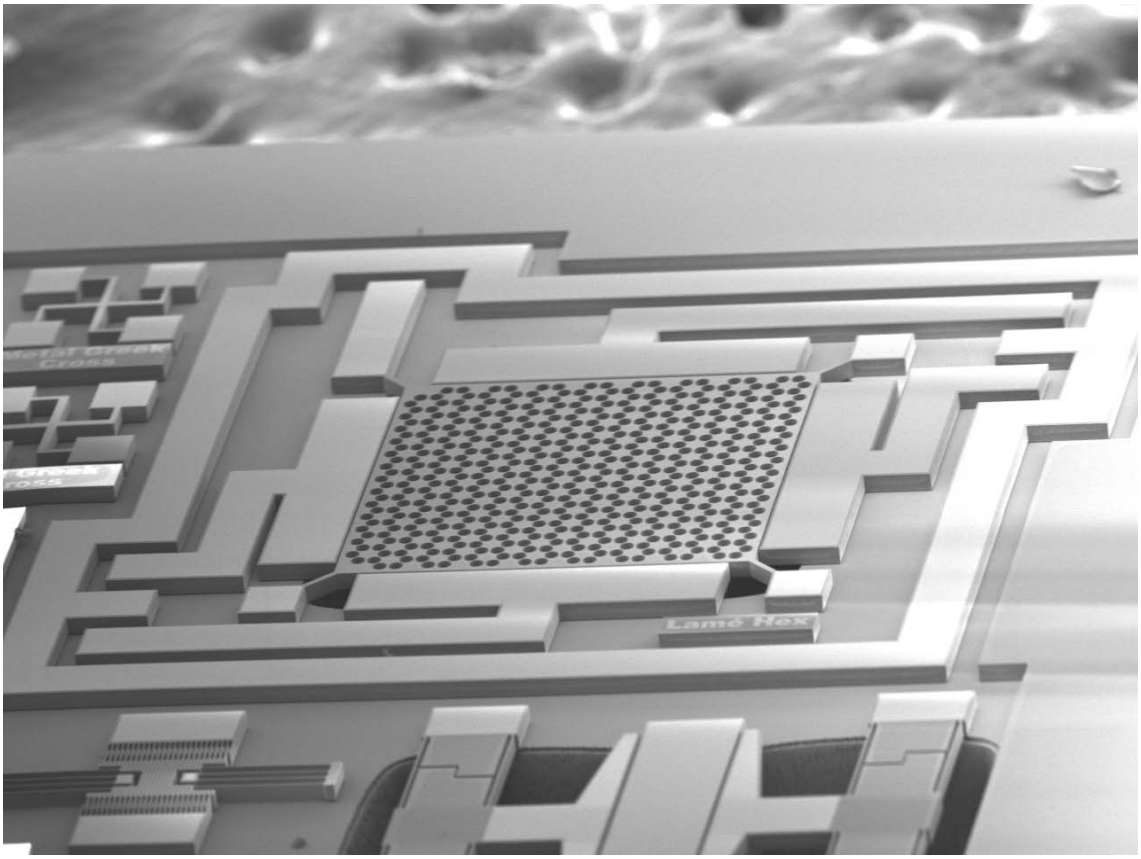

Figure J.1: Scanning electron microscope image of the prototype phononic band gap quasi-crystal device, which was utilized to investigate the electrostatic actuation of phononic band gap quasi-crystal devices.

it should be noted that the prototype P^{n}BG QC has a different transducer geometry, which rigidly anchors to the substrate a larger portion of the fixed transducer).

This section developed insight into electrostatic actuation of P^{n}BG QCs and the understanding that the flat edges and anchors of the prototype P^{n}BG QC in Figure J.1 produce in-gap defect states. This data was utilized to develop the P^{n}BG QC architecture that is presented in the body of this thesis.

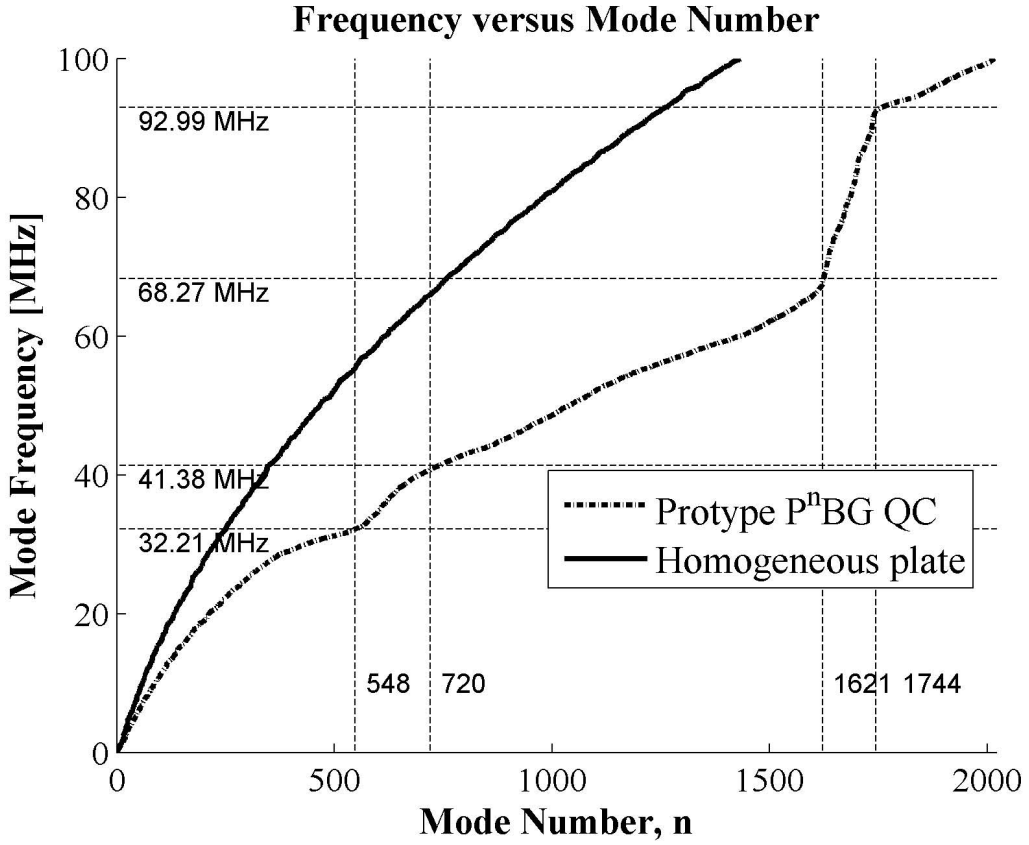

Figure J.2: FEM model of the mode number versus frequency characteristic of the prototype phononic band gap quasi-crystal shown in Figure J.1.

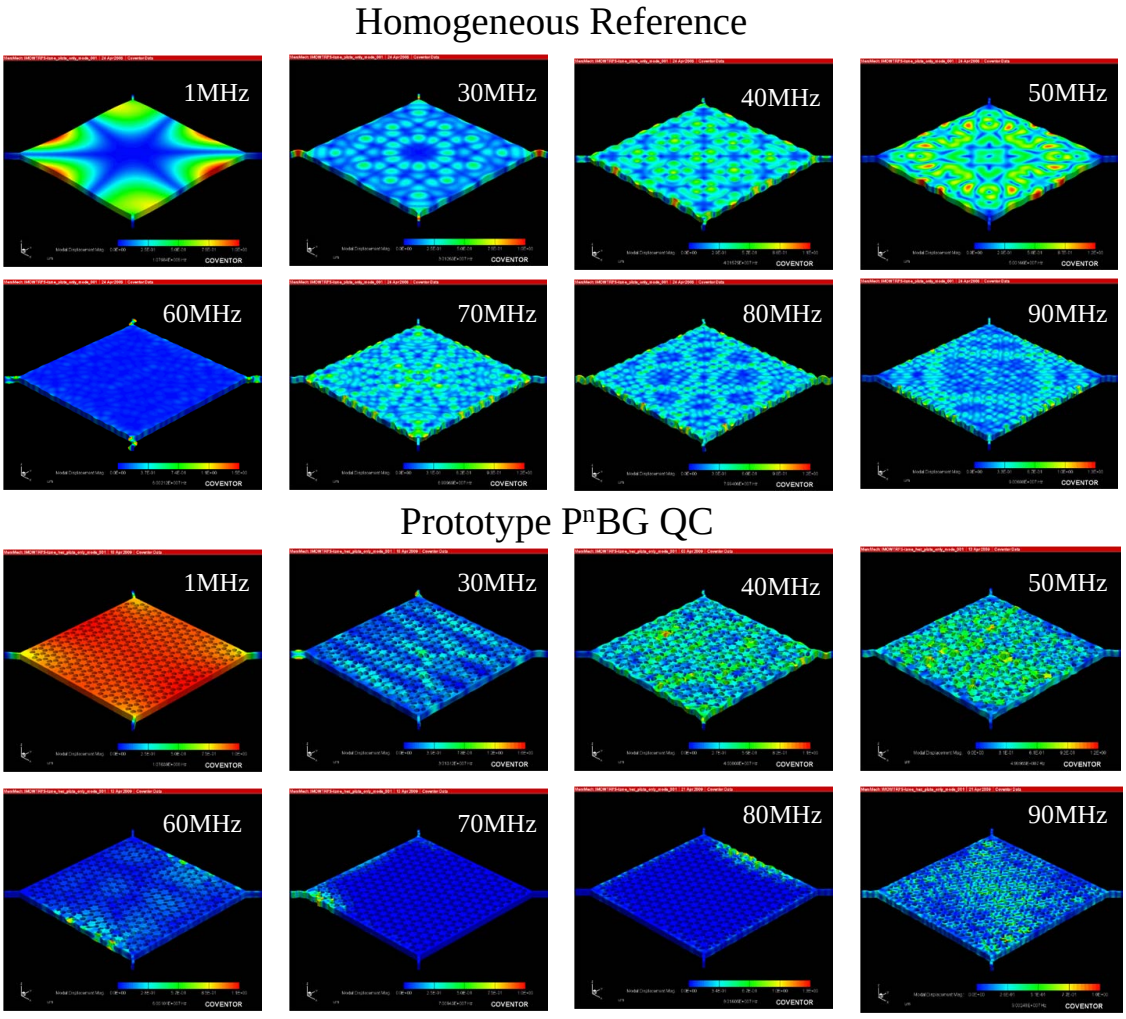

Figure J.3: Comparison of mode shapes of a homogeneous plate versus the prototype phononic band gap quasi-crystal over the frequency range from 0 to 100 MHz at a frequency spacing of 10 MHz. The homogeneous plate appears to have vibrational activity at most modes whereas P^{n}BG crystal appears to display an approximately 20 MHz frequency span over which modes occur largely due to edge vibrations while the center of of the prototype phononic band gap quasi-crystal is relatively stationary.

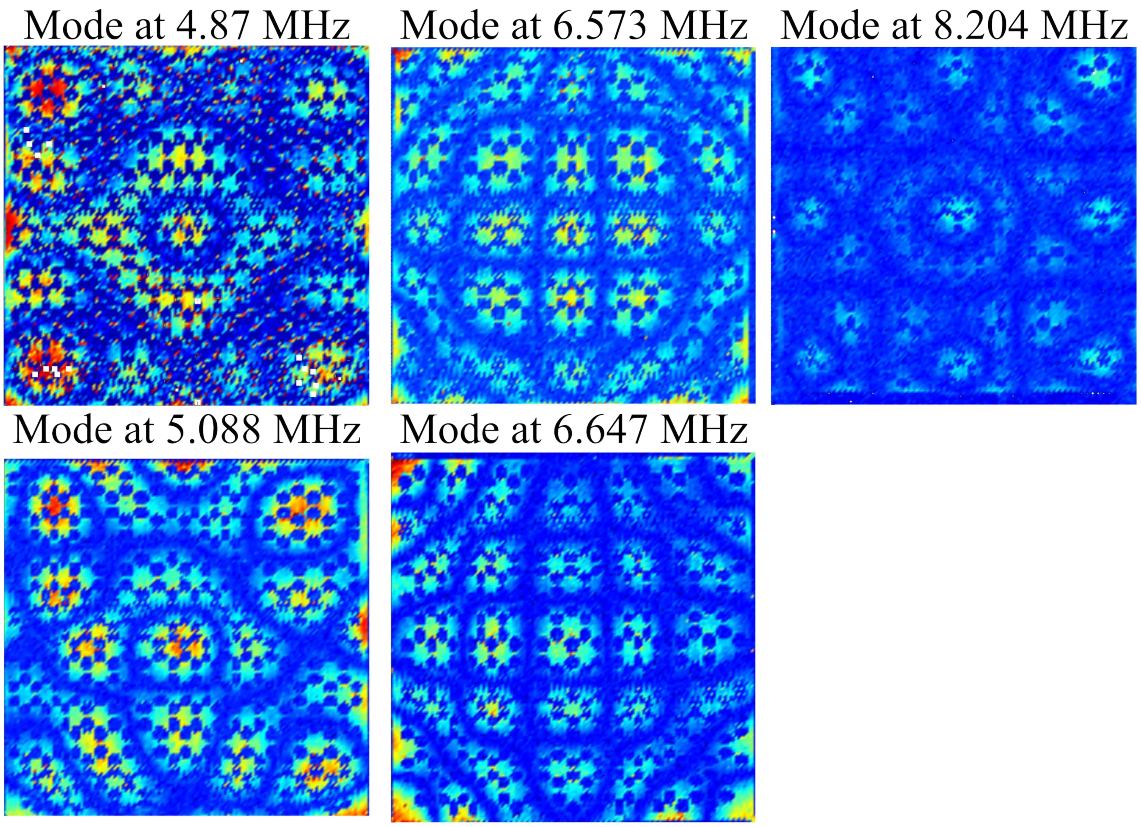

Figure J.4: Mode shapes actuated utilizing the electrostatic transducers on the prototype of the phononic band gap quasi-crystal that is depicted in Figure J.1.

J.2 Harmonic Analysis Measurements of the Fixed Electrode of the Electrostatic Transducers

Harmonic analysis measurements at three points on the fixed electrode of the S2 P^nBG QC are displayed in Figure J.5 juxtaposed with a harmonic analysis measurement taken at a point in the interior region of the S2 P^nBG QC. As may be viewed in Figure J.5, the fixed electrode of the S2 P^nBG QC displays resonant activity over the 50 kHz to 20 MHz range and so does not behave as an ideal fixed electrode.

In Figure J.5, it may be observed that the resonant peaks are more sparsely spaced in the harmonic analysis measurements taken at points 1, 2 and 3 on the fixed electrode than at the point on the S2 P^nBG QC. Thus, the spectrum of the fixed electrode and S2 P^nBG QC display unique traits. The particular harmonic analysis measurement taken at point 3 on the fixed electrode displays a notable absence of normal modes from approximately 9 MHz to 12 MHz, while the harmonic analysis measurements at points 1 and 2 appear to display some resonant peaks within the 9 MHz to 12 MHz frequency regime. The aforementioned absence of normal modes within the 9 MHz to 12 MHz frequency regime occurs only within the spectrum taken at one point and so may not represent band gap like phenomenon; however, may be further investigated.

The non-ideal behavior, discussed in this section, of the fixed electrode may be further investigated for its potential effect on the actuation of P^nBG QCs.

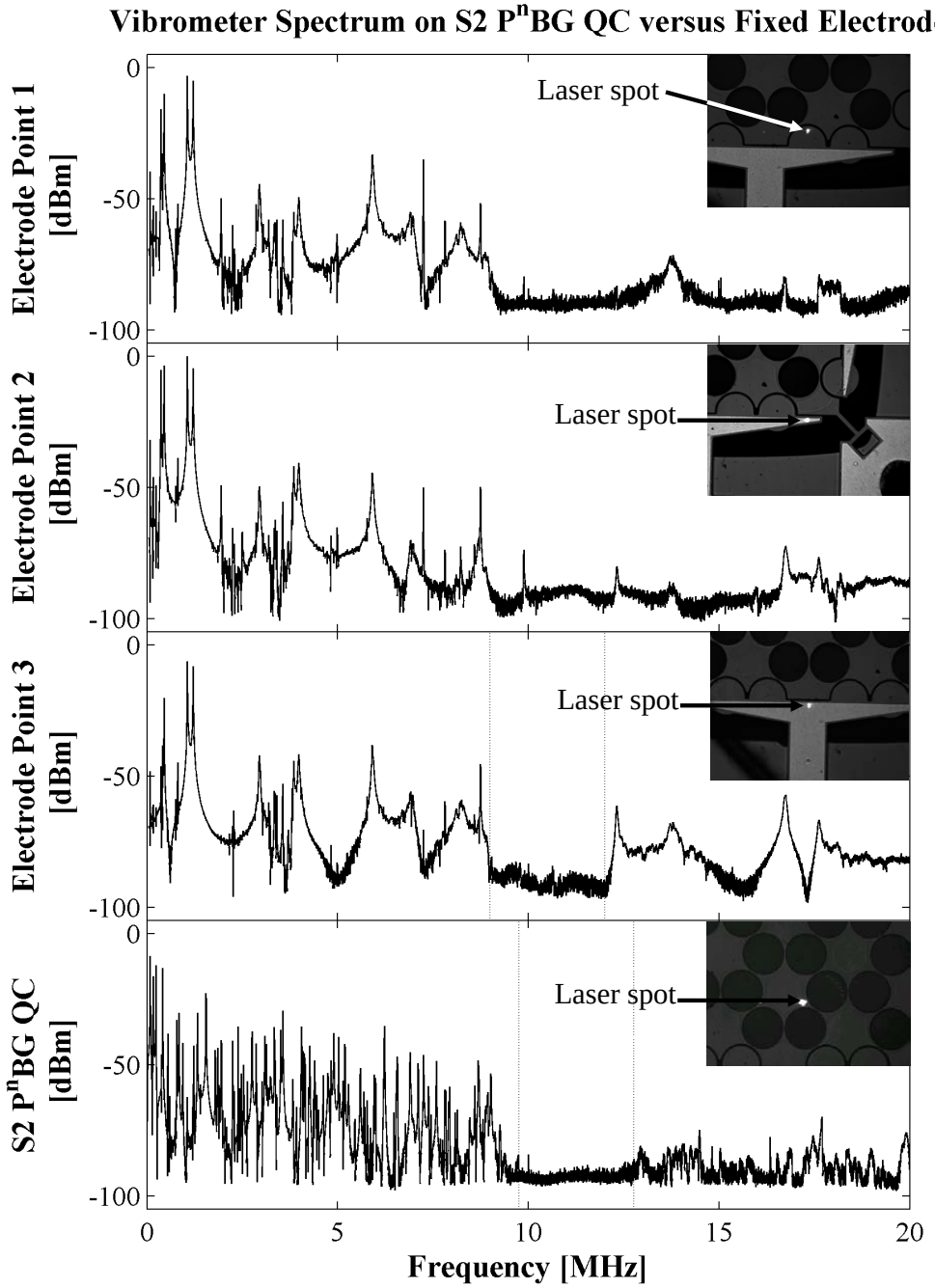

Figure J.5: Harmonic measurements at three points, denoted by the white laser spot in each inset, on the fixed electrode of the S2 phononic band gap quasi-crystal juxtaposed beside a harmonic measurement taken in the interior of the S2 phononic band gap quasi-crystal.

References

[1] M. M. Sigalas and E. Economou, *Solid State Communications*, vol. 86, no. 141, 1993.

[2] M. Sigalas and E. Economou, *Journal of Sound and Vibration*, vol. 158, p. 377, 1992.

[3] M. Kushwaha, P. Halevi, L. Dobrzynski, and B. Djafari-Rouhani, *Phys. Rev. Lett.*, vol. 71, no. 13, p. 2022, Sep. 1993.

[4] M. Kushwaha, P. Halevi, G. Martinez, L. Dobrzynski, and B. Djafari-Rouhani, "Theory of acoustic band structure of periodic elastic composites," *Phys. Rev. B.*, vol. 49, p. 2313, 1994.

[5] D. W. Wright, "Time-varying phononic crystals," Ph.D. dissertation, University of Tonrto, Toronto, 2010.

[6] S. Mohammadi *et al.*, "Large simultaneous band gaps for photonic and phononic crystal slabs," *Conference on Lasers and Electro-Optics/Quantum Electronics and Laser Science Conference and Photonic Applications Systems Technologies*, 2008.

[7] M. Ziaei-Moayyed *et al.*, "Silicon carbide phononic crystal cavities for microme-

chanical resonators," *Proceedings of the 24th International Conference on Micro-Electro Mechanical Systems, Cancun Mexico*, p. 13771381, 2011.

[8] Z. Liu *et al.*, "Locally resonant sonic materials," *Science*, pp. 1734–1736, 2000.

[9] P. Sheng and C. T. Chan, "Classical wave localization and spectral gap materials," *Zeitschrift Fur Kristallographie*, vol. 220, pp. 9–10, 2005.

[10] R. Norris, J. Hamel, and P. Nadeau, "Theoretical study of phononic band gap crystals with fractal inclusions," *Journal of Applied Physics*, vol. 103, no. 10, pp. 104 908–104 908–7, Mar. 2008.

[11] S. Halkjaer *et al.*, "Maximizing band gaps in plate structures," *Struct Multidisc Optim*, pp. 263–275, Jul. 2006.

[12] G. Gazonas *et al.*, "Genetic algorithm optimization of phononic bandgap structures," *International journal of solids and structures*, pp. 5851–5866, Jan. 2006.

[13] M. M. Sigalas and E. N. Economou, "Elastic waves in plates with periodically placed inclusions," *Journal of Applied Physics*, vol. 75, no. 6, pp. 2845–2850, Mar. 1994.

[14] M. Kafesaki and E. Economou, "Multiple-scattering theory for three-dimensional periodic acoustic composites," *Physical review B*, p. 993, Nov. 1999.

[15] M. Sigalas and E. Economou, "Band structure of elastic waves in two-dimensional systems," *Solid state communications*, pp. 141–143, Feb. 1993.

[16] F. Ulaby, *Fundamentals of Applied Electromagnetics*. Upper Saddle River, NJ: Prentice Hall, 2001.

[17] B. A. Auld, *Acoustic Fields and Waves in Solids, Volume I.* Malabar, FL: Krieger Publishing Company, 1973.

[18] M. M. Sigalas *et al.*, "Importance of coupling between longitudinal and transverse components for the creation of acoustic band gaps: The aluminum in mercury case," *Applied Physics Letters*, no. 16, pp. 2307–2309, Apr. 2000.

[19] B. A. Auld, *Acoustic Fields and Waves in Solids, Volume II.* Malabar, FL: Krieger Publishing Company, 1973.

[20] G. Kino, *Acoustic waves : devices, imaging, and analog signal processing.* Prentice Hall, 1987.

[21] B. E. Teich *et al.*, *Fundamentals of Photonics.* John Wiley and Sons, Inc., 1991.

[22] M. Palaniapan and L. Khine, "Micromechanical resonator with ultra-high quality factor," *Electronic Letters*, Sep. 2007.

[23] D. Weinstein, "Dielectrically transduced single-ended to differential mems filter," in *2006 IEEE International Solid-State Circuits Conference*, Feb. 2006.

[24] T. Mattila *et al.*, "A 12 mhz micromechanical bulk acoustic mode oscillator," *Sensors and actuators A*, pp. 1–9, Jun. 2002.

[25] S. Bhave and R. Howe, "Silicon nitride-on-silicon bar resonator using lateral electrostatic transducers," in *The 13th International Conference on Solid-State Sensors, Actuators and Microsystems*, 2005, pp. 2139–2142.

[26] G. G. Yaralioglu *et al.*, "Lamb wave devices using capacitive micromachined ultrasonic transducers," *Applied Physics Letters*, vol. 78, no. 1, 2001.

[27] M. Badi, "Capacitive micromachined ultrasonic Lamb wave transducers," Ph.D. dissertation, Stanford University, Stanford, 2004.

[28] O. Oralkan *et al.*, "Capacitive micromachined ultrasonic transducers: Next-generation arrays for acoustic imaging?" *IEEE Transactions on ultrasonics, ferroelectrics, and frequency control*, vol. 49, no. 11, pp. 1596–1610, Nov. 2002.

[29] A. Alastalo, "Analysis of a mems transmission line," *IEEE Transactions on Microwave Theory and Techniques*, pp. 1977–1981, Aug. 2003.

[30] A. Alastalo *et al.*, "Microelectromechanical delay lines with slow signal propagation," *J. Micromech.. Microeng.*, pp. 1854–1860, Aug. 2006.

[31] S. Bhave *et al.*, "Fully-differential poly-sic lame mode resonator and checkerboard filter," *Proceedings of the 18th IEEE International Conference on Micro Electro Mechanical Systems*, 2005.

[32] T.-T. Wu *et al.*, "Frequency band-gap measurement of two-dimensional air-silicon phononic crystals using layered slanted finger interdigital tranducers," *Journal of Applied Physics*, vol. 97, no. 094916, 2005.

[33] B. Bayram, "Acoustic crosstalk reduction method for cmut arrays," *2006 IEEE Ultrasonics Symposium.*

[34] S. Mohammadi *et al.*, "Support loss suppression in micromechanical resonators by the use of phononic band gap structures," *Proceedings of SPIE*, Feb. 2010.

[35] Y. Pennec *et al.*, "Tunable filtering and demultiplexing in phononic crystals with hollow cylinders," *Physical Review E*, vol. 69, pp. 1–6, Apr. 2004.

[36] Y. Zheng, "Biosensors on surface acoustic wave phononic band gap structures," *NNIN REU Site: Microelectronics Research Center, Georgia Institute of Technology*, p. 156, 2004.

[37] S. Datta, *Surface Acoustic Wave Devices*. Englewood Cliffs, NJ: Prentice Hall, 1986.

[38] A. Trusov and A. Shkel, "Capacitive detection in resonant mems with arbitrary amplitude of motion," *Journal of micromechanics and microengineering*, pp. 1583–1592, Jul. 2007.

[39] W. Johnson and L. Warne, "Electrophysics of micromechanical comb actuators," *Journal of microelectromechanical systems*, pp. 49–59, Mar. 1995.

[40] T. Hirano *et al.*, "Design, fabrication, and operation of submicron gap comb-drive microactuators," *Journal of microelectromechanical systems*, vol. 1, no. 1, pp. 52–59, Mar. 1992.

[41] Y. Sun *et al.*, "A bulk microfabricated multi-axis capacitive cellular force sensor using transverse comb drives," *J. Micromech. Microeng.*, pp. 832–840, Oct. 2002.

[42] S. Mohammadi *et al.*, "Complete phononic bandgaps and bandgap maps in two-dimensional silicon phononic crystal plates," *IEEE Electronics letters*, Aug. 2007.

[43] Y. Suxia, "Ultrasonic properties of phononic crystals," Ph.D. dissertation, Hong Kong Univ. of Science and Technology, Hong Kong, 2002.

[44] J. Sun and T. Wu, "The study of acoustic band gaps in 2-D air/aluminum and steel/epoxy phononic structure," *Key Engineering Materials*, vol. 270-273, pp. 1127–1134, 2004.

[45] J. Hamel and R. Norris, "Acoustic band gap filters: The next generation of micro-electro-mechanical filters for on-chip silicon radio frequency applications," *Proceedings of the 20th Canadian Conference on Electrical and Computer Engineering*, 2007.

[46] (2007) MEMSCAP - The Power of a Small World. [Online]. Available: http://www.memscap.com

[47] MEMSCAP foundry, "SOIMUMPs run 31."

[48] P. Sheng and C. T. Chan, "Classical wave localization and spectral gap materials," *Zeitschrift Fur Kristallographie*, vol. 220, pp. 9–10, 2005.

[49] S. John, *Phys. Rev. Lett.*, vol. 58, p. 2486, 1987.

[50] E. Yablonovitch, *Phys. Rev. Lett.*, vol. 58, p. 2059, 1987.

[51] F. Meseguer, M. Holgado, D. Caballero, N. Benaches, C. Lopez, J. Sanchez-Dehesa, and J. Llinares, "Two-dimensional elastic bandgap crystal to attenuate surface waves," *Journal of Lightwave Technology*, vol. 17, p. 2196, 1999.

[52] M. Sigalas, "Defect states of acoustic waves in a two-dimensional lattice of solid cylinders," *Journal of Applied Physics*, vol. 84, no. 6, 1998.

[53] C. Goffaux and J. Vigneron, "Theoretical study of a tunable phononic band gap system," *Phys. Rev. B*, vol. 64, p. 2001, 2001.

[54] M. Kushwaha and P. Halevi, "Band-gap engineering in periodic elastic composites," *Appl. Phys. Lett.*, vol. 64, p. 1085, 1994.

[55] J. Sanchez-Perez, D. Caballero, R. Martinez-Sala, C. Rubio, J. Sanchez-Dehesa, F. Meseguer, J. Llinares, and F. Galvez, "Sound attenuation by a two-dimensional array of rigid cylinders," *Phys. Rev. Lett.*, vol. 80, p. 5325, 1998.

[56] D. Bria, B. Djafari-Rouhani, A. Bousfia, E. E. Boudouti, and A. Nougaoui, "Absolute acoustic band gap in coupled multilayer structures," *Europhysics Letter*, vol. 55, p. 841, 2001.

[57] A. Khelif, P. Deymier, B. Djafari-Rouhani, J. Vasseur, and L. Dobrzynski, "Two-dimensional phononic crystal with tunable narrow pass band: application to a waveguide with selective frequency," *J. Appl. Phys.*, vol. 94, p. 1308, 2003.

[58] M. Kafesaki, M. Sigalas, and N. Garcia, "Frequency modulation in the transmittivity of wave guides in elastic-wave band-gap materials," *Phys. Rev. Lett.*, vol. 85, p. 4044, 2000.

[59] I. Psarobas and M. Sigalas, "Elastic band gaps in a fcc lattice of mercury spheres in aluminum," *Phys. Rev. B*, vol. 66, pp. 052 302–1, 2002.

[60] C. M. Soukoulis, *Localization and Propagation of Classical Waves in Random and Periodic Structures.* New York: Plenum, 1993.

[61] C. Goffaux and J. Vigneron, "Theoretical study of a tunable phononic band gap system," *Physical Review B*, vol. 64, no. 075118, 2001.

[62] X. Li *et al.*, "Large acoustic band gaps created by rotating square rods in two-dimensional periodic composites," *Journal of Physics D: Applied Physics*, vol. 36, pp. L15–L17, Dec. 2003.

[63] C. Soukoulis, *Photonic Crystals and Light Localization in the 21st Century.* Netherlands: Kluwer Academic Publishers, 2001, pp. 69–82.

[64] F. Meseguer and M. Holgado, "Rayleigh-wave attenuation by a semi-infinite two dimensional elastic-band-gap crystal," *Physical Review B*, vol. 59, no. 19, May 1999-I.

[65] R. James *et al.*, "Sonic bands, bandgaps, and defect states in layered structures-theory and experiment," *Journal of the Acoustical Society of America*, vol. 97, no. 4, pp. 2041–2047, Apr. 1995.

[66] F. M. de Espinosa, E. Jimenez, and M. Torres, "Ultrasonic band gap in a periodic two-dimensional composite," *Physical Review Letters*, vol. 80, no. 6, pp. 1208–1211, Feb. 1998.

[67] J. Snchez-Prez *et al.*, "Sound attenuation by a two-dimensional array of rigid cylinders," *Physical reivew letters*, pp. 5325–5328, Jun. 1998.

[68] C. Rubio *et al.*, "The existence of full gaps and deaf bands in two-dimensional sonic crystals," *Journal of Lightwave Technology*, vol. 17, no. 11, Nov. 1999.

[69] O. Sigmund and J. Jensen, "Systematic design of photonic band-gap materials and structures by topology optimization," *Phil. Trans. R. Soc. Lond. A*, pp. 1001–1019, Mar. 2003.

[70] A. Khelif *et al.*, "Complete band gaps in two-dimensional phononic crystal slabs," *Physical Review E*, 2006.

[71] J. Hsu and T. Wu, "Efficient formulation for band-structure calculations of two-dimensional phononic-crystal plates," *Physical Review B*, Oct. 2006.

[72] ——, "Lamb waves in binary locally resonant phononic plates with two-dimensional lattices," *Applied physics letters*, May 2007.

[73] R. Sainidou and N. Stefanou, "Guided and quasiguided elastic waves in phononic crystal slabs," *Physpical Review B*, May 2006.

[74] J. Vasseur *et al.*, "Experimental and theoretical evidence for the existence of absolute acoustic band gaps in two-dimensional solid phononic crystals," *Physical reivew letters*, pp. 3012–3015, Apr. 2001.

[75] J. Vasseur, "Waveguiding in supported phononic crystal plates," *Journal of physics: conference series.*

[76] P. Russell *et al.*, "Sonic band gaps in pcf preforms: enhancing the interaction of sound and light," *OPTICS EXPRESS*, p. 25552560, 2003.

[77] V. Laude *et al.*, "Phononic bandgap guidance of acoustic modes in photonic crystal fibers," *Physical Review B*, p. 14, 2005.

[78] P. Dainese *et al.*, "Raman-like light scattering from acoustic phonons in photonic crystal fiber," *OPTICS EXPRESS*, p. 41414150, 2006.

[79] D. Barker and W. Owens, "Us patent 7292740 - apparatus and method for controlling transmission through a photonic band gap crystal," Patent, 2007.

[80] M. Bernal, *Ferroelectric crystals for photonic applications.* Springer, 2009.

[81] T. Gorishnyy *et al.*, "Hypersonic phononic crystals," *Physical review letters*, p. 115501, Mar. 2005.

[82] S. Benchabane *et al.*, "Evidence for complete surface wave band gap in a piezoelectric phononic crystal," *Physical Review E*, 2006.

[83] A. Khelif *et al.*, "Ultrasonic and hypersonic phononic crystals," *Proc. of SPIE*, vol. 6901, pp. 1–10, 2008.

[84] R. Norris, "Two-dimensional phononic crystal simulation and analysis," Master's thesis, University of Waterloo, Waterloo, 2006.

[85] W. Yang, , and L. Chen, "The tunable acoustic band gaps of two-dimensional phononic crystals with a dielectric elastomer cylindrical actuator," *Smart Materials and Structures*, no. 1, pp. 1–6, Feb. 2008.

[86] R. C. Norris, P. Nieva, and J. S. Hamel, "Analytical analysis of a discrete mems diatomic mass-spring phononic band gap crystal for vibration stabilization applications," *Proceedings of IEEE Sensors 2008*, 2008.

[87] R. Olsson *et al.*, "Micromachined bulk wave acoustic bandgap devices," *Proceedings of the The 14th International Conference on Solid-State Sensors, Actuators and Microsystems, Lyon, France*, pp. 317–321, Jun. 2007.

[88] I. El-Kady *et al.*, "Phononic band-gap crystals for radio frequency communications," *Applied Physics Letters*, no. 23, pp. 1–3, Jun. 2008.

[89] R. Olsson *et al.*, "Microfabricated vhf acoustic crystals and waveguides," *Sensors and Actuators A: Physical*, p. 8793, 2008.

[90] S. Mohammadi *et al.*, "Evidence of large high frequency complete phononic band gaps in silicon phononic crystal plates," *Applied Physics Letters*, no. 22, pp. 1–3, Jun. 2008.

[91] N. Kuo *et al.*, "Microscale inverse acoustic band gap structure in aluminum nitride," *Applied Physics Letters*, pp. 1–3, 2009.

[92] S. Mohammadi *et al.*, "High-q micromechanical resonators in a two-dimensional phononic crystal slab," *Applied Physics Letters*, no. 5, Feb. 2009.

[93] N. Kuo and G. Piazza, "1 ghz phononic band gap structure in air/aluminum nitride for symmetric lamb waves," *Proceedings of the 24th International Conference on Micro-Electro Mechanical Systems, Cancun Mexico*, p. 740743, 2011.

[94] R. C. Norris, J. S. Hamel, and P. N. Nieva, "Silicon-itegrated phononic bandgap ccrystal platform for sensors and signal processing elements: Theory and experiment," *Proceedings of IEEE MEMS 2011*, 2011.

[95] O. Holmgren *et al.*, "Analysis of vibration modes in a micromechanical square-plate resonator," *J. Micromech. Microeng.*, vol. 19, no. 1, pp. 1–11, Dec. 2009.

[96] J. Lee and A. Seshia, "5.4-mhz single-crystal silicon wine glass mode disk resonator with quality factor of 2 million," *Sensors and Actuators A: Physical*, vol. 156, no. 1, pp. 28–35, Nov. 2009.

[97] S. Senturia, *Microsystem Design.* Norwell, Massachusetts: Kluwer Academic Publishers, 2001.

[98] K. Wang and C. Nguyen, "High-order medium frequency micromechanical electronic filters," *J. of Microelectromechanical Systems*, 1999.

[99] R. Weigel *et al.*, "Microwave acoustic materials, devices, and applications," *IEEE Transactions on Microwave Theory and Techniques*, vol. 50, no. 3, pp. 738–749, Mar. 2002.

[100] M. Sigalas and N. Garcia, "Theoretical study of three dimensional elastic band gaps with the finite-difference time-domain method," *Journal of Applied Physics*, vol. 87, no. 6, pp. 3122–3125, Mar. 2000.

[101] Y. Tanaka *et al.*, "Band structure of acoustic waves in phononic lattices: Two-

dimensional composites with large acoustic mismatch," *Physical review B*, pp. 7387–7392, Sep. 2000.

[102] Y. Cao *et al.*, "Finite difference time domain for band-structure calculations of two-dimensional phononic crystals," *Solid state communications*, pp. 539–543, Sep. 2004.

[103] W. Axmann and P. Kuchment, "An efficient finite element method for computing spectra of photonic and acoustic band-gap materials," *Journal of Computational Physics*, pp. 468–481, 1999.

[104] S. Zhang and J. C. J. Hua, "Experimental and theoretical evidence for the existence of broad forbidden gaps in the three-component composite," *Chinese Physics Letters*, pp. 1303–1305, Mar. 2003.

[105] Y. Liu and L. Gao, "Explicit dynamic finite element method for band-structure calculations of 2d phononic crystals," *Solid state communications*, pp. 89–93, Aug. 2007.

[106] C. Goffaux and J. Sanchez-Dehesa, "Two-dimensional phononic crystals studied using a variational method: Application to lattices of locally resonant materials," *Physical review B*, Apr. 2003.

[107] Z. Hou *et al.*, "Singularity of the bloch theorem in the fluid/solid phononic crystal," *Physical review B*, Jan. 2006.

[108] Z. Yan and Y. Wang, "Wavelet-based method for calculating elastic band gaps of two-dimensional phononic crystals," *Physical review B*, Dec. 2006.

[109] G. Wang *et al.*, "Lumped-mass method for the study of band structure in two-dimensional phononic crystals," *Physical review B*, May 2004.

[110] J. Jensen, "Phononic band gaps and vibrations in one- and two-dimensional mass-spring structures," *J. of Sound and Vib.*, vol. 266, no. 5, pp. 1053–1078, Oct. 2003.

[111] T. Ohminato and B. Chouet, "A free-surface boundary condition for including 3D topography in the finite-difference method," *Bulletin of the seismological society of america*, pp. 494–515, Apr. 1997.

[112] C. Kittel, *Introduction to Solid State Physics*. New York, London, Sydney: John Wiley Sons, Inc., 1966.

[113] R. Wei *et al.*, "Phononic band structure in a two-dimensional hybrid triangular graphite lattice," *Physica B*, vol. 404, p. 37953798, Jun. 2009.

[114] CMC. (2011, May) Canadian microelectronics corporation. [Online]. Available: http://www.cmc.ca

[115] K. Miller *et al.*, *SOIMUMPs Design Handbook, rev. 4.0*. MEMSCAP, 2004.

[116] D. Pozar, *Microwave engineering*. John Wiley Sons, Inc., 1998.

[117] L. Khine, "12.9mhz lame-mode differential soi bulk resonators," *TRANSDUCERS EUROSENSORS 2007*, pp. 1753–1756, 2007.

[118] L. Khine and M. Palaniapan, "High-q bulk-mode soi square resonators with straight-beam anchors," *Journal of Micromechanics and Microengineering*, vol. 19, no. 1, 2009.

[119] S. Rojas *et al.*, "Properties of silicon dioxide films prepared by low-pressure chemical vapor deposition from tetraethylorthosilicate," *Journal of Vacuum Science Technology B: Microelectronics and Nanometer Structures*, vol. 8, no. 6, pp. 1177–1184, Nov. 1990.

[120] G. Rebeiz, *RF MEMS THEORY, DESIGN AND TECHNOLOGY*. Hoboken, NJ: Wiley, 2003, pp. 327–328.

[121] ANSYS®, "Release 11.0."

[122] D. Halliday, R. Resnick, and J. Walker, *Fundamentals of Physics, Extended*. Hoboken, NJ: Wiley, 2005.

[123] L. Meirovitch, *Elements of vibration analysis*. New York, NY: McGraw-Hill, Inc, 1986.

[124] G. Rebeiz, *RF MEMS THEORY, DESIGN AND TECHNOLOGY*. Hoboken, NJ: Wiley, 2003, pp. 30–31.

[125] W. Thomson, *Vibration Theory and Applications*. Englewood Cliffs, N.J.: Prentice-Hall, Inc., 1965, p. 25.

[126] L. Meirovitch, *Elements of vibration analysis*. New York: McGraw-Hill Inc., 1986.

[127] T. Rossing and N. Fletcher, *Principles of vibration and sound, Second Edition*. New York, New York: Springer, 2004.

[128] Coventor, Inc., *CoventorWare Analyzer Version 2010 Reference MEMS and Microsystm Design*. www.coventor.com: CoventorWare, 2010.

[129] *Polytec Vibrometer Controller OFV-5000*. Polytec Inc., 1998.

[130] Coventor, Inc., *CoventorWare Analyzer Version 2010 Reference MEMS and Microsystm Design*. www.coventor.com: CoventorWare, 2010.

[131] D. Miller *et al.*, "Characteristics of a commercially available silicon-on-insulator mems material," *Sensors and Actuators A*, Apr. 2007.

[132] Ioffe physico-technical institute. (2008, Mar.) Mechanical properties, elastic constnants, lattive vibrations of silicon (si). [Online]. Available: http://www.ioffe.rssi.ru/SVA/NSM/Semicond/Si/mechanic.html

[133] W. Sharpe *et al.*, "Measurements of young's modulus, poisson's ratio, and tensile strength of polysilicon," *IEEE*, pp. 424–429, 1997.

[134] Micragem. (2011, May) Micralyne. [Online]. Available: http://www.micralyne.com/micragem/

[135] (2011, May) Veeco. [Online]. Available: http://www.veeco.com/

[136] Polytec. (2011, May) Polytec. [Online]. Available: http://www.polytec.com/us/

[137] W. Thomson, *Vibration Theory and Applications.* Englewood Cliffs, N.J.: Prentice-Hall, Inc., 1965.

[138] Coventor, Inc., *CoventorWare® ANALYZER version 2010 reference MEMS and microsystems design.* Coventor, Inc., 2010.

[139] G. Rebeiz, *RF MEMS THEORY, DESIGN AND TECHNOLOGY.* Hoboken, NJ: Wiley, 2003, p. 475.

[140] J. Kim, D. Cho, and R. Muller, "Why is (111) si a better mechanical material for mems?" *Transducers 2001, Munich, Germany*, pp. 662–665, Jun. 2001.

[141] ANSYS, Inc., *Release 11.0 Documentation for ANSYS Workbench.* ANSYS, Inc., 2011.

[142] L. Meirovitch, *Elements of vibration analysis.* New York: McGraw-Hill Inc., 1986, p. 225.

[143] P. G. Datskos *et al.*, "Nanocantilever signal transduction by electron transfer," *JOURNAL OF NANOSCIENCE AND NANOTECHNOLOGY*, vol. 2, no. 3/4, pp. 369–373, Feb. 2002.